# Ceramic powder-based hybrid binder jetting system

Qirong Chen

Université Polytechnique HAUTS-DE-FRANCE

INSA INSTITUT NATIONAL DES SCIENCES APPLIQUÉES HAUTS-DE-FRANCE

## Thèse de doctorat

## Pour obtenir le grade de Docteur de

**L'UNIVERSITÉ POLYTECHNIQUE HAUTS-DE-FRANCE – INSA HAUTS-DE-FRANCE**

Discipline, spécialité selon la liste des spécialités pour lesquelles l'École Doctorale est accréditée :

**Chimie des matériaux**

**Présentée et soutenue par Qirong CHEN**

**Le 19/01/2022, à Maubeuge**

**École doctorale :**

Ecole Doctorale Polytechnique Hauts-de-France (ED PHF n°635)

**Équipe de recherche, Laboratoire :**

Laboratoire de Matériaux Céramiques et de Mathématiques (CERAMATHS)

# Procédé hybride de fabrication additive par projection de liant sur lit de poudre céramique

**JURY**

**Président du jury**

- Jozef VLEUGELS, Professor in University, Katholieke Universiteit Leuven, Leuven

**Rapporteurs**

- Jens GÜNSTER, Professor in University, Bundesanstalt für Materialforschung und -prüfung, Berlin
- Ghislaine BERTRAND, Professor in University, CIRIMAT-ENSIACET, Université de Toulouse, Toulouse

**Examinateurs**

- Francis CAMBIER, Dr, President of ECerS, Belgium Ceramic Research Centre, Mons
- Hélio JORGE, Dr, Centro Technologico da Cerâmica e do Vidro, Coimbra
- Anne LERICHE, Professor in University, Université Polytechnique Hauts-de-France, LMCPA, Maubeuge (Thesis Director)
- Fabrice PETIT, Dr, Program Manager, Belgian Ceramic Research Centre, Mons (Thesis co-director)
- Enrique JUSTE, Dr, Project Leader, Belgian Ceramic Research Centre, Mons (Co-supervisor)
- Marie LASGORCEIX, Dr, Senior Lecturer, Université Polytechnique Hauts-de-France, LMCPA. Maubeuge (Co-supervisor)

**Membres invités**

- Emiel SPEETS, Dr, R&D Manager, Foseco Nederland BV, Hengelo
- Charles DUTERTE, Dr, R&D Manager, Optec Laser Systems, Frameries

# Table of Contents

**Table of Contents**

**Table of Contents**

**Table of Contents**

# List of abbreviations

| | |
|---|---|
| BJ | Binder Jetting |
| AM | Additive Manufacturing |
| PSD | Particle size distribution |
| T.D | True Density |
| RP | Rapid Prototyping |
| ASTM | Standard Terminology for Additive Manufacturing |
| SLA/SL | Stereolithography |
| DIY | Do-It-Yourself |
| SLM | Selective Laser Melting |
| SLS | Selective Laser Sintering |
| 3DP | 3D-Printing |
| LOM | Laminated Object Manufacturing |
| DIP | Direct Inkjet Printing |
| DIW | Direct Inkjet Writing |
| FDM | Fused Deposition Modelling |
| PBF | Powder Bed Fusion |
| CNC | Computer Numerical Controlling |
| CAD | Computer Aided Design |
| ffc | Flow factor coefficient |
| DEM | Discrete Element Modelling |
| FEM | Finite Element Modelling |
| DS | Double-Smoothing |
| DOD | Drop-on-Demand |
| CJ | Continuous-jet |
| LT | Layer Thickness |
| BS | Binder Saturation |
| PMMA | Polymethyl methacrylate |

| | |
|---|---|
| DTA | Differential thermal analysis |
| BAM | Bundesanstalt für Materialforschung und -prüfung |
| LBM | Laser Beam Melting |
| LSD | Layer-wise Slurry Deposition |
| PDC | Polymer-Derived Ceramic |
| FD | Freeze Drying |
| SP | Spray Drying |
| CSP | Cyclone fraction of Spray drying |
| SSA | Specific surface area |
| BET | Brunauer Emmet Teller |
| SEM | Scanning Electron Microscopy |
| TGA/TG | Thermogravimetric analysis |
| Micro/µ-CT | X-ray microtomography |
| PU | Polyurethane |
| ZTA | Zirconia toughed alumina parts |
| BSE | Back Scattered Electron |
| UV | Ultra-Violet |
| XRD | X-ray diffraction analysis |
| DLP | Digital Light Processing/Projection |
| SiC | Silicon Carbide |
| EBM | Electron Beam Melting |
| DED | Direct Energy Deposition |

## List of abbreviations

| | |
|---|---|
| LENS | Laser Engineered Net Shaping |
| LSF | Laser Solid Forming |
| DLF | Directed Light Fabrication |
| DMD | Direct Metal Deposition |
| EBAM | Electron Beam AM |
| WAAM | Wire + Arc AM |
| CIM | Ceramic Injection Molded |
| LPDM | Linear Packing Density Model |
| SSM | Solid Suspension Model |
| CPM | Compressible Packing Model |
| CPFT | Cumulative (volume) Percent Finer Than |
| AFDZ | Andreassen, Funk, Dinger and Zheng |
| SPACE | Software Package for the Assessment of Compositional Evaluation |
| ESA | Electric Sonic Amplitude |
| FWHM | Full width at half maximum |

## List of abbreviations

| | |
|---|---|
| $V_{Bulk}$ | Bulk volume / ml |
| $V_{Tapped}$ | Tapped volume / ml |
| $\sigma_1$ | Consolidation stress / $N/m^2$ |
| $\sigma_2$ | compression stress / $N/m^2$ |
| $F_a$ | Interparticle force / N |
| $m_g$ | Particle weight / g |
| Re | Reynolds number / a.u |
| We | Weber number / a.u |
| Oh | Ohnesorge number / a.u |
| $\rho$ | Density / $g/cm^3$ |
| $\upsilon$ | Droplet velocity / m/s |
| L | Characteristic length of the nozzle / m |
| $\mu$ | Viscosity / $N.s/m^2$ |
| $\sigma$ | Surface tension / N/m |
| $\upsilon_{min}$ | minimum ejecting speed / m/s |
| d | diameter of the nozzle / m (Chapter 1); adsorption depth / m (Appendix 3) |
| f(R) | Function of surface roughness |
| $V_{Binder}$ | Deposited binder amount in selected area / ml |
| $V_{Pores}$ | Pores volume in selected area / ml |
| p | Porosity / a.u |
| $V_{Selected}$ | Volume of binder depositing area / ml |
| $V_{Origin}$ | Deposited binder volume when dilation equals to 1 / ml |
| $\lambda_c$ | Cutoff (Roughness measurement) / a.u |
| Ra | Arithmetical mean deviation / µm |
| Rz | Maximum height of profile / µm |
| $\sigma_{sv}$ | Solid-vapor surface tension / N/m |
| $\sigma_{sl}$ | Solid-liquid interfacial tension of the liquid drop on solid substrate / N/m |
| $\sigma_{lv}$ | Liquid -vapor surface tension / N/m |
| $\theta$ | Contact angle / ° (Chapter 3); Angle of connected surfaces after laser treatment / ° (Chapter 4); Angle of repose / ° (Appendix 2); Angle that the cavity wall / ° (Appendix 3) |
| $W_a$ | Adhesion work / $J/m^2$ |
| $W_c$ | Cohesion work / $J/m^2$ |
| h | Penetration depth in Washburn equation / m |
| t | time / s |
| r | Pore radius / m |
| $\eta$ | Dynamic viscosity / $N.s/m^2$ |
| $P_c$ | Capillary pressure / pascal |
| $\zeta$ | Zeta potential / mV |
| $T_{pre1}$ | Pre-sintering temperature before infiltration / ℃ |
| $T_{pre2}$ | Pre-sintering temperature between infiltrations / ℃ |
| $F_g$ | Gravity / N |
| $F_b$ | Buoyancy / N |
| $F_c$ | Capillary force / N |
| $I_{a1}$, $I_{a2}$, $I_{a3}$ | first, second, third absorbed energy |

**List of abbreviations**

| | |
|---|---|
| $I_{r1}$, $I_{r2}$, $I_{r3}$ | first, second, third reflected energy |
| $d_{10}$ | diameter of a sphere at which 10% of the particles in the sample are smaller |
| $d_{50}$ | diameter of a sphere at which 50% of the particles in the sample are smaller |
| $d_{90}$ | diameter of a sphere at which 90% of the particles in the sample are smaller |
| PRF | Pulse repetition frequency / kHz |
| WF | Waveform number / a.u |
| $F_0$ | Laser fluence / J/cm$^2$ |
| P | Power / w |
| $\omega_0$ | Beam waist / μm |
| E | Laser energy / J |
| f | Frequency / Hz |
| $\upsilon_{ls}$ | Laser scanning speed / mm/s |
| $r_s$ | Curvature radius for sharpness / μm |
| $d_m$ | Particle size of mixed composition / μm |
| $D_m$ | Maximum particle size / μm |
| n | Degree of an "ideal" curve equation / a.u (Appendix 2); number of laser reflections / a.u (Appendix 3) |
| $T_n$ | Index relies on maximum size of aggregate and "ideal" curve degree / a.u |
| q | Distribution index / a.u |
| $d_{m0}$ | Minimum particle size of the distribution / μm |
| $f^*$ | Maximum packing ratio of whole system / % |
| $f_s$ | Fraction of small particles / % |
| $f_l$ | Fraction of coarse particles / % |
| X | Proportion of large particles in mixed system / % |
| $X^*$ | Whole system / a.u |
| $f_1$ | Relative density of the whole system (more large particles) / % |
| $f_2$ | Relative density of whole system (more small particles) / % |
| $\nu_n$ | Volume fraction of voids in finest component / % |
| V | Volume of the solid / ml |
| $X_n$ | volume fraction of finest component / ml |
| $Q_a$ | Absorbed laser energy / J |
| $C_P$ | Specific heat at constant pressure / J/kg/K |
| $\kappa$ | Thermal conductivity / w/ (m.K) |
| $\alpha$ | Thermal diffusivity / m$^2$/s |
| $\tau$ | Critical thermal relaxation time / s |
| $V_{evaporation}$ | Liquid-vapour velocity / m/s |

## List of abbreviations

| | |
|---|---|
| $d_{evaporation}$ | Vaporization depth / m |
| c | Light speed, $3*10^8$ m/s |
| $T_b$ | Boiling point / K |
| $L_V$ | Latent heat of vaporization / J/kg |
| $t_P$ | Laser ON-time / s |
| $d_{ablation}$ | Ablation depth / m |
| D | Ablation crater diameter / m |
| $Q_{th}$ | Threshold laser energy / J |
| $\mu_a$ | Adsorption coefficient of the ceramic / $m^{-1}$ |
| $F_{th}(N)$ | Ablation threshold with N effective pulses / $J/cm^2$ |
| N | Effective number of pulses / a.u |
| S | Incubation coefficient / a.u |
| CS | Compressive strength / Pascal |
| F | Rupture load / N |
| $l_1$, $l_2$ | side lengths of the cuboids / m |

# List of abbreviations

# List of Figures

**List of Figures**

**List of Figures**

**List of Figures**

**List of Figures**

## List of Figures

# List of Tables

## List of Tables

# Introduction

Advanced ceramics are widely used in high-end engineering due to their low density, outstanding mechanical strength alongside with their excellent thermal, corrosion, and wear resistance. However, shaping ceramics using conventional manufacturing technologies remains highly challenging, time-consuming, and practically limited in terms of achievable designs.

These drawbacks restrict an even wider use of ceramics despite their formidable potential. Additive manufacturing (AM) technology holds the promise to fabricate complex shape ceramic parts with rapidity and cost-efficiency. Numerous researches have been conducted on AM with ceramic materials to unleash its potential in different industrial sectors, such as medical engineering, aerospace, filtration industry, etc. However, AM is still restricted by numerous issues which inhibit further development.

In an attempt to overcome these limitations, the European research project DOC-3D-PRINTING (cordis.europa.eu/project/764935) was established in the framework programme H2020 / Marie Skłodowska-Curie Actions to develop the whole value chain of ceramics 3D printing with a special emphasis on medical and aerospace applications. The project covers all aspects of AM from the manufacturing of feedstocks to the development of new processes/technologies and even the evaluation of products for commercialization. The whole team includes six academic, one non-profit association, and seven non-academic partners with varied experiences. There are in total 14 early-stage researchers (Ph.D.) involved in 5 packages: materials feedstock, process equipment, design products, testing standards, modeling and characterizations.

The presented work belongs to the 1st package: materials feedstocks, which aims at developing feedstocks customized for 3D-printing at a reduced cost. Specifically, the present three-years long doctoral study focuses on “Ceramic powder-based hybrid binder jetting process” which was mostly conducted in Belgian Ceramic Research Centre (BCRC, Mons, Belgium). Part of the job (some characterizations, impregnation tests) was carried out in Laboratoire des Matériaux Céramiques et Procédés Associés (LMCPA), Université Polytechnique Hauts-de-France (UPHF, Maubeuge, France) for a total duration of approx. 3 months. The presenter also stayed for 5 weeks in Marion Technologies (Pamiers, France) to prepare alumina powder optimized for binder jetting. The work done there consisted in alumina synthesis and its subsequent spray drying with the aim to get a deeper comprehension of the processes.

# Introduction

Binder jetting (BJ) which consists in binding powders by depositing binder is one of the most promising techniques in the additive manufacturing landscape. It combines indeed several advantages: it is fast, cost-efficient, compatible with a broad range of materials and a real free-form technology. Most of the time, flowability is a powder pre-requisite to ensure the smoothness of powder bed and no cracks formation. This explains that spray dried spherical powders are preferred. Ceramic objects have still to be sintered after printing but the full density cannot be achieved: as the process usually fails in obtaining highly compact powder beds, the sintered bodies are usually not dense. Combined with the rather poor finished surface of the printed bodies, BJ is not considered as suitable to manufacture structurally resistant parts. These two main limitations are still plaguing BJ despite the numerous advantages this technology offers. Numerous researches have been conducted to overcome these limitations. The progresses are real but limited and very often at the expense of new and unexpected limitations. The task of improving BJ is complexified by the lack of systematic and comprehensive studies to develop suitable ceramic powder feedstocks.

The present manuscript reports new results aiming to overcome the two major BJ limitations: the low sintered density and the raw finished surface of manufactured parts. The study was conducted by using a customized binder jetting machine designed jointly by the BCRC and OPTEC Laser Systems (Frameries, Belgium). This machine is fully “opened” meaning that every internal system (hardware and/or software) can be manipulated easily in order to improve the process.

After a review of the literature (Chapter 1), the powder properties (particle size distribution (PSD), morphology, flowability, packing rate, and roughness of powder beds), as well as printing parameters (recoating speed, binder saturation, and layer thickness) were optimized in Chapter 2 to reproduce state-of-the-art results in terms of density, roughness, and mechanical strength. The influence of different factors was carefully studied. This first part of our study was a baseline over which original experiments were carried out to further enhance the sintered density and roughness.

To overcome the first challenge which is the increase of part density, an efficient yet simple post-impregnation process was developed and the results are presented in Chapter 3. Printed bodies were first pre-sintered and then impregnated with pure ceramic suspensions before final sintering. The influence of several parameters such as multiple impregnations, slurry solid loading, pre-sintering temperature, impregnation duration, and particle size distribution of powders used for printing were studied in different ways using various characterization techniques. Using this methodology, sintered densities up to 90% of the T.D have been obtained which presents an improvement of more than 30% over the non-infiltrated samples.

Finally, preliminary results on a new approach to improve the finished surface of printed bodies which was the second challenge of the work are reported in Chapter 4. A laser was mounted in the BJ machine with the aim to refine the contours of each printed layer through a controlled ablation of the powder beds. Although this hybrid technology is still very crude, dramatic improvements of surface finish and sharpness of simple shapes are reported (approx. by a factor 3).

# Introduction

# Chapter 1. Current state of the art

## 1. Ceramic materials

Ceramic is one of the most ancient synthetic materials whose first traces date back several thousand years. Once humans discovered that clay could be found in abundance and formed into objects by first mixing with water and then firing, a key industry was born. The oldest ceramic artefact is dated as early as 28,000 BC during the late Palaeolithic period. The first pottery appeared in China dated to 18,000 – 17,000 BC. The use of ceramic materials increased intensively during the Neolithic period. Clay-based ceramic were used to fabricate containers, art objects, tiles and bricks in the early time. Until the 16$^{th}$ century, the expertise of China was strongly recognized in the development of high temperature kilns capable to sinter porcelain with very low porosity. After the industrial revolution, advanced ceramic materials based on purified natural raw materials or chemically synthesized powders have significantly developed in various fields including electronic, optical, medical, energy, automotive and aerospace. Advanced ceramics are now considered as strategic materials thanks to their excellent properties.

Typical advanced ceramics include alumina, zirconia, silicon carbide, silicon nitride and titania-based materials. These ceramics present good performance in terms of hardness, physical stability, extreme heat resistance, chemical inertness, biocompatibility, superior electrical properties etc. However, they also suffer from a low impact strength and a high brittleness (in comparison with more ductile materials like metals)[1]. Traditional shaping methods for ceramics include slip casting, tape casting, shell casting, gel casting, pressing and so on [2]. Nevertheless, complex shapes are extremely complicated to fabricate because casting molds cannot be made easily, machining is tricky and geometrically limited. On the contrary, Additive Manufacturing (AM) seems to be perfectly suited for the shaping of ceramics. With the promise to be design-independent with much less waste compared to subtractive manufacturing, AM appears even more interesting for ceramics than it is for other materials[3-6].

## 2. Additive Manufacturing

### 2.1. Introduction

Additive manufacturing (AM) also named as 3D printing or Rapid Prototyping (RP) refers to the manufacturing of 3D products by the addition of successive layers of materials. The definition is given by ASTM F2792-12a (Standard Terminology for Additive Manufacturing

Technologies) as the "process of joining materials to make objects from 3D model data, usually layer upon layer, as opposed to subtractive manufacturing methodologies, such as traditional machining" [7]. The first concept was introduced by Charles Hull in 1983 in a process known as stereolithography (SLA) [3]. Afterwards, other technologies were developed subsequently relying on different physical or chemical principles as well as other materials. AM technologies have progressed significantly in recent years and nowadays they are widely used in various researches and industries. Compared to traditional manufacturing, AM can be much more efficient when it comes to producing prototypes or small series of parts showing high level of geometrical complexity. Those technologies are characterized by a very rational use of raw materials, producing less waste compared to subtractive technologies. They are also much easier to implement than conventional manufacturing methods as they mostly rely on the definition of a STL file which can be seen as the numerical twin of the part to be produced. The complete sequence of any AM process is graphically pictured in Figure 1.

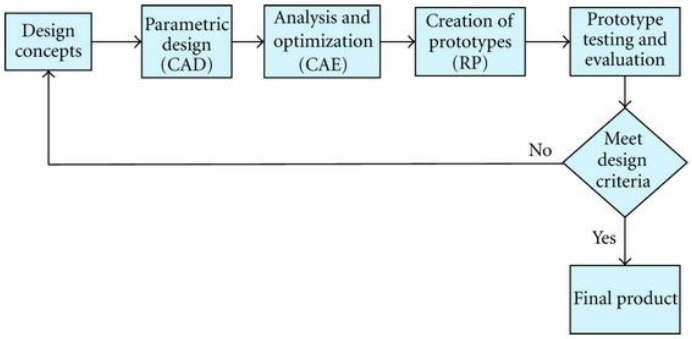


Figure 1. AM development cycle[8]

Due to the advantages in designing, the overall rapidity and cost-efficiency of AM, these technologies have spread easily in certain industries. They show a very large potential for customization of parts in various sectors: aerospace, automotive, biomedical [9], architectural modelling, energy applications, arts or even do-it-yourself (DIY) [3, 10-12]. Since AM avoids adding materials cost due to mold making and ease the process from traditional machining to get a part, it really eliminates several of the typical problems encountered in conventional processes. AM has also grown commercially in recent years with the emergence of desktop scale printers very used-friendly for day-to-day use. AM manufacturers have emerged and grow up well such as Electro Optical Systems (EOS) in Germany, Arcam in Sweden, 3D Systems, Optomec, Z Corporation in US, Lithoz in Austria, Admatec in the Netherland, 3D-Ceram in France among many others [10]. Current uses of AM in the industry are many folds. Printed models are used for architecture design, medical and automobile applications. Precision parts are now routinely produced by selective laser sintering / melting (SLS/SLM) in automotive and aerospace. At the same time, some companies are now producing 3D-printed implants to help patient recovery from diseases or accidents. More recently, the building sector

started to consider AM as a valuable approach to rapidly erect houses. Some were effectively built in a few hours in China demonstrating great potential [13].

Despite tremendous progresses, AM is still plagued by numerous issues which inhibit its forward development. According to Tuan D. Ngo et al. [3], void formation, anisotropic microstructure and mechanical properties, divergent from design to execution and layer-by-layer appearance are the main challenges for AM. Printing speed and cost reduction are not satisfactory neither and need to be improved for a full adoption in mass production. Improving AM reliability by working on raw materials to ensure their efficiency and performance stability over time (and production batches) is also a critical requirement. Another limitation of AM comes from the multiplicity of available technologies. No technology is by far superior to the others. On the contrary, each one has its own benefit and drawback. Hence, according to the technical specifications of the parts, the AM technology has to be carefully selected [10]. The advantages and limitations of each AM process are discussed in more details in section 2.2 (Chapter 1).

## 2.2. Classification

Different classification systems have been used and reported according to the personal expertise and convenience of different researchers. A common classification consists in dividing AM according to starting materials: (1) liquid based (Stereolithography, Multi jet moulding, etc); (2) filament/paste based (Fused deposition modelling, Robocasting, etc); (3) powder based (Binder jetting/3D printing, Selective laser sintering, Selective laser melting, Electron beam melting, etc) and (4) solid sheet (Laminated object manufacturing)[10]. For ceramics, certain authors have proposed another classification based on the underlying physical principles, choice of materials and the requirement of a post-treatment after printing or not (Zocca et al. [4] Table 1). AM technologies are categorized to powder-based 3D printing (P-3DP/BJ), powder-based selective laser sintering (P-SLS), stereolithography (SLA/SL), slurry-based 3DP (S-3DP), laminated object manufacturing (LOM), direct inkjet printing (DIP), filament extrusion 3D printing: direct ink writing (DIW), robocasting and fused deposition modelling (FDM). For the assessment of part dimension, dimensional indexes are utilized (XS = 100 µm, S =1 mm, M = 10 mm, L = 0.1 m and XL = 1 m). On top of these three features, they further enhance the classification by adding new contents to precise the characteristics of each process: density of struts, monolithic parts or not, dimension, surface quality, precision, cost, direct or indirect methods. Among these parameters, struts density relates to technologies that can provide a dense material without any residual porosity. Monolithic refers to as technologies able to generate parts without residual microporosity regardless of volume and thickness. Cost involves feedstock price and equipment capex. Finally, direct means that the material is directly deposited only in the selected position giving the desired shape of parts. On

the other hand, indirect means that excess materials surrounding the printed parts need to be removed after printing to release the part. Both direct and indirect AM processes present advantages and drawbacks depending on part requirements. Although more complicated, this classification is interesting for researchers as it brings a deeper understanding of each individual technologies.

Also, regarding to the production of ceramic parts in single- and multi- step processes, AM processes may also be separated into single-step AM and multi-steps AM (which in fact are closely related to direct / indirect methods). Principles of this classification have been clarified by the authors as a way to understand the origin of defects in AM parts. To explain more, thermal cracks are always caused by thermal shocks generated by the laser-beam heating in single-step processes while cracks are caused by thermal treatment after printing in a multi-step process [14].

With the development of AM process, new hybrid AM technologies have also been invented that further complexifies the classification. One of the clearest classifications is that from ASTM (ASTM F2792-12a) that is shown Figure 2. This one states that there are 8 families of Additive Manufacturing processes including hybrid as the $8^{th}$ one (others are vat photopolymerization (SLA/SL), powder bed fusion (PBF/SLS/SLM), binder jetting (3DP/BJ), materials jetting, sheet lamination (LOM), materials extrusion (FDM/DIW/Robocasting), direct energy deposition and other hybrid technologies) [15]. This classification is simple and can be easily extended to encompass new technologies. In this classification, the hybrid family comprises all technologies combining at least two distinctive processes in one single machine setup. Some examples of AM shaping of ceramics with these different technologies are given in Appendix 1.

Table 1. Main Characteristics of Additive Manufacturing Technologies used for Ceramics from[4]

| Technology | Feedstock | Dense struts (dense ceramic, but limited volume) | Monolithic | Part dimension (size that can be produced economically) | Surface (quality of parts, not of single struts) | Precision | Cost of feedstock preparation | Cost of process | Direct versus indirect |
|---|---|---|---|---|---|---|---|---|---|
| P-3DP/BJ | Solid | No | No | M-XL | Medium | 100 µm | Low | Medium | Indirect |
| P-SLS | Solid | No | No | M-L | Medium | 100 µm | Low | High | Indirect |
| P-SLM | Solid | No | No | M-L | Medium | 100 µm | Low | High | Indirect |
| S-3DP/BJ | Liquid | Yes | Yes | M-XL | High | 100 µm | Low | Medium | Indirect |
| S-SLS | Liquid | Yes | Yes | M-L | High | 100 µm | Low | High | Indirect |
| SLA/SL | Liquid | Yes | No | XS-M | High | < 1 µm | Medium-High | Medium | Indirect |
| LOM | Solid | Yes | Yes | M-L | Medium | 100 µm | Medium | Medium | Indirect |
| DIW/ Robocasting | Liquid | Yes | No | S-XL | Low | 10 µm | Low-Medium | Low | Direct |
| FDM | Liquid | Yes | No | S-M | Low | 100 µm | Medium | Low | Direct |
| DIP | Liquid | Yes | Yes | S-M | Medium | 10 µm | High | Medium | Direct |
| Direct Dep | Liquid | | | | Low | | | | Direct |

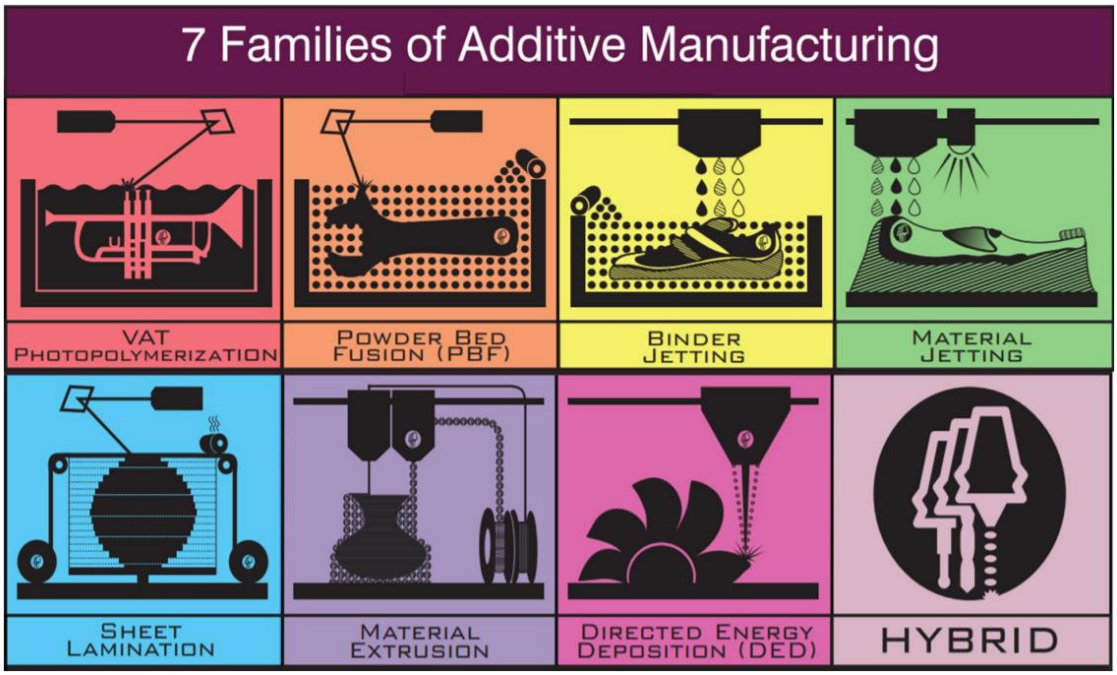


Figure 2. 7 Families of Additive Manufacturing from[15]

## 2.3. Challenges of AM for ceramic materials

Each current AM processes has its own advantages and drawbacks. On the one hand, the specificities of each technique limit the materials that can be used with it. On the other hand, the properties of parts that can be obtained are also restricted by the distinctive features of each technology. For instance, SLA is not suitable when it comes to print highly massive parts because of debinding issues. Densities of SLA parts are however usually not an issue. On the opposite, conventional BJ is known to be suitable to produce large objects but with a low density. It is not limited either in terms of materials. Considering now PBF, the available machines on the market are designed for metals but unfortunately not suitable for ceramics. As some ceramic materials have low absorption capacity and sensitivity to the typical laser wavelength, optical additives must be added to the ceramic powder, which obviously changes the chemistry of the raw materials. A second limitation comes from the high sensitivity of ceramics to thermal shock which requires heated bed and enclosure at very high temperatures (more than 1000°C) to prevent those defects. These technologies are not yet readily available on the market. Resolution of parts fabricated by robocasting and FDM remains poor and removal of the organic phase remains a challenging task, similar to SLA. To improve the resolution, the size of the nozzle must be small but then the processes are losing reliability and productivity.

In the opinion of N.Travitzky et al.[16], the most severe limitation for AM is related to the restrictions caused by material selection and aspects linked to the inner architectural design of the manufactured parts. They have suggested that the future progress in the field should not

only be based on the improvement of the existing technologies but also on the development of new methods. Hybridization is an attempt to overcome the limitations of existing approaches among others. From Zocca et al.[4], the challenges posed by AM in general are even more pronounced for ceramics and are multiple:

1) the superior physico-chemical properties of advanced ceramics critically depend on their microstructure, which is linked to particle characteristics and sintering, so as their composition;

2) monolithic dense ceramic parts are generally produced through fine particles which unfortunately show a poor flowability not compatible with most powder-bed AM technologies: spreading fine and sub-micrometer powders into thin layers is almost impossible using conventional recoating methods. Fine particles are inclined to agglomeration and electrostatic charging leading to poor packing density of powder bed.

As a general concern of AM with ceramic materials, dimensional accuracy, isotropic behaviour, achieved final density and surface finish still remain critical issues as parts are obtained in a layer-by-layer approach [16]. Rough surfaces and dimensional inaccuracy of the printed parts may result from 'stair-effects' due to slicing of the object or the use of very coarse powders. Post-treatments such as computer numerical controlled (CNC) milling or decreasing the layer thickness is a part of the solution but all these comes at the expense of higher costs and energy consumption.

# 3. Binder jetting

## 3.1. Brief introduction

### 3.1.1. History and mechanism of binder jetting

Binder jetting (BJ) was invented and patented in 1993 at MIT by M.J.Cima et al[17, 18].The first scientific interest for ceramic BJ was the manufacturing of parts for use as shells and cores for casting of metal components [19]. Figure 3 depicts the principle of BJ. Powders are deposited by a recoater (i.e., a feeding tool) from the powder tank to the manufacturing tank. The recoater can be a wiper or roller, this second choice being more typical and efficient[20]. A software is used to slice the 3D CAD file (Computer aided design) of the object and prepare a numerical twin of each layer before printing. To ensure consolidation of the layers, a liquid binder is selectively deposited on the powder bed to reproduce each layer, binding particles together. Some systems use a heater to evaporate the solvent contained in the binder, control the moisture or even cure the binder after deposition [20]. After the binder has been deposited, the liquid coats particles and spread in the powder bed. As the liquid attempts to minimize the surface energy by decreasing the ratio of surface/volume and the area of liquid/vapor interface, a capillary pressure is generated which brings together neighbor particles. This is the core

mechanism of the binder jetting process. Additionally, the particles may bring even closer after binder drying which is also beneficial as it may causes higher densification levels. The part is built up through a layer-by-layer printing and the final part is cleaned through a de-powdering step which consists in removing the excess powder surrounding the part. The resolution of the printed part is partly related to the layer thickness (which is controlled by the piston moving the manufacturing platform) and by the particle size. The first research conducted by the group of M.J.Cima has certainly laid a solid foundation of binder jetting technology for further researches.

BJ is still the fastest existing AM technology which makes it highly cost-efficient as already said. It is also compatible with a broad range of materials, such like ceramics, polymers but also metals. There is virtually no size limitation for the printed parts: some commercial machines are now used to print architectural items at 1:1 scale.

Despite obvious advantages, BJ is still plagued by original sins. The rather low packing density of powder beds and the use of coarse spherical particles (in order to ensure flowability) are responsible of low sintered density and poor finished surfaces. Post-treatments are sometimes considered to enhance the quality of products (like molten metal infiltration). Nonetheless, it is also essential to try to eliminate these disadvantages by optimizing (if possible) the printing process itself without recourse to any subsequent treatments. Various review articles have discussed BJ and compare it with other AM techniques, giving some insight of future outlook as well [3-6, 8-16, 20-36].

From a commercial point of view, the first machines were marketed by Z Corporation as soon as 1994 [22]. Later, other companies successfully developed their own technology such as ExOne and Voxeljet, further increasing the number of compatible materials and potential uses of the technology. After patents expiration, additional companies entered this market including Desktop Metal and more recently HP[20, 37]. The build rate of 3D printing (3DP is the other name of BJ) is limited by the rate at which binder can be delivered to the powder bed [38].

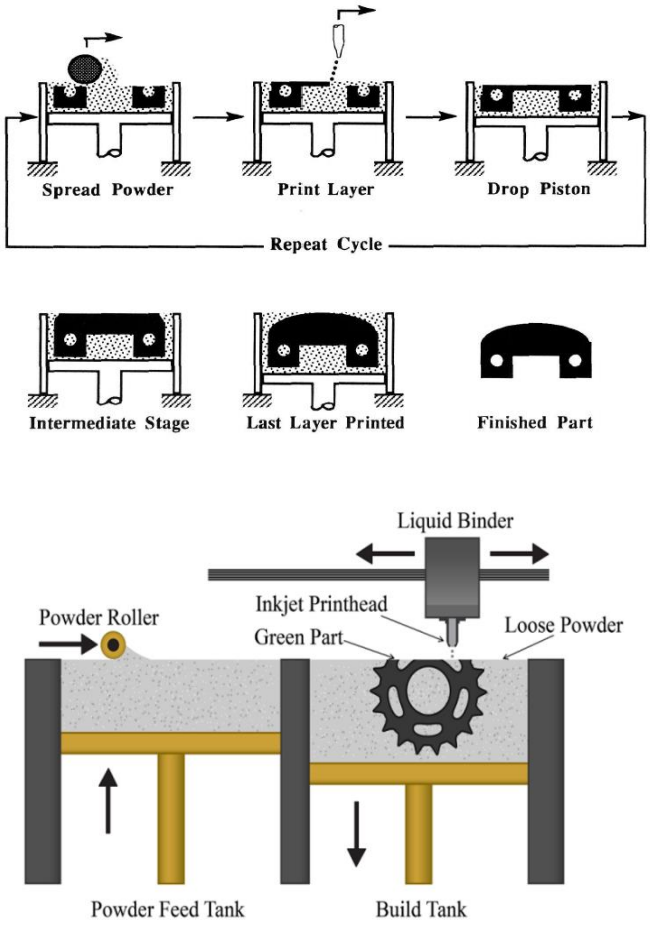


Figure 3. Binder jetting process. Upper: Binder jetting principle from [19]; Latter: Binder jetting process (Image courtesy of 3DEO)

Figure 4 illustrates the major components included in any binder jetting machine as summarized by Du wenchao et al. [22]. Powder and binder are prepared prior printing. After printing (or during printing depending on the device/binder), the green parts are usually heated up to a specific temperature (typically 200 ℃). Most of the time, the thermal treatment aims at activating and strengthening the green parts by polymerization, cross-linking, solvent evaporation, or other mechanisms according to the characteristics of materials themselves. Afterwards, debinding is conducted to remove the binder inside of the 'green part' by heating it between 600 ℃ to 800 ℃ with a certain dwelling time. Heating rate requires to be carefully controlled and the program is determined using TGA analysis. After debinding, sintering is conducted by heating the part to the suitable temperature (lower than the melting temperature of ceramic material) during a certain time. The sintering step increases the density by mass diffusion across the boundaries and inside ceramic particles. Some relevant details of debinding and sintering will be discussed in the subsequent section 3.3 (Chapter 1).

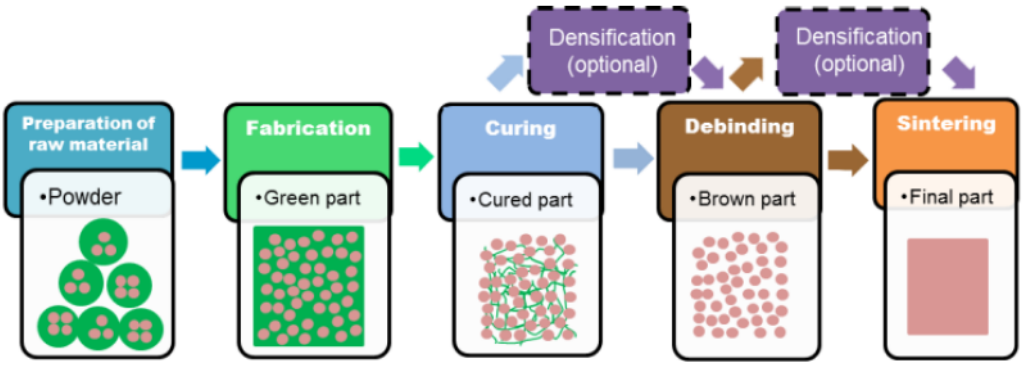


Figure 4. Steps of binder jetting additive manufacturing from [22]

### 3.1.2. Comparison with other AM techniques

Compared with other AM technologies, BJ presents different advantages that have been well summarized in [6]. The technology is virtually compatible with every material available in a powdered form and there is no extensive laser experimentation conducted compared with SLM / SLS[39]. Nevertheless, BJ parts require further thermal treatment while SLS/SLM directly finish the step during printing process. Some liquid binders used in BJ are water-based and almost no organic phases exist in the system which simplifies the thermal processing after printing in comparison with SLA[40]. Easiness of scale up also gives superiority to BJ since the product size and resolution are not limited as they are in other approaches, such as DIW, FDM and SLA. Though final parts fabricated from conventional BJ have higher porosity, it can be actually suitable for scaffold fabrication, filter, membranes … which all need porous bodies [41, 42]. Thus, BJ shows greater potential than traditional machining and other AM techniques thanks to high flexibility to produce parts for different industrial sectors. This will be discussed more in the next section. Build rate in BJ printing could reach up to 1.1 inches per hour (z-direction) regardless of object size, a number which is typically 10 times larger than in other AM processes [43]. Furthermore, very large parts can be printed using BJ. For instance, the workpiece shown in Figure 5 [4] produced by Desamanera is 1.28 m wide up to 3.5 m.

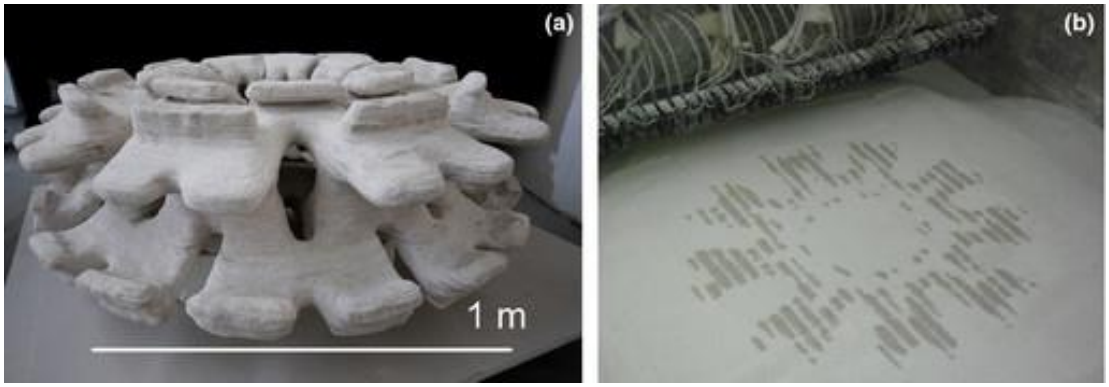


Figure 5. Large part printed by BJ. (a) powder-based 3D printed "The Flower" artwork model (the part is 1.28 m in diameter); (b) image of a layer during the 3D printing process (model designed by Yassi Mazandi; image courtesy of Antonino Italiano, Desamanera SRL, Italy) from [4]

### 3.1.3. Main characteristics of BJ parts

To characterize products fabricated with BJ, density and porosity are the two main properties. There are unfortunately different terminologies giving different assessment of these properties (Du Wenchao[22]). This author has listed the different terminologies according to published reports and papers (Table 2) showing that the definition of density varies indeed from authors to authors.

Table 2. Classification of densities and porosities from[22]

| Terminology | Definition |
|---|---|
| Loose powder density | Bulk density of freely settled powder |
| Tapped powder density | Density of powder after standard tapping process |
| Powder bed (packing) density | Density of powder that is spread on a platform |
| Green part density | Density of part just after all layers finished |
| Sintered part density | Density of part after sintering |
| Strut (skeleton) density | Density of "matrix" or "frame" of a part with designed pores |
| Final part density | Density of part after all processing steps |
| Theoretical (full) density | Density calculated from atomic weight and crystal structure |
| Relative density | Ratio of the absolute density to the theoretical density |
| Macro porosity | Volume percentage of designed pores |
| Micro porosity | Volume per percentage of pores from processing |

The value of packing density may change according to the printing parameters (layer thickness and spreading mechanism). Final density governs the mechanical behaviour of the part (compressive strength, flexural strength, hardness, fracture toughness, …). For all practical purposes, the green part density and sintered density are probably the most relevant ones.

Meanwhile, BJ parts are usually very porous even after sintering (rarely exceeding 65% of the T.D). Summary of densities of BJ parts found in the literature for different materials is reported

in Table 3. For certain applications, the pores distribution is also important. This is particularly true in bone tissue engineering since the requirement of cell in-growth and subsequent tissue formation need pores and cavities. Printed scaffolds have to be fabricated with well-defined macro porosity and micro porosity.

Table 3. Relative sintered densities of ceramic materials from [22]

| Material | Relative sintered density (%) |
|---|---|
| Alumina | 48 -71.4 |
| Tricalcium phosphate | 39 – 73 |
| Barium titanate | 22.5 – 65.2 |
| Silicon carbide | 24 – 35 |
| Titanium carbide | 24 – 32 |

Numerous studies have been conducted to improve BJ. These works have been focused on the study of several influencing factors intervening at different stages of the process: during printing, during finishing or after sintering. Those factors can be classified into four different groups: powder properties, binder properties, process parameters, and feature designing [30] and their respective influence are discussed in section 3.2 (Chapter 1).

## 3.2. Influencing factors in BJ process

### 3.2.1. Powder properties

Powder properties are essential in conventional BJ (eg. using dried powders): they will directly impact the packing density of powder bed and the final density of products. Utela et al.[6] declared that the most important powder property is the ability of deposition which is dictated by the size and shape of particles. Inter particle forces vary with particle size, morphology, particle surface, composition, temperature and humidity. All these characteristics will affect the powders behavior and the reached packing density of powder bed [44].

*i. Powder flowability*

Flowability is the ability of a powder to move over itself when being displaced [45]. It is typically measured with a Hall Flow meter according to standard ASTM B213[30]. For dry powder bed-base-techniques, flowability is a prerequisite to ensure successfully powder layer spreading and further printing. If the flowability is adequate, it helps spreading thin and homogeneous layers of grains. It can be easily understood that it will ultimately govern printing resolution, dimensional accuracy, and general quality of the printed products [30]. On the contrary, a poor powder flowability causes unsuccessful spreading with powder beds full of defects or cracks and a packing degraded by agglomerates.

In the literature, different methods are applied to test the flowability of powders:

(1) Bulk density of the powder is the ratio of the mass of untapped powder sample and its natural deposited volume including the contribution of the interparticle void volume. Bulk density is related not only to the true density of powder, but also reflects the spatial arrangement of particles inside the bulk. Measuring bulk density accurately is not an easy task since the volume without tapping is difficult to measure with good reproducibility. Hence, each measurement of bulk density has to be done under same conditions. Tapped density is the density value attained after mechanically tapping the powder contained in a vat. After obtaining the value of bulk density and tapped density, Hausner ratio [46] and Carr index [47] could be calculated in order to directly express the flowability of the powder materials. Hausner ratio is a common index to assess the flowability of a powdered material while Carr index rather indicates its compressibility. The formulas to calculate the Hausner ratio and Carr index are defined as follow.

$$\text{Hausner Ratio} = V_{Bulk}/V_{Tapped} \tag{1}$$

$$\text{Carr index} = 100\,\frac{V_{Bulk} - V_{Tapped}}{V_{Bulk}} \tag{2}$$

$V_{Bulk}$ is the measurement of freely settled volume of powder and $V_{Bulk}$ is the volume of powder after tapping. $V_{Bulk}$ and $V_{Tapped}$ have similar value when the powder shows good flowability. In this case, a low Carr index is obtained. The value of Hausner ratio is always larger or equal to 1. According to the literature, powders are considered to exhibit relatively good flowability when Hausner ratio is less than 1.19 or Carr ratio is less than 16[48].

(2) Angle of repose is defined as the angle that differentiates the transitions between phases of the granular material [49]. The most used definition of the angle of repose is the steepest slope of the material which is measured from the horizontal plane on which powder can be steady without collapsing[50]. The angle of repose could also indicate the cohesiveness of a powder [51-53]. Compared to free-flowing particles, it is hard to obtain the angle of repose of cohesive powders. Therefore, indirect methods have to be used, such as the angle-composition plot method [54]. In general, the angle of repose is related to the static friction coefficient and the angle of internal friction. Numerous factors also affect the value of angle of repose like for instance, grain size and morphology, interface friction angle, roughness of the base, pouring height, and so on. To measure the angle of repose, different methods are developed and summarized in the review [55]. Tilting box method, fixed funnel method, revolving cylinder/drum method, hollow cylinder method and tilting cylinder method can be applied according to the requirements and applications.

(3) Flow rate is also another commonly used metric as mentioned in [56-59]. The concept is determined by the time required for a defined volume of powder to flow through the small opening of a metal funnel.

(4) Revolution powder analyser is a dynamic method in which a rotating drum is partially filled with particles and then rotates. A digital camera coupled with a computer take images and perform analysis during drum rotating. Different powder characteristics can be collected, analysed such as avalanche angle, avalanche energy, surface fractal, sample density, volume expansion ratio, fluidized volume slope, fluidized height slope, and final settling time [55].

(5) The mock powder spreader system which is presented in Standards, I. I., ISO 4325:1977[30].

(6) Powder rheometer and rotational cell [60].

(7) Flow factor coefficient (ffc) is defined as the ratio of consolidation stress ($\sigma_1$) and compression stress ($\sigma_2$) and can be measured from a ring shear tester[22].

(8) In addition, the ratio between the attractive interparticle force ($F_a$) and the gravitational force acting on each individual particle (which is directly related to the particle weight $m_g$), which is also called Bond Number (BN) [61]:

$$BN = F_a/m_g \quad (3)$$

Flowability of fine ceramic powders (< 10 μm) is usually very poor. Particles stick together and do not flow easily. It has been reported that powder flowability can be improved when the particles radius increased over 20 μm. On the contrary, when the particles radius is lower than this value, the interparticle attraction force would dominate and worsened the flowability [62]. From the research of Schade et al. [63], it was experimentally demonstrated that powder flowability and PSD have an inverse relationship. Therefore, powder flowability will be problematic and limited due to the increased tendency of powder agglomeration when the particle size decreases. However, the size of granules cannot be arbitrary. There is in BJ an obvious tradeoff between flowability, printability and sinter ability. Non-spherical particles exhibit a poor flowability due to higher interparticle adhesion or forces caused by mechanical interlocking of angular particles [60, 64]. This is the reason why spray drying is the preferred process when it comes to producing spherical free-flowing particles from finely raw powder [57, 65, 66]. As an alternative approach to increase flowability, certain authors have proposed to deposit on the surface of powders thin coatings through treatments like plasma or chemical vapor deposition [45]. Additionally, environmental influences such as humidity also affect powder flowability in two aspects: by absorbing moisture which creates bridges between

powder particles and reduces the flowability or by serving as lubricant to reduce the interparticle attraction forces so that flowability [67, 68].

Overall, flowability of the powder is strongly interrelated with other parameters including powder morphology, PSD and mean size of particles, powder composition and also the condition in surrounding environment.

*ii. Particle size distribution*

Based on the usual requirements of conventional binder jetting, the mean size of powders falls in a range between 0.2 µm to 200 µm [22] or slightly lower: from 0.1 to around 150 µm [30]. Particle size larger than 20 µm are typical for a deposition in the dry state, while particle size smaller than 5 µm can be deposited in the wet state but for a completely different BJ process [69]. Much finer particles although more relevant for sintering (around 1 µm) tend to form agglomerates because of van der Waal's forces and moisture effect [70]. They cannot be well-deposited in the dry state. For a PSD between 16 to 63 µm, the green density of printed parts can be expected to be around 50% of true density in case of pure spherical particles. Because of their high surface area, finer particles (< 20 µm) initiate sintering faster than larger particles and favour higher densification [30]. Although PSD after spray drying is always a Gaussian distribution (also known as normal distribution), it is possible to alter the proportion of coarse and fine powders (through sieving for instance) so as to get PSD significantly different from Gaussian distribution.

In general, coarse powders with large particle size exhibit good flowability but a poor sinterability. On the contrary, fine powders have good sinterability but a poor flowability. A mix between two such powders can therefore be expected to behave better in BJ. At fine scales, the Van der Waals forces between different particles increase with the decrease of particle size which drastically reduces the flowability by overcoming the gravitation force [71]. For instance, in ref. [72], two powders with distinct average diameter showed distinct flowability assessed by the Hausner ratio. The finer powder showed a value of 1.29 while the coarser one was just reaching 1.11. Although the difference may seem tiny, it had a significant impact on the sintered density. Fine particles led to parts having 64.5 % density while only 61 % was reached in the case of the coarser particles.

In the literature, parts that have been successfully fabricated from fine powder (especially less than 20 µm) showed higher mechanical strength [30]. The explanation is well known: (1) for fine particles, there is an increased number of contact points that will help diffusion and necking during sintering process; (2) experimentally, it was shown that the smaller particles help the binder spreading and bonding and (3) higher capillary forces are generated in beds formed with fine particles which helps particles to get closer through drying. Lu et al.[73] report another benefit in using finer particles: parts printed with smaller TiNiHf particle size resulted not only

in a higher mechanical strength but also in a smoother surface finish (Figure 6). However, for fine particles, the binder spreading time is much longer such that the processing time is increased. Besides, the whole process loses some reliability as agglomerates and macro-voids formation tend to increase with fine grains. All in all, it appears that the optimization of PSD is absolutely mandatory in every BJ process.

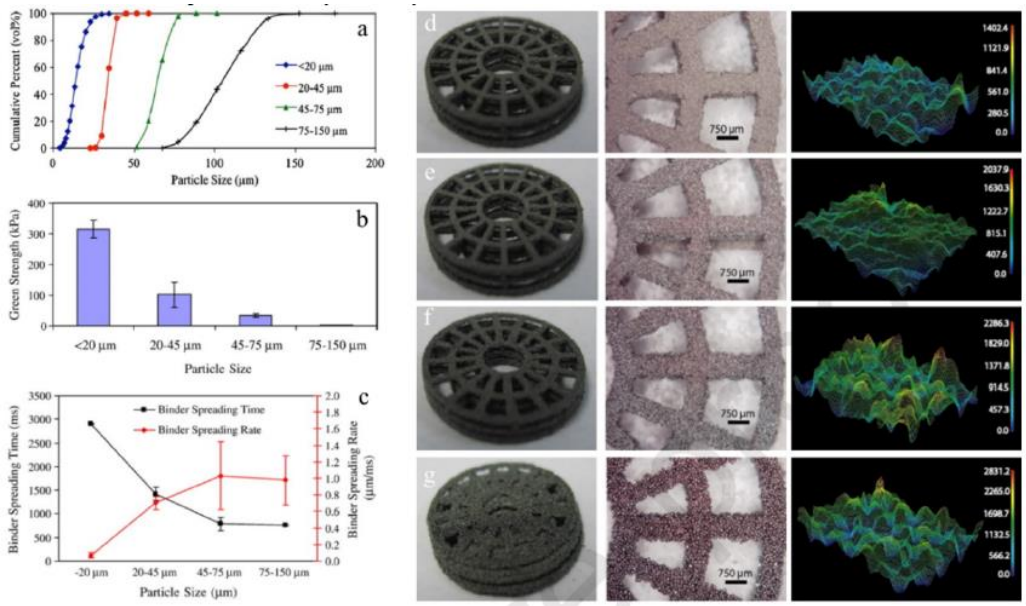


Figure 6. Influence of PSD on quality of printed parts. a): PSD of different TiNiHf powders; b): Mechanical strength of printed parts; c): comparison between binder spreading time and binder spreading rate. Printed mesh structure with different TiNiHf powders: d): less than 20 μm; e): 20 - 45 μm; f): 45 – 75 μm; g): 75 - 150 μm (left side are the optical 3D images of structure; middle side are 2D mesh wire structure; right side are surface 3D profiles of mesh structures) from [73]

As suggested previously, multi-powder system is sometimes considered as a smart way to improve the packing density while keeping the apparent flowability as a satisfactory level. A simple multi-powder PSD can be made by mixing several mono-powders and was the topic of a relevant literature paper [22]. Some complementary information about the PSD optimization can be found in the paragraph 3.2.2.

*iii. Powder morphology*

Particle morphology plays a significant role in binder jetting as well. It affects several properties of the powder and consequently impacts the powder bed itself. Compared to spherical particles, faceted or anisotropic particles have much more frequent interparticle contact, and the increased internal friction lowers the spread-ability [35]. However, the packing ratio can be enhanced sometimes for high aspect ratio particles [18]. Irregularly shaped powders can also be used when the feeding system uses a reverse-rotating roller [74] or a hopper which deposits the powder by vibrating a reservoir above the powder bed [75].

Different powders have been tested with binder to assess the influence of powder morphology on bonding and strength of the printed objects. The results proved that powder morphology controls the amount of particles bounded by one single binder droplet [38]. Spherical particles were bounded more significantly with smaller amounts of binder since it easily segregates at the neck location between grains. On the contrary, irregular particles are bonded together across large flat face.

In the above-mentioned reference, ballistic impact was also mentioned as having a noticeable influence on the process. The binder droplet impacts the powder bed with a certain kinetic energy that may create some damages. One solution to eliminate the negative influence of ballistic effect is to increase the cohesive strength of the powder bed. Two different methods are suggested. The first one is by adding a certain amount of moisture to the powder bed by applying a mist (introduced in [76] as well). The other one is to coat particles with a polymeric material on their surface that may react with the binder thus increasing the bonding. This turns out as a working solution according to pictures shown in Figure 7.

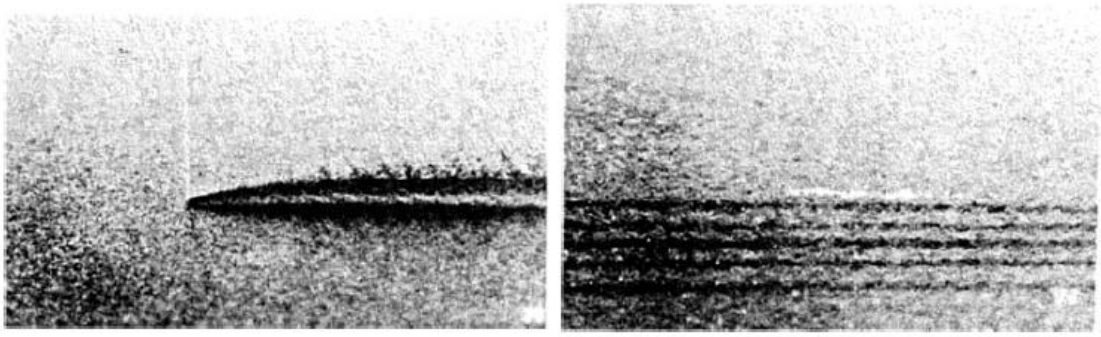

Figure 7. Ballistic effect. Left: Ballistic impact on loose powder bed; Right: Ballistic impact on ‘fixated’ powder bed from [38]

Granulated powder does not only enhance the flowability of powders and packing density of powder beds, but it also improves the green density and sintered density of printed samples [77]. By the way, the smoothness of both powder bed, printed and sintered samples were improved as well using granulated powders.

Moreover, particle encapsulation was conducted on spherical crystalline alumina particles with amorphous alumina powders (Figure 8) [78]. This new approach was aimed to increase the “sinterability” of the printed body while keeping the good flowability of spherical granules. The results have shown that indeed, sintered samples exhibited an improved necking during sintering, a larger shrinkage and a better compressive strength compared with samples prepared with non-coated granules.

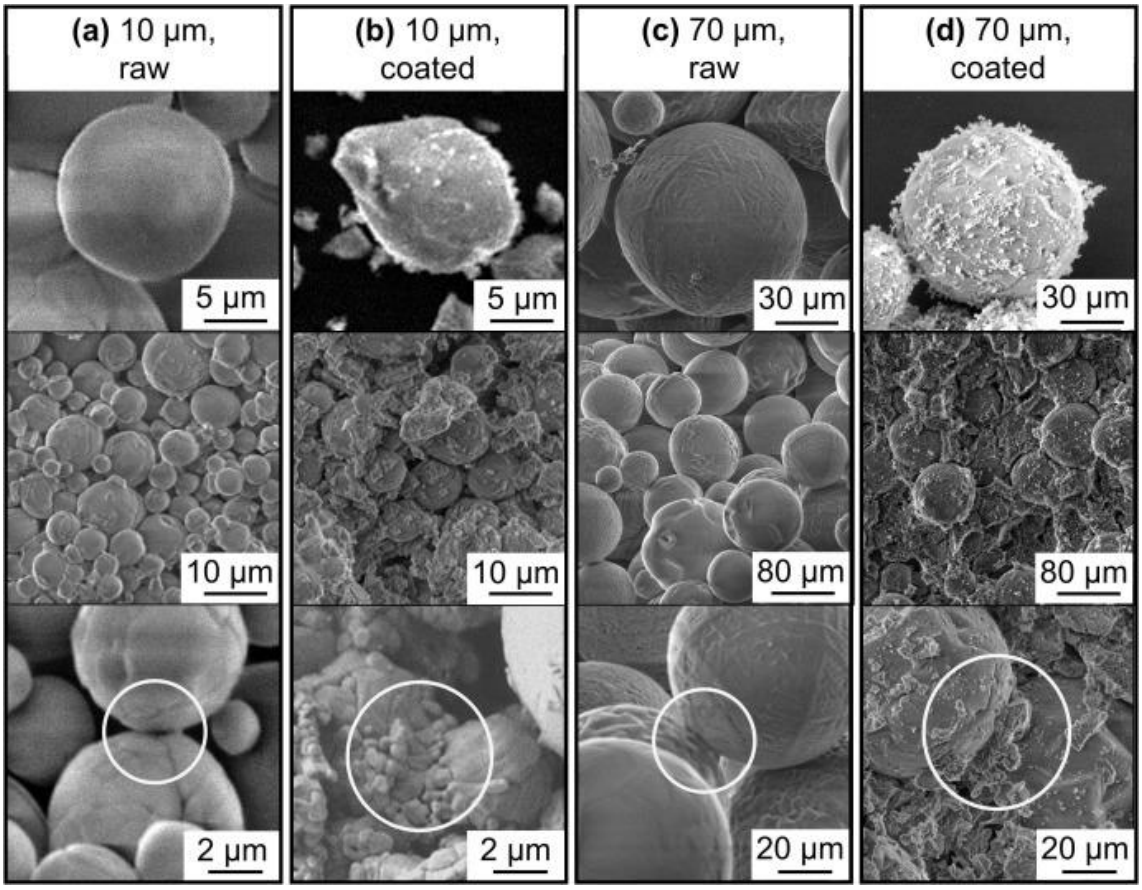


Figure 8. Particle encapsulation to enhance the sinterability. Morphologies of particles (top row), the fracture surfaces of the pressed parts (middle row), the necking between sintered parts (bottom row) for a): 10 µm raw; b): 10 µm encapsulated; c): 70 µm raw; d): 70 µm encapsulated powders, material: Alumina, from [78]

### 3.2.2. Powder bed properties

Properties of powder bed is the foundation of the BJ process no matter with dry or wet mode and the formation of powder bed depends on the powder properties and powder deposition mechanism [22]. The characteristics of powder bed (packing density and smoothness) directly influence the properties of final products which is the most critical character in BJ. Roughness of powder bed and final products is decided by the powder characteristics. Therefore, a basic entry point to improve the performance of the usual dry powder bed approach is the modification of powders as described in section 3.2.1 (Chapter 1). Flowability [20, 79-82], particle size distribution, morphology and surface coating [83, 84] or other treatment [85, 86] of powders have all been studied in the literature to improve the quality of powder beds.

As there are different processes and machines, the requirements for powders also change. However, in order to achieve a high density after sintering, the packing density of the powder bed must the highest possible. It was reported that the theoretical packing density for mono-sized spherical powders is about 60 % of the true density [80]. Different researches have been

carried out to optimize experimental packing and also calculate the theoretical one for powders in different conditions [81-86]. Nevertheless, real powders do not behave exactly like models and experimental values differ significantly from calculated ones. For instance, the powders are usually not perfectly rounded and/or do not have a perfect smooth surface. These features cannot be easily handled by numerical models. Nevertheless, discrete element modeling (DEM) and finite element modeling (FEM) are developing a lot and new tools are now available to model and get a deeper understanding of the spreading and packing process [87-93].

*i. Powder bed packing and spreading*

Packing density is a crucial parameter which determines the arrangement of inner network of particles and how intense these particles contact [30]. During the spreading process to create new layers, packing density evolve as it is the cumulative summation of the contribution of each individual layers. After printing completion, packing density may thus be higher than the packing density of a single layer because of the pressure exerted by the recoater on the previously deposited layers. Measured bulk density and tapped density of any powder can be considered as defining a range between the lowest and highest value of reachable packing density [30]. Compared to small particles, large particles have higher flowability and packing. Broad PSD results in a higher packing compared to a narrower distribution [87, 88]. Powders with appreciable flowability for the deposition of thin layers exhibit a typical particle size range > 20 μm which usually does not provide sufficient sintering activities to get fully dense ceramic parts [4]. It also has been proven that powder packing density of even coarser particles (> 70 μm) becomes only function of PSD and particle morphology but relatively independent of particle size [89]. The same authors confirm that higher interparticle forces form among fine particles which negatively impact packing.

Despite the influence of PSD and powder morphology on packing, several other factors have also to be taken into consideration, such as the type of technologies used for the powder spreading as well as the layer thickness. For instance, powder bed can be compacted by using mechanical vibration, acoustic energy, sonic/ultrasonic vibrations or with piezoelectric scraper [69]. Besides, the compaction could be done directly by spreading a layer with counter-clockwise rotating roller, raising the manufacturing tank, and rolling over the powder bed a second time with the roller spinning along the traverse direction to give pressure on powders [18]. Another approach shares similar mechanism, by spreading two ultra-thin layers instead of just a single thick layer giving an overall better packing. In general increasing packing also impact positively some requirements of BJ such as the binding strength in the green stage [90]. Similarly, a better packing density often means a better sintered density as well as a higher mechanical strength [91]. Recently a novel method to enhance the packing density has been disclosed. Called double-smoothing (DS), it helps increasing packing by spreading ultra-thin

layers of powders(Figure 9 (a)) [30]. Compared with single move counter-rolling spreading method, DS spreading reduces the cavities formation in powder bed (Figure 9 (b)) and drastically increases the green density (Figure 9 (c)).

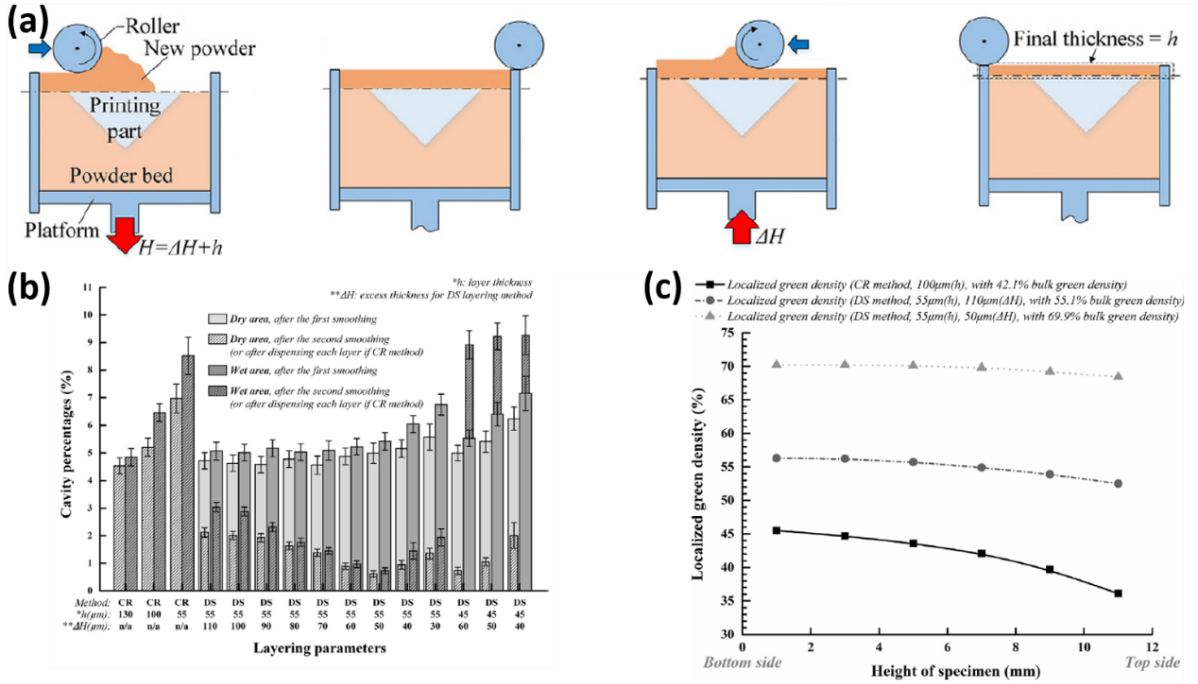


Figure 9. Double Smoothing process. a): Double smoothing layering steps; b): Cavity proportion observed in the powder-layering tests; c): Results of uniformity analysis along specimen's height from [92]

*ii. Multimodal powder packing system*

Various approaches have been put forward to enhance packing density. An approach relies on adding fine particles to fill the void spaces between coarse particles to increase the overall packing and hopefully the final density. This also changes the PSD from a gaussian distribution to a multi-modal one. In comparison with powders having just a broad PSD range, multi-modal or bimodal powder system will be more efficient to reach the goal. Because the void sizes are characteristically determined by the larger particles, a multi modal PSD can be fine-tuned (ie. determining the optimal fine particle size) to get a more desirable and compact packing than a random distribution [93]. Hence, the determination and optimization of particle size for the different powder fractions as well as their ratio is important. According to some researches, higher size ratio between two fractions in powder system results in a higher packing density [94, 95]. A significant number of papers are reporting using multi-modal powders. Beside of ceramic materials, metal powders were used to conduct the multi-modal system and the achieved packing density is sometimes impressive [88, 96, 97].

For simplicity reasons, bimodal PSD system are more considered in the literature. They are obtained by mixing two different powders with PSD and volume ratio determined so as to get a better packing density compared to a monomodal system. According to the bimodal powder packing theory [98], the most effective bimodal ratio (coarse to fine) was reported at 7:1. From theoretically calculation, the packing density of the bimodal powder system (7:1) can reach 86.8 % relative density. However, the actual packing density would be much lower than this level because of inhomogeneous distribution of particles, interaction forces between particles and other experimental factors. Karapatis et al. [99] have adjusted the ratio between coarse particles and fine particles to 10:1 to enhance the packing density of direct laser sintering method with nickel powders and achieved 63 %. This has to be compared to the theoretical packing density of this ratio that should be around 82 % [98]. Bai et al. [100] have shown that flowability of powders, powder bed density and sintered density of printed part can be improved by up to 15 %, 16.2 % and 12.3 % respectively by introducing bimodal powders system. However, mixture of extra-large particles and fine particles has failed to improve the sintered density due to limited sign of necking and coarsening because of the large particle radii. In this case, the sintered part is mainly composed of a rigid skeleton of large particles with an average particle size of 75 µm which prevented further densification in presence of fine grains. Furthermore, Lanzetta et al. [101] also revealed that bimodal powders system gave advantages on surface finishing of printed parts and after sintering because the fine powders filled the voids between large granules and made the surface smoother. On the other hand, Zhou et al .[90] reported that adding fine calcium phosphate powder to a powder bed had no positive effect on improving packing density, meanwhile, the flowability of mixed powder was reduced. Sun et al.[102] have investigated the effect of PSD on the final relative density by mixing powders of different size with glass-ceramic materials. The flexural strength of parts fabricated with monomodal powders with size between 45 µm – 100 µm reached 3.5 MPa. The value reached 13.9 MPa after mixing previous powder with 40 wt % powder for a size between 1 – 20 µm. Similar results are also reported for parts made by mixing different hydroxyapatite powders [103]. Moreover, some research also has shown that a 10 % increase of fine particles could improve the apparent density of powder bed from ~ 77 % to ~ 88 % [104]. Furthermore, multi-modal powders systems not restricted to a “simple” mix between two powders were also tested [100, 105]. The difficulty of multi-modal powders system is how to homogeneous mix powders and generate suitable PSD.

Very few articles can be found discussing the influence of a multimodal PSD on the roughness of the as printed and sintered part unfortunately. In general, an appropriate mixture powder system should be determined by considering not only PSD of particles and ratio between coarse fraction and fine fraction, but also the chemical and physical properties of material itself. The

conditions of mixing between coarse and fine fractions may also explain some discrepancies in the literature.

### 3.2.3. Binder properties

The binder plays a major role in BJ since it binds particles together to fabricate 3D-objects. Both physical properties and chemical properties of binders significantly influence the quality of the bonding strength with powders.

But the binder has to fulfill other requirements. One is particularly obvious: it should be printable without causing nozzle clogging. To ensure printability, the binder has to be jetted out from nozzles which requires proper rheology, surface tension and stability. Meanwhile, a good wetting behaviour with the powder bed is also expected to provide an efficient diffusion of binder throughout the porosity. Additionally, if a strong bonding is expected, aggregation of undesirable grains on the printed parts should be avoided.

Good stability during storage and use should be ensured so that it will not solidify in printhead or leaking out from nozzles. For storage, a criterion is to avoid cross-linking of components [30]. Another requirement is a complete disappearance after thermal debinding so as to avoid the presence of any residue which could affect the final properties of parts [6, 30].

The nature of the most common binders and binding mechanism are described in the following section.

*i. Classifications of binders*

Mostafaei [30] proposes a simple classification by assuming that binders belong to any of 3 categories which are solvent-based binder (organic or water-based), acid-based binder and metal salts binder.

- solvent-based: it relies on a simple liquid deposition and hydration-activated binding;
- acid-based system: binding mechanism depends on acid-based reaction;
- metal salts: specific to metal powders, the mechanism is related with liquid drying and salt recrystallization;

Binding mechanism includes liquid drying and salt recrystallization. In addition, recrystallization process works with any powder material unless it is soluble in the salt solution [106].

However, a more convenient classification assumes that binders should be classified according to their state: there are therefore in-liquid binders, in-bed binders, phase-changing binders and

sintering inhibition binders [6, 30]. Some common binders reported in the literature are summarized in Table 4 according to this classification.

Table 4. Summary of the most typically used binders in BJ and associated binding mechanisms

| Binding mechanisms | Used materials |
|---|---|
| in-liquid | Organic (butyral resin[17], polymeric resins[107], polyvinyls[83], polycarbosilazane[17], polysiloxanes[108], aluminum amides[109]); Inorganic(colloidal sillca[17, 110], aluminum nitrate[111]) |
| in-bed | Deposited liquid with maltodextrin[112], sucrose[107] |
| phase-changing | 2-methylpropane-2-OL[18] |
| sintering-inhibition | Metal flakes[113] |
| hydration-based | Deposited liquid with plasters[114], cements[115] |
| acid-based | Polyvinyl pyrrolidone[116] |
| metal salts | Silver nitrate[106] |

These different families can be described as follow:

- in-liquid: binders in which binding agents are completely contained;

In-liquid binders are the most common ones with a broad range of materials choices (organics, inorganics, solvents, ...). In BJ, utilization of polymers inside of the printhead may also result in clogging of nozzles. Therefore, rheology and chemical stability are critical issues. Besides, binder removal after printing through thermal processing need to be investigated since thermal treatment of crosslinked polymers remains a difficult task.

- in-bed: adhesive agents are mixed with powders on powder bed, liquid deposited on powder bed helps to dissolve the agent in order to have bound reactions;

In this case, it is important that adhesive components are active enough to be dissolved in the liquid and provide sufficient mechanical strength to support the desired structure. Different methods have been proposed [22]. The first one is called binder pre-mixing. In this case, the binder is uniformly mixed with ceramic particles and the mix is milled and sieved. The other one is named as “binder pre-coating”. In this case, the binder is dissolved in a suitable solvent and mixed with the ceramic grains. The slurry is then dried using spray drying or simple evaporation and then, milled and sieved in order to have binder-coated ceramic powders.

- phase changing: the solidification of printed part relies on phase-change of deposited materials;

Phase changing mechanism is limited to special materials. The general principle is as follows: a room temperature solid material is deposited on the powder bed at its melting temperature,

then binds the powder materials and finally returns back its original solid form when the temperature cools down [17].

- sintering inhibition binders: printed part with powder bed will be thermal treated after printing by utilizing special agents.

During the process, sintering inhibitors, heat-isolating materials, heat reflective materials and chemical oxidizers are selective deposited on the selective area [117] and the non-printed area will be the final part after thermal treatment. The main drawback of this approach is the necessity to print on the whole powder bed (except the part) which produces large amounts of materials waste.

The most used binders that are reported in literature have been summarized by Du Wenchao et al. in Table 5 [22]. They include carbohydrates (such like dextrin, maltodextrin, and starch), acids (phosphoric acid and acrylic acid), polymers and commercial (eg. not well described) binders.

Table 5. Binder materials used in binder solution and corresponding fraction in green part adapted from [22]

| Binder | Fraction / wt% | Saturation / vol% |
|---|---|---|
| Phosphoric acid | 5 - 23.8 | 41.4 – 46 |
| Phosphoric acid & isopropanol | 10 - 14 | 14 – 28 |
| Acrylic acid | / | / |
| Polymer | 10 | / |
| Commercial Zp-7 | 40 | / |
| Commercial Schelofix | / | / |

Certain authors tried to enhance the binding and subsequent packing density through the dispersion of nanoparticles in the binder as a filler. The idea is to deposit the finest particles in the voids between the coarser grains particles and also increases the thermal activity, hopefully leading to a higher sintered density. Shrinkage is also expected to be reduced. Different researchers have put forward this method [118-122]. Density and mechanical strength were obviously improved. However, the results were not stable enough and the authors report significant risks of nozzle clogging. Although promising this approach seems to fail in terms of process reliability. Bai et al. [120] have compared the printing effect of organic binder, colloidal organic and inorganic binder (with nano-sized copper powders) to binder copper powders as shown in Figure 10. Their conclusion was that the inorganic colloidal binder yielded the highest final density.

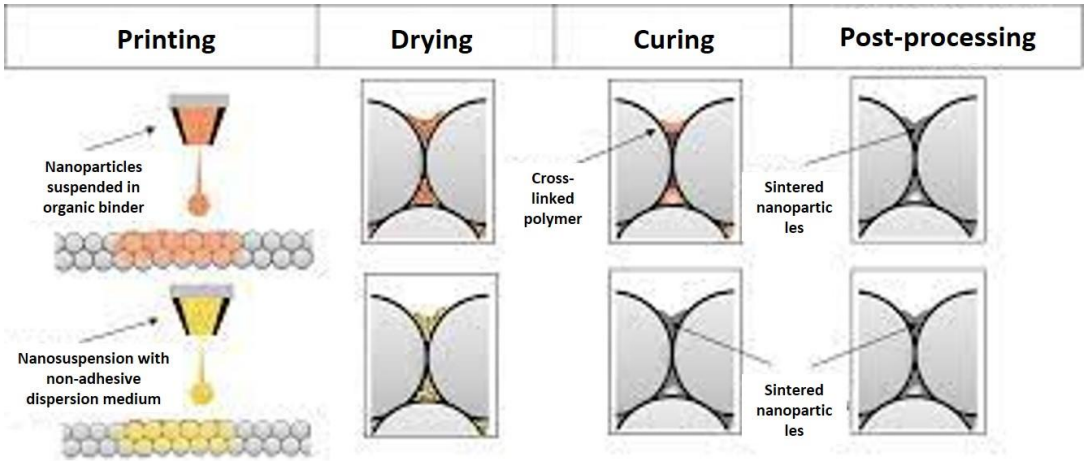


Figure 10. Schematics of the use of colloidal organic binder with dispersed nanoparticles at different stages of binder jetting process from [120]

As a matter of fact, a suitable binder not only depends on the powder to be bound but also on the technology itself. Not all printing systems are the same. Therefore, a suitable binder for one specific BJ machine would not necessarily give proper results on another system.

*ii. Binder formulation*

The most important objective that any binder has to satisfy is a reliable deposition [6]. To give more insight to the readers about the difficulties that may occur during printing, we will mostly consider in this part the case of "In-liquid binder" which is the most discussed one in the literature.

As demonstrated in [115], an effectively functional binder should ensure a smooth ejection from the printhead and a quick penetration of the powder. It should also reach the interface with the previous layer to ensure bonding between layers. Rapid deposition of binder is recommended to decrease the whole processing time because a binder which is not fully hardened can influence the deposition of the next layer [17].

Therefore, in order to formulate a suitable binder, different components or modifiers need to be added to fine tune its properties and guarantee the best properties for the final parts. As reminded in [115], a typical binder may contain a number of such components. There might by: water, surfactants, organic solvents, buffers, biocides, sequestering agent, viscosity modifier, low molecular weight polymers, lithium ion sources, etc. Other researchers have also found that humectants may help on reducing clogging inside of nozzle. The same groups also reported that pH indicator may help the printing [110]. Additionally, flowrate enhancer could increase the deposition rate of the binder [6]. Sometimes, dyes are also added in the binder as modifiers [107]. Thickening agents are used as well to control the droplet spreading [70]. Addition of all those modifiers depends on the basic requirements of products and technical

specificities of the process. As a matter of fact, properties of powders also determine which kind of additive need to be used.

*iii. Various binder properties*

Rheology, surface tension and stability are three important properties of the binder which also decide the printability. Characteristics of the binder have to properly match the specifications of printhead otherwise the whole process will lack reliability. Normally printheads have an optimal and limited range for both viscosity and surface tension as well as a suitable range for particle size distribution if there are fine powders added in the binder [6].

Viscosity of the binder is easily influenced by additives (usually polymers) and other factors including pH of the solution, solid loading if fine powders are added. Maximum fluid viscosity is around 20 cps for most commercial ink jet printheads to guarantee smooth printing process [123], though some printheads are designed to reach up to 100 cps. Whenever the binder contains powders, increase of solid loading leads to a higher viscosity for the binder and more significant risk of nozzles clogging. Larger particle size could reduce the viscosity at constant solid loading although with associated higher risk of nozzle clogging [124]. No matter what the function of added surfactants or polymers, it has been reported that shortened polymer chain [115, 124] or less polymer loading [125] led to lower viscosity of the solution. Furthermore, modifying pH value of the solution to change the surface charge or addition of diluent (e.g., low molecular weight polyethylene glycol) are options to decrease the viscosity of the binder as well.

Altering surface tension could be easily achieved by adding a surfactant or a fluid with different surface tension. The minimum surface tension is set at around 35 mN/m [108]. The surface tension of water is 72 mN/m which already exceeds the extreme specification value of commercial printheads. As reported in [126], the surface tension of one water-based binder could be reduced around 35 % by adding 20 vol% methanol with lower surface tension. However, Utela et al. [6] have described that the mechanism of how surfactants lower the surface tension in the binder liquid may be detrimental to other aspects. As expressed, ‘Extra surfactant in a solution group together into micelles and as new liquid surfaces are exposed the surfactant migrates to these surfaces and acts to lower the surface tension. This is problematic for BJ because the migration of the surfactant to the newly created liquid surfaces is not necessarily able to match the speed at which the drop surfaces can be created’. Subsequently, the surface tension experienced by the printhead may be similar to that of the bulk fluid without the added surfactant [6].

They also reported that rehydration is also critical since it may affect stability during printing. The liquid which is not self-soluble may have some difficulty to dissolve clogs inside printhead and finally compromises the ejection. Therefore, the rehydration behaviour of the binder is

important, especially for a binder containing some solid loading which is more prone to clogging. More generally, viscosity, surface tension, pH value, time, temperature and even moisture are all influencing the stability of the binder in a very intricated way. A further difficulty for binders containing solids is that the colloids can easily settle down which is another source of clogging. Bredt JF et al.[110] demonstrated that by using optical transmission through the liquid sample and looking for premature polymerization or coagulation which are signals of unstable binder. Before printing, it was also suggested to carry a filtration step to remove agglomerates [127].

*iv. Printability*

Printability is an obvious prerequisite. In general, BJ processes use drop-on-demand (DOD) inkjet deposition. The principle of DOD is pushing fluid out of a nozzle with a burst of pressure [30]. The difference between DOD and continuous-jet (CJ) is compared in more details in section 3.2.5 (Chapter 1).

As said previously, rheology, surface tension and other physical properties of the binder have to be fine-tuned for a good compatibility with the powder. But the same properties also have to be within a suitable range for the binder to be ejected out of the printhead [128]. According to references [128, 129], the ejection behaviour of a binder droplet is determined by three physical parameters, which are Reynolds number (Re), Weber number (We) and Ohnesorge number (Oh). The calculation of these parameters is given as below.

$$Re = \frac{\rho v L}{\mu} \tag{4}$$

$$We = \frac{v^2 \rho L}{\sigma} \tag{5}$$

$$Oh = \frac{\mu}{\sqrt{\rho \sigma L}} = \frac{\sqrt{We}}{Re} \tag{6}$$

where ρ, μ, σ are the density (kg/m$^3$), viscosity (N.s/m$^2$) and surface tension (N/m) of the binder. υ and L are velocity of the droplet (m/s) and characteristic length of the nozzle (m) respectively.

Ohnesorge number correlates the viscous force and surface tension [30]. Fromm et al. [130] have studied the droplet formation mechanism and directly relate the parameter Z (=1/Oh) which is reversed Ohnesorge number to assess the printability of the binder. Reis et al.[131] have further investigated the influences of Z. They reported that 1<Z<10 was the suitable range for the binder to be smoothly ejected out from the printhead. Viscous forces dominate and

prevent the ejection of the binder from nozzles when Z<1. In the case Z>10, satellite droplets flow out behind the main drop. These different situations are illustrated in Figure 11.

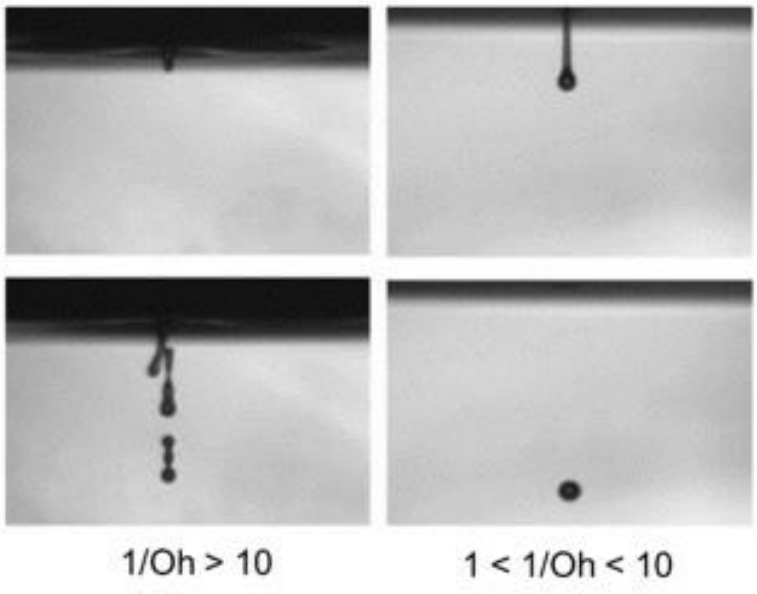


Figure 11. Ejection images of binders showing the effect of the non-dimensional value Z(1/Oh) from [30]

Ejection speed of the binder has to be controlled in an appropriate value to overcome the surface tension with the nozzle and avoid any splashing on the powder bed [27]. Derby et al.[128] reported two limiting conditions defining a range of stable printing behaviour. The first limit is that for which the binder droplet possesses a minimum speed to overcome the surface tension effects and ejection out of the nozzle. This result was also supported by the work of Duineveld [132]. The same research group also found that the Weber number should be higher than 4 to resolve the problem which is also expressed by the following equation [27].

$$We = v_{min}(\frac{\rho d}{\sigma})^{\frac{1}{2}} > 4 \quad (7)$$

where $\upsilon_{min}$ and d are minimum ejecting speed and the diameter of the nozzles in printhead.

The second limiting condition is that for which the ejection speed of the binder droplet produces splashing on the powder bed. Stow et al. [133] came up with the droplet splashing Eq. 8.

$$f(R) < We^{1/2}Re^{1/4} \quad (8)$$

where f(R) is the function of surface roughness [27].

All these parameters allow to define a proper "printability" region for any binder. What should be noted here is that a Newtonian rheological behaviour is assumed for the binder. In addition, density of the droplet and its volume also influence the splashing as well but it is not satisfactorily handled by the previous equations. McKinley [129] proposed a diagram to help

visualizing the printability region with Oh-Re for the X axis instead of We-Re as it is more conventionally plotted (Figure 12).

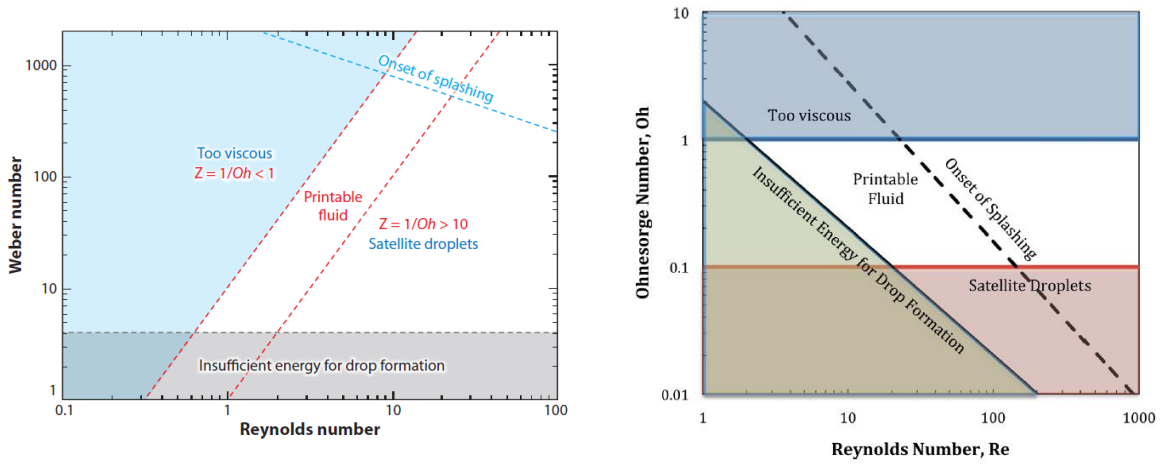


Figure 12. Printability zone of a binder. Left: Printable region of stable binder droplets. The printable region is interlaced by four dotted lines. Outside of the region, the binder is not suitable for printing because of inappropriate viscosity, splashing, or generating satellite droplets, and insufficient energy for drop formation from [128]; Right: Redrawn printable region of stable binder droplets by using the Ohnesorge number as the ordinate axis in stead of the Weber number ($We = (ReOh)^2$ [129]).

In some cases, satellite droplets can be smoothly ejected out from the nozzles without any problem. However, the shape of the droplet changed from cylindrical to spherical after travelling certain distance between nozzle and powder bed which apparently influences the dimensional accuracy of printed part.

Generally speaking, for conventional BJ process, Mostafaei [30] proposed to consider three requirements for a binder to be suitable with a printhead.

1) Reactivity - it has to be considered since the reactivity might cause erosion and malfunction in the nozzles;

2) Stability – undesirable evaporation and curing should not happen to prevent blockage of the nozzle;

3) Cleanness – the binder should react with a cleaning fluid for an efficient nozzle cleaning step or maintenance. Even though, incidents could happen due to temperature or moisture in the atmosphere which lead to the binder reaction or solidification.

### 3.2.4. Wetting behaviour between powder and binder

Wettability is the preference of a liquid phase to be in contact with a solid phase. It is therefore critical in BJ where a liquid binder is projected onto a powder and influences several aspects

of BJ. The resolution of printing depends on the binder saturation and binder spreading within the powder bed both of which being related to wettability. Mechanical resistance of printed (and sintered) product is also related to wettability. Poor wetting behaviour leads to a heterogeneous distribution of binder that may create some weak points in the green body where it is lacking.

From the literature, the entire process of interaction between powder and binder has been investigated after the binder jetted out from nozzles of printhead. A specific research has shown the wetting behaviour between binder and different powder beds through real-time images at the end of impact-driven spreading phase [134]. It has shown that powder beds composed by smaller particles resulted in larger spreading diameter at the end of the impact-driven phase. On the contrary, the spreading diameter of the binder droplet decreased with the increase of particle size of powder.

Infiltration kinetics of the binder is a highly complex phenomenon occurring on different time scales. It is governed by droplet volume, initial velocity, viscosity of binder and roughness of the powder bed [135]. Binder wetting is also affected by droplet velocities, viscosities, contact angles occurs on a typical time < 100 μs [94, 136, 137]. In a second step, the penetration of droplets takes place on a supplementary time of about 0.1 – 1 s [27, 138]. Generally, as the binder droplets contact the top surface of powder bed, the wetting behaviour initiates. Binder spreading over powder bed is then driven by the kinetic energy of droplets, resulting in the formation of bonds connecting adjacent grains. Further penetration of the binder will then depend on the porous characteristics of the powder bed and of the binder, such as viscosity, contact angle and surface tension [30]. The mechanism of binder spreading and penetration has been graphically presented in Figure 13 a), b), c). It should be noticed that the gravity effect on the binder is negligible since the mass of droplets is very tiny [139]. After a while, the binder stops spreading and drying occurs thus reaching an equilibrium condition called saturation [30].

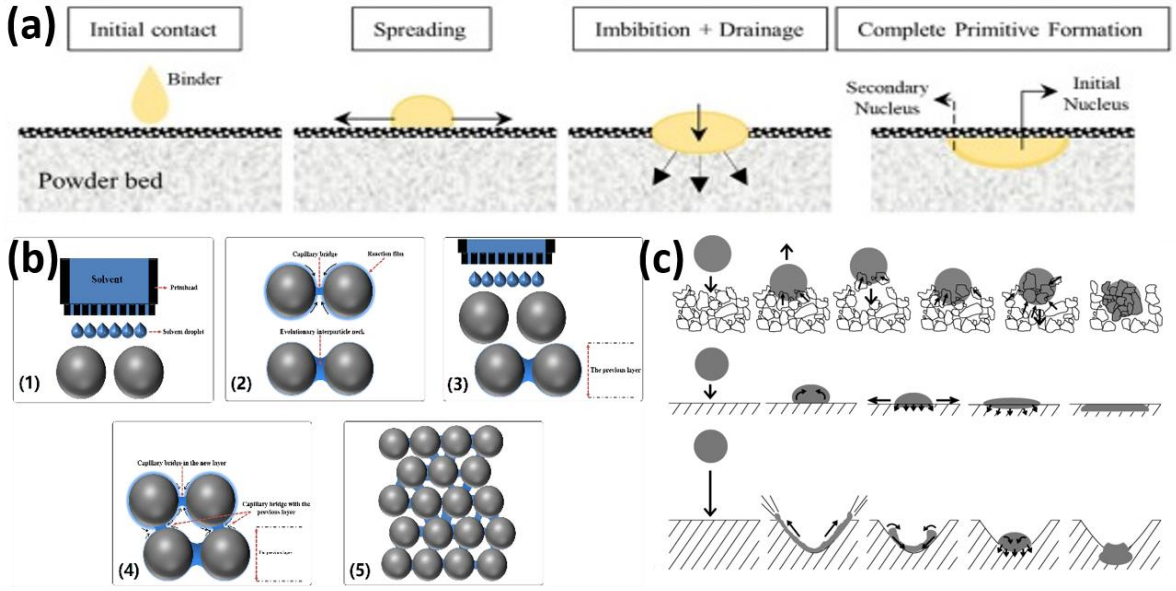


Figure 13. Wetting behaviour between binder and powders. a): Schematic of primitive formation process during interaction between powder and binder [135]; b): Micro-scale of binder-powder interaction during printing process: (1): Binder ejected out from printhead and deposits on the powder bed; (2): Wetting behaviour of adjacent particles surfaces leading to the formation of capillary bridges and neck formation; (3): New powder layer is spread on the previous printed layer; (4): Formation of new capillary bridges among previous particles and new introduced particles; (5): finished printed parts in micro-view [140]; c): Three different granule formation mechanisms: top: Tunneling mechanism; middle: spreading mechanism; bottom: crater mechanism [141]

Over-wetting and slow reaction between the binder and powder may cause a significant decrease of smallest feature size [71]. In this case, the printed layer may also lack the required mechanical strength to withstand the stacking with the next powder layer.

From the observation reported in [30], the general behaviour of the binder within the powder bed is also related to the macroscopic surface roughness and pore morphologies. Nevertheless, Amir Mostafaei et al [30] suggested that internal microscopic surfaces along the powder particles is not really wetted by the binder. As a consequence, there might be an overestimation of the real binder saturation level in most papers. Therefore, determining the real behaviour of binder is still a subject of intense researches. It is suggested for instance that a tunnelling mechanism happens with fine and non-flowable powders, during which the binder droplet will bond aggregates in all directions to form big granules with some protrusions due to the insufficient binder spreading. Models and experiments suggest that spreading and crater formation are both taking place with coarse and free-flowing powders with differences only coming from the drop velocity. As long as the powder bed is dense “enough” with low velocity drops, binder spreading happens readily across the top surface to bond grains taking the form of flat disks. By contrast, a high droplet velocity may form a crater on the powder bed. In this

case, the droplet spreads along the walls of the crater and forms agglomerates with irregular shape [141, 142].

In order to better understand the interaction between powder and binder during printing, real time observations are reported by using high speed x-ray imaging [143]. The results show that two points are critical: the interaction depth and the powder ejection from the surface of the bed as presented in Figure 14. According to the review [30], interaction depth is determined by the droplet velocity which ultimately ejects surrounding particles from the top surface. This interaction causes the formation of sub-surface pores in printed area. In some circumstances, a continuous gap between two printed layers can be created which will increase the binder penetration time due to kinetic problems. The same gap also implies that more shrinkage happens along the z-direction during thermal treatment.

If some particles are ejected out in a significant amount, large vacancies are created on the powder bed that cannot be refilled by the subsequent powder spreading. This of course will create large pores in the final product. Surface roughness and dimensional accuracy will also suffer from these ejected powders. It should be noticed that since the preferred powder are free flowing and spherical, they are also easier to be ejected which might be an issue. Finally, it seems that for spherically shaped particles, the interaction depth is higher than in beds formed with irregular particles because of mechanical interlocking effect between angular particles.

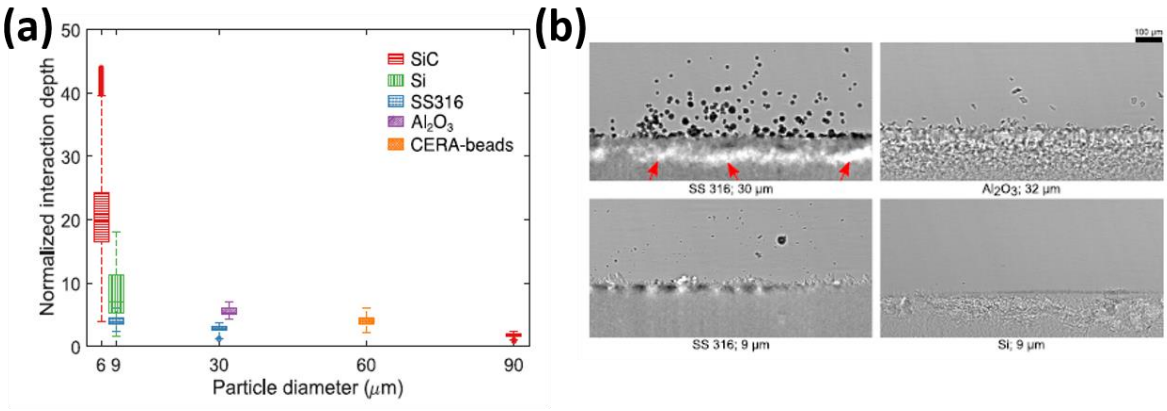


Figure 14. Interaction between binder and powders. a): Interaction depth as a function of powder size; b): real time images of binder deposition on powder bed and surrounding powders ejection [143]

### 3.2.5. Printing process parameters

*i. Powder spreading method*

Spreading/feeding method is one of the key points to successfully create the perfect powder bed surface without any cracks or defects. Two main feeding systems are commonly used in BJ: a recoater or a hopper. The recoater can be a simple blade or a roller. Its function is to bring the fresh powders from the feeding tank to the manufacturing tank. For reasons that will

become clear later, rollers are preferred to simple blades as they help compacting the powder bed, especially counter-rotative rollers [144]. Certain machines use a hopper instead of a feeding tank to store the powder. The hopper moves above the powder bed and supplies powders through vibrating or shaking [75, 145, 146]. A hopper or counter-rotative roller are helpful for sticking powders or for powders exhibiting a poor flowability in general.

In the literature, the spreading speed is a vague term which encompasses different definitions. It may be the hopper displacement speed (mm/s), the oscillatory speed of the hopper (rpm), the recoater displacement speed (rpm) or the roller rotational speed (rpm). Although different, all these speeds have strong influence on the powder deposition.

An appropriate range of roller traverse speed (0.1 – 16 mm/s) is suggested in [30]. However the authors insist that inhomogeneous powder beds could possibly result for traverse speeds larger than 4 mm/s. Shrestha et al. [147] have found that 6 mm/s is the optimum for an accurate powder deposition. Obviously, these values depend dramatically on the powder itself. However, a commonly reported result, roughly independent on the powder is that higher resolutions can be achieved at lower spreading speeds but at the expense of an increased processing time. Parteli et al. [148] have studied powder spreading through numerical simulations by considering a counter-clockwise rotating roller. Their model shows that if the traverse speed is too high then there is a surface roughness increase of the powder bed. They also showed that the powder morphology, its surface texture as well as that of the roller influence the quality of the powder bed. Furthermore, it appears that all these factors have an influence on the compaction of the powder and particle segregation. An example of such a simulation is shown in Figure 15 where the spreading behaviour of a given powder is highlighted.

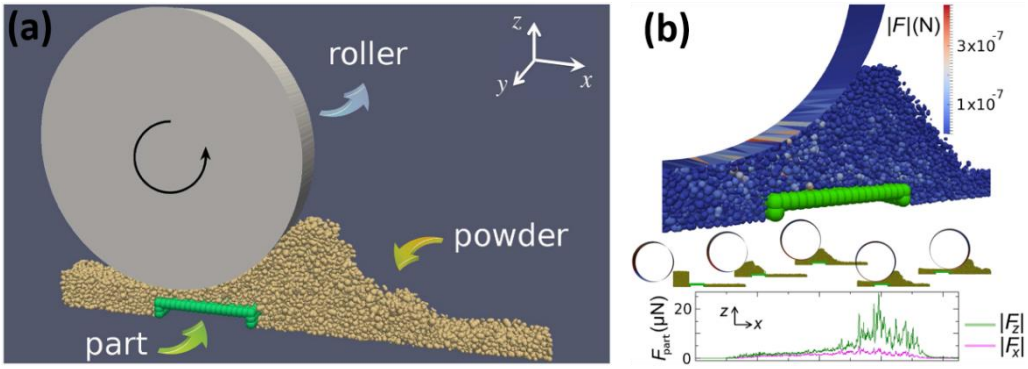


Figure 15. Powder spreading by using the roller. a): Schematic view of the main element from the simulation; b): Schematic of the powder roller interaction during printing in which the magnitude evolution of the total force on the part in the horizontal and vertical directions as a function of time from [148]

*ii. Printing methods*

As introduced before, there are two different technologies to deposit liquid binder in BJ: drop-on-demand (DOD) (Figure 16 right) and continuous-jet (CJ) (Figure 16 left). DOD method produces individual droplets on demand that are selectively deposited on the printed area. This technology exists under two forms: some printheads are purely piezoelectric ones while some others are called thermal inkjet. The pressure in piezoelectric head is created by expanding a piezoelectric crystal while the mechanism in thermal inkjet head is to generate a thermal bubble via flash boiling the binder [30]. It should be paid attention that the binder might evaporate in the thermal inkjet printhead [149]. There might also be some issues due to the vaporization of some binder which produces sometimes a discontinuous ejection.

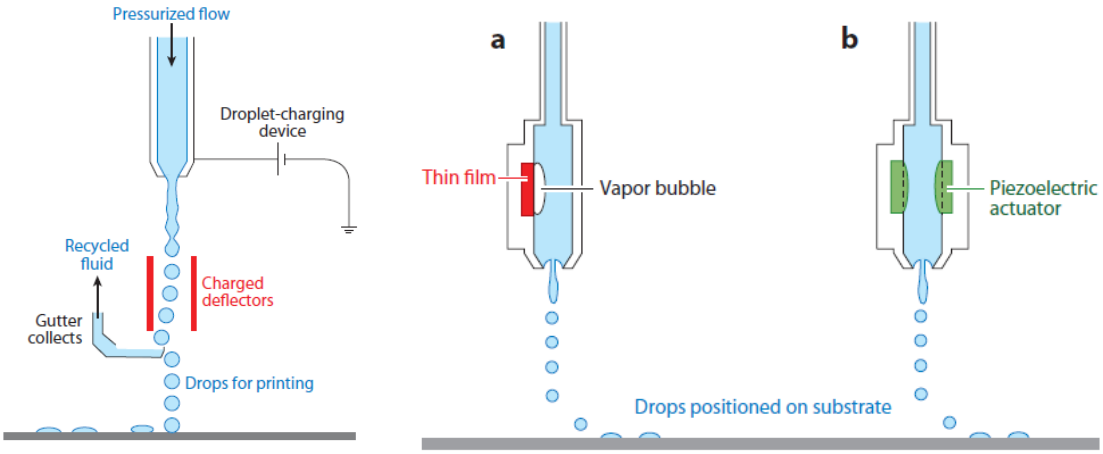


Figure 16. Schematic diagram of continuous inkjet (left) and drop-of-demand (right) from [128]

Continuous inkjet (CJ) method generates continuous binder droplets. They reach higher printing rates compared to DOD [30]. However, the binder droplets have to be drained into a gutter or tank when the deposition is not needed. Nevertheless, according to some authors, this technology present specific advantages among which a high productivity [17, 30].

*iii. Printing speed*

Printing speed is no doubt a matter of technology: it is bounded from the top by the maximum frequency at which the printhead can eject ink. It is also limited by the fluid behaviour of the ink. At high ejection frequencies, segregation of individual binder droplets is unavoidable.

Miyanaji et al. [219] revealed that a higher printing speed is correlated to a reduction of printing accuracy regardless of printing direction. The researchers also showed that since the velocity of the binder droplets increases with printing speed, the ink splashes on powder which degrades the surface finishing. The study also underlined that the dimensional accuracy along the y-direction could be more influenced compared to the x-direction when the printing direction was

along the y-direction and nozzles line was aligned vertically with printing direction as illustrated in Figure 17.

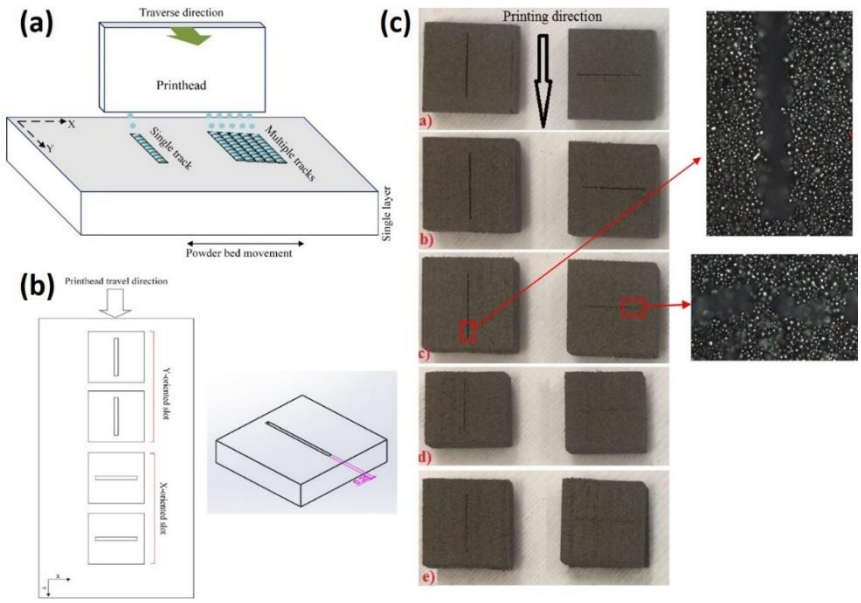


Figure 17. Effect of printing speed on printed parts. a)-b): Schematic of printing direction and designed geometry of printed area; c): Printed parts with various printing speeds (a): 20 mm/s; (b): 100 mm/s; (c): 300 mm/s; (d): 700 mm/s; (e): 1000 mm/s, with enlarged pictures to show the difference between different direction tracks from [150]

*iv. Drop spacing and nozzles spacing*

Several parameters influence the quality and homogeneity of printing on single layer: droplet size, spreading method, printing line spacing, ejection speed and material diffusion throughout the powder bed. Penetration and spreading of binder droplets inside the powder bed is basically related to the properties of powders, such as particle size distribution, morphology, specific surface area and packing density.

On the top surface where binder droplets fall, spacing between individual droplets and printing lines (nozzles spacing) dictate the precision of printing. Line spacing needs to be sufficiently low to ensure a good stitching between the printed lines, an obvious condition to get a strong layer. Meanwhile, printing duration and droplet volume will also affect these spacings. Larger droplet volume decreases the droplet spacing, all other conditions being unchanged. Nevertheless, the resolution of printing can be reduced and over-saturation might happen if the amount of ink deposited per surface area is too high. This becomes critical if multiple passes are considered: a common practice in BJ is to multiply the number of prints of the same layer to prevent a lack of ink because of clogged nozzles (Figure 18).


Figure 18. Nozzle clogging or insufficient nozzles spacing induced failed printing from [139]

*v. Printing orientation*

There is a limited literature about the influence of printing direction for ceramics binder jetting. However, some references can be found for metals with conclusions that can probably hold for ceramics as well. Thus Oh et al.[151] have printed samples for 3-point bending tests with 420 stainless steel powder to investigate the influence of different printing orientation. They have found that the bending strength (in the green state) for the y-oriented samples was 2 times better than the x-oriented parts. Reasons of the observed results were explained by an asymmetrical binder spreading, an insufficient penetration of the aqueous binder vertical to the printhead moving direction, and some discontinuities in the binder distribution between consecutive hatch lines. The obtained results are expressed in Figure 19.

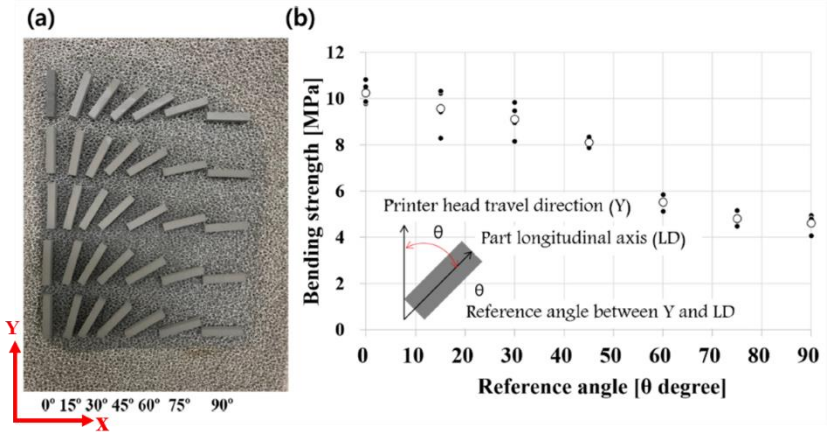


Figure 19. Effect of printing orientation on bending strength of printed parts. a): Green body samples printed by stainless steel powder; b): 3-point bending strength according to reference angles [151]

Other researchers have also found the same trend that y-oriented samples expressed better mechanical properties and lower porosity because of more uniform layers of powder along the y-axis during printing[152]. Meanwhile, z-oriented samples showed the worst mechanical strength because of a higher number of printed layers in comparison with either x- or y-oriented samples. And the advocated reason for that is the presence of defects formed beside the connecting zone of inter-layers or poorly bonding along intra-layers[153]. Optimization of printing orientation not only improved the mechanical properties and porosity, but also enhanced the surface topography [154].

*vi. Layer thickness*

Layer thickness (LT) is defined as the height of each layer that is spread by the recoater to form the bed along Z-axis. In general, the value of layer thickness floats from 15 up to 300 μm. Smaller layer thickness could render better surface finishing since it will decrease the staircase effect but this is detrimental for the manufacturing time and energy cost [155]. The same authors also concluded that a layer thickness of 100 μm when using lithium alumino-silicate ceramic powder with an average particle size 70 μm led to the lowest porosity and the highest relative density. According to this study, the layer thickness has to remain just slightly larger than the particle size. The data has been graphically illustrated in the review and shown in Figure 20 [22]. Other researchers suggest that the layer thickness should be 3 times the average particle size [70, 76, 156]. It should be twice this value for other authors [157] or just higher than the largest particle size for some others [107, 158]. A shared result show that thicker layers reduce the powder bed density which of course impacts the mechanical properties after sintering [152].

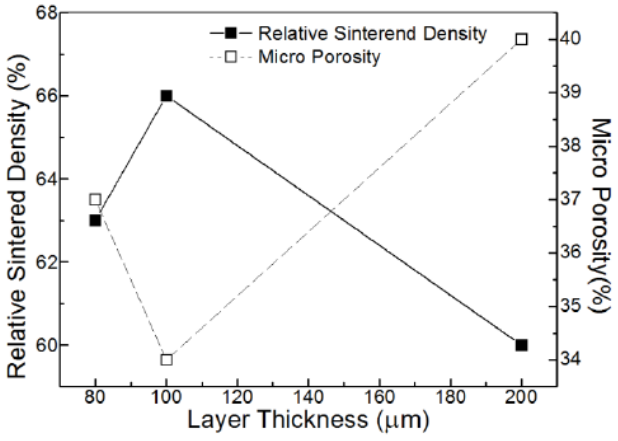


Figure 20. Effect of layer thickness on porosity and strut density of printed and sintered parts from [22]

Particle size and layer thickness are strongly interrelated. To meet some requirements (in terms of resolution for instance) of the printed part, they both have to be modified or altered. Though

fine particles with a narrow size distribution could give the advantage of a denser packing and a better surface roughness, the approach is practically limited as already explained [159-161]. For thicker layers and/or coarser powders, there might be also some issues to ensure an effective binder penetration within the powder bed. In general, particle size is not a freely altered-parameter in BJ: it is determined a priori and cannot be easily changed or modified without affecting the whole process.

*vii. Binder saturation*

Binder saturation (BS) is the parameter which defines the amount of binder deposited in the void volume of the powder bed [22]. To alter the binder saturation, there are many options. One solution is to change the amount of binder jetted out from printhead. Another one is to change the droplet overlapping as described in (Figure 22) [162]. The last one consists in multiplying the number of passes for a given layer.

The value of binder saturation firsthand affects the binder penetration and its subsequent spreading inside the powder bed. Less obviously, it will also influence how the binder interacts with the powder. As a result, improper binder saturation may result in poor printings (degraded quality or even broken parts) [163, 164].

The calculation of binder saturation can be done according to Eq. (9) and Eq. (10) in which $V_{Binder}$ and $V_{Pores}$ are the volume of deposited binder on printed area and volume of void space inside of the powder bed respectively. The p is the porosity of the powder bed. Volume of the whole printed part could be calculated by multiplying surface area and layer thickness. The value of binder saturation might exceed 1, since the binder dries out after a while and more volume of binder can be deposited in the voids [72]. Binder saturation is strongly dependent on layer thickness.

$$BS = V_{Binder}/V_{pores} \tag{9}$$

$$BS = \frac{V_{Binder}}{p * (Surface\ area * Layer\ Thickness)} \tag{10}$$

As demonstrated in [22], low binder saturation leads to limited contact and bonding between the powder and the liquid binder, which will result in poorer density and mechanical properties. By contrast, over-high binder saturation gives extensive binder spreading out of selected area which limits the printing resolution and the mechanical strength. Therefore, finding the optimized binder saturation is a critical (preliminary) objective in BJ. Examples are shown in Figure 21 to compare printed results with sufficient and insufficient binder saturation levels.

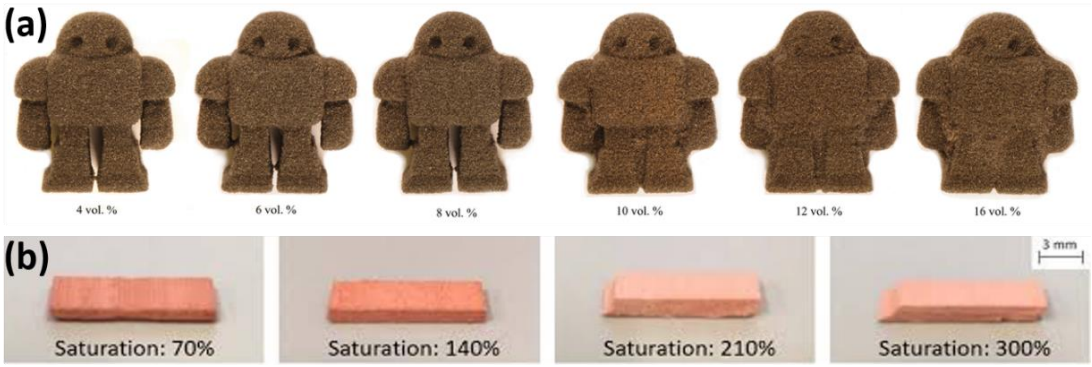


Figure 21. Influence of binder saturation on printing quality. a): Influence of excessive binder on dimensional of printed part from[165]; b): Printing effect comparison of sufficient and insufficient binder saturation level from [120]

There is a wealth of papers aiming to determine the influence of binder saturation on printing results [166-170]. It appears that lower binder saturation would cause layer delamination and a significant porosity which usually appears after thermal treatment. The explanation relies on the poor interlayer bonding and low particle sticking because of the limited amount of deposited binder. By contrast, over-saturation may lead to extra powder particles sticking on the periphery of the parts, resulting in a higher surface roughness and some dimensional inaccuracy for printings. Furthermore, higher binder saturation level means longer printing time and extensive drying process (each layer has to be almost fully dried before stacking the next layer) [163, 165, 171]. Hence, modifying the binder saturation is essential not only for the quality of printed part but also for optimizing the economy and materials cost.

Miyanaji et al.[97, 167] described that internal surface area does not help the wetting behaviour between powder and binder and leads to an overestimation of binder saturation level. Their results support the idea that wetting is not homogeneous during the binder penetration and spreading. More specifically, the binder does not successfully reach all the voids and remains confined in some regions of the bed. Research on binder droplet infiltration also has been developed via both simulation and experimental methods [172].These works confirm that there are two dominant factors : (1) powder bed packing (the interstitial voids increase and infiltration reduces with the increase of porosity) and (2) contact angle (the real amount of binder penetrating the bed decreases as the contact angle increases).

One single droplet determines the minimum binder saturation. Through simulations confirm that there are two different ways to change the binder saturation (already suggested by experimental works): (1) increasing or decreasing overlapping between droplets (2) overlaying droplets, ie. deposit droplets on the same area multiple times. The corresponding methods are illustrated in Figure 22.

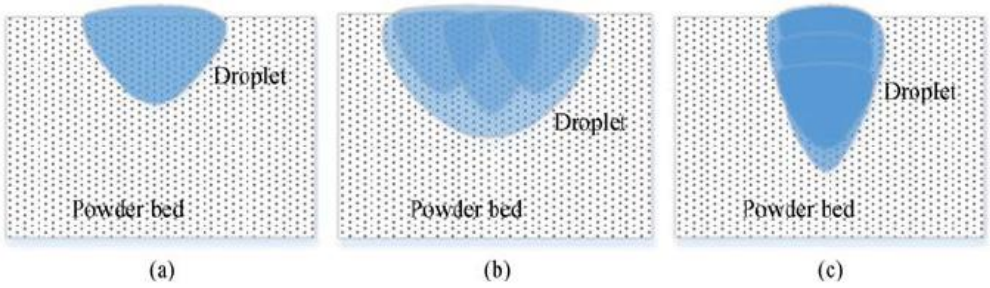


Figure 22. Binder saturation level control methods: (a): original single droplet; (b): overlapping droplets; (c): overlaying droplets from [139]

Powder bed packing influences the apparent wetting behaviour of powder and binder. For certain authors, a better wetting can be obtained with a denser powder bed probably through capillary effects [157]. An optimized binder saturation is also beneficial both for the mechanical strength and for the printing resolution. This is particularly obvious with the following results showing TiNiHf parts (Figure 23). It graphically illustrates that an optimized binder saturation level can be found for any given layer thickness. Unfortunately, it is always a matter of fine tuning and simply increasing or decreasing the binder saturation in an arbitrary way is not suitable to achieve the best possible quality for the printed parts.

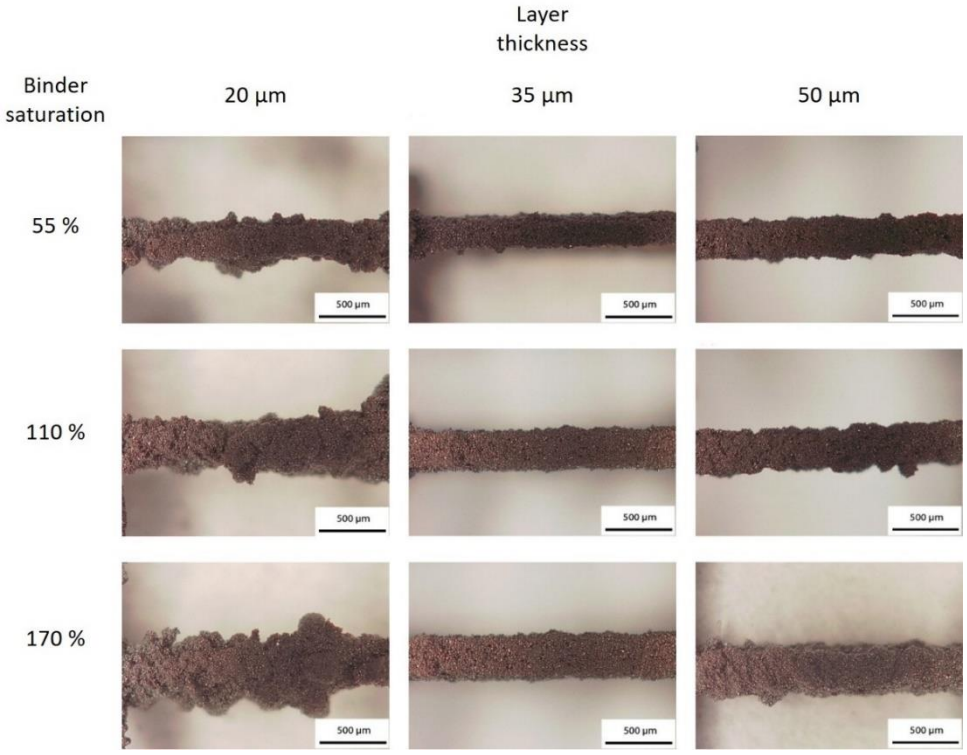


Figure 23. Optical micrographs of 3D printed TiNiHf square wire with different printing parameters (binder saturation and layer thickness) from [157]

The suitable binder saturation range differs significantly between available studies. For instance, Szucus et al.[173] increased the sintered compressive strength of hydroxyapatite

scaffolds from 0.156 MPa to 0.35 MPa and compressive modulus from 4.3 MPa to 11.1 MPa by increasing the binder saturation of a disodium phosphate binder from 25% to 45%. In the study from Gaytan et al.[174], the relative density of sintered barium titanate specimen increased with the increase of binder saturation from 75 % to 120 %, but the trend was opposite in the saturation range from 60 % to 75 %. Melcher et al.[175] have worked out that the relative density of sintered composite alumina parts enhanced from 56 % to 67 % with the increase of binder saturation level from 14 % to 35 %. According to Shrestha et al. [147], a 70% binder saturation is a satisfactory value whatever the layer thickness, roller rotation speed and feed to powder ratio. Patirupanusara et al.[176] investigated how the binder content influenced the printing process of polymethyl methacrylate (PMMA). More than 10 % of binder content is needed in order to successfully print parts with PMMA powders. However, binder content higher than 40 % generates parts distortion. Density was enhanced from 600 to 750 $kgm^{-3}$ when the binder content was increased from 20 % to 60 %, and the porosity was reduced obviously from 57 % to 42 %. Therefore, for these authors the most optimized binder saturation value is somewhere between 30 % - 40 %.

Combined effects of layer thickness (0.1 mm and 0.087 mm) and binder saturation (90 % and 125 %) were also evaluated with different methods (geometrical measurements, surface roughness and mechanical strength) using ZP102 (plaster) powder [169]. A considerable influence from inappropriate binder saturation levels is reported: (1) deterioration of dimensional accuracy; (2) poor surface finish; (3) distortion; and (4) cracks and defects. Similarly, increasing binder saturation in a suitable range will result in an enhancement of tensile and flexural strength as well surface finishing. However, interesting result was reported in [30] that the lateral binder spread is more pronounced than along the vertical direction, so that increasing layer thickness leads to lower mechanical strength and higher flexural strength with a better surface finishing when the saturation grade is even.

*viii. Binder spreading*

Binder spreading may occur in the lateral direction (e.g. in the building plane) or along the vertical direction. In another word, binder saturation level impacts the binder spreading together with packing rate of powder bed and powder properties. The spreading distance on lateral direction is always larger than along the vertical one. This is due to the fact that lateral binder spreading occurs along any direction around 360° while it is only along one unique direction in Z. Spreading is also larger for higher layer thickness and coarse particles. Coarse particles also bring faster lateral spreading.

Pore size distribution, shape of pores and uniformity of powder bed are all influencing the way the binder spreads. Certain authors have reported that more time is needed for the binder to penetrate a structure containing irregularly and non-uniformly distributed pores. Similarly tiny

particles are more prone to create agglomerates and formation of macro-voids in the beds which both help to increase the binder penetration depth (but not uniformly) [30, 90, 177]. Also, homogeneous distributions of pores provide more options for the binder to go through the bed more easily (thus reducing the penetration time). The mechanism is illustrated in Figure 24. In the figure, homogeneous powder bed (left) with random close packing is composed by free-flowing powders with Hausner ratio of approx. 1. Contrarily, heterogeneous powder bed (right) with irregular packing is composed by adhesive powders with Hausner ratio much larger than 1 [177].

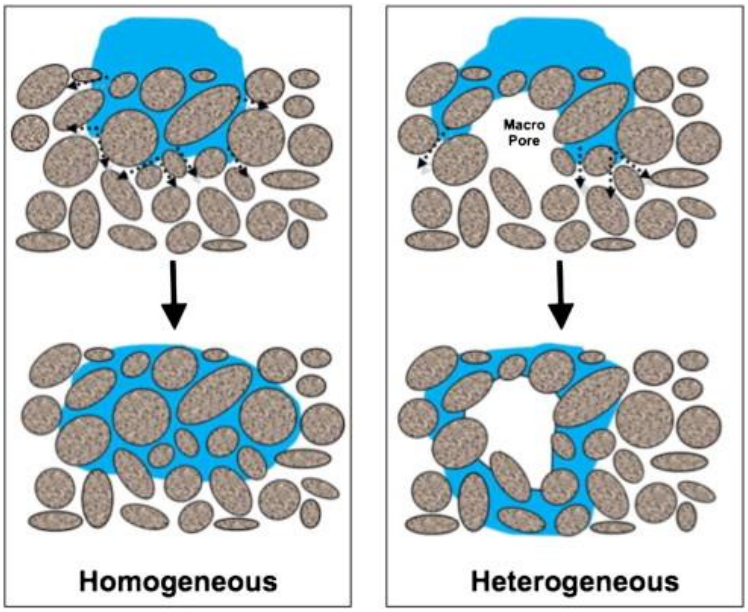


Figure 24. Different penetration behaviour within homogeneous powder bed (left) and heterogeneous powder bed (right) [90]

Capillary forces may also influence binder spreading in a positive way forcing the binder to flow through the porosity. However, Kathy. Lu et al. found that small pores and high surface area in the powder bed overcome the beneficial effect of capillary force, and hinder binder penetration [73].

*ix. Optional drying / heating step*

After each layer printing, there is still the option of a further drying or heating up (mandatory for certain binders). The thermal conditions are determined by the binder saturation level, its composition and chemistry, the layer thickness and a number of other parameters (such like thermal conductivity, surface area, permeability...) [30].

Phenolic binders are common in commercial machines and they do not need any heating. However, polymeric binders have to be dried around 15 – 45 seconds per layer for curing [30]. Drying not only affects printing accuracy and surface roughness, it may also influence the deformation during printing and after sintering.

Miyanaji et al.[97, 139] have studied drying in different situations which are also depicted in Figure 25. They have concluded that all previously dried layers underneath the last printed layer are preventing vertical binder penetration or spreading and the binder diffusion only occurs inside of the new spread layer. The importance of drying is highlighted in Figure 25 (a) that shows that sample with well-dried binder exhibits a much better dimensional resolution. If printing is pursued whenever the printed layers are not fully dried, the sample may be distorted. The newly deposited binder tends to accumulate and this over-saturation causes plastic deformation.

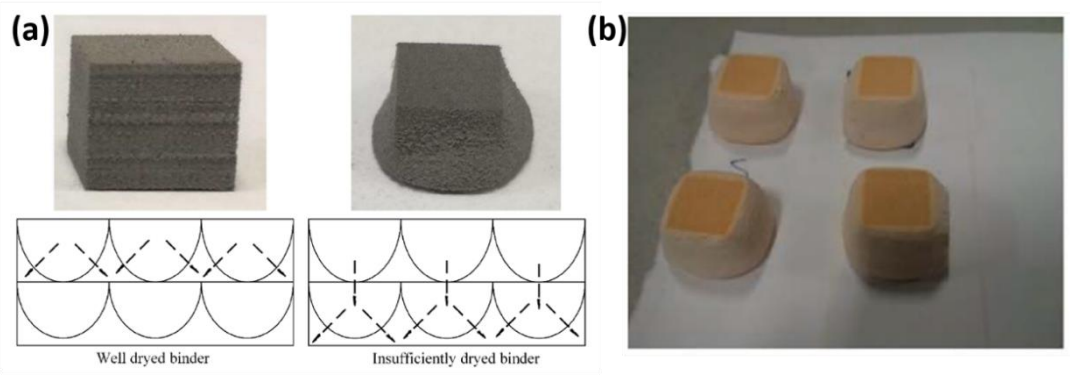


Figure 25. Influence of drying process on printed parts. a): Schematic of parts printed with different in-process drying steps from[97]; b) Examples of binder jetted parts of excessive binder saturation with sufficient drying from [139]

Another element reported in the literature is that excessive drying may result in noneffective inter-layer bonding of green parts [30]. This is explained by the fact that there is no residual/undried binder remaining in the previously printed layer that can help bonding at the interface with the new layer. Thus, the whole object looks like a collection of separated layers instead of a continuous block. As a matter of fact, the mechanical strength of the green body is exceptionally poor.

### 3.2.6. Green body strength

Green body strength is critical since it determines whether or not the object can be easily de-powdered without damage. It also dictates the resolution of the parts. It is related to the chemical nature of the binder, its saturation and its interaction with powder. In the worst case, a printed part with a low strength will not survive the de-powdering step and will break. Conversely, a part with an over-strong strength may stick too much on the manufacturing platform. As explained in [30], existing standards for powdered materials could be used to assess the strength of binder jetted parts. One may cite for instance the references ASTM B312-14 and MPIF 41 which specify the conditions of testing for test bars in a 3-point bending mode [178, 179].

Kathy. Lu et al. noticed that as powder packing rate increases (large particle size powder bed has the highest packing rate in the study), the green strength decreases (a result which is clearly counterintuitive). According to the author, several reasons may explain this surprising result. First, the number of contact points between particles (TiNiHf in this case) have effects on structure strength. Although finer powders have lower packing rate, they also develop more contact points on a given cross section area. Second, finer particles have a higher tendency to orient binder flow which then concentrates at the contact points (Figure 26). The contact points and the bonding strength at the contact points play obviously an important role and possibly offset the adverse impact from the lower powder packing rate[73].

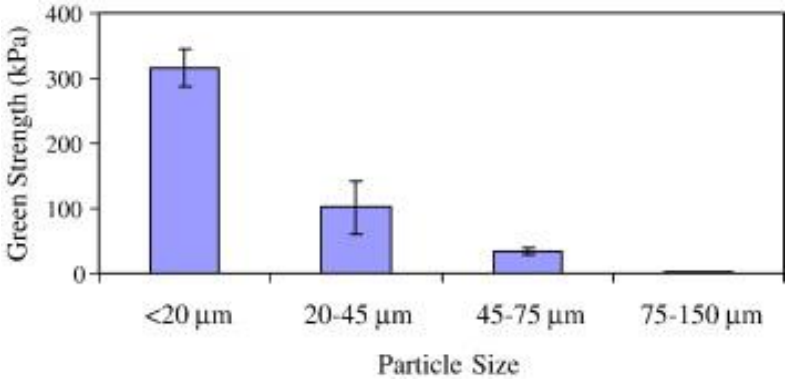


Figure 26. Green strength of 3D mesh structures from TiNiHf particles with different size from [73]

## 3.3. Post treatment after printing

### 3.3.1. Drying/Curing

Curing step after printing relies on similar mechanisms than those involve in drying/curing after each layer printing. It is actually more usual (as well as easier and faster) to cure the whole printed part to increase the mechanical strength. The main objective of the drying/curing process is the remove the binder in excess and/or to increase its strength so as to facilitate its removal from the surrounding powder [6]. Parameters of drying/curing (curing temperature, curing time, atmosphere, etc.) depend on binder properties, geometrical complexity of the parts, wall thickness and the overall volume of printed parts. For commercial binders that cure, the typical condition mentioned in[30] is to treat samples at 185 – 200 °C for about 8 hours.

### 3.3.2. De-powdering

The de-powdering step is one of the trickiest, time and energy consuming part in any BJ process. In general, the printed part should have enough green body strength to survive this step. Nonetheless, de-powdering has to be carried out very carefully since any part with complex structure and thin wall thickness can still be broken easily. Different methods may be selected to conduct the work, such as brushing, compressed air blowing, vibration and use of vacuum. Wet de-powdering may also be considered if the binder in the part is not dissolving in the

solution and strong enough. In this case, ultra-sonic bath can be an effective option. In addition, microwave-induced boiling, $CO_2$ bubble generation in soda water, and boiling fluid inside the internal channel have been considered as well, even if less common [119, 180, 181].

### 3.3.3. Debinding

Before sintering, residual binder and other organic phases contained inside the printed body have to be removed completely so as to permit to the part to sinter successfully. By conducting differential thermal analysis (DTA), the burning out temperatures of the various volatile phases can be determined easily. As the final result of debinding may be affected by the part complexity and size, the experimental temperatures are slightly increased higher than the measured ones so as to decompose all the polymers [30]. The heating ramp should not exceed the transport velocity of the products of pyrolysis, because of the excess pressure of the gaseous products that could result in damage [182]. Since BJ parts are usually highly porous, debinding is less delicate than in other AM technologies like stereolithography for instance.

The mechanism underlying debinding involves chemical and physical processes. The physical ones are well listed in [183]: capillary flow, low pressure diffusion process and high pressure permeation process. The capillary force is generated through the transportation of liquid polymer from huge to small pores. The liquid is evaporated when it reaches the surface because of large vapor pressure. Increasing temperature also increases the volatilization kinetics. However, when the temperature is up to a critical one, the capillary forces cannot saturate the demand of volatilization of the liquid, so that the vapor is pulled back to the green body. During debinding, polymers are decomposed by thermal treatment into low molecular weight parts and they are completely removed by diffusion and permeation. Migration of the volatile phases in the green body depends on the mean free path of the generated gas species. In addition, the mean free path changes with pressure, molecular weight of the gas and porosity. Normally, diffusion is controlled by low temperature and small pores. On the contrary permeation is controlled by large pores and high vapor pressures, where the laminar flow dominates allowing gas to exit from the compact [182]. The chemical mechanisms are related to the thermal degradation of polymers into volatile parts by pyrolysis. This proceeds through homolytic decomposition (symmetric decomposition of the duplet) of C-C bonds leading to radical cracked products [184].

Commonly used binders are water-based. Since they only contain limited amounts of organic phases, debinding can be performed together with sintering. However, for other binder systems containing high amounts of organics, debinding has to be carried out separately from sintering. There should be no residual left from binder after debinding process. Nevertheless, sometimes some residual oxygen and carbon residues are tolerable [185, 186].

### 3.3.4. Sintering

Sintering is an important and necessary step in the fabrication of ceramic materials. It is the process through which a powder compact becomes a solid. The process reduces porosity through diffusion of atomic species at high temperatures (but still lower than the material melting point). The main driving force for sintering is the reduction of the surface energy associated with pores and/or internal interfaces. Since reduction in free surface is linked to the reduction in surface energy, sintering occurs as a result of a more stable energetic configuration [187]. Shrinkage is a secondary effect of sintering and results from the material contraction associated to pores disappearance. Sintering can be helped by the presence of a liquid (i.e. liquid phase sintering) or a reactive phase at the grain boundaries.

The mechanism of sintering process is composed by four different stages described hereafter and illustrated Figure 27.

- Prior sintering, the grains just form a discrete assembly with a loose arrangement;
- Initial sintering stage forms necking between grains in contact. The atomic mobility is activated by surface diffusion mostly [188, 189]. The necks form rapidly but with a limited volume change and porosity reduction [30]. Diffusion transports materials from the surface of grains to the necking area at contact points. A linear shrinkage of around 3% is usually noticed [188-190]
- Intermediate stage is characterized by grain coarsening, high densification and formation of isolated pore structures. This stage is going to happen at temperatures for which diffusion takes place at the lattice and grain boundaries. During this intermediate stage which exhibits the most intensive diffusion, densification up to 92% can be achieved [30]. The necks formed during the previous stage may grow to reach up to 30% to 50% of the powder diameter. Tubular and originally interconnected pores are closing [188-190]. At the same time, isolated pores are formed as the consequence of neck growth and the formation of new contact points when shrinkage occurs. As a consequence, outward diffusion from the materials center to the surface renders powder surface flattening and part densification[30].
- Final sintering stage is about pores shrinking, pores closure and grain growth. In general, final stage of sintering starts simultaneously at middle moment of intermediate stage. This stage starts usually when the density increases to around 95% and sintered necks are half of the powder diameter [30]. During this stage, closed pores are progressively filled up by diffusion to achieve the maximum density. It should be noticed that grain growth and pore coarsening may also occur[190, 191].

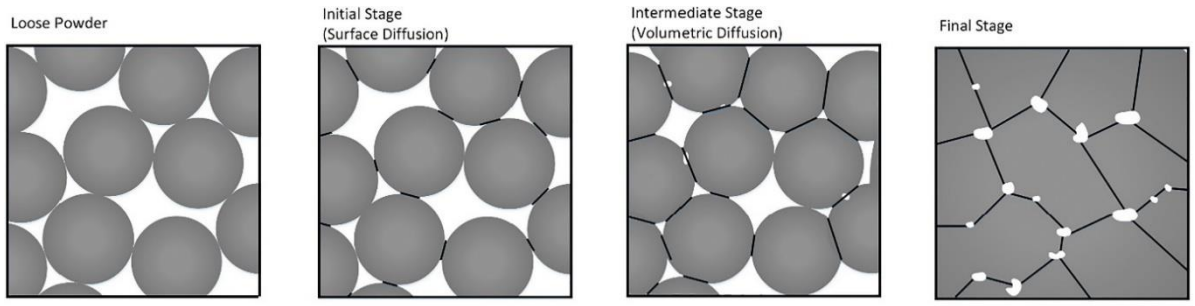


Figure 27. Different stages during a complete ceramic sintering process [192]

Normally, higher sintering temperature and longer dwelling time promote a better particle diffusion and improve the density (Figure 28) [22]. A similar trend is reported in the literature for binder jetting parts as well, especially in the works of Gaytan et al. [174] and Suwanprateeb et al. [22, 193]. Similarly Miyanaji et al.[139] also confirm that increasing the dwelling time appropriately also helps to further increase the density of part.

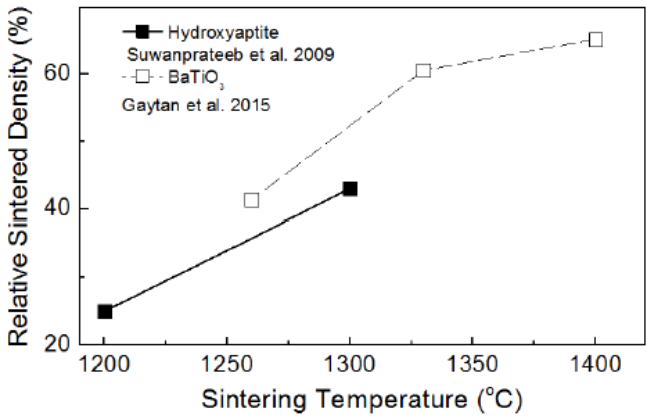


Figure 28. Relative density of sintered parts under different temperature from [22]

## 3.4. Innovative BJ processes

### 3.4.1. Gas assisted powder bed BJ

In powder bed AM, printed sample distortion or layer displacement always occurs due to the poorly packed powder bed that is not stable enough to resist to the forces generated from subsequent spreading and deposition. The lateral displacement of the printed object could happen. The exerted forces apply perpendicularly to the gravitational force but also tangential to the powder bed surface which results in the displacement of the object in the direction of recoating [194]. Low packing density is the main cause of this phenomenon. Sometimes support structures surrounding the printed sample are designed and serve as a fixture to keep the object tightly bonded to the building platform. However, this approach could not perfectly solve the problem. In an attempt to increase the packing density and limit the instabilities of

the beds, some researchers in Bundesanstalt für Materialforschung und -prüfung (BAM, Berlin)[194] presented a novel process named "gas flow assisted powder bed".

In their approach, the bottom side of a conventional printer is connected to a vacuum pump which generates an air flow through the powder bed and produces drag forces on particles along gravity direction. A filter made of porous sinter-steel serves as the building substrate and prevents the powder to pass through and being sucked inside of the vacuum pump (as shown in Figure 29 (a)). Figure 29 (b) illustrates the forces applied on individual particles at a micro scale. The effect of the gas flow actually shares similar mechanism with slip casting, since the gas flow induced forces that resembles capillary forces. The sum of all induced forces can be integrated out and the resulting average force is parallel to gravitation. As an obvious advantage, this approach might also be efficient to work with fine particles showing poor flowability but better sinterability. Experiments showed indeed a positive effect on the power compaction especially with fine particles. The relative density of powder beds from both free-flowing granules and fine particles (alumina) exceeded 43 % T.D which is impressive for dry powder bed AM [194]. Besides, the "vacuum forces" also facilitate fine particles to fill in the voids between large granules increasing packing more efficiently. The process also broadens somehow the powder specifications with less stringent requirements. This approach was also successfully applied to tricalcium phosphate powders [195].

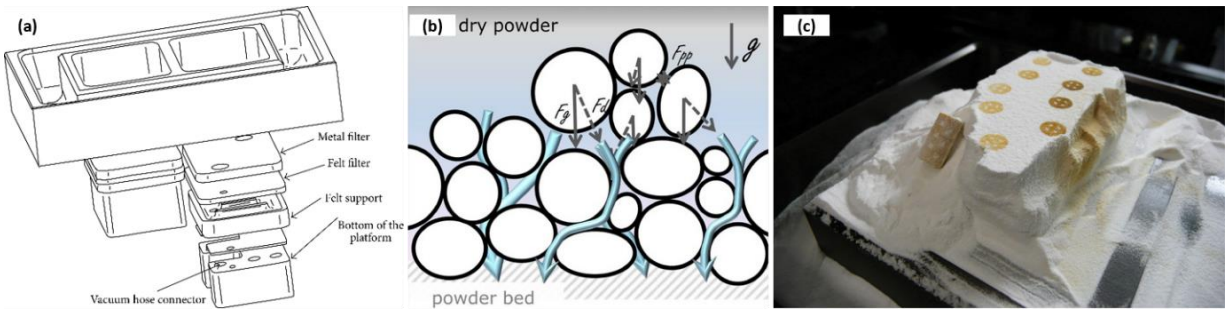


Figure 29. Gas-assisted powder bed. a): Drawing of the vacuum 3D print setup from[194]; b): Micro-view of gas flow assisted powder deposition: Fg = mg, m: mass of the individual particles and g: gravitational constant, Fpp: interparticle force, Fd: the force induced by the gas flow into the porous substrate[4]; c):Printed cylinders without support structure by applying the gas flow-assisted powder bed setup [194]

Since the external force helps to keep the powder bed in a compacted state, the process was tested under zero or µ-gravity environment to show its potential for space applications[196]. The work combined laser beam melting (LBM) and gas flow assisted powder bed and was conducted in three DLR's (Deutsches Zentrum für Luftund Raumfahrt) parabolic flight campaigns and operated by the French company Novaspace in Bordeaux. The setup shown in Figure 30 (A) is similar to the one discussed previously. In this case, the laser beam was replaced by an inkjet printing device to bond the grains together. Principles of a µ-gravity flight

is illustrated in Figure 30 (B). In the first step, the plane gradually reached an inclination up to 47° to reach an acceleration of 1.8 g (hyper gravity) (pull-up). Afterwards, the plane flied the cap of the parabola until 42° and 22 seconds of µ-gravity condition was experienced. Then, another 1.8 g condition followed (pull-out) at the end of parabola underwent the steep descent into a steady flight phase. Since the µ-gravity experiencing time was limited, powder bed spreading and laser melting were performed in different stages of the whole flight and both of them were performed in the stage of µ-gravity for comparison. Figure 30 (C) presents the setup of printer, laser, pumping and inert gas control system (nitrogen atmosphere used for steel powder laser processing). Final results illustrated that gas flow-assisted technique successfully helped LBM process conducted in µ-gravity environment. For demonstrative purposes, a 12 mm wrench was manufactured (Figure 30 (D)). The properties of product had no obvious difference compared with parts printed under 1.8 g, 1 g, or 0.1 g.

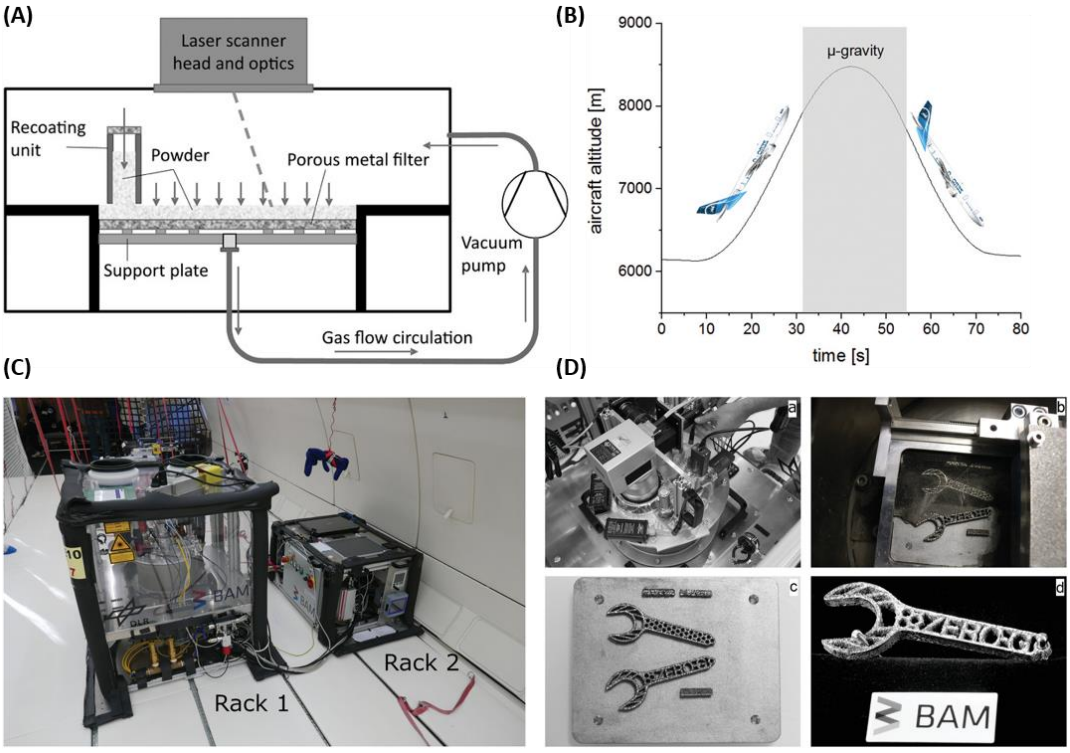


Figure 30. µ-gravity BJ printing test. a): Scheme of gas flow - assisted powder deposition unit; b): Schematic of the airplane flying a maneuver called “parabola”; c): Setup of LBM in µ-gravity with gas pumping and control system; d): Laser setup, different views of printed wrench. from[196]

### 3.4.2. Slurry powder bed BJ

*i. Foundation work of slurry-based binder jetting system*

Despite the fact that coarse powders possess a good flowability, they also lead to low packing density and poor sintering. On the contrary fine particles are much more prone to sintering but since multiple forces are involved, they tend to form aggregates and poor powder beds. In order

to increase the packing density of powder beds, a slurry containing a much finer powder could be a valuable option. This idea is to keep the fine powder for the benefit they bring to the process (sintering activity) while allowing their spreading (not possible in the dry state). This possibility was first considered for additive manufacturing many years ago [197-199]. Slurry-based binder jetting process was proposed in [200] by spraying or rastering a dispersed slurry with substantially amount of sub-micro ceramic powders onto a porous substrate. Properties of the slurries are similar as in slip casting. Different materials were used to test the printing capability of the method. The principle of slurry-based binder jetting process is shown in Figure 31. The sprayed slurry is undergoing a slip casting like process to compact the powder bed and a heating process can be applied after spraying (and binder deposition) to strengthen the bed. As said in the article [200], the typical solid content of the slurry is typically between 30 to 35 vol%. After drying the sprayed layer, the binder is selectively deposited using a conventional inkjet printer and the process is repeated until the part is completely built up. When it is done, the whole part can be removed by re-dispersing the printed part with surrounding powder bed in an ultrasonic bath. While the packing density of powder beds composed by spray dried granules was not more than 35%, with this method it reached up to 67%.

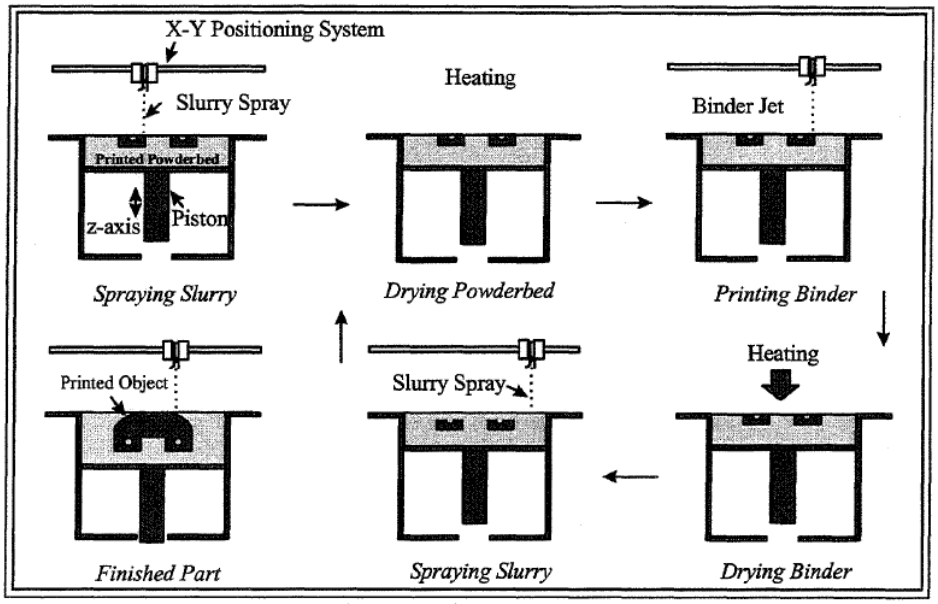


Figure 31. Schematic process of slurry-based binder jetting from [200]

In order to have stable printing process and good final properties, the quality of the microstructure of the powder bed should be well-controlled. Different parameters influence the property of the powder bed, such like stability of the slurry, powder morphology, and also the raster variables. It has been mentioned that slurry powder bed does not contain any lamination defects between different layers but incidentally some little pores around 2 to 3 μm in size [200]. These pores are suspected to result in an inappropriate spraying especially sprayed line spacing. To overcome this barrier, a new layer forming method was invented by the same group

several years later which is called line merging [198]. Line merging makes the slurry spread more continuous and eliminates the line ridge effects. The nozzle path of conventional jet spraying is maintained in this new approach, however, the inter-arrival time is reduced drastically and the slurry chemistry is adapted to decrease the rate of slip casting. Thus, line N+1 is sprayed before line N is completely slip cast which creates a continuous deposition process and a good interfacial bonding. Powder beds comparison between conventional spray method and line merging method are pictured in Figure 32.

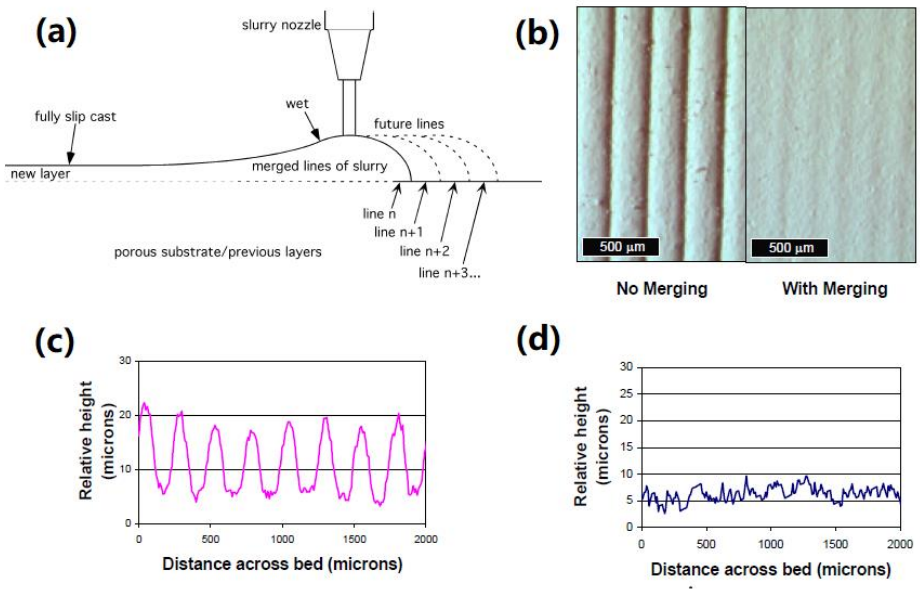


Figure 32. Line merging in slurry-based BJ process. a): Diagram of line merging principle; b): Surface profile of conventional and line merging obtained powder beds; c), d): Profilometry measurements of conventional and line merging powder beds from [198]

Apart from the spraying process itself, the authors demonstrate that raster displacement was less efficient than vector printing, which could be carried where the outline of the layer is first rastered and then the interior part is sprayed with raster type.

Binder selection is critical in the slurry-based approach as more requirements are needed in comparison with conventional BJ [198]. Binder has to penetrate powder beds with higher green density (thus with a lower level of porosity and finer pores) and provide enough strength for the part to survive the re-dispersing process. That means that the binder has to be insoluble during redispersion. Three different binders (polymeric particle suspended binder, emulsion and homogeneous solution phase) were assessed and compared through investigating the wetting behaviour and interaction with powders. Solution phase binder was proven to give a good penetration and a satisfactory spreading in the powder bed as long as its molecular weight does not exceed 5000 g/mol.

This process, not only increases the density of final parts, but also clearly improves the surface roughness and printing resolution. According to the author [198], the smallest layer thickness of slurry-based binder jetting could reach 13 µm. Combined with the use of finer powders, this explains why better surface finishes as shown in Figure 33, can be obtained.

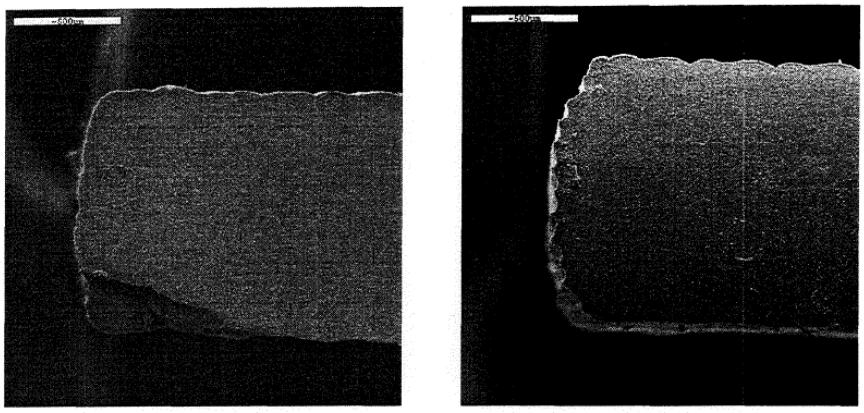


Figure 33. Cross section of printed alumina parts and effect of the layer thickness; a): parts with 50 µm layer thickness; b): parts with 100 µm layer thickness from [200]

Different ceramic materials have been successfully tested with this method by the group of M.J. Cima, such as alumina, silicon nitride or lead zirconate titanate. For instance, printed parts with alumina powder (0.5 µm) with slurry-based binder jetting process reached 98.7 % relative density, a value very close to that obtained from pure slip casting (99.0 % relative density). Different parts with complex geometry have been printed with different functions as shown in Figure 34. Nevertheless, it appears that the printed parts looked restricted in size which might due to the machine design limit or the tricky re-dispersing process (higher green density of powder beds). This may explain why this technology was not progressing more after these first papers.

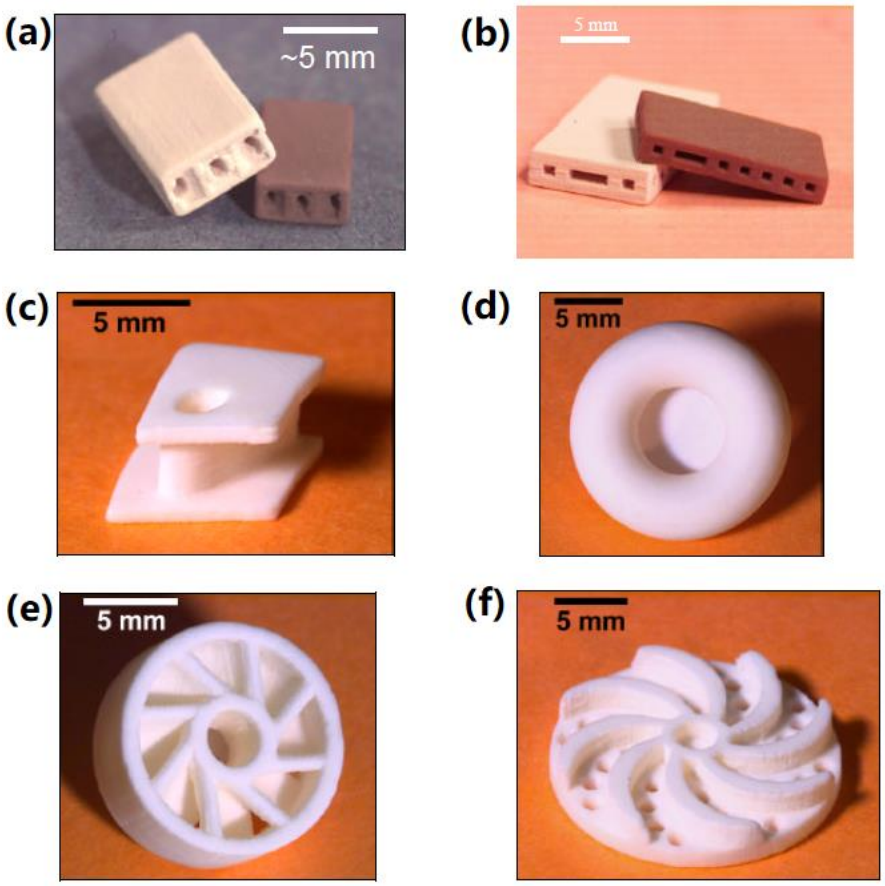


Figure 34. Different parts printed from slurry-based binder jetting process; a): Green and dense $BaTiO_3$-based radio frequency (RF) filters; b): Green and dense $BaTiO_3$-based electromagnetic band gap (EBG) devices; c): Dense $Al_2O_3$ stator; d): Dense $Al_2O_3$ toroid; e): Dense $Al_2O_3$ rotor; f): Dense $Al_2O_3$ sample geometry from [198]

*ii. Layer-wise slurry deposition (LSD) process from BAM*

Many years after the seminal work of M.J.Cima, the approach was rediscovered and improved by Jens Günster et al. [201]. The revised technology was then called Layer-wise Slurry Deposition or LSD. Originally it was combined with laser treatments to ensure consolidation [202, 203]. The liquid suspension of ceramic particles is spread as a thin layer comparable to tape casting but the difference between LSD and slurry-based binder jetting [17] is the slurry deposition method that differs. LSD uses a doctor blade to spread the slurry instead of nozzle spraying. After spreading, each layer is dried and the binder is conventionally deposited. The powder beds are treated with a laser [201-203] or more recently with binder [204]. Both fabrication methods have been successfully carried out with nice results. Figure 35 shows some printed cups by LSD with laser sintering process. In the following, we are mostly concentrating on the use of LSD for binder jetting.

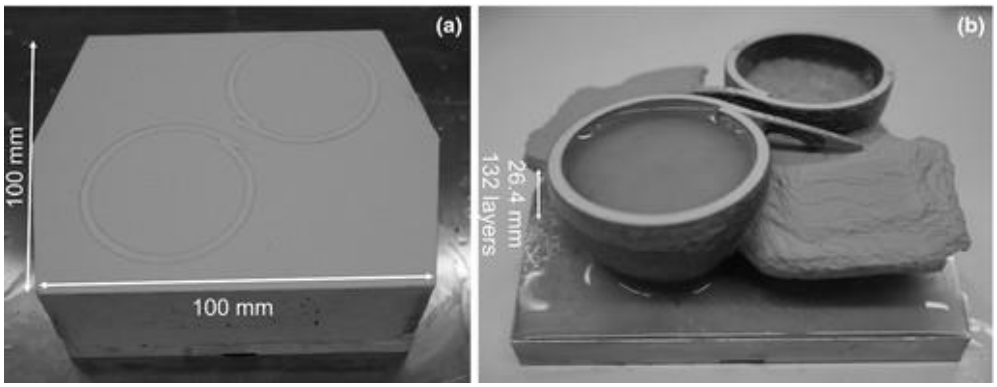


Figure 35. Release of two espresso cups made of porcelain by employing the Layer-wise Slurry Deposition (LSD) technology. (a) powder bed, formed by 132 layers with a thickness of 200 μm, containing the two laser-sintered cups; (b) cups partially released from the powder bed from [4]

In the LSD approach, one layer of slurry is spread and deposited on a porous substrate. It is then dried at room temperature or sometimes heated a bit. The binder is then deposited using a conventional inkjet system. The next layer is then directly spread on the previous layer using the same doctor blade system. During the slurry deposition, the cast formation kinetics follows a conventional square-root-of-time law. Water content in the suspension is drained from the slurry to the porous substrate because of capillary forces (and through the previously deposited layers). This leads to a higher green density which is typically comprised in a range of relative density of about 55 – 70% [204]. The LSD scheme is explained in Figure 36. The speed of the recoater (the blade) has be carefully selected so as to prevent high shear stresses to create inhomogeneous deposition and non-uniform layers which influence the final printing quality. A typical speed of 50 mm/s is chosen to ensure a good quality [4].

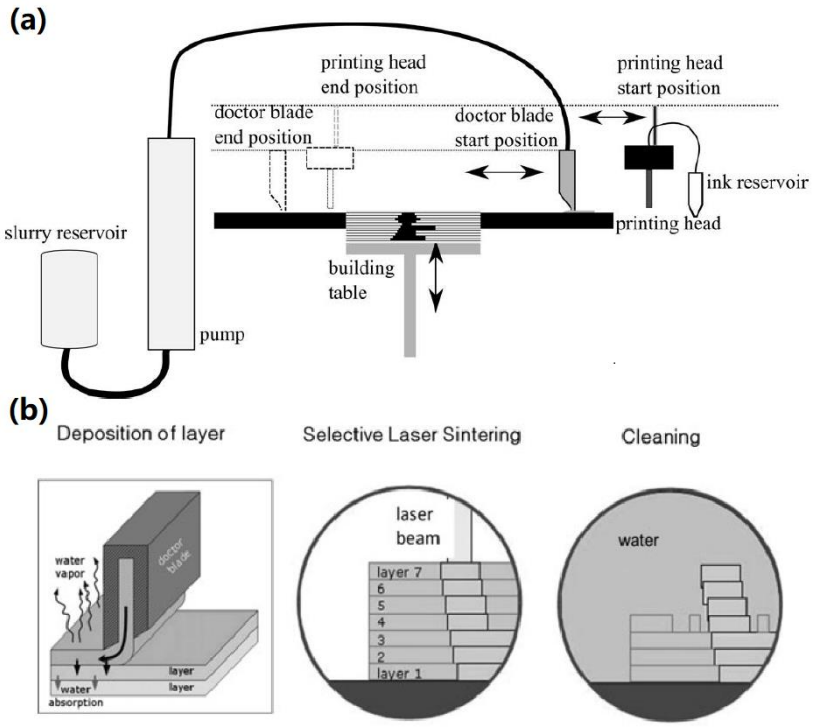


Figure 36. LSD process. a): Scheme of LSD process and b): slurry powder bed spreading from [203, 204]

The same team has also conducted inter particles force analysis in an attempt to explain the cast formation (in Figure 37). Forces acting on individual particle are shown in the diagram. As the slurry comes in contact with the previously dried powder, the capillary forces drag the liquid phase of the slurry into the porosity. During the process, the newly deposited particles follow the liquid flow and settle at places where they tend to maximize the contact with the other grains. More globally, the packing is a random one. According to the authors, the particles in the suspension exert no influence on the deposition process of settling particles. Four forces are acting simultaneously on each particle: gravity force (Fg), interparticle force (Fpp, Van der Waal's force), another force (Fd) induced from the flow of the suspension medium and finally buoyancy (Ff).

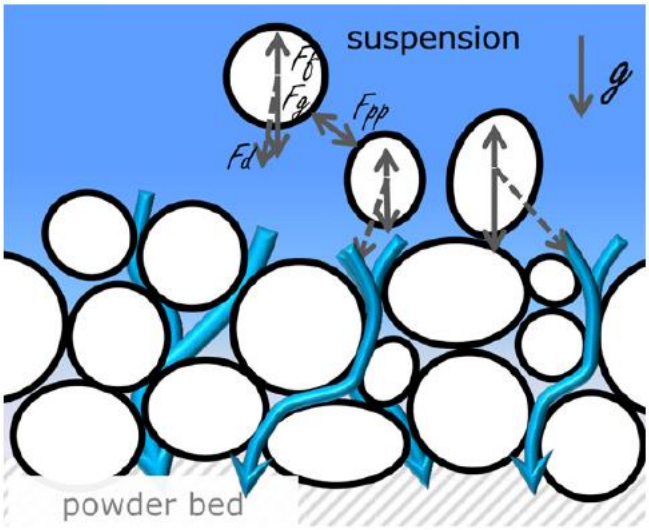


Figure 37. Illustrating mechanism diagram of forces analysis on particles in LSD deposition [4]

LSD has opened the door to the use of original binder systems. Zocca et al.[204] used for instance, an alginate binder to bond alumina powders. The binding mechanism is activated because of cross-linking of sodium alginate by bivalent cations. The gelation of alginate gives high strength to the printed part which is sometimes a major limitation in BJ. Alginate also has other interesting features such as an improvement of the rheological properties of the slurry which is highly suitable for a better control of the process. The amount of alginate used in the research was only 0.3 wt%. After printing the part is removed from the surrounding powder bed by rinsing with deionized water and treated in a furnace as usually. Relative density of final printed alumina part reached more than 99%. Green bodies, sintered parts and morphology of parts non-sintered and sintered (different sintering temperature) are illustrated in Figure 38.

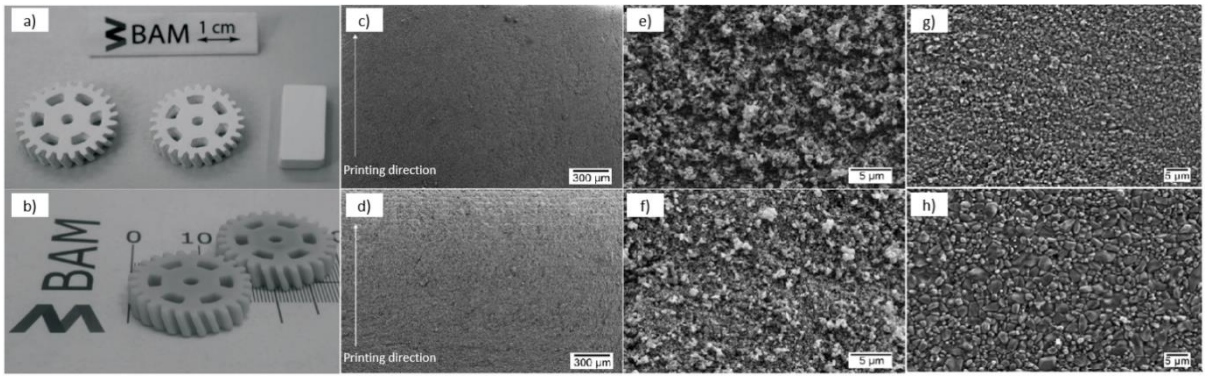


Figure 38. Parts printed by LSD process and sintered. a), b): Green bodies and sintered bodies of LSD-printed alumina toothed wheels; c), e): SEM images of the fracture surface of the cross section of alumina green bodies fabricated by LSD process with layer thickness at 50 µm; d), f): Enlarged scale SEM images corresponding with c), e); g), h): SEM images of sintered alumina parts by LSD printing and sintered at 1540°C and 1600°C

Moreover, the group in BAM tested also other ceramic materials such as porcelain [205], silicon carbide [206]. Layer-wise slurry deposition is a nice approach to get higher powder bed packing density, smooth surface finishing and defects-free part. The major concern about this technology is the cleaning step which can be time consuming and expensive. It is not guaranteed that scaffolds or any other part with internal channels for instance can be processed this way and survive cleaning.

### 3.5. Application fields of BJ ceramic parts

BJ is widely used in casting industry due its versatility to produce molds or cores rapidly and with a high level of complexity. Different papers have discussed BJ for sand casting [207, 208]. They demonstrate that the porosity of printed molds and cores is highly beneficial to gas transport and give some weakness to the body that is helpful to remove them from the casted part [208]. Though mass production with BJ is not yet as cost-effective as traditional methods (when parts are identical), it becomes a serious competitor for low or intermediate production volume or for mass customization [20].

Meanwhile, BJ for molds manufacturing also allows the incorporation of monitoring devices to control the molding process, in the view of J. Walker et al [209, 210], something which is not possible with more conventional techniques. Shangguan et al.[211, 212] have found that the richness and freedom of BJ in designing a mold may serve also to improve the cooling process. These authors report a significant improvement in BJ-printed rib-reinforced molds instead of dense traditional molds for casting aluminum alloy 365. Moreover, curing heat treatment effect on permeability and compressive strength of the mold[213], the resulted roughness of casted products[214], generated gas from the mold after casting and improved dimensional resolution[215] were also investigated.

BJ also has a huge potential in medical field as mentioned in [20], including denture framework [216], surgical implants [217] and pharmaceutics [218]. In pharmaceutics, researchers have discovered [219, 220] that controlling the drug release rate can be achieved by printing drug delivery device with BJ (with commercial applications already on the market). Basically, the idea is to use the inner porosity of printed pills as a reservoir to active principles. Following this idea, Fu et al. [221] demonstrated that 98.5 % of a drug can be released in just 2 minutes after the device wetting and disintegration. The group of M.J. Cima used resorbable polyesters as a base material to investigate drug release. They showed that drug release rate can be controlled very accurately using this technology [222]. Different kinds of bio-ceramic materials have been processed with BJ to fabricate complex architectures. For example, Hydroxyapatite [57], β-tricalcium phosphate [170, 223, 224], brushite and monetite [41], apatite-wollastonite glass ceramic [193, 225], and bioactive glass [155] have all been reported. BJ was demonstrated

to be very suitable to manufacture scaffolds for bone engineering [226]. Butscher et al.[45] have reported similar results where the residual porosity is helpful to biological cells.

Additionally, certain electronics parts have also been printed using BJ. Even though the requirement of stacking multiple materials is difficult to achieve with the method, several interesting results have been reported [227, 228]. As an example, Rojas et al.[228] reported the fabrication of various 'Radio-Frequency' electronic components including antennas, filters and feed horns. Complicated designs could effectively reduce the total weight of the components while keeping their functionality to a satisfactory level. Similarly, barium titanate was printed to produce capacitors and piezoelectric devices [174]. Promising piezoelectric properties were obtained, even if the density and the grain size of final products after thermal treatment were far from the optimum. Polymer-derived ceramic (PDC) materials were also considered in some papers which also offer some advantages. A high polymeric density around 80 % T.D could be reached thanks to a local dissolution of the pre-ceramic polymer by the solvent of the binder which improves filling the inter-particles voids [229].

# 4. Conclusion and outlook

Overall, BJ possesses its own disadvantages and drawbacks compared with other AM techniques as mainly explained in section 3.1.2 (Chapter 1). After looking through the numerous researches that have been conducted, it appears that conventional BJ is still plagued by a poor sintered density (for technical ceramics) and finish surface (very rough). Novel systems are tested that may help to overcome these limitations. However, they also come at the expanse of new issues (in LSD, the de-powdering step is time consuming).

One issue of conventional BJ is the dynamic interactions between the binder droplets and the powder (Ziaee [20]). These authors considered that there is great need to progress in the utilization of finer particles so as to enhance the mechanical property. Innovative post-treatments also hold some promises to improve the quality of printed parts. Interestingly, the greater attention will be paid when the process application in space thrive in future, which will drastically accelerate the advancements in the process capabilities. Du Wenchao et al.[22] have expressed their opinions for future research directions of BJ. At first, further researches have to be carried to understand parameter-property relationships. Current studies are sometimes inconsistent with strange reported results usually considering only a few parameters. The results are also limited because of some specific choices in terms of materials and experimental conditions. Therefore, a wider range of input parameters should be investigated to get a broader script about parameter-property relationships. A fundamental understanding of the process physics could provide new insights about the mechanisms. Secondly, sintered density needs to be improved. Reached density in current researches is not sufficient for high mechanical loading tests and applications. Thus, increasing the sintered density is strongly recommended

to widespread the applications of binder jetting process with ceramics. Last not the least, more industrial applications should be developed with the process. Currently, casting mold and tissue engineering still dominate the application fields of the process, a few works focus on electric functional parts.

According to present authors, there are also a few aspects on which attention should be paid to enhance the quality of printed products. Poorly defined commercial binders are used in numerous researches thus neglecting the detailed bonding mechanisms. Therefore, chemical interactions between powders and binders should be more carefully addressed (such an attempt was done with alginate binder in [204]). The hardware is also an important point to be modified. Since most researches were conducted on commercial BJ, the range of certain parameters are restricted to the capabilities of the machine. There might be some interesting discoveries to be done by testing significantly different parameters or settings.

# Chapter 1. Current state of the art

## Objective and methods of the thesis

The present work is an attempt to circumvent the limitations inherent to the conventional BJ process. It is divided into different chapters, each presenting the results obtained on specific elements for the improvement of the process. The results of each chapter have been the subject of a scientific article published or in the process of being published.

In order to improve the process, a work only oriented to the raw materials would be insufficient: it is mandatory to combine material studies with specific and innovative machine developments. Thus, the binder jetting equipment used for this study is a prototype co-developed by CRIBC and OPTEC. This machine combines a conventional BJ process with an in-situ laser to improve the resolution of the printed parts as well as their surface finish. As such, the equipment uses a hybrid process combining additive and subtractive manufacturing.

**Chapter 2** is devoted to the study and development of an alumina powder compatible with the equipment as well as to the optimization of the printing and densification conditions. The aim of this preliminary work was two-fold: firstly, to reproduce the state of the art of alumina manufacturing by binder jetting and secondly to develop a comprehensive methodology for the preparation of suitable ceramic powders and optimization of printing parameters for the customized machine (but in fact for all the machines technologically similar). This was also the technological baseline from which all further developments have been evaluated.

The influence of the powder characteristics (particle size distribution, morphology, flowability, packing density and roughness of powder beds) and printing parameters (recoating speed, layer thickness and binder saturation) were carefully assessed and are here reported. The mechanical performances of sintered bodies were also evaluated and compared with the literature. This chapter coincides roughly with the first published paper [230].

**Chapter 3** describes the approach we decided to follow to enhance the density of sintered parts, i.e., the post-infiltration of pre-sintered bodies with a ceramic suspension. Different factors suspected to influence the process have been carefully studied such as the number of successive infiltrations, the pre-sintering temperature (rarely reported), solid loading, the infiltration duration, etc. The density and porosity distributions inside of the samples were also analyzed using different tools combining SEM, X-ray Microtomography and porosity measurements. All this is the topic of the second paper which has been submitted at the time of writing.

**Chapter 4** reports the preliminary studies of the hybrid process to improve the surface roughness and dimensional accuracy of fabricated parts. The idea was to use the laser operated in pulsing mode to refine the outline of each printed layer or inside of each fresh printed layers to produce sharper edges. A parametric study was carried out to assess the effects of different laser parameters like laser power, repetition frequency and scanning speed. The influence of

the laser refining evaluated with the sharpness and roughness of laser treated bodies compared with the “only printed” counterparts. This part of the work corresponds to the third paper which will be soon submitted as well.

# Chapter 2. Binder jetting process with ceramic powders: influence of powder properties and printing parameters

## 1. Introduction

### 1.1. Background

Binder jetting (BJ) is an inkjet-based process to create 3D objects using powders [17]. The process consists in spreading thin layers of powder, with printhead selectively ejecting and depositing binder droplets on a powder bed layer by layer to produce the object. Among all additive manufacturing (AM) technologies, BJ is one of the most promising way to process ceramic materials as it allows a high level of design freedom and ease of scale up. In addition, the absence of supporting structures for parts comprising overhangs or bridges and compatibility with a broad range of materials are also advantages [22]. BJ possesses a relatively high building rate compared to other AM technologies and large objects (more than 1 $m^3$) can be built. For instance, a 100-nozzles printhead can fabricate parts at building speeds about 200 $cm^3$/min [45]. Nevertheless, drawbacks still exist in conventional BJ process such as low packing density and consequently low sintered density of final parts. Poor finish surface could be resulted from limited layer thickness (LT) and coarse powder (flowability is a requirement for the process).

Powder bed properties are the foundation of BJ. Their characteristics are strongly dependent on the powder features and on the deposition mechanism (i.e. the recoater), which is a key component of the machine to build parts reliably and fast [20]. Particle size distribution, morphology and flowability influence primarily the printing process as they all dictate the packing density of the powder beds and subsequently the quality of sintered parts. According to numerical and mathematical models which aim at assessing the behaviour and compaction of powder, the flow characteristics of powders is a critical point [62]. The flow depends on the inter-particle forces which vary with particle size, shape, specific surface area, composition, and external parameters such as temperature and humidity. Nevertheless, as a general rule of thumb, a suitable powder for BJ should exhibit grains with a well-rounded shape and a particle

size distribution close to a monomodal one. These criteria are required to ensure a sufficient flowability of the powder which remains a basic requirement for this process. If the powder flowability is poor, beds are usually full of large defects and the printing of parts becomes highly challenging. Unfortunately, if ensuring flowability of the powder is beneficial for printing, however, it is highly detrimental for packing density and sintering. Several studies have been carried out to optimize the packing both experimentally and numerically [48, 98, 231-234]. Using coarse particles implies that the packing density is low and full densification cannot be reached during sintering: large voids remain between grains and the whole part is highly porous. For most uses, post-infiltration is necessary to fill in the open porosity [235]. In some cases, liquid phase sintering helps in obtaining higher sintered densities, unfortunately not all ceramics are sintered with a liquid phase. To optimize the particle size distribution for packing, an alternative approach for densification is to blend fine and coarse powders. It is sometimes a valuable option but it usually comes at the expense of powder flowability. Whether or not this solution is functional, it depends on the machine itself, especially of the powder deposition system. If the recoater is a simple wiper with a blade-like shape then powder flowability is mandatory. On the contrary, a rotating roller or a counter-rotating roller [144] are more forgiving and allow to use less flowable powders. Sometimes a combination of two systems (a hopper and a roller) is utilized [75, 145, 146].

## 1.2. Motivation

To alleviate the issues related to the powder flowability, new approaches using fine powders and slurry deposition systems have been considered recently to enhance the green packing density [7]. Although the results are promising, there are still some specific issues that need to be addressed for these approaches to become fully mainstream. Highly compact powder beds formed with fine powders make the de-powdering step extremely challenging. Since the powder surrounding the part is no longer loose, removing it by brushing without breaking the part itself can be a hard and time-consuming task.

For a newcomer in BJ technology who would like to develop its own ceramic powders, there is no all-sided recipe available in the literature that could be applied straightforwardly and there is no real comprehensive methodology explaining how to process ceramic powders for BJ. This chapter attempts to develop a comprehensive procedure to get ceramic powders highly optimized for conventional BJ. The work starts from the basic level, i.e., by considering an extremely fine commercial alumina powder and describes how such a powder can be further processed to make it compatible with BJ. It is shown that printing parameters have to be modified accordingly to achieve maximum density of printed parts after sintering. Although the final performance of the sintered parts will be dramatically affected by the machine itself,

the whole procedure and optimization steps here can be straightforwardly applied to any other systems be it a custom or a commercial machine.

# 2. Experimental

## 2.1. The machine

The binder jetting machine (Figure 39) used in this research is a custom-made system developed by BCRC in collaboration with OPTEC laser systems (Belgium). The fundamental principle is based on the conventional binder jetting systems[17], e.g. powders are delivered by a recoater (a simple doctor blade in this study) from a feeding tank to a manufacturing tank. Two manufacturing tanks with different size (10 cm * 10 cm and 20 cm * 29 cm) can be chosen according to the dimensions of designed product. The material feeding tank has 20 cm * 29 cm size. A disposable printhead is mounted in the machine (Xaar 128, United Kingdom). This cheap printhead is perfectly suitable for R&D and it is compatible with a broad range of inks and aqueous binders.

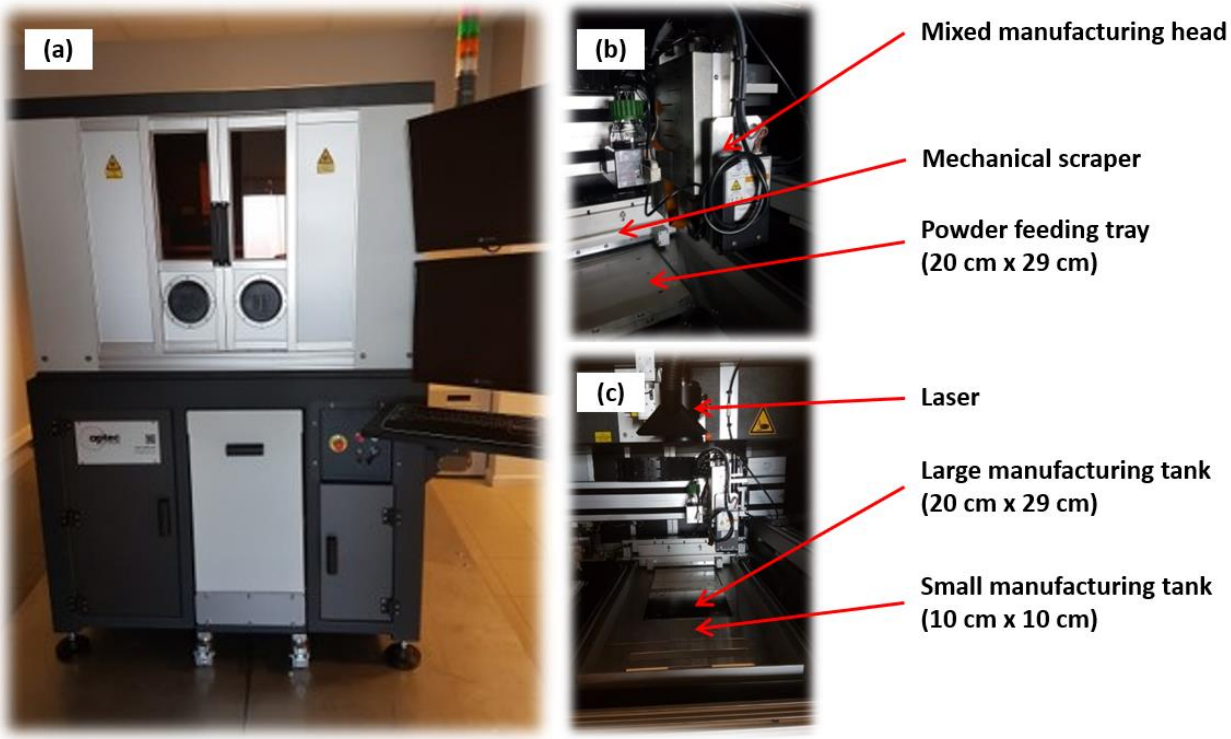


Figure 39. The customized binder jetting machine in BCRC & OPTEC. a): Outlook of the machine; b), c): Inner details of the machine and setups

## 2.2. Materials and methods

The whole study was carried out using a fine alpha-alumina powder which is labelled hereafter as Al-P (P172LSB, Alteo, France). As this powder is not free-flowing, it is not directly compatible with the machine which requires a minimum flowability for an efficient powder spreading. Consequently, it was further processed to shape granules or agglomerates with better flowability. An aqueous slurry containing 70 wt% of alumina dispersed with 1.5 wt% (in respect to the weight of powder) of carboxylic acid dispersant (Dolapix-CE64, Zschimmer& Schwarz, Germany) was ball milled during 12 hours with alumina media to break agglomerates. To change the size and morphology of the granules, the slurry was then dried using two different routes, e.g., freeze drying and spray drying. Main part and cyclonic part of the spray dried powders (Niro, GEA, Germany) are hereafter referred to as Al-SP and Al-CSP. Furthermore, the main part of the granulated powder was split in two batches after sieving at 100 μm to assess the influence of the granule size. The fine fraction is labelled as Al-SP1 while the coarse one (i.e. granule size over 100 μm) is Al-SP2. Finally, freeze drying (Martin Christ, Germany) was also carried out (pressure: 0.5 mbar; slurry was frozen under 77K with liquid nitrogen; trap temperature: 183K; duration: 24 hours). The dried powder was then sieved at 200 μm to obtain a non-spherical powder but yet agglomerated powder (labelled as Al-FD). At the end, a total of 6 different processed powders was produced for further investigation.

The particle size distribution (PSD) was measured by laser scattering on a Malvern Mastersizer 2000 in dry mode (Malvern Instruments GmbH, Germany). Specific surface area (SSA) was determined by FlowSorb III surface area analyzer (Micromeritics, USA) with nitrogen adsorption, applying the Brunauer Emmet Teller (BET) equation. Prior SSA measurements each powder was further dried in an oven for 24 hours at 110 °C. Morphology of grains was observed by scanning electron microscopy (SEM) (Tescan, Czech Republic) and density of powders was measured using a pycnometer (Micromeritics, USA). Flowability is the ability of a powder to move over itself when being transferred and spread by the recoater. To assess the flowability of different powders, Hausner ratio (H) [46] and Carr ratio (C) [47] were calculated (Eq. 1 and 2 in Chapter 1). Tapped density and bulk density were also determined using a Densitap ETD 20 (Granuloshop, France) machine.

In order to have a better understanding of the powder behaviour within the binder jetting machine, a specific setup was fabricated to mimic how the powder spreads. A rubber mold with an inner cavity of known shape and volume was designed Figure 40(a). Powder is then filled into the mold with the wiper of the machine Figure 40(b). Packing density is then calculated by weighting the mold content and dividing it by the cavity volume. Although this thick powder bed is noticeably different from a stack of thin layers, it may give some insight on the powder ability to re-arrange itself during spreading. Roughness measurements of the powder beds were

also carried out with 3D laser scanning microscope (VKX-250, Keyence, Japan). Arithmetical mean deviation (Ra) and maximum height of profile (Rz) are the two indices which have been calculated to assess the smoothness of powder beds which is expected to be related to the amount and size of packing defects. Roughness was measured on 4 cm track length along the spreading direction and analyzed by filtering with a cutoff of $\lambda_c$ = 8 mm for powder bed.

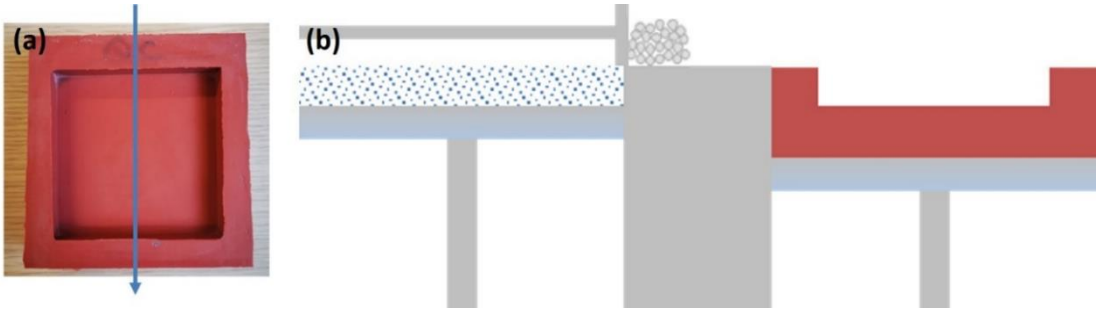


Figure 40. Scheme to measure packing density. (a): Rubber Mold; (b): Method to have simple powder bed with packing density measurement

The commercial water-based binder used in this work is Tethonite (Tethon3D, USA). To assess the compatibility of this binder with the printhead, it was further characterized in terms of viscosity (Thermo Fisher, Rheometer, USA), surface tension (KRÜSS, Tensiometer, Germany) and density. Classically, printability of a binder is determined by two parameters, e.g. the Ohnesorge number (Oh) and Reynolds number (Re) [129] which were introduced in Chapter 1 already. The printhead mounted on the machine is a Xaar 128 model whose main relevant characteristics are given by the supplier: the typical jetting speed is 5 m/s and the characteristic length is evaluated to 5 μm.

Binder saturation (BS) is the parameter which defines the fraction of binder filling in the void volume of the powder bed [22]. Layer thickness is set before printing. Binder saturation and layer thickness are graphically illustrated in Figure 41. $V_{Binder}$ is the amount of binder deposited on the powder bed and $V_{Selected}$ is the volume of the selected area where binder deposits in powder bed of each layer. The binder goes into the voids of powder bed which is quantified as $V_{Selected}$ multiplies porosity of powder bed. BS calculation was done according to Eq. (11), in which $V_{Binder}$ and $V_{Pores}$ are the volume of deposited binder on printed area and volume of pores (voids) inside the bed respectively. $V_{Origin}$ is the original volume of binder jetted out from printhead while dilation is just a multiple number of $V_{Origin}$ which is manually controlled by the machine (e.g., dilation 20 means that 20 times $V_{Origin}$ is jetted out from the printhead). The p is the porosity of the powder bed. The value of binder saturation could exceed 1, since the final amounts of deposited binder can be more than the void space of powder bed (as a consequence of drying) [72].

$$BS = V_{Binder}/V_{pores} = \frac{Dilation * V_{origin}}{p * (Surface\ area * Layer\ Thickness)} \quad (11)$$

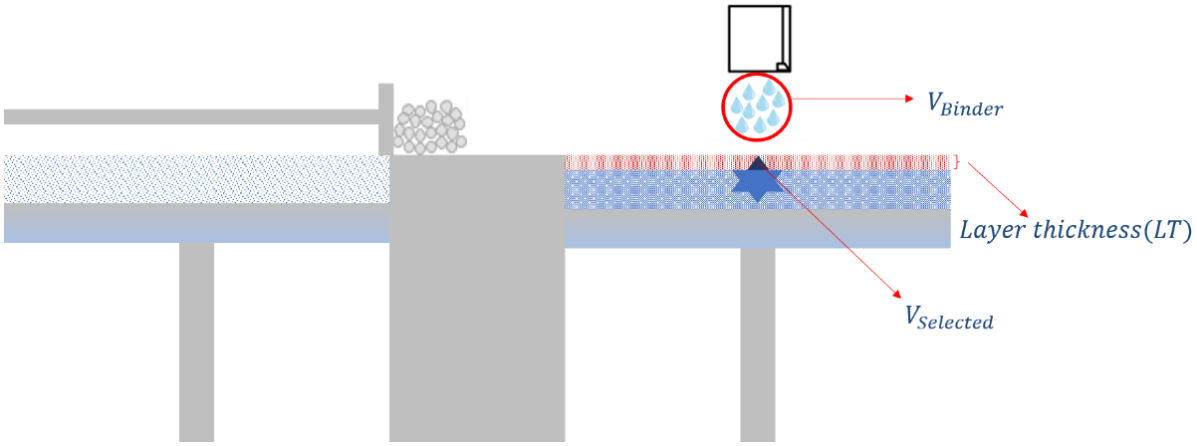


Figure 41. Schematic to illustrate the binder saturation and layer thickness

Before printing large objects, the influence of spreading speed was investigated as it is one of the key points to successfully obtain powder beds without cracks or defects. Two different speeds for the wiper (50 mm/s and 10 mm/s) were selected and assessed. The tests were carried out on three different spray dried powders (Al-SP, Al-SP1, Al-SP2). Layer thickness and binder saturation were kept constant during tests with varied spreading speed, i.e., 250 μm and 43% respectively.

Effects raised from binder saturation were investigated together with layer thickness and packing density. If packing density is mostly related to the powder properties and powder feeding method, layer thickness is a free setting of the machine. As mentioned in Chapter 1, improper binder saturation may result in defected parts (even broken ones) and a poor resolution. Figure 42 explains different situations that may result from inappropriate amounts of deposited binder. Low binder saturation causes weak bonding between different layers after printing, while the binder could not penetrate the layer thickness to overlay with previous layer printed. The situation is similar to an excessive layer thickness. Furthermore, insufficient binder saturation could not supply enough bonding strength to printed green body. On the contrary, over binder saturation lowers the printing accuracy since the binder spread in powder bed out of the selected area. Furthermore, mechanical strength of green layer might decrease due to noneffective bonding and printed layer might be mud-like. Therefore, binder saturation level has to be fine-tuned to successfully print parts with high resolution and sufficient bonding strength.

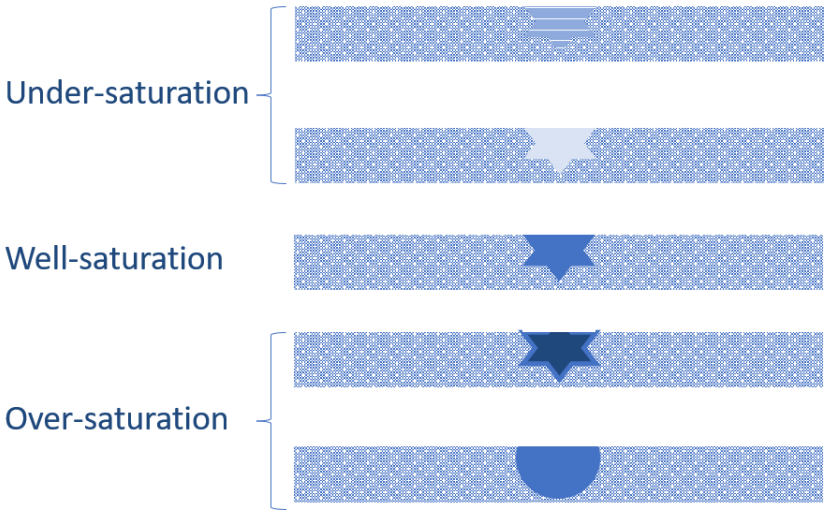


Figure 42. Schematic influences of binder saturation on printed parts

For testing, simple square shapes made by a stack of 10-layers were printed using a broad range of printing parameters to find out possible correlations between binder saturation and apparent printed part quality. Different LT and BS were applied during these preliminary tests in ranges that were empirically determined for each powder. Absence of macroscopic defects and apparent good bonding were selected as (crude) criteria to bound the ranges. The corresponding ranges were found to give acceptable results: Al-SP (LT: 50 µm - 250 µm with 50 µm increment; BS: 36 % - 286%); Al-SP1(LT: 50 µm – 250 µm with 50 µm increment; BS: 35 % - 278 %); Al-SP2(LT: 100 µm – 300 µm with 50 µm increment; BS: 43 % - 286 %). For these tests, the size of each printed area was 4 cm * 4 cm and the volume of deposited binder was recorded. Binder saturation was finally calculated according to Eq. 11.

Thermogravimetric analysis -TGA (Linseis, Germany) was conducted on printed green bodies with heating rate of 3℃ until 1500℃, to define the thermal treatment profiles (Figure 43). Mass of measured sample did not change anymore over 500 ℃ which implied that binder in printed part was completely removed.

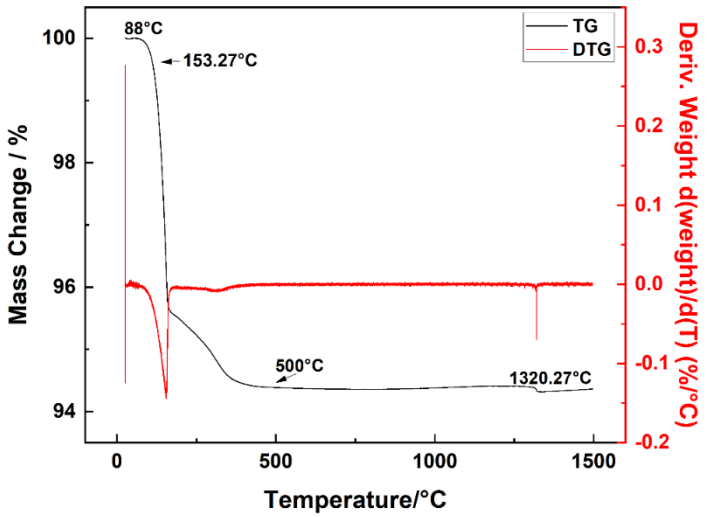


Figure 43. TG analysis of printed part

Accordingly, samples were debinded at 500 ℃, and heating rate and dwelling duration were set at 3℃/min and 4 hours respectively. The samples were then sintered at 1600 ℃ with a heating rate 5℃/min and a dwell time 6 hours in air which is the recommended temperature for the raw powder. After that, the furnace was naturally cooled down. The whole sintering cycle is illustrated in Figure 44.

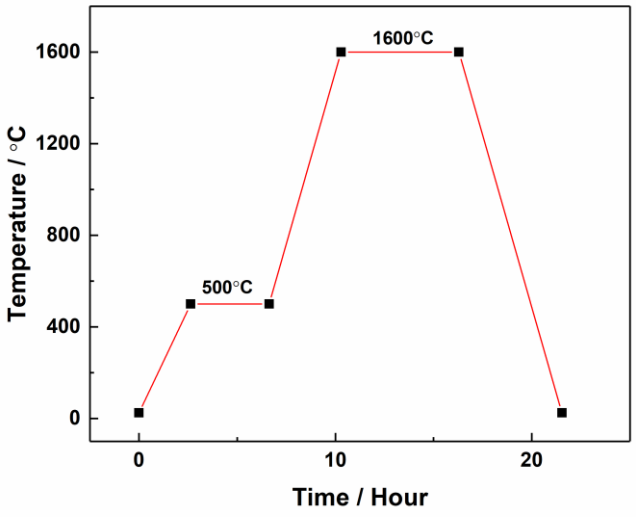


Figure 44. Designed sintering process of printed parts

Dimensions of green and sintered bodies were measured to calculate shrinkage. Densified samples were characterized in terms of density and porosity by the Archimedes method. Microstructures and inner structures of samples were observed by SEM. Finally, compressive

strength measurements of cuboids (1.0 cm × 1.0 cm × 1.5 cm) were carried out at room temperature using a universal testing machine (Zwick, Z100, Germany) with crosshead speed of 0.5 mm/min and expressed as the ratio between the load at rupture and the top surface of samples. Moreover, the roughness measurements of the printed-sintered parts were conducted with a 3D scanner (VR-3200, Keyence, Japan). The line roughness measurements were performed on 6 mm track length and analyzed with applying reference plane and no filter, and the surface roughness was assessed on areas with size 6 mm * 6 mm. A minimum of 3 samples was measured per powder and printing conditions. Micro-CT (Phoenix Nanotom, Baker Hughes, USA) measurements were conducted in Université de Toulouse (France). Other parts (such as benchmark items, filters and scaffolds) were also printed out after optimization of the printing parameters for illustrative purpose. The whole processing route is depicted in Figure 45.

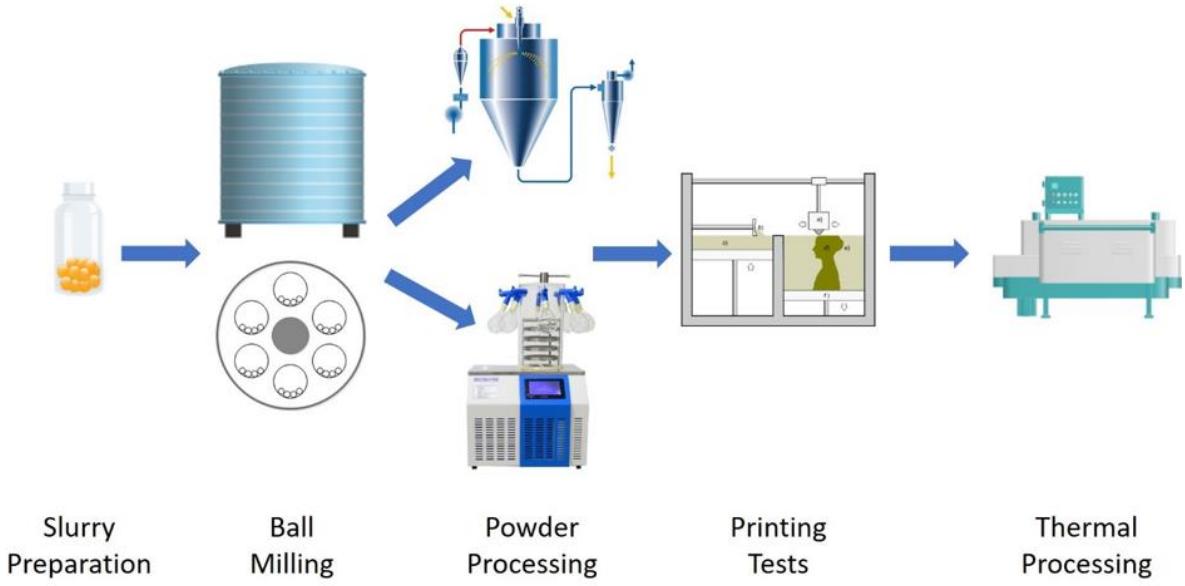


Figure 45. Synoptic of the experimental processing chain [236-238]

# 3. Results and discussion

## 3.1. Characterization of raw powders and binder

### 3.1.1. Particle size distribution and morphology

SSA and PSD of powders are summarized in Figure 46 and Table 6. As expected, SSA of the different powders are very similar and not affected by the drying process. In conventional BJ, the suitable range of granule size is between 0.1 to around 150 µm [30]. Particle size of the as-supplied Al-P powder is very fine and around 0.4 µm. However, it is strongly agglomerated and much coarser in the dry state. Comparing to other powders, Al-P has the broadest particle size distribution and shows irregularly shaped agglomerates which are clearly not suitable for

BJ. Particles with spherical shape are preferred in powder bed-based AM as they exhibit better flowability and lead to more homogeneous powder beds due to the low inter-particle friction [22]. Starting from a well dispersed slurry followed by freeze-drying broke most of the agglomerates but not completely (as shown on SEM figures of the powder): the PSD of the Al-FD powder is still broad, although a bit narrower than Al-P. Irregular shaped agglomerates as shown by the Al-FD may be suitable in BJ but only for a feeding system using reverse-rotating roller [74] or for a hopper depositing the powder by vibrating the reservoir above the manufacturing platform [75]. Nevertheless, packing density values of irregular particles are usually lower than values obtained with well-rounded shape grains. From that point of view, spray dried powders seem to be more suitable for BJ as they usually exhibit a nice spherical shape with a typical Gaussian PSD. As shown in Figure 47, spray drying indeed produced spherical particles, although some donut-shape granules can be noticed (Al-SP). The cyclone fraction Al-CSP appears spherical as well but with a smaller PSD. Coarse powders with large particle size exhibit better flowability but poorer sinterability compared to fine powders. Due to their high surface area therefore higher energy state, finer particle size (especially < 20 μm) lead to faster sintering process and higher densification. Unfortunately, it is always detrimental for flowability and packing density [30]. Therefore, a trade-off between flowability and sinterability is unavoidable in conventional BJ. The consequence of sieving the Al-SP powder into Al-SP1 and Al-SP2 is noticeable in Table 6. Particle size distribution and specific surface area of different powders as this creates significantly different PSD. Comparing the behavior of free-flowing powders with various PSD is also relevant as the corresponding powder beds will react differently to the binder penetration.

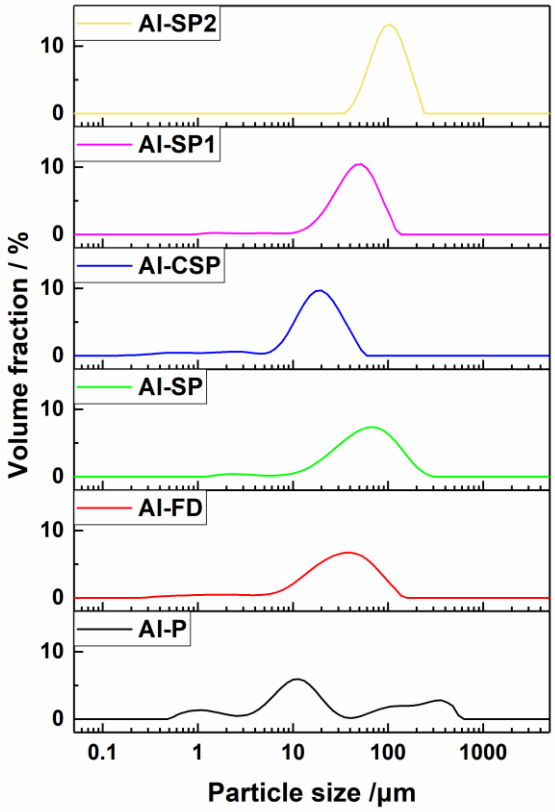


Figure 46. Particle size distribution of different tested powders

Table 6. Particle size distribution and specific surface area of different powders

| Powder | Description | SSA($m^2$/g) | d10(µm) | d50(µm) | d90(µm) |
|---|---|---|---|---|---|
| Al-P | Raw alumina | 7.6 | 2.3 | 14.9 | 323.3 |
| Al-FD | Freeze dried | 6.6 | 12.8 | 51.7 | 160.3 |
| Al-SP | Main fraction of spray dried | 7.3 | 20.7 | 61.8 | 143.5 |
| Al-CSP | Cyclone fraction of spraying dried | 6.8 | 7.0 | 18.2 | 35.5 |
| Al-SP1 | Sieved (<100 µm) from Al-SP | 7.0 | 18.9 | 44.2 | 83.3 |
| Al-SP2 | Sieved (>100 µm) from Al-SP | 6.9 | 70.9 | 106.7 | 161.2 |

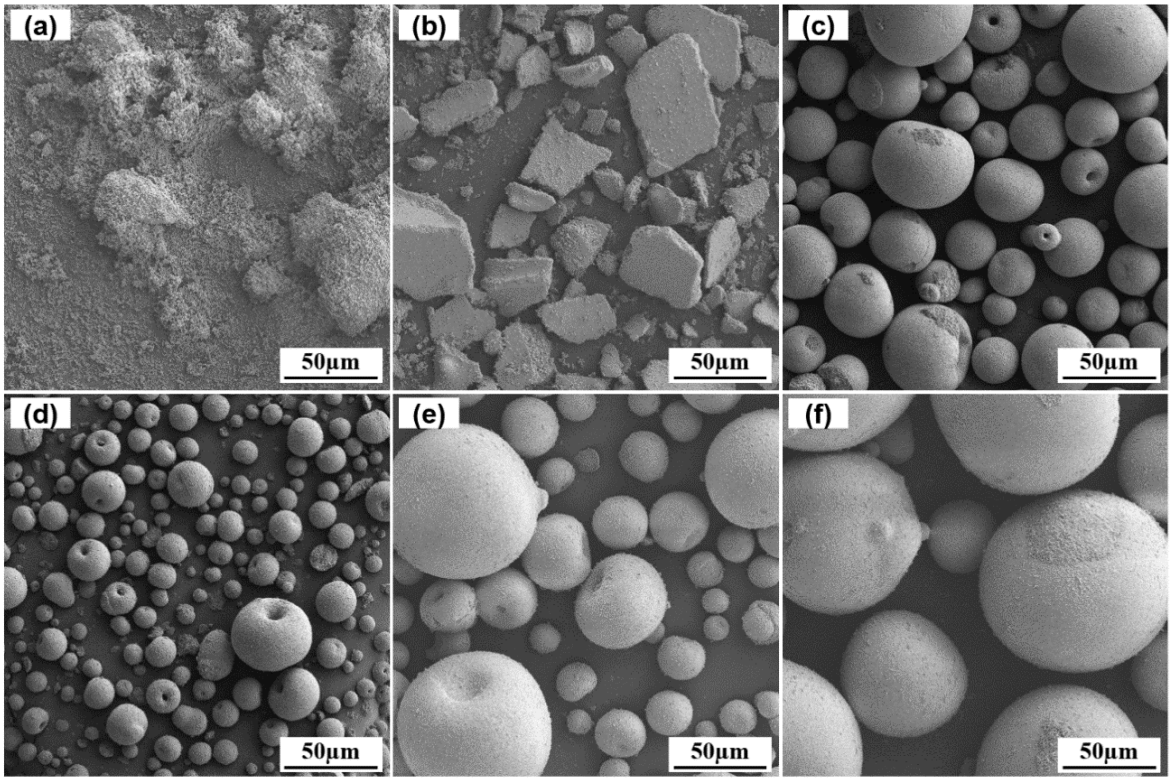


Figure 47. Morphology of different powders: (a): Al-P; (b): Al-FD; (c): Al-SP; (d): Al-CSP; (e): Al-SP1; (f): Al-SP2

### 3.1.2. Flowability

It has been reported in the literature that a good flowability can be obtained for Carr ratio < 16 and Hausner ratio < 1.19[48]. Flowability is also well assessed by the difference between tapped density and bulk density. All these values have been calculated for the different powders and reported in Figure 48. As shown, Carr ratio and Hausner ratios of all spray dried powders are better than the threshold values. The only exception is the cyclone fraction Al-CSP because of its finer size resulted larger inter-particle forces even though the particle morphology is spherical. These results are consistent with previous works showing that flowability will be improved for particle radius over approx. 20 µm. On the contrary, when the particle radius is smaller, the interparticle attraction force (Van der Waals) dominates and decreases the powder flowability. A direct consequence is a poorer powder bed layering and a degraded surface finish [27, 30, 60, 62-64].

Coarse fraction of the spray dried powder (Al-SP2) shows the best flowability because of low friction effect favored by the larger particle size and sphericity of particles. On the contrary, the fine fraction Al-SP1 exhibits poorer flowability, even lower that the un-sieved powders Al-SP. Additionally, differences between bulk density and tapped density of spray dried powders are also much smaller than for the “cohesive” powders as observed in Figure 48 (c), e.g., Al-P

and Al-FD. In general, flowability also depends on the environment as temperature and moisture are known to make some differences. Moisture absorption may create bridges between powder particles reducing flowability although sometimes it may act as a lubricant to reduce interparticle attraction forces [67, 68]. Hence, the powders were dried before printing to remove residual moisture[85, 86].

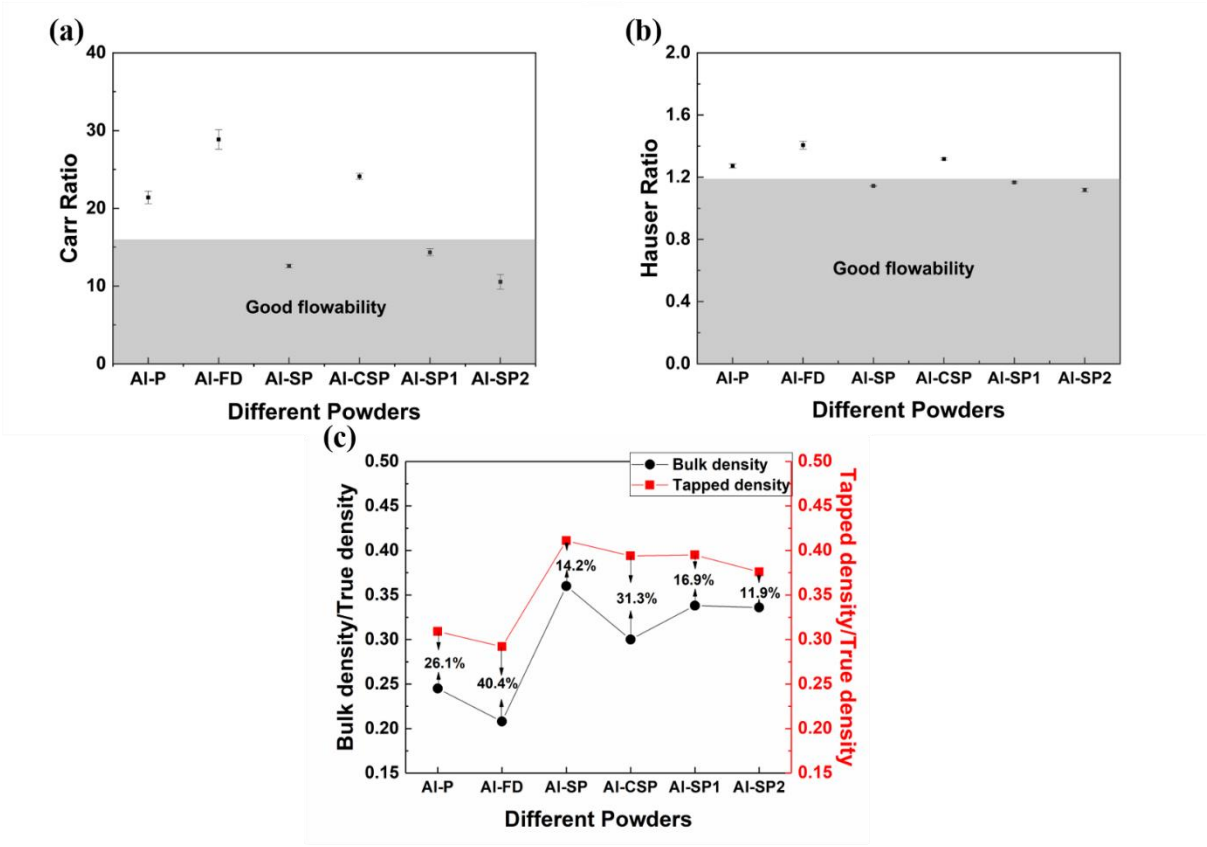


Figure 48. Flowability of different powders. (a): Carr ratio of different powders; (b): Hausner ratio of different powders; (c): Difference between bulk density and tapped density of different powders

### 3.1.3. Binder properties

More than 90 wt% of used binder is water. The viscosity of the binder is extremely low reaching 1.2 cP at shear rate 200 $s^{-1}$. Other added compositions aimed to modify the binding and wetting properties of the binder in terms of printability from nozzles and reaction with powders. Measured surface tension and density of this binder are 30.9 mN/m and 1.0 $g/cm^3$ respectively. By applying the characteristic length and jetting speed of printhead, Ohnesorge number and Reynolds number were calculated and reported in Figure 49. This figure also shows the usual printable region for inkjet printing. Though the calculated point locates in the satellite droplets region instead of the perfectly printable fluid region, it was nevertheless considered as suitable: after testing ejection was smooth, quite reliable and a good bonding between grains was noticed.

Comparatively, if the point had been located in the “high viscosity” region, there would have been some risks of nozzle clogging and printhead damaging.

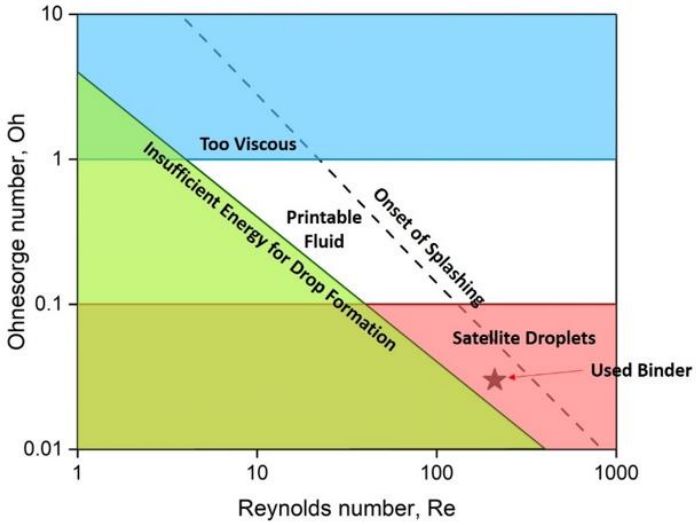


Figure 49. Printability region for inkjet, adapted form [129]

## 3.2. Characterization of powder beds

Properties of powder beds strongly and directly influence the quality of final printed parts in accordance with packing density and surface smoothness. Properties of powder beds are strongly related with the characters of powders. Figure 50 shows images of the top surfaces of different powder beds. Obvious defects or flaws were observed in powder beds made from cohesive powders (Al-P (Figure 50 (a)) and Al-FD (Figure 50 (b)) and cyclonic spray dried powder (Al-CSP (Figure 50 (d))). By contrast, the surfaces of powder beds formed by spray dried powders (and free-flowing) were smooth.

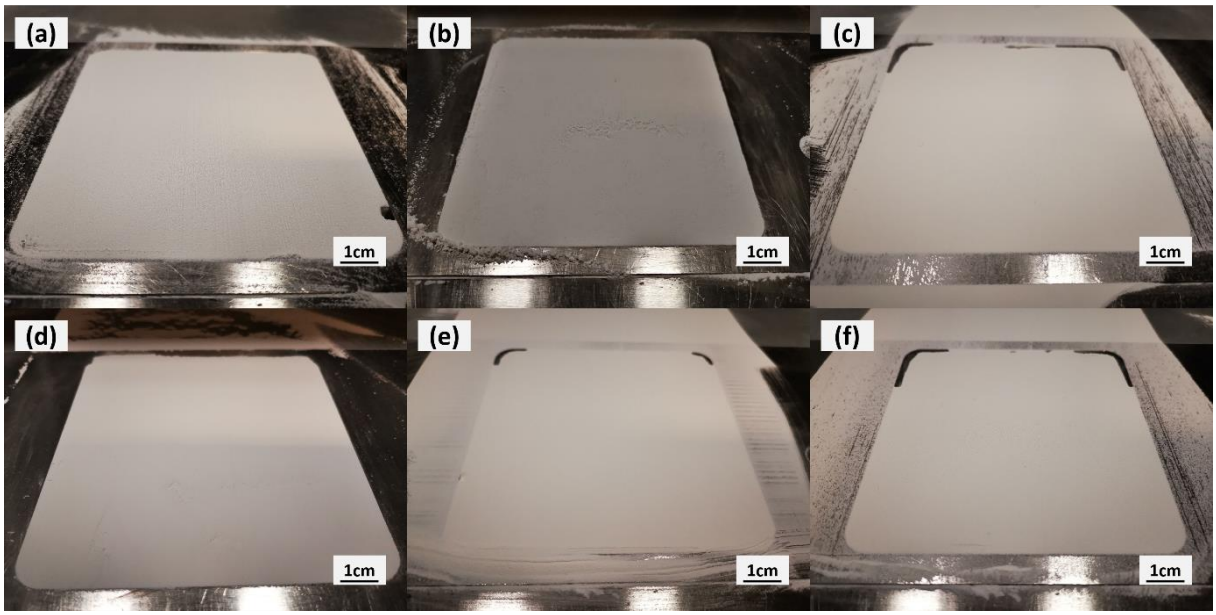


Figure 50. Images of different spread powder beds; a): Al-P powder bed; b): Al-FD powder bed; c): Al-SP powder bed; d): Al-CSP powder bed; e): Al-SP1 powder bed; f): Al-SP2 powder bed

### 3.2.1. Packing density

Packing density is not only dependent on the powder characteristic but is also related to the layering mechanism. For instance, it is well known that a counter rotative roller will give a better packing than a simple roller because of compaction effects from the roller[74]. Therefore, the free-flowing behaviour of the powder, although being critical is not the only parameter to be considered. The packing density of the whole powder bed is a non-linear cumulative summation of the packing of all individual layers: the final packing of a powder bed could be higher than the packing of each single layer because of cumulative effects of pressure applied during the whole process.

By using the rubber mould depicted in Figure 40 (a), it was possible to get an insight of the packing behaviour of each powder (Table 7). Laser optical images of the bed top surface were also taken giving some qualitative information about how well the powders spread (Figure 51). Agglomerates with irregular shape were noticed for powders Al-P, Al-FD from which the calculated packing density is much lower compared to free-flowing spherical powders. Powder beds formed with the spray dried powders present more homogeneous beds and higher packing densities compared to the previous powders. According to the literature [87, 88], a broad PSD results in a higher packing compared to a narrower PSD. Not surprisingly, among all spray dried powder beds, the highest packing density was obtained for Al-SP which also exhibited the broadest PSD among all tested powders. A positive influence of this broad PSD on the sintering behaviour is expected as well.

Table 7. Packing density of different powder beds

| Powder | Description | Packing density / True Density |
|---|---|---|
| Al-P | Raw alumina | 25.4% |
| Al-FD | Freeze dried | 22.3% |
| Al-SP | Main fraction of spray dried | 34.8% |
| Al-CSP | Cyclone fraction of spray dried | 27.2% |
| Al-SP1 | Sieved (<100µm) from Al-SP | 33.0% |
| Al-SP2 | Sieved (>100µm) from Al-SP | 34.7% |

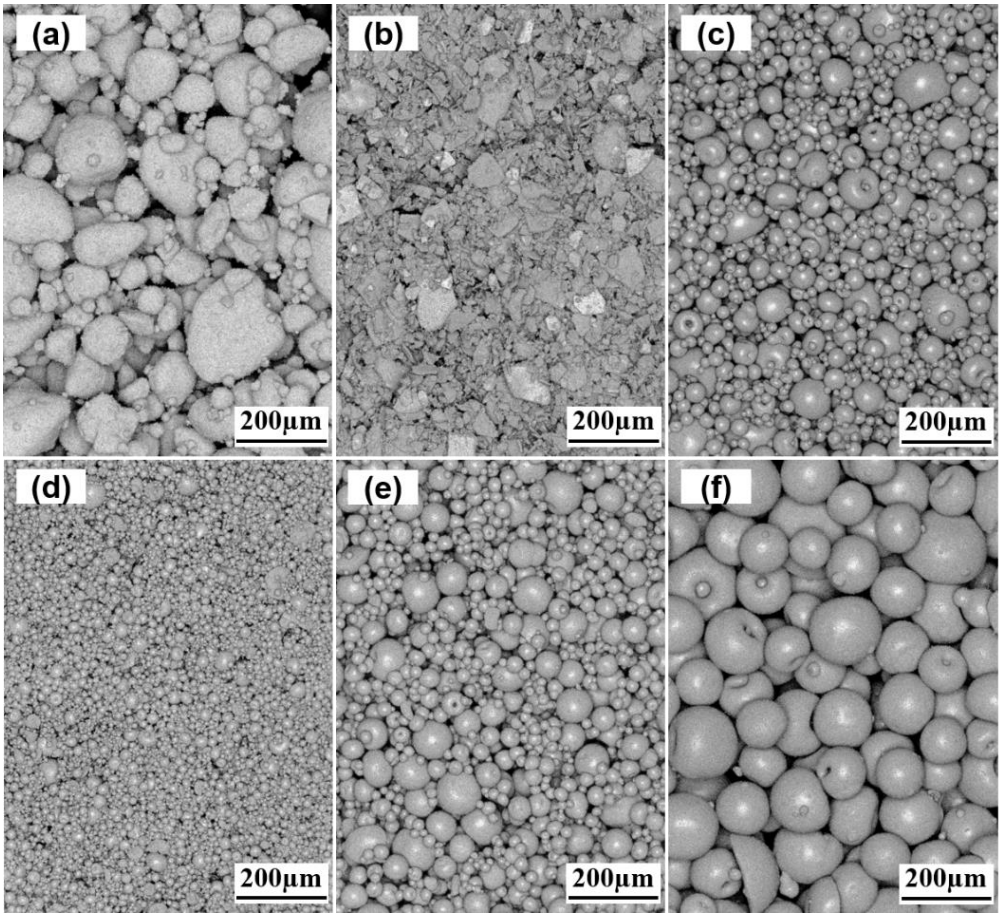


Figure 51. Optical laser images of different powder beds: a): Al-P; b): Al-FD; c): Al-SP; d): Al-CSP; e): Al-SP1; f): Al-SP2.

### 3.2.2. Roughness

Figure 51 shows the profiles of scanning line on different powder beds. Roughness analysis of powder beds was also carried out with results reported in Table 8 and Figure 52. The vertical axis is the profile of line scanning on different powder beds from the measurements of laser scanning. Scale of the vertical axis with each powder bed (-360 µm – 360 µm) is the same for all powders to ease reading the results. For non-spherical particles, the poor flowability due to higher interparticle adhesion or forces caused by mechanical interlocking is a reason for an

inefficient powder spreading [60, 64]. Usually, those powder beds exhibit defects and cracks as well as a very low packing density [30]. Consequently, it is expected that the powder bed roughness will be high for poorly flowable powders and angularly shaped grains/granules. This is exactly what was observed in the results.

For the Al-P, the powder bed is very rough and shows high local Z-value fluctuation which can be explained by the low aptitude of this powder for rearrangement. As a matter of fact, the powder is not suitable for the process (at least for a machine equipped with a blade recoater). Same result holds for the powder Al-FD for which surface analysis shows an unexpected high roughness and defects of significant size as well. Fine particles also exhibit poor flowability because of the strong attraction forces (Van der Waals) between particles which drastically reduce the powder flowability. Even if it was expected, only the powder beds formed by spray dried powders showed smooth top surface without any noticeable cracks or defects. For the Al-CSP powders, the roughness reached the lowest value. However, small defects were still noticed which may turn into large porosities on the sintered parts. No such things were observed for Al-SP and Al-SP1 powders. For Al-SP2, the roughness was higher probably because of the large granule size. It should be noticed that for Al-SP (e.g., the powder sieved at 100 µm), the bed looks more homogeneous than Al-SP1.

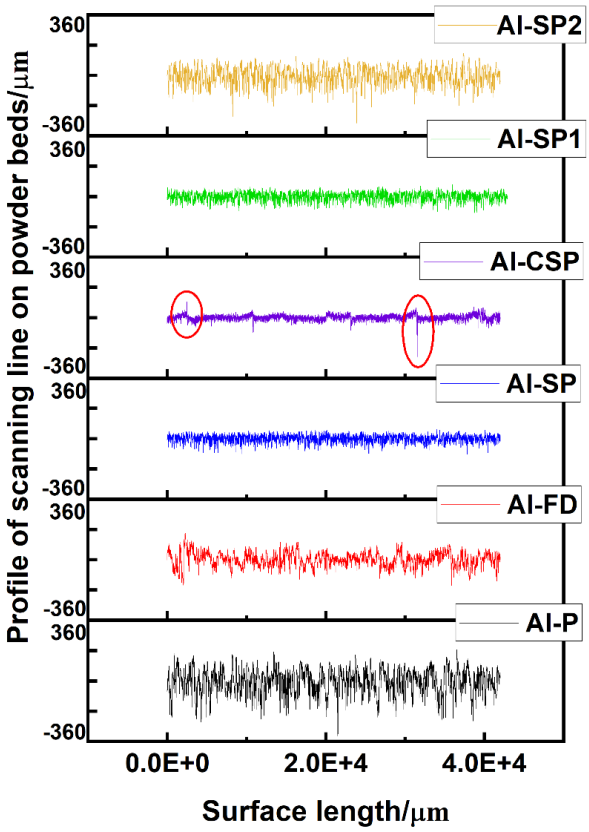


Figure 52. Profile of scanning line on different powder beds

Table 8. Roughness values of different powder beds with a cutoff of $\lambda_c$ = 8 and 4 cm track length

| Powder | Arithmetical mean deviation (Ra)/μm | Maximum height of profile (Rz) /μm |
|---|---|---|
| Al-P | 56.9 | 405.5 |
| Al-FD | 33.5 | 283.4 |
| Al-SP | 12.0 | 216.6 |
| Al-CSP | 17.0 | 147.2 |
| Al-SP1 | 20.0 | 154.8 |
| Al-SP2 | 43.0 | 315.3 |

## 3.3. Optimization parameters of printing

### 3.3.1. Interaction between powders and binder

As demonstrated in section 3.2 (Chapter 2), cohesive powders create defects on powder bed that results in a poor surface. These powders were obviously not suitable for our process. Packing densities were also too low with the obvious consequence of not providing enough strength for handling of the printed products. In addition, the packing defects may also act as a source of failure during the recoating process.

A simple "one-layer printing" test was conducted with the 6 powders to get some insights about the interactions between powders and binder. The results are illustrated in Figure 53. Figure 53 (c), (e) and (f) show perfectly printed squares and a quite good smoothness in all cases. Besides, circumstances like layer delamination, binder under-saturation or over saturation were never noticed with these powders. Low degree of shrinkage (resulting from drying) of printed layers with the surrounding powder was observed with Al-P powder bed (Figure 53 (a)). Nevertheless, delamination or damage of previously printed part could happen when the new layer spread. Mud-like printed result which could be explained as binder over-saturation was obtained from Al-FD powder (Figure 53 (b)). It may be assumed that lateral spreading of binder dominated instead of penetration due to the poor wettability with the powder bed and/or small channel size. Some warping also appeared after printing with Al-CSP. In this case, it could be assumed that particles were tightly bonded due to the finer and more reactive particles and the bonding stresses were not homogeneously distributed on printed area. Shrinkage of the printed part from surrounding appeared as well. Finally, only the three spray dried powders (Al-SP, Al-SP1, Al-SP2) were certified as appropriate for further testing as already suggested in section 3.2 (Chapter 2).

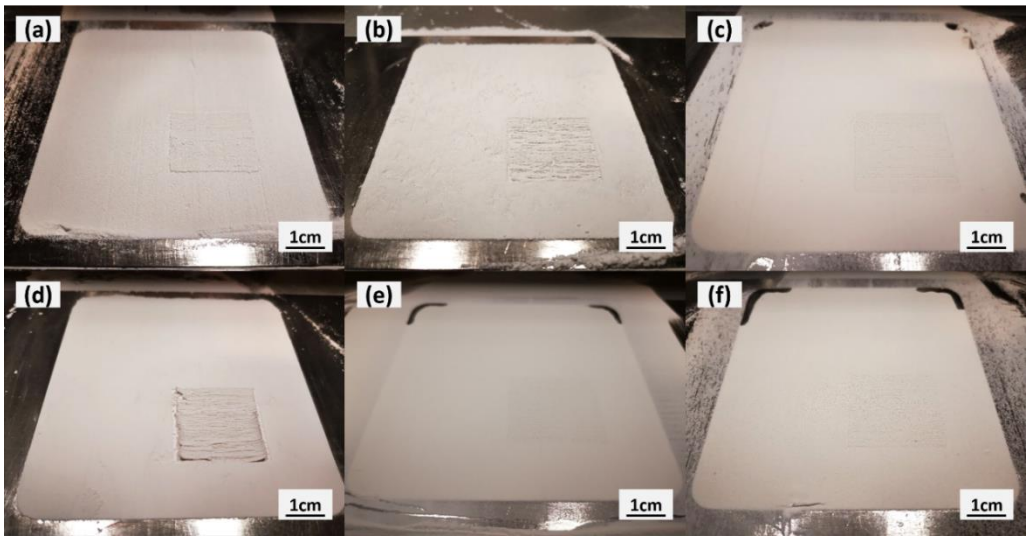


Figure 53. Simple test to verify the interaction between powders and binder with same binder amounts deposited. a): test on Al-P powder bed; b): test on Al-FD powder bed; c): test on Al-SP powder bed; d): test on Al-CSP powder bed; e): test on Al-SP1 powder bed; f): test on Al-SP2 powder bed

### 3.3.2. Spreading of speed of wiper

Results are graphically reported in Figure 54 in the specific but illustrative case of Al-SP2 powder bed. At lower speed (10 mm/s), large defects were noticed whose size may extend up to a few centimeters (in length). Printed parts did not usually survive during powder spreading. Those defects were aligned perpendicularly to the wiper displacements and created large gaps in the powder beds affecting several consecutive layers. They tended to appear suddenly after

a certain number of layers. On the contrary, for a spreading speed set at 50 mm/s, no such defects were noticed and the whole powder beds remained smooth without any crack or defect in the subsequent tests. As it is obvious that the spreading speed dramatically influences the powder bed quality. Then it was kept at 50 mm/s in all subsequent tests.

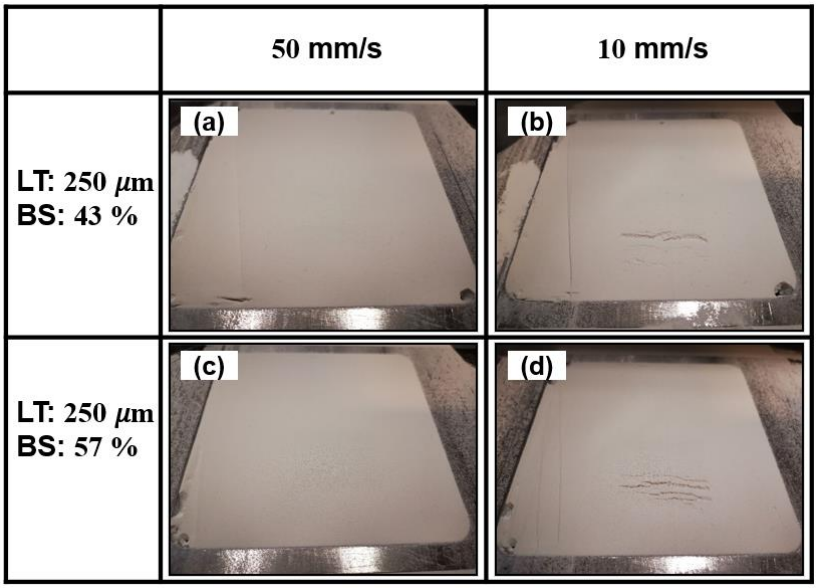


Figure 54. Effect of recoating speed on finished powder beds. a) – d): Results of spreading new powder on previous printed layer with different conditions (LT and BS, with different spreading speed at 10 mm/s and 50 mm/s)

### 3.3.3. Layer thickness and binder saturation

Layer thickness (LT) is simply the height of each powder layer. In general, this value ranges between 15 – 300 µm [30]. It cannot be considered as an arbitrary parameter as it should be related to the powder PSD. The typical value range of LT is between 2 to 3 times the mean particle size. Layer thickness also dictates the printing accuracy: decreasing and narrowing the particle size distribution permits thinner layers with the noticeable consequence to decrease staircase effect. Unfortunately, despite bringing numerous advantages, fine particles generally do not flow freely and tend to agglomerate much, which ultimately degrades the quality of the powder bed [159-161]. All in all, layer thickness is mostly a tradeoff between printability, resolution and sintering behaviour.

Binder saturation (BS) determines the amount of binder within the void volume of the powder bed [22]. It can be changed easily by modifying the amount of binder jetted out from the printhead or through droplet overlapping or any other overlaying mechanisms as described in [162]. BS firsthand affects how deep the binder will penetrate the powder bed and how it will spread laterally. Of course, not all BS can be realized in practice as it is related to the binder wetting behaviour and permeability of the powder bed. The shape of grains and the bed packing

density will therefore also contribute to the achievable values of BS. Large amounts of research have been undertaken to investigate the influence of BS on printed results [166-170].

For the present study, a first series of experiments were carried out in order to determine the range of compatible layer thickness and binder saturation for each powder. For these tests, 10-layers squares (4 cm * 4 cm) were printed with different conditions of LT and BS (Figure 55). Once the minimum layer thickness was defined for each powder, a parametric study was undertaken to assess the influence of the BS. Firstly, a 50 µm layer thickness was tested with Al-SP ($d_{50}$=61.8 µm) and Al-SP1 ($d_{50}$=44.2 µm), and the tests only succeeded randomly. In most cases, the printed parts broke during the stacking process because of the pressure exerted by the wiper during the powder recoating. By multiplying the tests, it turned out that the process became reliable and the results reproducible only when the layer thickness is larger than the d90 of the PSD. This result confirmed the previously reported conclusion from the literature. As discussed in [163, 165, 171], lower binder saturation or higher layer thickness would cause layer delamination and high grade of pores which might appear after thermal treatment. Taking examples, there were no well-bonding effects printing with Al-SP at BS < 36 %, Al-SP1 at BS < 35 %, and Al-SP2 at BS < 43 %, and the green body were fragile and easily broken during the de-powdering step. Figure 55 shows the successfully 10-layers printed squares that survived from the de-powdering step.

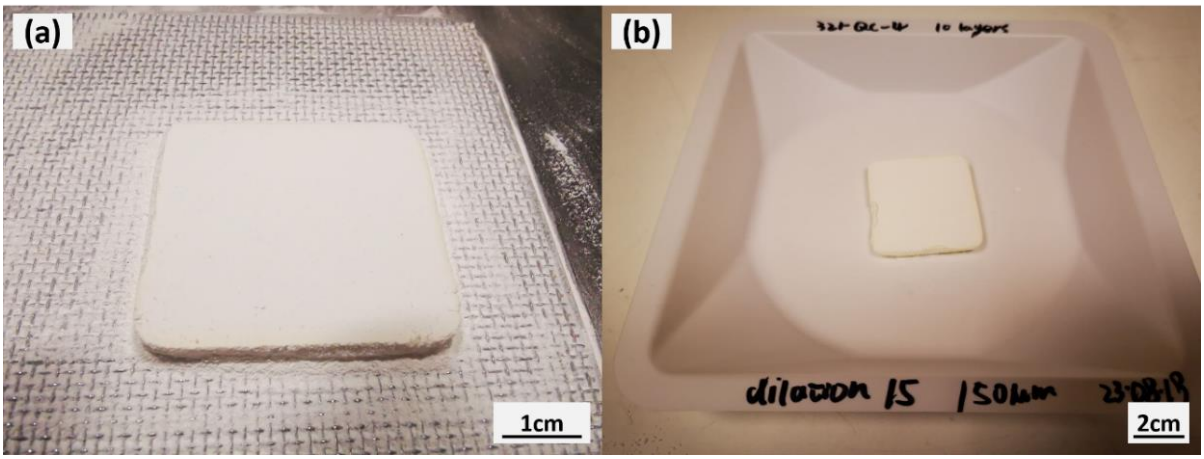


Figure 55. 10-layers square printing tests to find compatible LT (150µm) and BS (67.3%) ranges with powder Al-SP1. a): successfully printed with well-bonding and no defects; b): survived removing step from manufacturing stage

The ability of binder to penetrate the whole thickness of thick layers is not guaranteed so that particles located in the lower part may not well bonded. Interfacial bonding between layers is also reduced. From that point of view, increasing LT produces similar effects to a decrease of BS (see also [30] ). For instance, printing condition of powder Al-SP2 with BS range 57 % -

71 % at LT 250 µm gave parts with sufficient mechanical strength to be handled in green state. Contrarily, decreasing BS to less than 43 % always generated collapse of the part.

To compensate, it might be tempting to increase BS. However, a too large amount of BS is not satisfactory either. The tests showed that over-saturation leads to extra powder particles to stick or bond on the surface, resulting in parts exhibiting an obviously degraded surface roughness and a poor dimensional accuracy of printed parts. This observation was previously reported for other materials as well [30]. The case with BS = 139 % with powder Al-SP1 was particularly interesting as the printed bodies became “plastic” showing a typical paste-like behaviour after removal from the powder bed. Maybe this could be avoided by considering longer durations for binder drying in between each layer but this was not tested (currently it is estimated that the time between two consecutive layer printing is approximately 1 min at room temperature). Such a behaviour is clearly not suitable to ensure printing accuracy and part stability especially during the thermal post treatment. Figure 56 shows parts printed with different parameters. Binder spreading occurs in the lateral direction as illustrated in Figure 56 (a). In this case, the coarse granule size results in large channels in the powder bed that favors this migration. On the contrary for almost the same saturation level, the results in Figure 56 (b) do not exhibit any shape distortion.

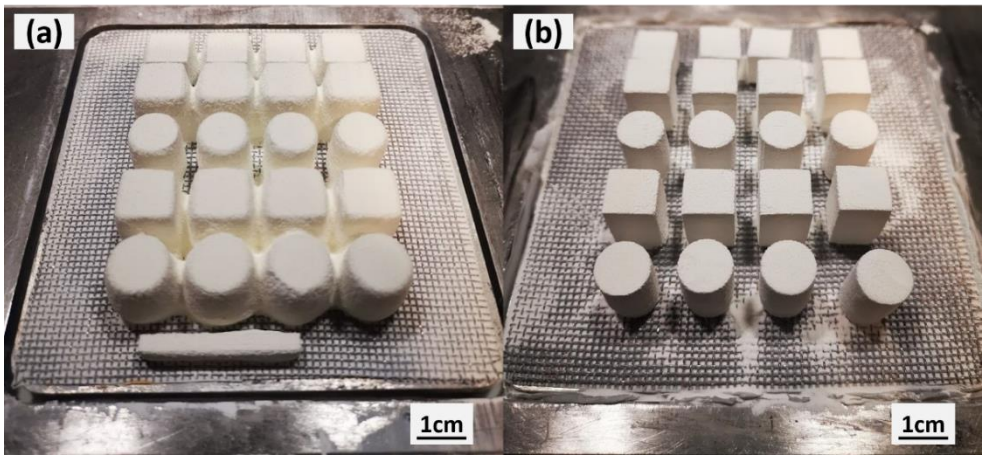


Figure 56. Printed green body of cuboids for mechanical tests. a): Powder Al-SP2, LT: 300µm, BS: 71%; b): Powder Al-SP1, LT: 150µm, BS: 70%

Literature also reports that improper binder saturation ultimately results in broken printed parts or printed parts without integrity and poor quality [163, 164]. Additionally, roughness of the final part is strongly related to the binder saturation level and shows dramatic increase for increasing value of BS. Optimizing the binder saturation is therefore essential to ensure obtaining the best printed and sintered quality. From an industrial perspective, it is also relevant as it may impart a non-negligible part of the printing costs [30]. Table 9 gathers the different sets of binder saturation / layer thickness for which printing parts was successful. It will be

shown later that although the range of suitable conditions is quite broad, significant differences have been noticed when it comes to sintered density and strength (section 3.4, Chapter 2).

Table 9: Suitable printing parameters for different powders in printing process

| | Layer Thickness/μm | Dilation | Porosity of powder bed/% | Binder Saturation/% |
|---|---|---|---|---|
| Al-SP | 150 | 20 | 65.2 | 95 |
| | 150 | 25 | 65.2 | 119 |
| | 200 | 20 | 65.2 | 72 |
| | 200 | 25 | 65.2 | 89 |
| | 250 | 20 | 65.2 | 57 |
| | 250 | 25 | 65.2 | 72 |
| Al-SP1 | 150 | 15 | 67.0 | 70 |
| | 150 | 20 | 67.0 | 93 |
| | 200 | 15 | 67.0 | 52 |
| | 200 | 20 | 67.0 | 70 |
| | 250 | 15 | 67.0 | 42 |
| | 250 | 20 | 67.0 | 56 |
| Al-SP2 | 200 | 20 | 65.3 | 71 |
| | 200 | 25 | 65.3 | 89 |
| | 250 | 20 | 65.3 | 57 |
| | 250 | 25 | 65.3 | 71 |
| | 300 | 20 | 65.3 | 48 |
| | 300 | 25 | 65.3 | 60 |

After printing, the parts still needed to be cleaned, brushed and polished due to cumulative binder diffusion effect as shown in Figure 57. By applying the printing parameters as shown in Table 9 for all three granulated powders, cuboids have been printed out (Figure 56). These parts were used to conduct mechanical testing and observe the microstructure after thermal treatment.

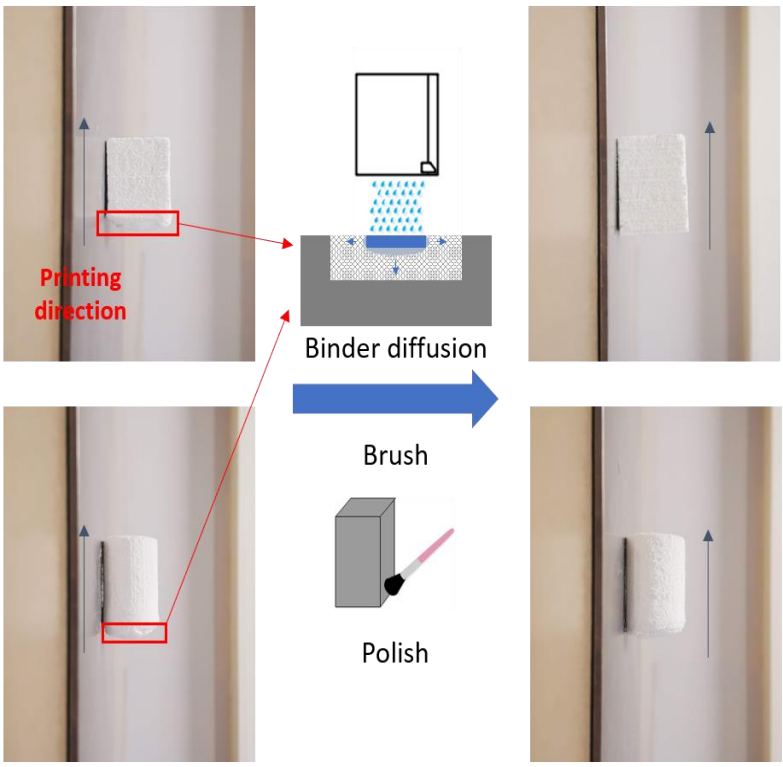


Figure 57. Brushing and polishing the inaccuracy part of samples caused by binder diffusion during printing

## 3.4. Characterization of sintered parts

### 3.4.1. Shrinkage, density and mechanical strength

All samples have been debinded and sintered using the same thermal cycle (section 2.2, Chapter 2). The measured density and shrinkage values are summarized in Table 10 – Table 12. Shrinkage values are quite similar whatever the powder and do not reveal any obvious trend or regularity. Linear shrinkage (height and width) and volume shrinkage in all samples keep steady at around 15 % and 40 % respectively.

Table 10. Density and shrinkage of printed-sintered samples from powder Al-SP

| | Volume Density/ T.D/% | Porosity/% | Closed Porosity/% | Height Linear Shrinkage/% | Width Linear Shrinkage/% |
|---|---|---|---|---|---|
| BS 95% LT 150µm | 62.8 | 37.2 | 1.0 | 15 | 15 |
| BS 119% LT 150µm | 64.2 | 35.8 | 0.9 | 16 | 15 |
| BS 72% LT 200µm | 62.0 | 38.0 | 1.1 | 16 | 15 |
| BS 89% LT 200µm | 64.0 | 36.0 | 1.1 | 16 | 15 |

| | | | | | |
|---|---|---|---|---|---|
| BS 57% LT 250µm | 59.0 | 41.0 | 0.7 | 16 | 15 |
| BS 72% LT 250µm | 60.7 | 39.3 | 0.5 | 16 | 16 |

Table 11. Density and shrinkage of printed-sintered samples from powder Al-SP1

| | Volume Density/ T.D/% | Porosity/% | Closed Porosity/% | Height Linear Shrinkage/% | Width Linear Shrinkage/% |
|---|---|---|---|---|---|
| BS 70% LT 150µm | 58.5 | 41.5 | 0.4 | 17 | 15 |
| BS 93% LT 150µm | 63.7 | 36.3 | 1.3 | 16 | 16 |
| BS 52% LT 200µm | 58.3 | 41.7 | 1.0 | 16 | 15 |
| BS 70% LT 200µm | 62.7 | 37.3 | 1.2 | 16 | 15 |
| BS 42% LT 250µm | 57.2 | 42.8 | 1.1 | 16 | 15 |
| BS 56% LT 250µm | 61.3 | 38.7 | 1.3 | 16 | 16 |

Table 12. Density and shrinkage of printed-sintered samples from powder Al-SP2

| | Volume Density/ T.D/% | Porosity/% | Closed Porosity/% | Height Linear Shrinkage/% | Width Linear Shrinkage/% |
|---|---|---|---|---|---|
| BS 71% LT 200µm | 56.1 | 43.9 | 1.2 | 16 | 14 |
| BS 89% LT 200µm | 56.4 | 43.6 | 1.4 | 15 | 15 |
| BS 57% LT 250µm | 53.8 | 46.1 | 1.3 | 16 | 16 |
| BS 71% LT 250µm | 56.2 | 43.8 | 1.3 | 16 | 16 |
| BS 48% LT 300µm | 53.3 | 46.7 | 1.7 | 16 | 15 |
| BS 60% LT 300µm | 55.4 | 44.6 | 1.6 | 15 | 16 |

Figure 58 highlights the compressive strength of sintered samples for the different powders under various printing conditions (both in terms of LT and BS). All three plots suggest a strength decrease with the increase of layer thickness. As the increase of layer thickness reduces the powder bed density, this result was expected and in fact was previously reported by other researchers [152]. The highest compressive strength among all groups reached 102.2 ± 11.1MPa (Al-SP), 79.4 ± 10.1MPa (Al-SP1) and 27.1± 6.0MPa (Al-SP2) respectively. The highest compressive strength of single part achieved 113.2MPa (Al-SP), 89.5 MPa (Al-SP1) and 31.5 MPa (Al-SP2). The largest values reported are likely related to the broad particle distribution especially Al-SP which favors the higher packing density as shown in Table 6 and Table 10. For Al-SP2, the coarse particles reduce the number of contact points per surface unit hence may degrade the sample strength. Also, it may be argued that the bonding between layers is most likely reduced because of the higher layer thickness. A similar explanation was advocated by Lu et al [73]. A very noticeable point is that compressive strength enhances with the increase of binder saturation at constant layer thickness. As an example, the average compressive strength of samples drastically increases from 22.8 MPa to 71.7 MPa with only 18 % addition of binder saturation printed under 200 μm layer thickness in the group of powder Al-SP1. It may be motivated to further increase the BS to enhance strength but as discussed previously, BS should be kept in suitable range to prevent over-saturation. There is therefore an optimum BS value for strength maximization. Similar conclusion holds for other powders as well.

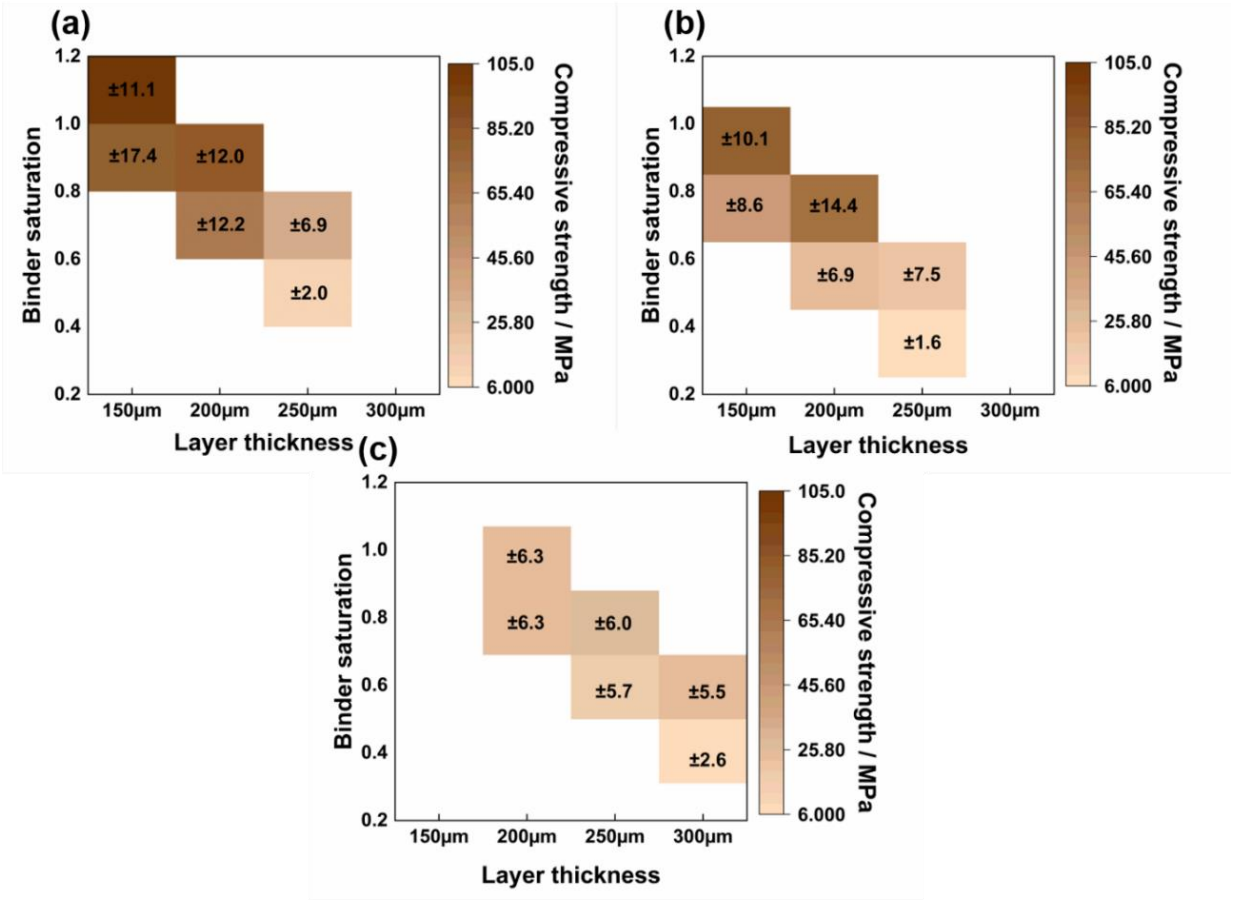


Figure 58. Compressive strength tests of printed-sintered samples (a): from powder Al-SP; (b): from powder Al-SP1; (c): from powder Al-SP2

In terms of layer thickness, it is observed that the mechanical strength decreases for larger values in the group of powder Al-SP (broader particle size distribution) when the binder saturation is close to its optimum, e.g., 72 %. The trend is the opposite in the group of powder Al-SP1 for a similar BS value, e.g., 70 %.

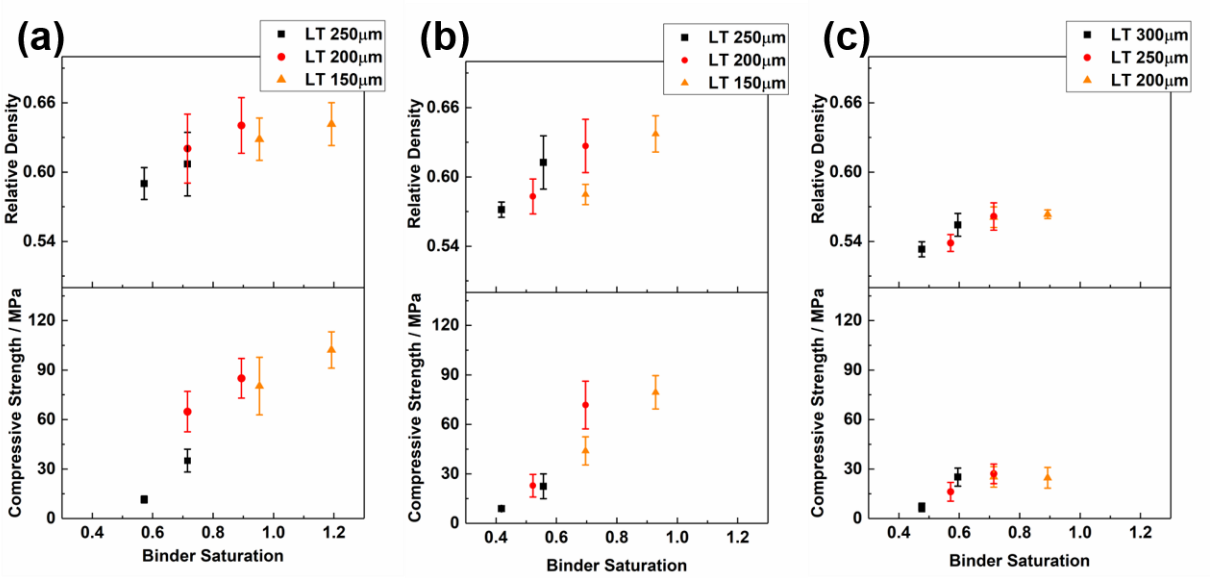


Figure 59. Relation between binder saturation, compressive strength and volume density of printed-sintered samples (a): from powder Al-SP; (b): from powder Al-SP1; (c): from powder Al-SP2

Figure 59 also depicts the evolution of density and compressive strength as a function of binder saturation. Different symbols with correlated color represent the various layer thicknesses for the different powders. As expected, relative density of samples apparently decides the compressive strength. The relative volume density of sample groups from different powder groups reaches 64.2±1.9 % (Al-SP), 63.7±1.6 % (Al-SP1) and 56.4±0.4 % (Al-SP2) respectively. What is more interesting is the fact that for each tested powder there is an obvious correlation between density/mechanical strength and binder saturation. The trend is roughly linear with the exception of Al-SP2 at the highest BS value. This trend is interesting as it suggests that BS is not only a relevant parameter to improve the green body strength, but also governs the final properties of the parts. It should have been expected from the very beginning as the green body strength was noticed to be highly dependent on BS (at least from a qualitative point of view). Of course, the green body strength also reflects the internal structure of defects: large defects in the green body will remain large after sintering. The main question is therefore: when all these defects appear? During the optimization of printing, it has been said that in the most extreme cases, the green body strength is so low that the parts do not survive the de-powdering step. The green body lacks cohesion and cannot withstand the mechanical stresses exerted by the brush. Something similarly probably happens during the powder recoating. If BS is too low, the green strength is low and the part being built cannot withstand the efforts exerted by the blade. Some defects are created (but not catastrophic ones) that will decrease sintered density and strength. Increasing further the BS probably reduce the size and number of those defects to a certain extent.

Indeed, even if the mechanical strength increases gradually, it seems to reach a plateau for large BS values. In fact, the existence of such a plateau was already anticipated during printing as very high values of BS make the parts very soft and plastic, something which was considered as detrimental to guarantee printing accuracy and structure integrity of parts.

Finally, it should be noticed that strengths for Al-SP and Al-SP1 are in the same range. On the contrary, strengths with Al-SP2 are much lower. This is most likely related to the coarser grains in the latter powder which reduce the number of contact points per surface area and / or large internal defects. What is interesting here is that despite the powder Al-SP also contains the coarse fraction, the strength does not seem to be affected much.

All in all, it appears that conventional spray dried powders are highly suitable for binder jetting, both in terms of shape and PSD. Layer thickness should always be considered over the d90 of the powder. Therefore, optimization of the process mostly relies in the determination of a suitable value for BS. According to our results, it appears that BS is probably one, if not the most critical parameter to ensure successful printing and optimization of sintered parts. Unfortunately, it seems that BS needs to be fine-tuned for each powder and each binder separately which might be time consuming. Nevertheless, the acceptable range of BS is already suggested by the results and previously reported ones in the literature. In the present work, the optimum seems to be 72 %. It is very close to values reported by other researchers. For instance, according to Shrestha et al. [147], 70% binder saturation is optimal with certain layer thickness, roller rotational speed and feed/powder ration values maintained at 100 μm, 6mm/s and 3:1 respectively. Patirupanusara et al. [176] demonstrated that more than 10 % of binder content is needed in order to print parts with PMMA powders. Density was enhanced from 600 to 750 $kg/m^3$ when the binder content was increased from 20 % to 60 %, and the porosity was reduced obviously from 57 % to 42 %. Therefore, a BS value close to 70 % seems optimal. Combined effects of layer thickness (0.1 mm and 0.087 mm) and binder saturation (90 % and 125 %) was also evaluated with different methods (geometry, surface roughness and mechanical strength) by Vaezi M et al. [169]. As expected, increasing BS in a suitable range resulted in an enhancement of both tensile and flexural strength as well as the surface finish of parts.

It should be noticed that the optimized conditions reported in this paper are not just satisfactory to print cuboids but are also valuable to print more complex shapes. Some examples of sintered parts are pictured in Figure 60 and Figure 61 illustrating the possibility to also print scaffold-like structure with complex inner design.

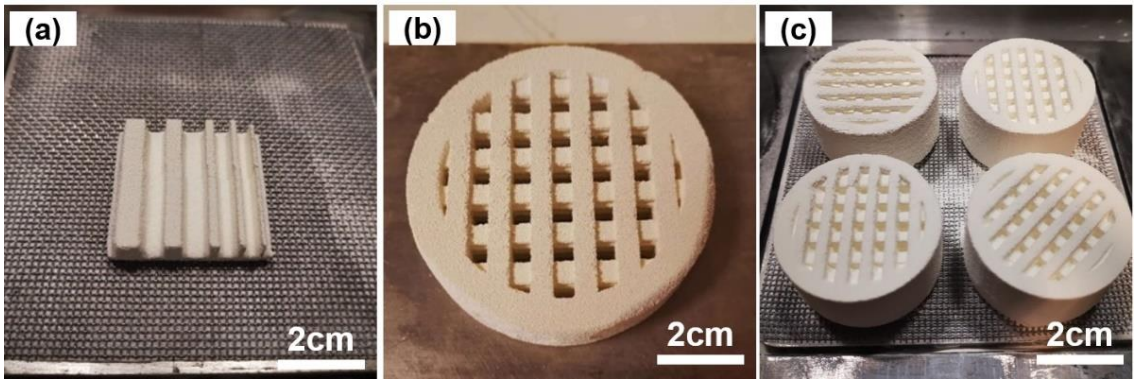


Figure 60. Printed green body of different complex shape parts: (a): Benchmark (Al-SP, LT: 200 µm, BS: 72 %); (b): Large size scaffold (powder: Al-SP2, LT: 300 µm, BS: 48 %); (c): Small size scaffolds (powder: Al-SP1, LT:150 µm, BS: 70 %)

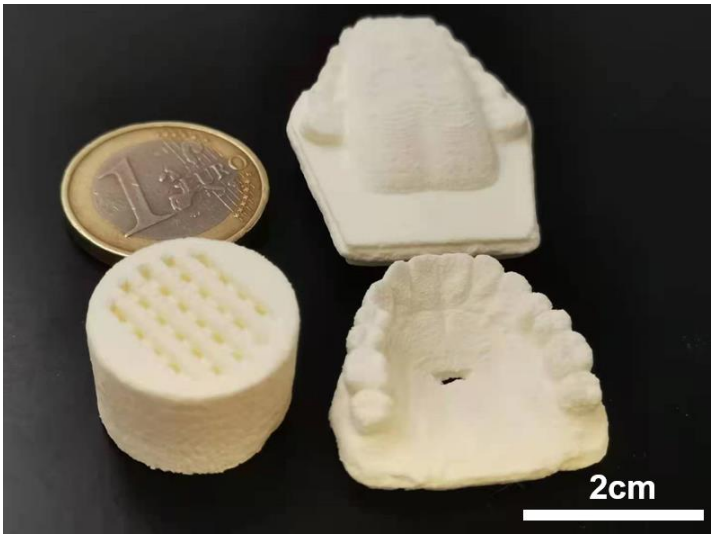


Figure 61. Printed-sintered teeth models (powder: Al-SP2, LT:200 µm, BS: 71 %) and scaffolds (powder: Al-SP1, LT:150 µm, BS: 70 %)

### 3.4.2. Morphology

Figure 62 shows the morphology of top surface of printed-sintered parts (under same conditions) from the three granulated powders. Necks between granules are easily noticed as a consequence of sintering. The surface of granules looks perfectly dense. As expected, large void remains in the parts that cannot be resorbed by high temperature diffusion. Most likely, granules sinter on themselves to almost full density and most of the residual porosity of parts remains located in between granules. Necking could be regarded also as a side proof to explain the mechanical strength of samples. All parts made from well-packed homogeneous powder beds show tight bonds between granules (Al-SP and Al-SP1) and relatively small vacancies. Smaller granules fill in the voids between large granules owing to broad particle size distribution. Some granules even start to lost their original “spherical shape” as a consequence of sintering (Figure 62). On

the contrary, SEM images of Al-SP2 samples (which exhibit the lowest density and strength) show much bigger voids after printing.

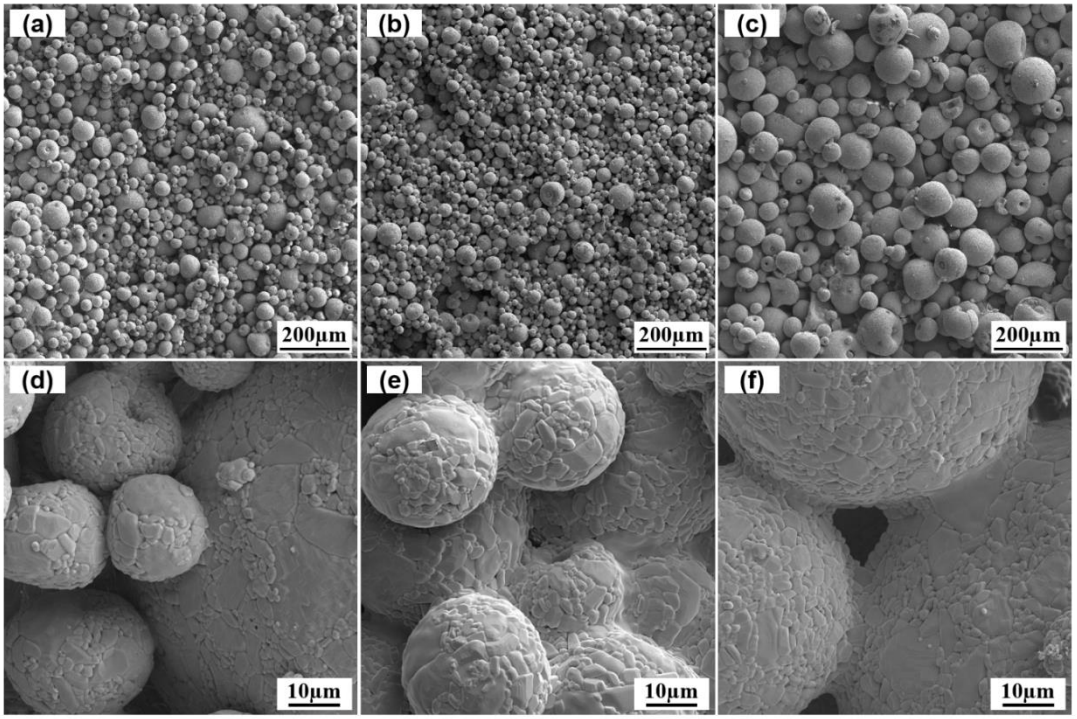


Figure 62. Morphology of top surface of printed-sintered (1600°C) cuboids from different powders; (a), (d): from Al-SP (Printed with BS: 72%; LT: 200 µm); (b), (e): from Al-SP1 (Printed with BS: 70%; LT: 200 µm); (c), (f): from Al-SP2 (Printed with BS: 71%; LT: 200 µm)

Additionally, roughness values (arithmetical mean deviation) of printed-sintered samples have been determined for the different tested powder. On the plot Figure 63, perpendicular lines and parallel lines refer to measurements done normal to the inkjet printing direction. For the top and horizontal surfaces, this corresponds to the direction along which the nozzles are moving during printing. For the side surface the perpendicular direction is that of layer stacking (Figure 63 (a)). Compared with top surface whose properties only depend on powder spreading and PSD, side surface is more influenced by the staircase effect, binder spreading/penetration inside of powder bed and bonding strength.

Top surface roughness of parts printed with Al-SP1 was the best due to the small particle size distribution. On the contrary, the values measured for Al-SP2 parts were the poorest. In general, roughness measured along both directions follow the same trend for the side and top surfaces as shown in Figure 63 (b). However, perpendicular roughness is different on the side surface with best values obtained for parts printed with Al-SP. This may be attributed to the broad particle size distribution and higher packing density for this powder, so that the influence of layering is reduced. It should be noticeable that perpendicular roughness on side surface of Al-

SP1 parts varied significantly in accordance with other measured data on these samples. Firstly, layering effect should dominate the variation because the parallel values on same surface was lower and less scattered. Besides, since the particle size distribution of Al-SP1 was the smallest ($d_{90}$ = 83.3 µm was smaller than half of layer thickness) with comparable low packing density, binder may not spread easily and penetrate into whole layer thickness thus creating a limited bonding at the interfaces. Particles might be brushed away during the de-powdering step and defects are likely created. A closer examination of the plots also shows that the side surface roughness is always higher than that on the top surface due to the imperfect connection between layers.

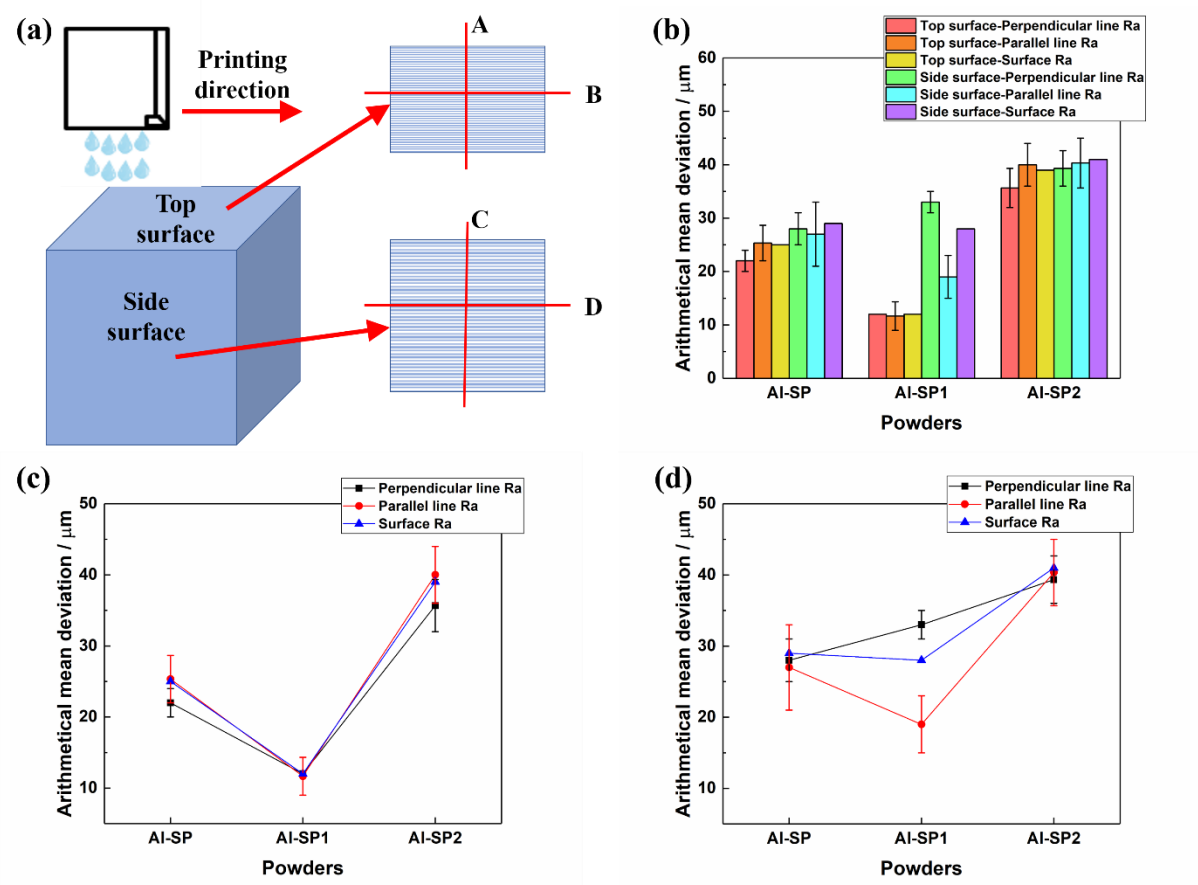


Figure 63. Roughness measurements on top surface and side surface of samples with perpendicular line roughness, parallel line roughness and surface roughness; a): Scheme of scanning perpendicular and parallel lines on top and side surface, A: perpendicular line on top surface, B: parallel line on top surface, C: perpendicular line on side surface, D: parallel line on side surface; b): Roughness comparison of top and side surface with different powders; c): Roughness measurements on top surface of samples; d): Roughness measurements on side surface of samples; all samples printed at LT: 200µm, BS:70%

### 3.4.3. Internal structure of printed and sintered bodies

The physical characterizations and SEM pictures shown previously confirm that a significant amount of porosity is still present inside the samples. It could be interesting to have a closer look on the inner structure of these objects and determine how the porosity is distributed.

Figure 64 shows the typical internal structure of printed-sintered samples. It is obvious that most granules survived sintering, showing limited necking in the cross-section surface. Substantial amounts of voids exist creating internal and fully connected channels throughout the samples.

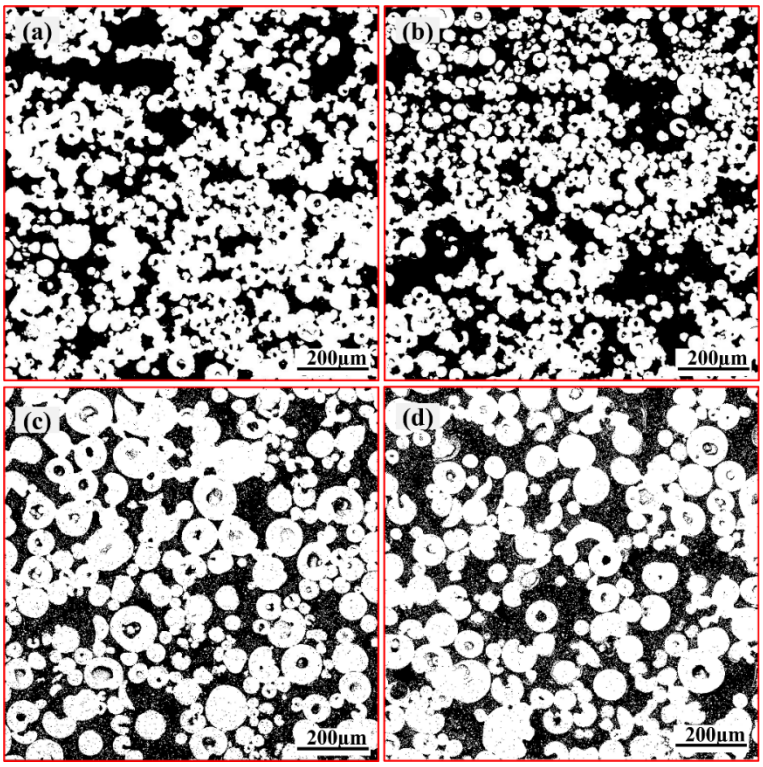


Figure 64.Cross-section BSE images of printed-sintered samples conducted with ImageJ; a), b): Samples with Al-SP1, LT: 200µm, BS: 70%; c), d): Samples with Al-SP2, LT: 250µm, BS: 71%

A complementary analysis of the internal structure was conducted through micro-CT to have a better view of the porosity distribution. Figure 65 (a) and (b) are cross section views of samples from the side view and top view obtained through micro-CT. No defect at the interface between layers can be noticed which suggests a rather good bonding (Figure 65 (a)). Along the printing direction (from the top-view), a texture can nevertheless be observed taking the form of linear tracks. This is an effect of the nozzle spacing and suggests that in some places not enough ink has been deposited.

Figure 65 (c) confirm in 3D what the cross sections showed: large pores are interconnected and form an open structure throughout the skeleton body. It will be shown later that these

internal channels can be exploited to increase the density of the sintered parts thanks to an infiltration process.

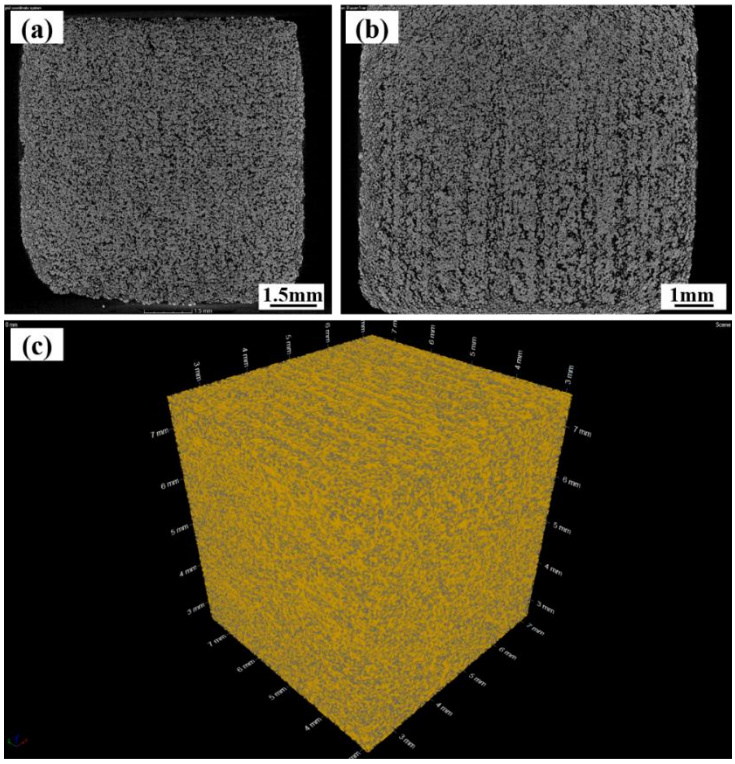


Figure 65. Micro-CT analysis on samples printed from powder Al-SP under LT (200µm) and BS (70%); a): Cross-section from side; b): Cross-section from top; c): Pores structure of the sample (Materials transparent, pores yellow color)

In addition, pore size distribution was also characterized using mercury porosimetry as shown in Figure 66. The cumulative intrusion amounts of samples printed with Al-SP (0.186 mL/g) was the lowest. This was expected as this sample exhibits the highest packing density. Comparatively, the pore size in samples printed with Al-SP2 is the highest which is an obvious consequence of the coarser granule size of Al-SP2.

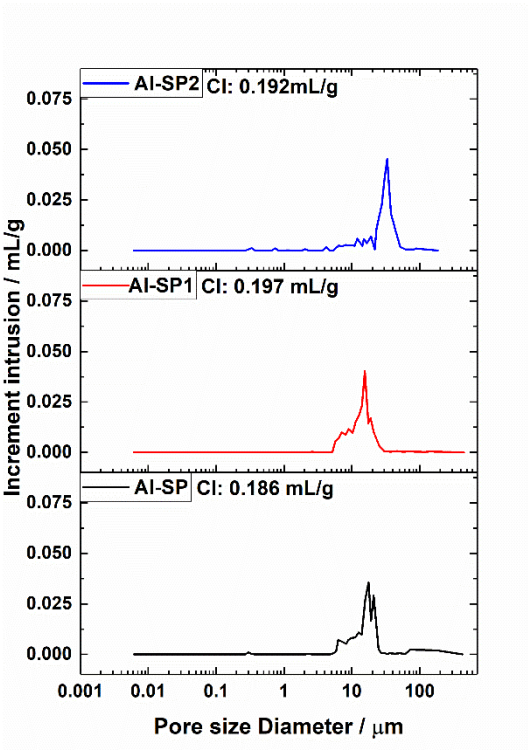


Figure 66. Pore size distribution of printed-sintered samples with cumulative

# 4. Conclusion

By optimizing shape and PSD of spray dried granules as well as printing conditions (layer thickness and binder saturation), well-shaped alumina parts were successfully printed with sintered density up to 64.2±1.9 % of theoretical density. The highest compressive strength achieved 113.2 MPa which is close to values reported in other works. For instance, the highest mechanical strength of alumina parts reached 131.9 MPa for 16 hours natural sintering (77.9 MPa under 2 hours sintering) with a BJ machine equipped with an anti-clockwise rotating roller [74]. The free-flowing powders obtained using conventional spray drying have been found to be optimal for BJ process with regard to the higher packing density and powder bed homogeneity.

For granule size below 100 µm, the PSD does not show any real influence on the final properties of parts. On the contrary, coarser granules with a narrower PSD, even if being suitable for layering, reveal very poor ability to ensure densification. Practically, the layer thickness should be slightly over the d90 of the used powder. Binder saturation was proven to be one of the most critical parameters. It governs the green body strength (and the possibility to improve the de-powdering process) and consequently the sintered properties (density and compressive strength). Based on the other published works in the field, the results suggest that a BS value close to 70 % is the optimum. It is expected that the whole optimization procedure described in the present work could be straightforwardly applied to other ceramic as well.

However, since the final obtained parts were still highly porous, modifications or enhancement of process have to be conducted to improve the quality of printed-sintered parts. According to literature, multi-modal particle systems could be used in order to increase the packing density of powder bed and consequently the sintered density of products[73, 97]. Another option is to consider post-treatments such as infiltration with molten melts, ceramic precursor or pure ceramic suspensions. In the subsequent part of this document, it will be demonstrated that post-infiltration with ceramic suspensions is a very effective way to reach higher densities [235, 239-241].

# Chapter 3. Post-infiltration to densify porous BJ ceramic parts

## 1. Introduction

As described in Chapter 1 & 2, ceramics parts obtained using conventional BJ exhibit a low sintered density and a rough finished surface, even though the powder properties and printing parameters are optimized. In an attempt to increase the density, different authors have reported a post-infiltration of the porous body with a material in different forms. This includes molten metals [175, 235], precursor solution [242-244], resin [245, 246] or ceramic suspension [239, 240]. The last approach can be considered as the most promising one as it allows to keep the chemistry of the original material. Despite a huge interest, few articles evoking this approach were found in the literature. In the following pages, the main results obtained in the literature as well as the challenges posed by this approach are reported. Finally, the approach followed in this work and the results that have been obtained will be presented.

### 1.1. Theoretical background

#### 1.1.1. Porosity in BJ parts and post-infiltration with a ceramic suspension

BJ printed parts are highly porous due to the low packing density of powder beds and the use of coarse ceramic particles, particularly when spray dried granules are considered. In this case, the pores in the sintered parts have two different origins:

- Pores may originate from the packing process. These “Inter-particle” pores become larger when the particle size of granules increases;
- Pores may result from the internal porosity of the granules that is not completely eliminated after binder burn-out and sintering [239]; This porosity will be called hereafter “Intra-particle”.

Both types of pores are pictured in the Figure 67. Obviously, Inter-particle porosity can-not be completely removed through sintering due to the morphology and size of granules. On the contrary, intra-pores can disappear completely during the thermal treatment because of their small size and the internal compacity of the granules which is undoubtedly higher than that of the powder bed. Infiltration addresses mostly the inter-particle porosity. The large pores located in between granules survive the sintering process and create large channels distributed

throughout the whole structure forming a network of open porosity. A ceramic suspension containing fine particles may diffuse through this porosity thanks to the gravity and capillary effects. After drying, the fine grains remain inside the porosity and accumulate locally thus reducing the channels openness and improving the density. This rough explanation of the mechanism of infiltration by a suspension should not hide the complexity of the process. In practice, its efficiency is governed by a number of parameters that we are now going to describe.

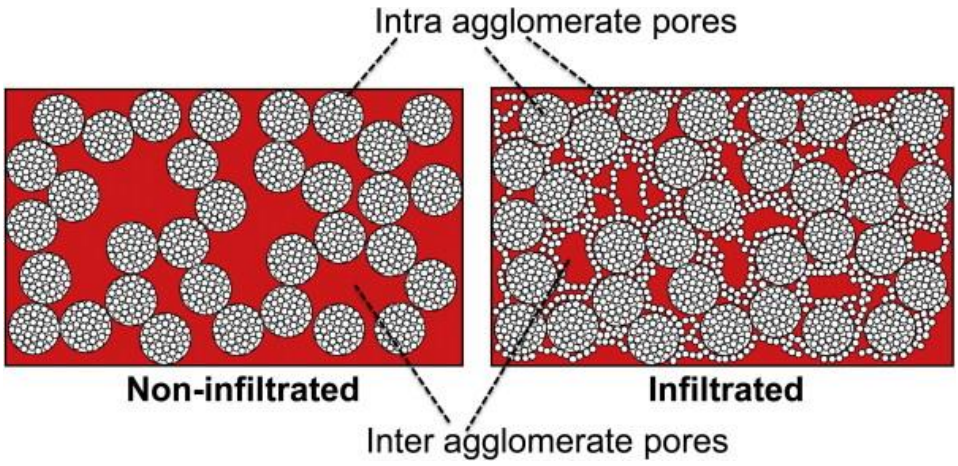


Figure 67. Inner view of non-infiltrated part and infiltrated part with different kinds of pores from [239]

### 1.1.2. Ceramic suspension infiltration

To successfully penetrates the porous body, any suspension has to fulfil some requirements. Among other parameters, it has to exhibit a good stability, a satisfactory wetting with the material of the body and a suitable infiltration kinetics [30]. The influence of each factor is briefly described hereafter.

*i. Wetting behaviour*

A proper wetting behaviour is an obvious prerequisite otherwise the suspension will not penetrate easily the skeleton body. The contact angle with the solid material should be less than 25° according to the literature [247]. Practically speaking, it can be measured with the usual sessile drop method and a high-speed camera. Contact angle (θ) of interface could be calculated with Young's equation:

$$\sigma_{sv} = \sigma_{sl} + \sigma_{lv} cos\theta \quad (12)$$

where $\sigma_{sl}$ is the solid-liquid interfacial tension of the liquid drop on solid substrate, $\sigma_{sv}$ is the solid-vapor surface tension and $\sigma_{lv}$ is the liquid-vapor surface tension. The wetting becomes harder when the contact angle getting larger. Figure 68 compares the good wetting and poor wetting situation refers to contact angle.

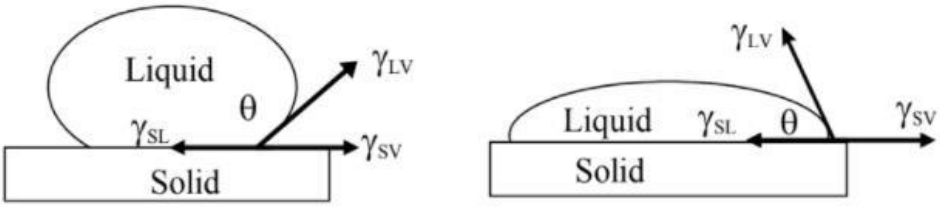


Figure 68. Sessile drop method measuring the contact angle; left: Poor wetting (θ>90°); right: good wetting (θ<90°) from[248]

*ii. Kinetics*

Wetting is not the sole requirement. Of course, it will dictate whether or not the suspension will penetrate the body but the penetration of the suspension inside the porous skeleton will depend on how it spreads. Two terms can be used to assess this specific property: adhesion work $W_a$ (Eq. 13) and cohesion work $W_c$ (Eq. 14).

$$W_a = \sigma_{lv} + \sigma_{sv} - \sigma_{lv} \tag{13}$$

$$W_c = 2\sigma_{lv} \tag{14}$$

Any liquid drop will well-spread on a solid surface whenever the adhesion work is larger than the cohesion work. This condition does not take into account the influence of an applied pressure onto the suspension. If a pressure is applied then the conditions of spreading are changed. Pressure-assisted infiltration is performed precisely when the wetting behaviour is poor. In that case, an applied pressure is needed to force suspension to go deep into the skeleton body [240]. Capillary effects also influence the penetration of the suspension. Washburn and Laplace equations [249] are good ways to understand the existing relation between the penetration depth, infiltration time with diffusion coefficient:

$$h = \sqrt{\frac{\sigma_{lv} \cdot t \cdot cos\theta \cdot r}{2\eta}} \tag{15}$$

In this Washburn's equation, h is the penetration length, t is the time, r is the pore radius, $\sigma_{lv}$ is the liquid surface tension, θ is the contact angle and η is the dynamic viscosity of the liquid. Diffusion coefficient is related the pore size, contact angle, viscosity and surface tension of the liquid. Capillary pressure ($P_c$) can be calculated with Laplace equation which is also related to the effective radius of the capillaries (r), surface tension (σ) and the wetting angle (θ):

$$P_c = \frac{2\sigma cos\theta}{r} \tag{16}$$

If the capillary force is too high because of extremely small pore size or improper surface tension, the suspension cannot infiltrate the porous body unless an external, counteracting pressure is applied.

*iii. Stability of the suspension*

Organic additives often are used as dispersants to increase repulsive forces between ceramic particles in suspension. Typically, these additives are charge-carrying long-chain polyelectrolytes. These additives adsorb on particle surfaces and modify the surface charge of these particles in suspension and thus enhance the interparticle electrostatic repulsion while further providing a steric barrier to agglomeration. Carboxylic acids have been shown to act as low molecular weight dispersants for aqueous suspensions of alumina. Such reagents are reported to impart negative surface charge on particles in suspension through the surface adsorption of the carboxylate anion (RCOO- ) [250]. The chemical formula of carboxylic acids is shown in Figure 69. Other dispersants are commonly used such as Ammonium polyacrylate[251] or polymethacrylic acid.

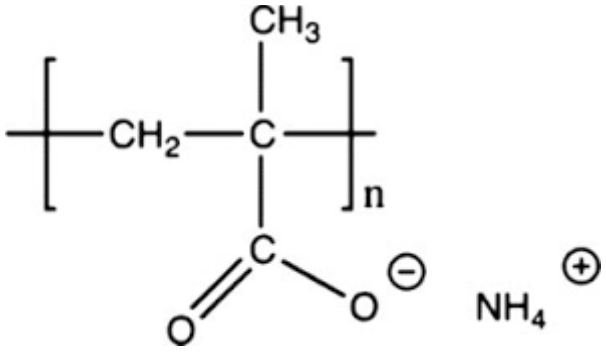


Figure 69. Chemical formula of carboxylic acid [250]

## 1.2. Literature survey of infiltration conducted with porous ceramic parts

As previously mentioned, only a handful of relevant papers have been identified in the literature to improve the density of porous parts manufactured by BJ through infiltration (infiltrations made with molten metals are not considered).

For instance, Eun-Hee Kim et al.[244] reported using tetraethyl orthosilicate and sodium methoxide to treat BJ printed parts (quartz sand and mullite). By filling-in the porosity of samples with the glassy phase, the mechanical strength was dramatically improved. Moreover, sol-gel solution containing aluminum chlorohydrate was also used as a precursor to infiltrate BJ printed alumina parts. Again the authors report after a suitable thermal treatment, an enhancement of the compressive strength and Young's modulus up to 179 MPa and 270.3 GPa respectively [243].

Similarly, Vogt et al.[241] strongly improved the compression strength of ceramic foams (manufactured by burning out the polyurethane (PU) template scaffold) by using pressure-less infiltration of a suspension containing 65 wt% solid loading. The compression strength of infiltrated alumina parts and zirconia toughed alumina parts (ZTA) were enhanced up to 100% and 388% with a weight increase of ca. 10% and 9% respectively. Figure 70 shows the

difference between a non-infiltrated and a completely infiltrated strut. Note that the infiltration was realized on pre-sintered bodies.

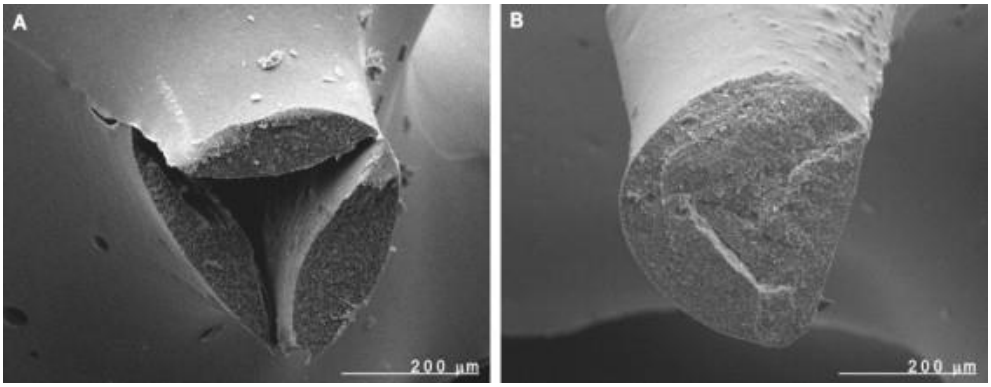


Figure 70. Pressure-less infiltration to enhance the strength ceramic foam. a) : Hollow alumina strut after burnout of the PU foam; b): Dense alumina strut after vacuum infiltration with alumina suspension and sintered at 1400°C from [241]

Maleksaeed et al.[239] have found that density, porosity, mechanical strength and surface roughness of BJ alumina products can be improved through pressure-less (low vacuum (0.1bar)) infiltration with dispersed alumina suspensions. This reference is one of the few found on this subject. As depicted in Figure 71, relative density of infiltrated parts was distinctly improved up to 86 %. It was reported that large inter-agglomerate pores can be eliminated while the intra-agglomerates pores are difficult to be removed. The same authors show that the infiltration efficiency improves with the solid loading to reach a plateau for a solid loading of 50 vol% as shown in Figure 71. For high solid loadings, the increased viscosity of the suspension becomes deleterious and prohibits the suspension to deeply penetrate the open porosity. Furthermore, even if higher solid loadings may improve the final density, they also tend to degrade the surface roughness and dimensional accuracy of final parts. Besides, a density gradient from surface to the centre of part is observed.

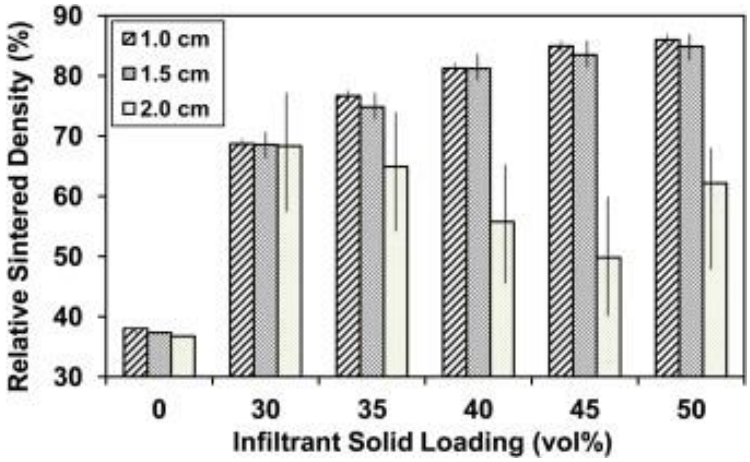


Figure 71. Relative sintered density of different size parts infiltrated with suspensions with various solid loading[239]

Cao et al. [240] further investigated the effects of various parameters on infiltration with alumina suspensions. Different applied pressures (pressure-less, 0.2, 0.5 and 0.8 MPa) and suspensions containing various solid loadings (30 and 40 vol%) were considered. Again, the results proved that the approach is more efficient to eliminate the larger pores (Figure 72) rather than the finer ones. The highest relative density, flexural and compressive strength achieved 73.2 %, 63.2 MPa and 450.2 MPa respectively after infiltration. All these values are still very low and far from being suitable for structural applications. However, a remarkable contribution of the study is that the samples with the highest density prior infiltration expressed lower final density but higher mechanical strength. Parts with lower density prior infiltration behaved oppositely. According to the authors, these results suggest that cracks are formed during sintering as a consequence of the introduced new particles. They suggested that pre-sintering temperature of printed parts might strongly influence the infiltration efficiency and formation of cracks but unfortunately, they did not conducted any experiment to confirm that statement [239].

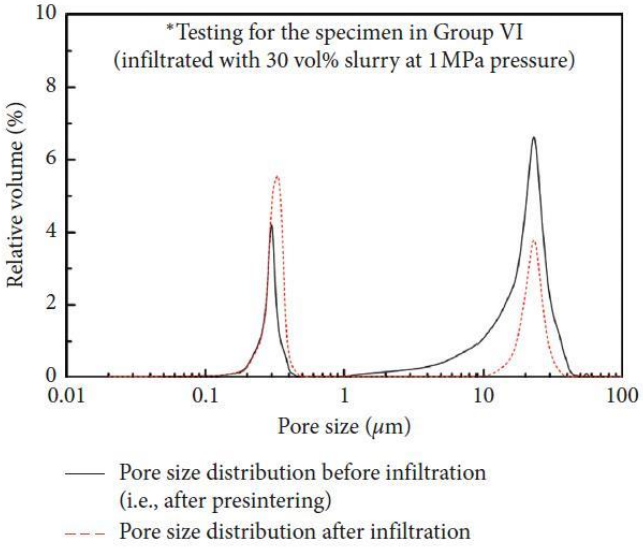


Figure 72. Pore size distribution before and after infiltration from[240]

### 1.3. Motivation

The possibility to improve the density of BJ parts with suspension infiltration is attractive. Despite the limited number of found references, the reported results are already very promising. Unfortunately, the published papers lacked relevant information although they were well conducted. For instance, the influences of infiltration duration, pre-sintering temperature, or even multi-infiltration rounds have not been studied.

This chapter aims at answering these questions. A detailed study to develop a better understanding of the post-infiltration of BJ printed ceramic objects is proposed. The objective is not only to improve the sintered density, it is also to develop a protocol simple enough to be easily transposed to other ceramic systems. To capitalize on past results, alumina was still selected as the model material (both for the printed bodies and suspensions). Influence of the pre-sintering temperature (e.g., consolidation of printed samples prior infiltration), number of successive infiltrations, solid loading in suspension and infiltration duration were all assessed. The study also brings new insights for identifying how the suspension infiltrates the samples and how the fine ceramic grains get distributed throughout the whole skeleton body. SEM imagery, micro-CT measurements and mercury porosimetry, appeared as a powerful tryptic to develop this understanding.

## 2. Experimental

### 2.1. Preparation of printed samples and suspensions

The alumina powder prepared in Chapter 2 was used for printing the test samples of this study. The spray dried powder (Al-SP) was sieved at 100 µm and divided into two parts: fine fraction (Al-SP1) and coarse fraction (Al-SP2). Relative density of printed cubes sintered at 1600°C

was measured to compared with samples infiltrated. The values are listed in Table 13 together with PSD of those 3 powders. Those samples (1.0 cm x 1.0 cm x 1.5 cm in the green state) were printed by applying a layer thickness of 200 µm and 70% binder saturation.

Table 13. PSD of powders and relative density of printed-sintered (1600℃) parts without infiltration

| | $D_{10}$ / µm | $D_{50}$ / µm | $D_{90}$ / µm | Packing density of powder bed / % | Relative density of BJ parts / % |
|---|---|---|---|---|---|
| Spray dried powder (Al-SP) | 16.7 | 52.8 | 119.0 | 34.8% | 57.1 |
| Fine fraction (<100µm) spray dried powder (Al-SP1) | 12.1 | 34.3 | 68.2 | 33.0% | 55.3 |
| Coarse fraction (>100µm) spray dried powder (Al-SP2) | 41.5 | 96.8 | 167.0 | 34.7% | 56.0 |

Before performing infiltration, all printed samples were debinded at 500 ℃ (heating rate: 3℃/min, dwelling time: 4 hours) and pre-sintered at different temperature 1200℃, 1400℃ or 1600℃ (heating rate: 5℃/min, dwelling time: 6 hours) in air atmosphere. The aim was to provide the sample a sufficient mechanical strength to survive the infiltration process. Meanwhile, the resulted shrinkage was also different due to the pre-sintering temperature. Thermal treatments are illustrated in Figure 73.

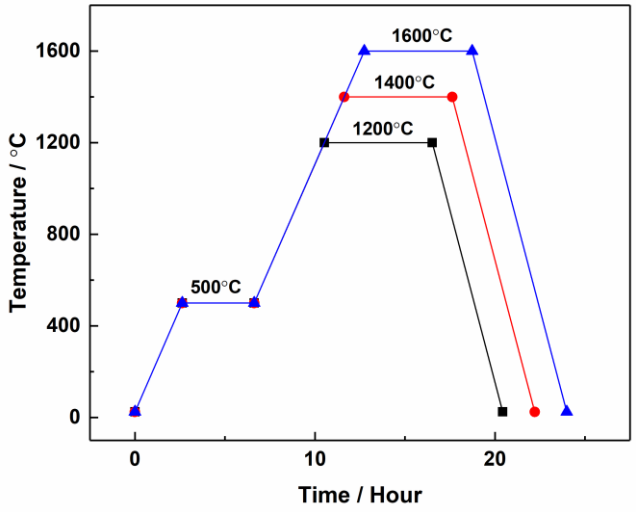


Figure 73. Thermal treatment profiles between multi-infiltrations

The un-granulated powder was used to prepare aqueous suspensions for infiltration. As in Chapter 2, Dolapix CE 64 (Zschimmer & Schwarz) was chosen as the dispersant. To fine tune the amount of dispersant, Zeta potential (ζ) (Acoustosizer II-M system, USA) analysis was performed under titration mode (which consists in a gradual addition of a dispersant solution into the suspension). The optimized amount of dispersant was determined (1.5 wt% in respect

to weight of solid content) when the zeta-potential value was the highest (-40 mV) and kept steady (Figure 74 (a)).

Aging tests were also carried out with Acoustosizer to assess the suspensions stability. The purpose of these tests was to determine whether the suspensions were sufficiently stable over long periods, equivalent to the infiltration time (Figure 74 (b)).

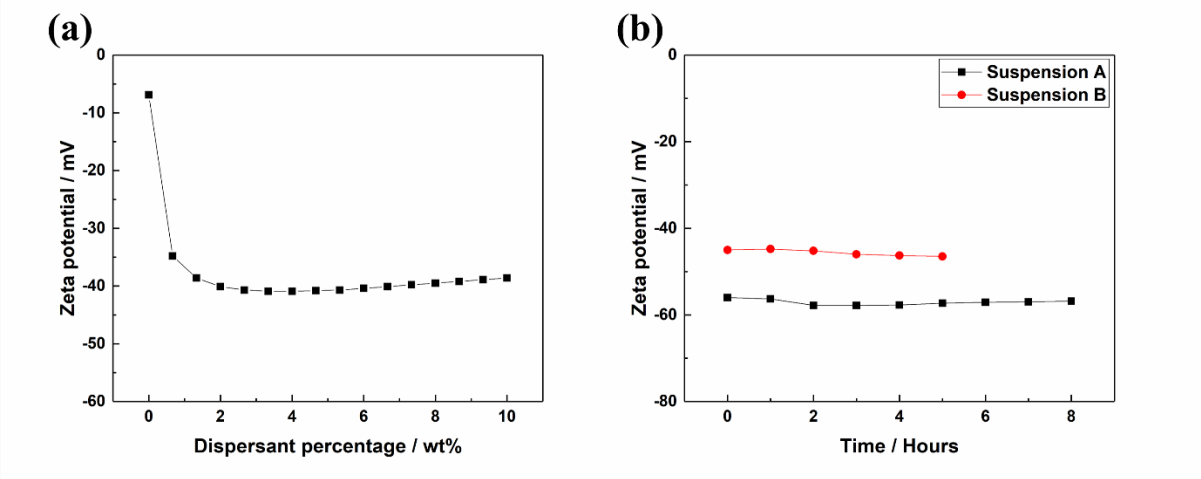


Figure 74. Stability tests in accordance with zeta-potential measured by Acoustosizer. a): Zeta-potential of suspension with varying amount of dispersant; b): Evolution of Zeta-potential for different durations without agitation

Two suspensions with different solid loading (50 wt% and 70 wt%) were finally prepared to investigate the influence of solid loading of suspension on properties of final parts. The aqueous suspensions (approx. 200 ml) containing the powder and the adequate dispersant content were homogenized by ball milling with different size of balls: 10 mm, 15 mm, 20 mm in diameter with mass proportion 25% : 50% : 25% respectively. Milling was performed on the roller bank (25 rpm) and lasted 48 hours to obtain homogeneous ceramic suspensions. Particle size distribution (PSD) was measured by laser scattering on a Malvern Mastersizer 3000 (Malvern Instruments GmbH, Germany). Suspensions were also characterized in terms of rheological properties (Thermo Fisher, Rheometer, USA).

In Table 14, the PSD of powders in suspension after homogenization and milling as well as suspensions viscosities are reported. Obviously, suspension B was much more viscous than A due to higher solid loading with a possible impact on the infiltration efficiency that will be discussed later in this document.

Table 14. Particle size distribution of powders in suspensions and viscosity of respective suspensions

| | D10/µm | D50/µm | D90/µm | Viscosity/cps at 1 $s^{-1}$ |
|---|---|---|---|---|
| Suspension A | 0.028 | 0.18 | 1.3 | 8.43 |
| Suspension B | 0.031 | 0.22 | 1.7 | 526 |

## 2.2. Infiltration process

Prior infiltration, all samples were dried in an oven at 100°C for 24 hours.

The entire designed infiltration process is shown in Figure 75 and comprises different steps.

a) Ceramic suspensions are poured into a chamber connected to a vacuum pump to create low vacuum atmosphere (around 0.1 bar [239]);

b) The pre-sintered samples are put inside of the chamber slightly above the suspension on a moveable platform. The pumping process then starts to remove all the air within the chamber and inside the pores (the real equipment is shown Figure 76). Pumping takes 2/3/4 hours. During this time the suspension is stirred continuously;

c) The samples are immersed completely without further stirring the suspension. Pumping is maintained during immersion. After the planned infiltration duration, it is stopped and the whole system just relaxes for 2 more hours. Finally, all samples are taken out carefully, slight wiped with wet tissue to remove the excess of suspension. Then the drying process followed.

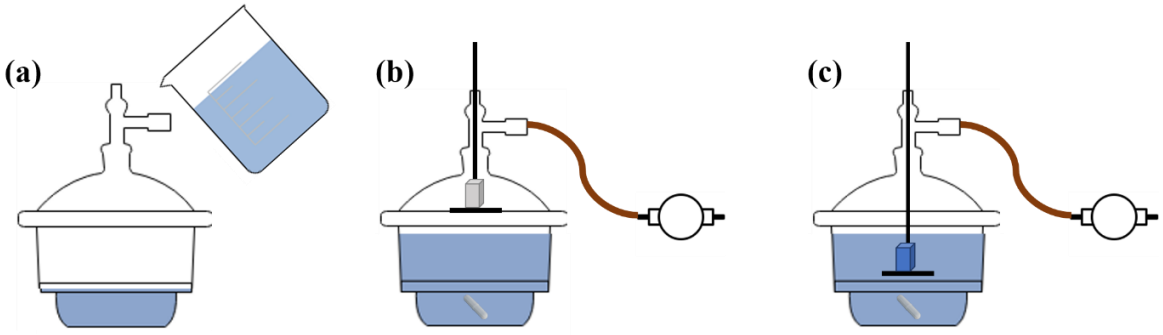


Figure 75. Schematic process of infiltration

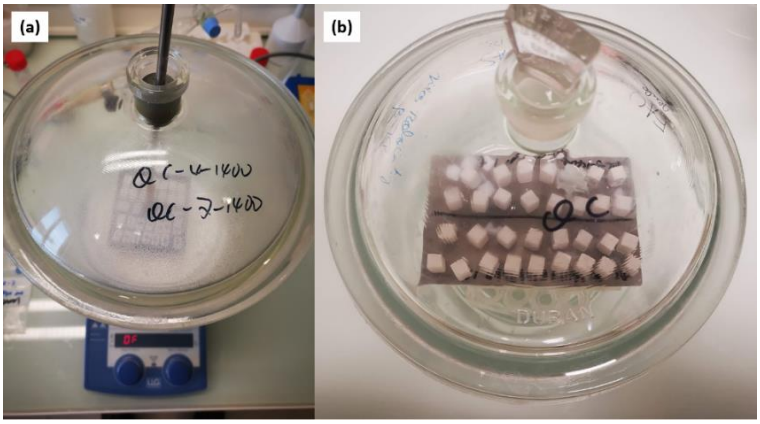


Figure 76. Experimental setup of infiltration. a): During infiltration process; b): Drying in the chamber with moisture

Figure 77 illustrates the process of multi-infiltrations.

Step 1: All samples are submitted to a first pre-sintering step at $T_{pre1}$ (1200/1400/1600°C for 6 hours in air and a heating ramp of 3°C/min). The objective is to make the samples strong enough to withstand handling and further treatments. Then the 1st infiltration is done. The resulting samples are separated into two batches. One half is directly sintered at 1600°C (6 hours) while the other half are pre-sintered again at temperature $T_{pre2}$ (1200°C for 2 hours whatever the initial $T_{pre1}$); The objective of this new pre-sintering step (with a heating ramp of 3°C/min) is to consolidate the ceramic grains deposited inside the bodies by the infiltration.

Step 2: These pre-sintered samples are then infiltrated for a 2nd time. When it is done, those samples are divided again. The first half are sintered at 1600°C while the other half are pre-sintered at $T_{pre2}$ (1200°C) as previously;

Step 3: Step 2 is reproduced for a 3rd infiltration. At the end, all samples have been sintered at 1600°C for 6 hours.

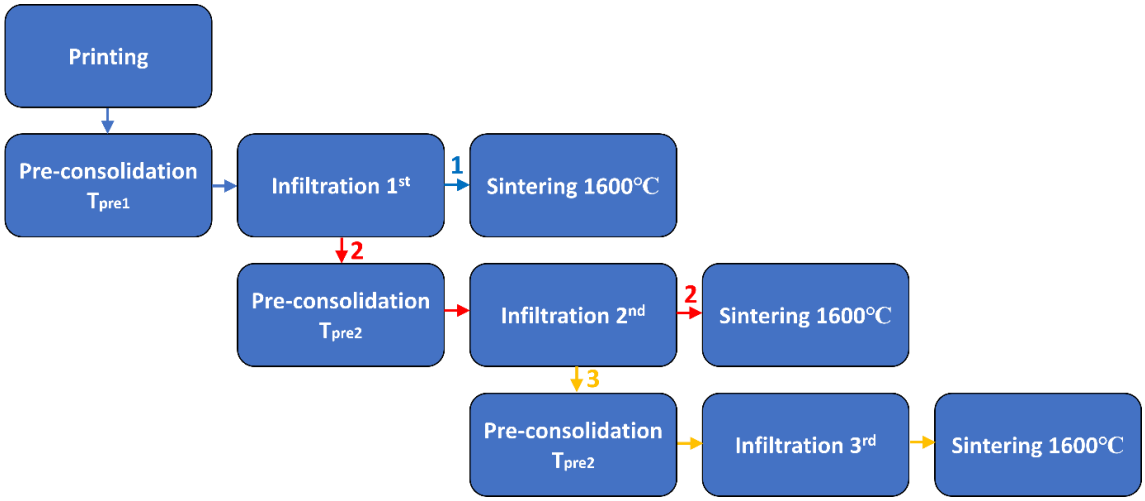


Figure 77. Scheme of multi-infiltrations process

To determine the pre-sintering temperatures ($T_{pre1}$, $T_{pre2}$) dilatometry was conducted on printed green bodies. As shown in Figure 78, sample started to shrink slightly at around 1050°C and the sintering stage should be located in intermediate stage [192, 252]. The 1200 °C pre-densification treatment that does not involve significant shrinkage will not cause large cracks formation.

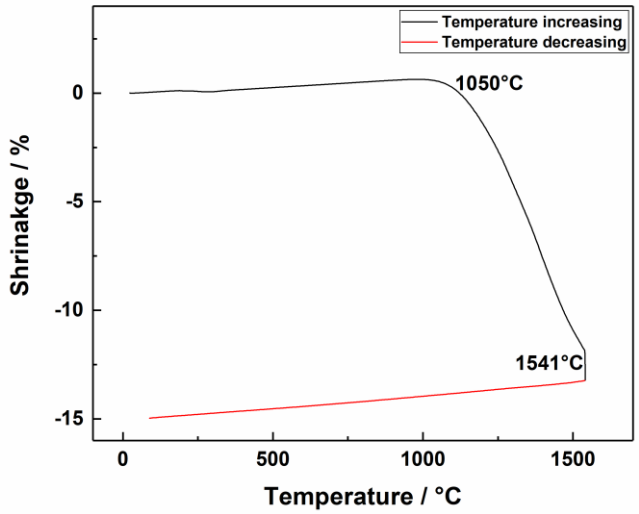


Figure 78. Dilatometry curve of green parts printed with alumina powders

All process parameters of different groups of samples are listed in Table 15. In total, 42 different conditions with diverse influencing factors were applied. Each group contained at least 4 samples to ensure the repeatability.

Table 15. List of infiltrated samples

| Group | Powder | Pre-sintering temp./℃ | Infiltration duration / Hours | Infiltration round | Suspension solid loading / wt% |
|---|---|---|---|---|---|
| 1 | Al-SP | 1200 | 2 | 1 | 50 |
| 2 | Al-SP | 1200 | 2 | 2 | 50 |
| 3 | Al-SP | 1200 | 2 | 3 | 50 |
| 4 | Al-SP | 1200 | 3 | 1 | 50 |
| 5 | Al-SP | 1200 | 4 | 1 | 50 |
| 6 | Al-SP | 1200 | 2 | 1 | 70 |
| 7 | Al-SP | 1400 | 2 | 1 | 50 |
| 8 | Al-SP | 1400 | 2 | 2 | 50 |
| 9 | Al-SP | 1400 | 2 | 3 | 50 |
| 10 | Al-SP | 1400 | 3 | 1 | 50 |
| 11 | Al-SP | 1400 | 4 | 1 | 50 |
| 12 | Al-SP | 1400 | 2 | 1 | 70 |
| 13 | Al-SP | 1600 | 2 | 1 | 50 |
| 14 | Al-SP | 1600 | 2 | 2 | 50 |
| 15 | Al-SP | 1600 | 2 | 3 | 50 |
| 16 | Al-SP | 1600 | 3 | 1 | 50 |
| 17 | Al-SP | 1600 | 4 | 1 | 50 |
| 18 | Al-SP | 1600 | 2 | 1 | 70 |
| 19 | Al-SP1 | 1200 | 2 | 1 | 50 |
| 20 | Al-SP1 | 1200 | 2 | 2 | 50 |
| 21 | Al-SP1 | 1200 | 2 | 3 | 50 |
| 22 | Al-SP1 | 1200 | 2 | 1 | 70 |

| | | | | | |
|---|---|---|---|---|---|
| 23 | Al-SP1 | 1400 | 2 | 1 | 50 |
| 24 | Al-SP1 | 1400 | 2 | 2 | 50 |
| 25 | Al-SP1 | 1400 | 2 | 3 | 50 |
| 26 | Al-SP1 | 1400 | 2 | 1 | 70 |
| 27 | Al-SP1 | 1600 | 2 | 1 | 50 |
| 28 | Al-SP1 | 1600 | 2 | 2 | 50 |
| 29 | Al-SP1 | 1600 | 2 | 3 | 50 |
| 30 | Al-SP1 | 1600 | 2 | 1 | 70 |
| 31 | Al-SP2 | 1200 | 2 | 1 | 50 |
| 32 | Al-SP2 | 1200 | 2 | 2 | 50 |
| 33 | Al-SP2 | 1200 | 2 | 3 | 50 |
| 34 | Al-SP2 | 1200 | 2 | 1 | 70 |
| 35 | Al-SP2 | 1400 | 2 | 1 | 50 |
| 36 | Al-SP2 | 1400 | 2 | 2 | 50 |
| 37 | Al-SP2 | 1400 | 2 | 3 | 50 |
| 38 | Al-SP2 | 1400 | 2 | 1 | 70 |
| 39 | Al-SP2 | 1600 | 2 | 1 | 50 |
| 40 | Al-SP2 | 1600 | 2 | 2 | 50 |
| 41 | Al-SP2 | 1600 | 2 | 3 | 50 |
| 42 | Al-SP2 | 1600 | 2 | 1 | 70 |

## 2.3. Drying

Drying was carried out after each infiltration steps. Different approaches were tested (in dry air, in water saturated air, with existence of silica gel, by modifying the temperature …) and the most suitable one was determined in its ability to reduce the number of cracks formed. The approach described hereafter is the one for which the results were the most promising.

Infiltrated samples are first put in a climatic chamber with moisture inside at room temperature for 4 days. Then they are put into an opened container on a wet napkin and placed in an oven at 35°C for 12 hours. The napkins were totally dried afterward and consequently samples were considered as completely dried as well. To prevent any re-hydration of the samples before sintering, they were put in an oven and heated up to 100°C for one hour. Surface morphology of samples dried with this procedure is shown in Figure 79. Despite the precautions taken, some tiny cracks can be noticed. Using a binder in the infiltration suspension may help preventing those cracks or generate cracks during thermal treatment. However, suspension composed with binder was not tested due to the time restriction.

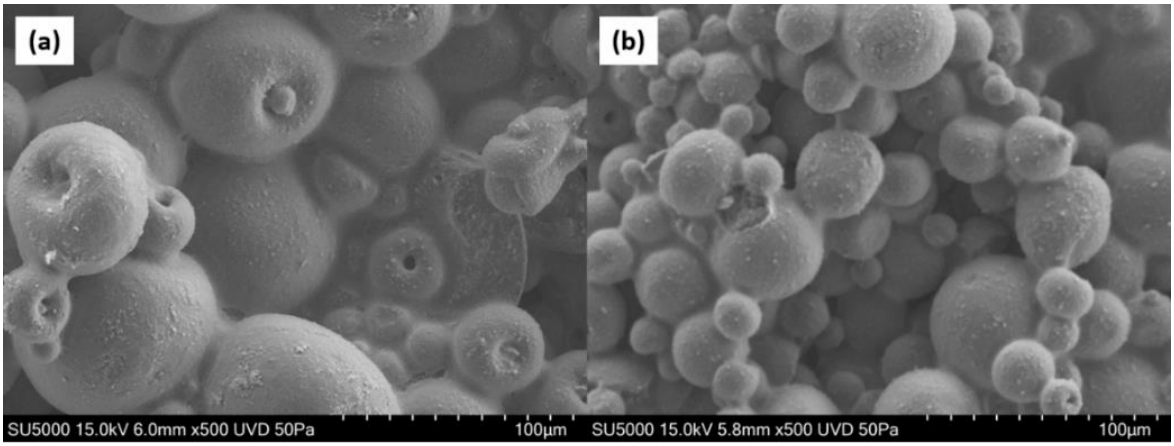


Figure 79. Surface morphology of samples with final drying program; a): Sample Al-SP pre-sintered at 1400°C and 1st infiltrated; b): Sample Al-SP1 pre-sintered at 1400°C and 1st infiltrated

## 2.4. Characterization methods with infiltrated samples

For the assessment of final parts, Archimedes method was used to measure the density and porosity. Pore size distribution of samples after different treatments were also investigated by AutoPore IV mercury porosimetry (Micromeritics, USA). Surface morphology and microstructures of final samples were coated with platinum under vacuum using an evaporating system (JEOL JFC-3000, Japan) and were studied by scanning electron microscope (SEM) (Tescan, Czech Republic). Roughness measurements on non-infiltrated and infiltrated sample side surfaces were conducted with 3D laser scanning microscope (VK-X200, Keyence, Japan). Arithmetical mean deviation (Ra) was calculated on 2 mm scanning track lengths along the printing direction (z) (no cutoff).

Micro-CT analysis (Phoenix Nanotom, Baker Hughes, USA) was performed in CIRIMAT (Université de Toulouse, France) to observe the microstructure of infiltrated parts and determine the distribution of the residual porosity. To get an insight about the location and size of pores inside the printed bodies, the strategy was to decompose each sample into cells of dimension ($1.4 * 1.4 * 1.4\ mm^3$). 7 consecutive cells formed a 'L' shape starting from the center of the sample and extended along horizontal and vertical directions (red color voxels in Figure 80) were selected. Porosity, pore volume distribution and pore structure were characterized in the corresponding cells and whole individual sample with largest volume could reach. After slicing the samples with x-ray perspective images, densities at different locations in horizontal and vertical directions inside of sample were identified in Figure 80.

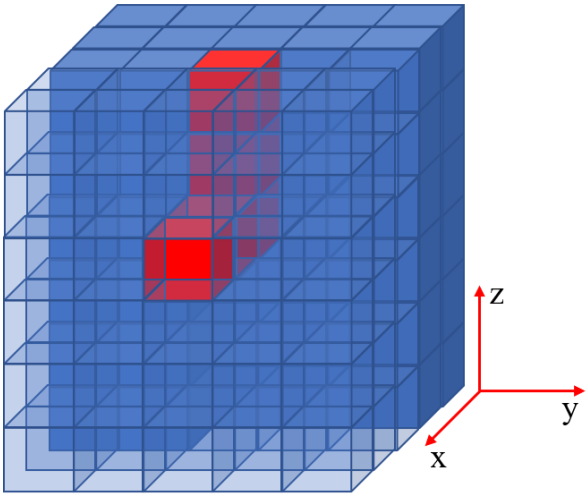


Figure 80. Cells discretization of samples to assess porosity by micro-CT

# 3. Results and discussion

## 3.1. Improvements of samples after infiltration

The density of all samples after the various infiltrations are listed in Table 16.

Table 16. Sintered densities of all infiltrated samples for different pre-sintering temperatures (infiltrated for 2 hours with 50 wt% solid loading suspension)

| Powder | Pre-sintering temp./°C | Infiltration round | Suspension solid loading / wt% | Average Relative density / % |
|---|---|---|---|---|
| Al-SP | 1200 | 1 | 50 | 74.1±0.9 |
| Al-SP | 1200 | 2 | 50 | 83.3±1.0 |
| Al-SP | 1200 | 3 | 50 | 87.9±0.5 |
| Al-SP | 1400 | 1 | 50 | 70.9±0.8 |
| Al-SP | 1400 | 2 | 50 | 79.4±0.8 |
| Al-SP | 1400 | 3 | 50 | 81.8±1.8 |
| Al-SP | 1600 | 1 | 50 | 68.4±0.8 |
| Al-SP | 1600 | 2 | 50 | 75.0±0.4 |
| Al-SP | 1600 | 3 | 50 | 77.5±1.9 |
| Al-SP1 | 1200 | 1 | 50 | 73.9±0.8 |
| Al-SP1 | 1200 | 2 | 50 | 82.5±0.9 |
| Al-SP1 | 1200 | 3 | 50 | 87.5±0.7 |
| Al-SP1 | 1400 | 1 | 50 | 68.7±0.8 |
| Al-SP1 | 1400 | 2 | 50 | 77.9±1.6 |
| Al-SP1 | 1400 | 3 | 50 | 82.2±0.3 |
| Al-SP1 | 1600 | 1 | 50 | 66.3±0.4 |
| Al-SP1 | 1600 | 2 | 50 | 73.2±0.9 |
| Al-SP1 | 1600 | 3 | 50 | 77.4±0.5 |
| Al-SP2 | 1200 | 1 | 50 | 70.5±0.8 |
| Al-SP2 | 1200 | 2 | 50 | 80.9±1.4 |
| Al-SP2 | 1200 | 3 | 50 | 86.4±1.3 |
| Al-SP2 | 1400 | 1 | 50 | 68.8±1.1 |
| Al-SP2 | 1400 | 2 | 50 | 77.8±1.0 |

| | | | | |
|---|---|---|---|---|
| Al-SP2 | 1400 | 3 | 50 | 81.8±0.4 |
| Al-SP2 | 1600 | 1 | 50 | 67.1±0.6 |
| Al-SP2 | 1600 | 2 | 50 | 73.5±0.7 |
| Al-SP2 | 1600 | 3 | 50 | 78.0±0.7 |

Figure 81 distinctly shows the density enhancement of samples after 3rd infiltration compared with non-infiltrated samples. Almost 33 % of relative density increment is achieved after 3 successive infiltrations for Al-SP samples (for which the highest enhancement is noted). Besides, densities of samples after one single infiltration and two infiltrations are enhanced by 18.6% and 27.2% respectively for Al-SP1 printed samples. The density enhancements are similar for all samples after 3 infiltrations whatever the powder used for printing.

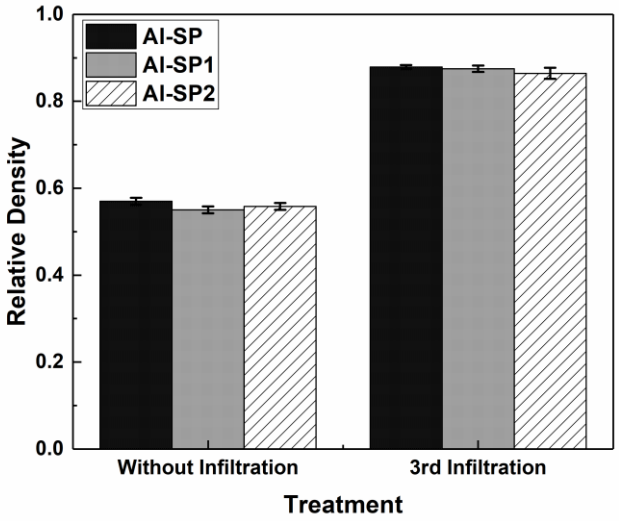


Figure 81. Density improvements of samples after infiltration compared with samples non-infiltrated after sintering

Figure 82 shows the typical surface morphology of sintered samples either non-infiltrated (Figure 82, a-b-c) or after 3 consecutive infiltrations (Figure 82, d-e-f). Most voids and mid-size pores noticed in non-infiltrated samples almost all disappeared after 3 infiltrations steps. The fine particles brought by the suspensions were sintered around and/or in between granules of the printed objects. The microstructures are obviously much denser. However, fine cracks are noticed at some locations (red arrows, Figure 82) that may result from improper drying conditions (as already noticed) or from a differential shrinkage occurring between fine grains and granules during the final sintering step.

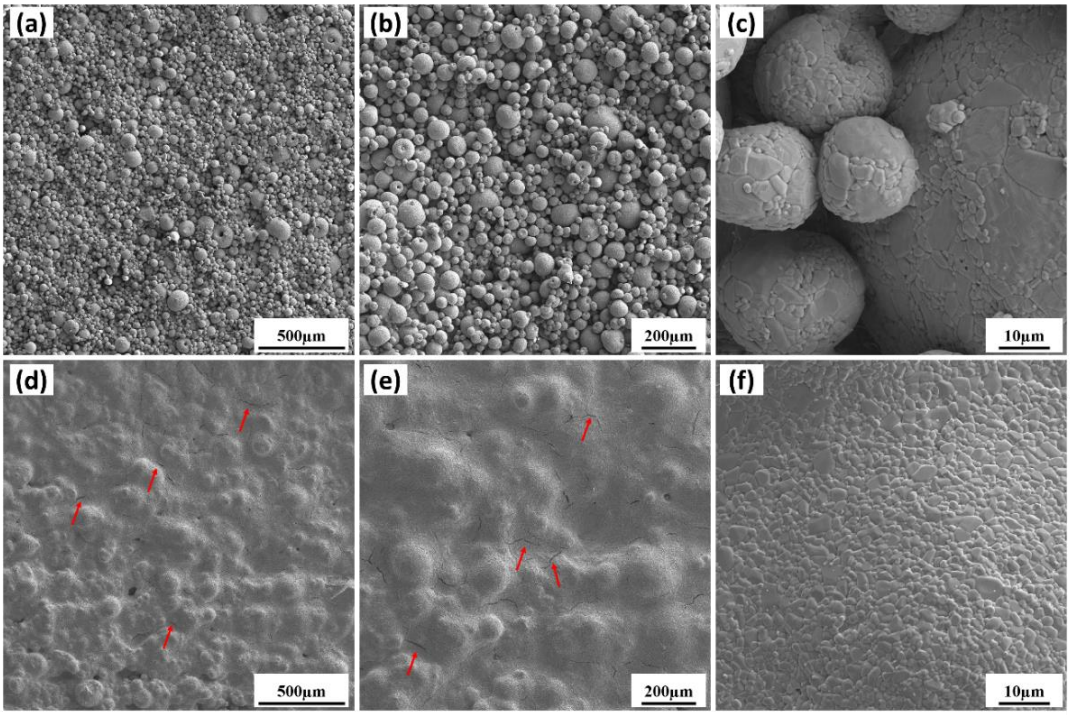


Figure 82. Surface morphology of samples non-infiltrated and infiltrated after sintering. a) – c): Parts printed with Al-SP powder and sintered at 1600°C; d) – f): Parts printed with Al-SP powder, pre-sintered at 1200°C, infiltrated 3 times and sintered at 1600°C

Micro CT confirms that most open pores are filled by the fine particles coming from the suspensions. Figure 83 illustrates the 3D pores-structure inside two illustrative samples without infiltration (Figure 83 a) and after three rounds (Figure 83 b). Calculation of the porosity of nearly whole samples volume shows a dramatic decrease, more than 35%. In sample Al-SP2 for instance, the global porosity (after sintering) decreases even more, starting at 45.82% for the non-infiltrated sample to 8.78% in the infiltrated one. However, contrarily to non-infiltrated samples, the pore-distribution in the infiltrated samples is no more homogeneous vertically throughout the whole body. On the contrary, the porosity distribution shows an obvious gradient phenomenon with most big pores located on top part of the samples and denser part at the bottom (Figure 83 b).

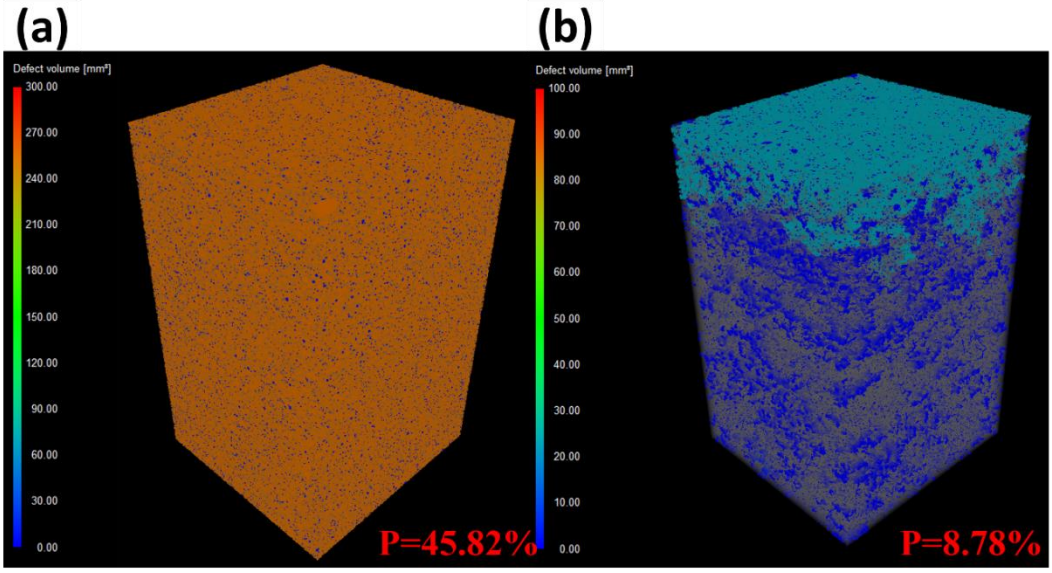


Figure 83. Porosity in samples printed from Al-SP2 powder 3D microstructure. a): Before infiltration; b): After 3 infiltrations

### 3.2. Porosity distribution & infiltration mechanism

To get an insight of the origin of the porosity gradient in the infiltrated samples, Micro-CT measurements have been carried out at different locations within the parts according to Figure 84 (a). As an example, Figure 84 shows the porosity gradient in the specific but illustrative case of sample Al-SP-1200-3$^{rd}$. The measurements made on other samples are qualitatively similar. Micro-CT brings interesting information about the porosity distribution. On top of the sample, porosity is not qualitatively reduced compared with non-infiltrated part. 3D reconstructed images show that the pores located in this region are still forming an open-pore-network. In this region, the local reduction of density after three rounds does not exceed 22 % (porosity decreased from 42.9% (non-infiltrated sample) to 21.32% (top cell of infiltrated sample Al-SP-1200-3$^{rd}$)) (Figure 84 (c)).

On the contrary, porosity was intensively reduced to less than 10 % in the center area and bottom part of samples. Porosity is therefore arranged along the Z axis of the sample with an obvious gradient as indicated by the red color bar (Figure 84 (c)). It is considered that this gradient simply mimics the distribution of the suspension within the sample during the infiltration process. After the sample are removed from the infiltration bath, the suspension progressively settles down and accumulates in the bottom part of the samples (as a consequence of gravity) where it dries out. If one compares the porosity in the cells located at the bottom of the samples (same Z), it is therefore not surprising that the values are really close and much smaller than the ones found at higher Z, showing almost no porosity gradient in the XY direction.

Since the printed bodies can be assumed to be isotropic in the XY plane, it is not surprising that porosity is roughly constant in horizontal planes. On the contrary, it is easier to imagine that the printed bodies are less isotropic along the Z axis. Furthermore, the movement of each single particle in the suspension results from a number of forces. Figure 84 (d) shows that gravity (Fg), buoyancy (Fb), interparticle force from surrounding particles (Fa) and capillary force from the pores (Fc) co-acted on particles to influence the infiltration process together. Gravity breaks the isotropy of the force field and will undoubtedly favour migration of the particles along the Z axis, at the bottom.

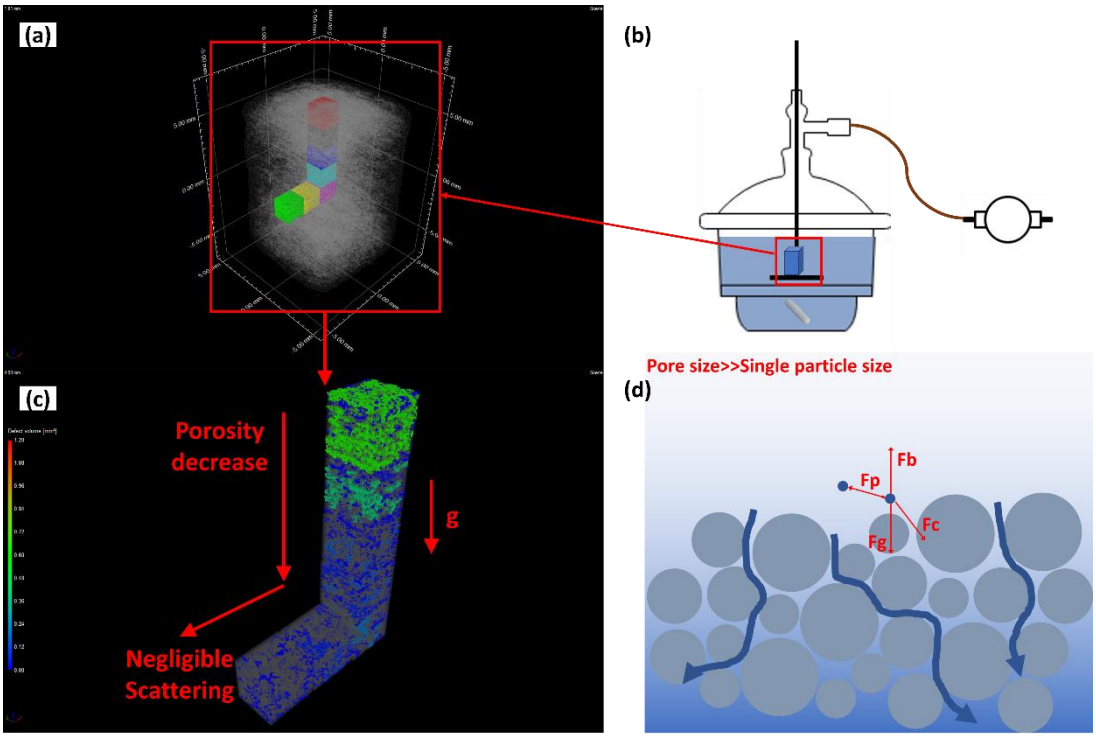


Figure 84. Infiltration mechanism analysis. (a): 7 cubes selection in the dimension of origin cuboid sample Al-SP-1200-3rd; (b): Scheme of sample being infiltrated and accordingly position in suspension; (c): Porosity gradience with 7 cubes along horizontal and vertical direction; (d): Dynamic mechanical analysis of particles in suspension during infiltration process inspired from [4]

The average porosity within each cell (1.4 * 1.4 * 1.4 $mm^3$) in the discretization scheme is shown in Figure 85 (example: Al-SP-1200-3rd). As expected, porosity decreases progressively from cell A to E, e.g., from the top to the central of the sample. It should be noted that there is a 10% variation density between the top and bottom surfaces which is clearly not negligible. On the contrary, the porosity in cells located on the same horizontal levels only scatters slightly. Table 17 also shows the results of similar measurements performed on the samples after 1st, 2nd, and 3rd infiltration rounds.

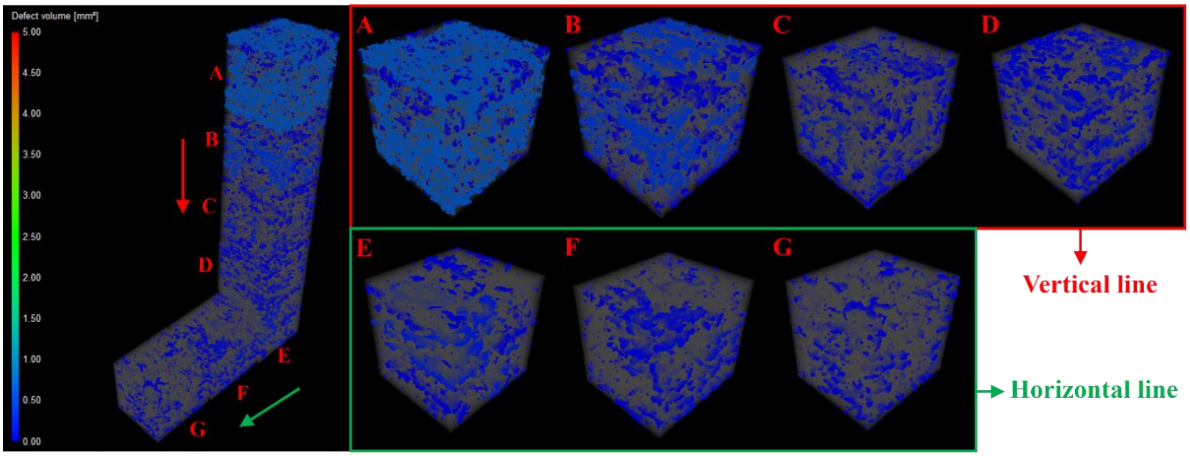


Figure 85. Pore gradience exhibition of pixel-cubes with sample Al-SP-1200-3rd

Table 17. Average porosity of each cell in different samples

| Cells number | Porosity from sample Al-SP-1200-1st / % | Porosity from Al-SP-1200-2nd / % | Porosity from Al-SP-1200-3rd / % |
|---|---|---|---|
| A | 32.56 | 26.08 | 21.32 |
| B | 33.22 | 28.08 | 16.02 |
| C | 31.26 | 29.44 | 9.4 |
| D | 21.25 | 16.58 | 11.05 |
| E | 11.83 | 9.47 | 9.62 |
| F | 16.96 | 11.17 | 9.76 |
| G | 20.52 | 13.67 | 6.49 |

Micro-CT cross-section images were taken at different locations in non-infiltrated and infiltrated samples. As an example, Figure 86 shows these images for sample Al-SP-1200 after 1 single infiltration and compare its non-infiltrated counterpart. As expected, non-infiltrated sample is highly porous, showing a network of pores homogeneously distributed throughout the skeleton body as view from the side (Figure 86 (b)). With the top-view image, defects generated by printing itself can be noticed with an alignment of pores along parallel lines. These lines are most likely formed by a lack of ink deposited on the powder bed between neighbor nozzles (Figure 86 (c)). For the infiltrated samples, when looked from the side, porosity gradient is also noticed. And the trend becomes much more obvious when looking at slices parallel to the building direction (z-axis). Figure 86 (g) taken from the top of the sample reveals that a significant number of pores have survived the infiltration process. This number of connected pores obviously decreases in the middle part of the sample (Figure 86 (h)) and it is even lower at the bottom (Figure 86 (i)). In all cases, porosity remains mostly located on top of the samples and decreases near the bottom confirming the density measurements in each cell reported previously.

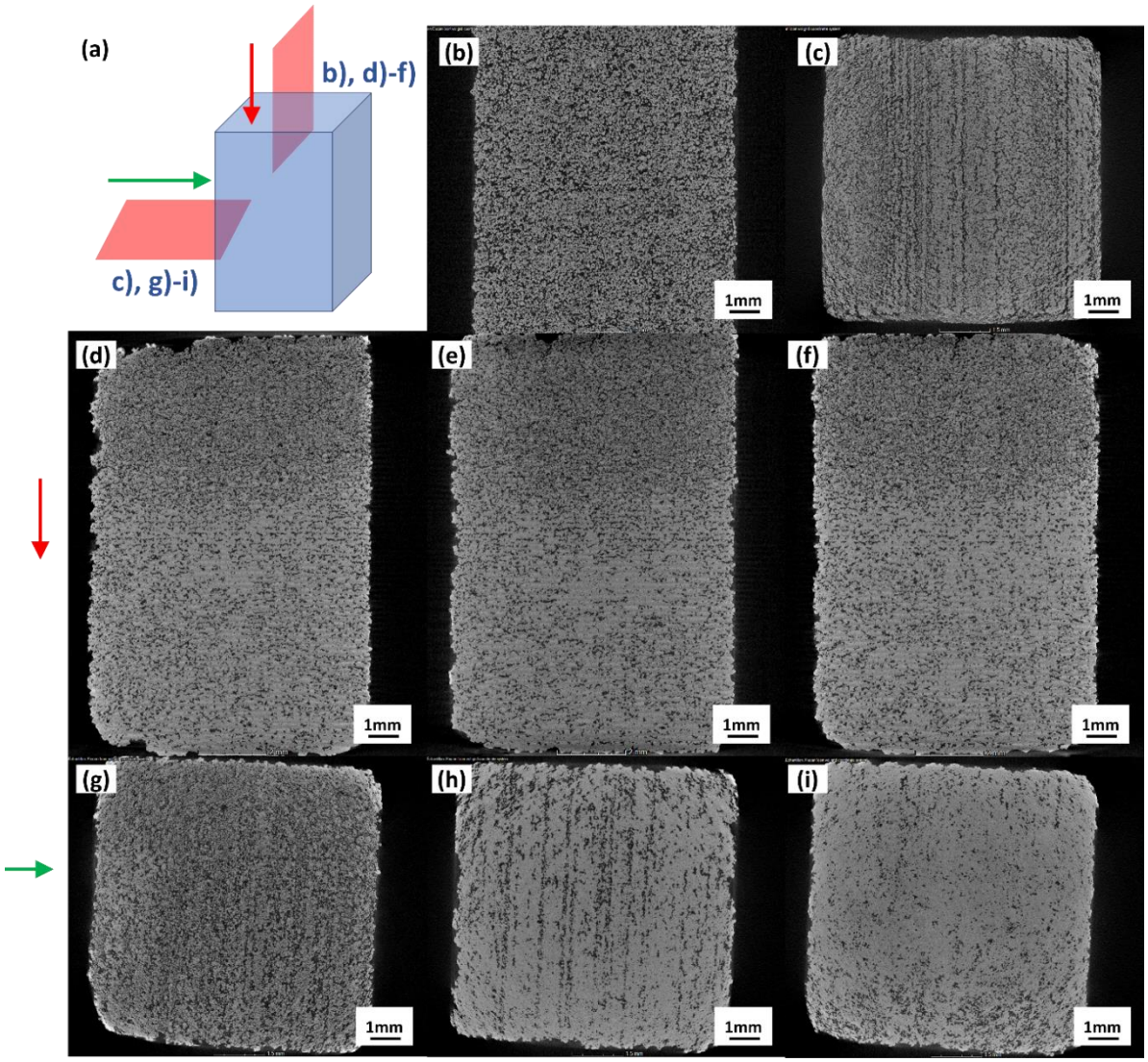


Figure 86. Slicing X-ray perspective images of sample Al-SP-1200-1st; a): Scheme on slicing cross-section images of samples; b): Side-view cross-section of non-infiltrated part; c): Top-view cross-section of non-infiltrated part; d)-f): Side-view cross section images of 3rd-infiltrated samples; g)-i): Top-view cross-section images of 3rd-infiltrated samples, red arrow is the direction from top to bottom when sample stood on substrate during infiltration

### 3.3. Infiltration and roughness

3D profile images and roughness values were measured at different locations on the side of infiltrated parts compared with non-infiltrated ones (Figure 87). As expected, non-infiltrated parts exhibit rough surfaces (Figure 87 (b)) due to the coarse granule size. After infiltration, it is not surprising that roughness measured in the upper part of the sample is not improved efficiently since most of the large pores are still present and the infiltration effect was not apparently worked as discussed above. On the contrary, surface of bottom part was

undoubtedly much flatter and smoother with an Ra (Arithmetical mean deviation) improvement of almost 50% (approx. 8 µm vs 17 µm).

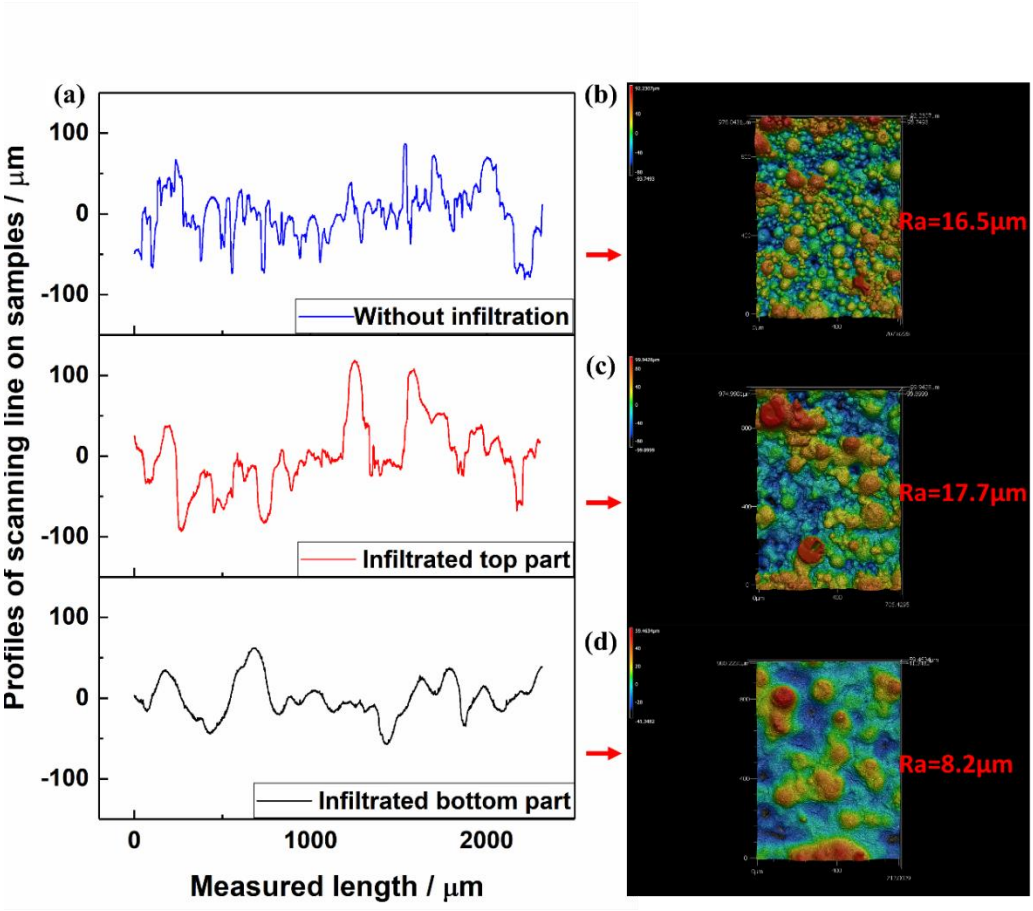


Figure 87. Roughness and 3D profile of surfaces of Al-SP printed samples non-infiltrated and 3rd infiltrated; a): Profile of line scanning on non-infiltrated sample and different areas on infiltrated samples; b): Profile of non-infiltrated sample; c): Profile of top area of infiltrated sample; d): Profile of bottom area of infiltrated sample

It should be noticed that we did not notice any significant evolution of the shape and dimensions of the parts with infiltration (Figure 88) as it is sometimes reported in the literature [239, 240]. This is not surprising as no shell of dried suspension was noticed surrounding the part by using suspension with low viscosity.

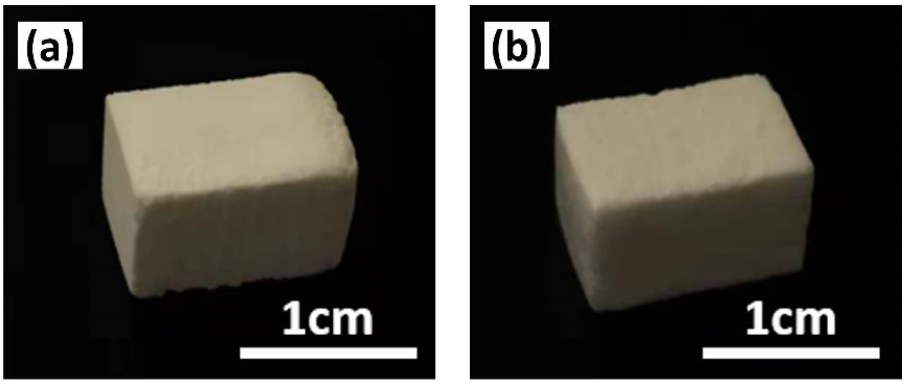


Figure 88. Samples before (a) and after (b) infiltration with suspension contained 50 wt% solid loading

## 3.4. Parametric study

### 3.4.1. Benefits of multiple infiltrations

The purpose of multi-infiltration processes is to reach densities higher than those obtained after a single infiltration. The idea is graphically depicted in Figure 89. Fine particles are first introduced in the porous skeleton bodies during the first infiltration. Thanks to the subsequent thermal treatment, these particles sinter with the porous body and are not being rinsed off in the next infiltration step. Then, more particles can be introduced in the skeleton bodies during the next infiltration. This sequence can be reproduced multiple times so as to get further increase of density. During this process, though the open porosity can be reduced significantly, new closed pores might be formed.

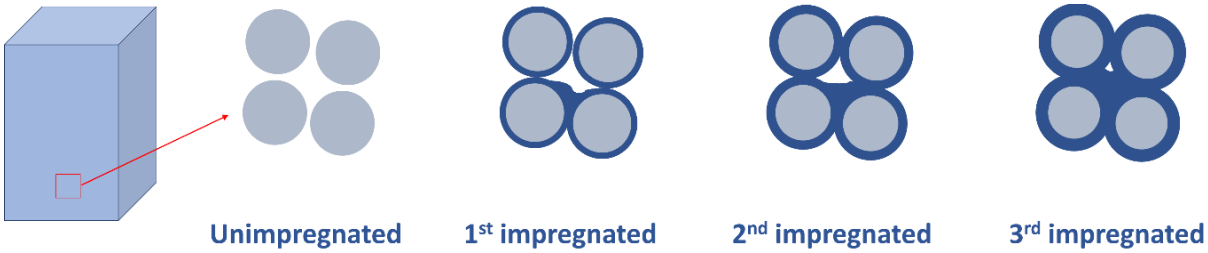


Figure 89. Schematic mechanism of influence of infiltration rounds on infiltrated samples

Figure 90 compares the evolution of the microstructure after successive infiltration rounds (1st, 2nd, 3rd). Obviously, the fine particles originating from suspensions are relatively well-spread inside of the skeleton body and form a continuum with granules after sintering. The voids and pores are filled more and more completely through repeated infiltrations. After 3 infiltrations, the granules have almost disappeared in the continuum (something which could already be noticed in Figure 90). Small cracks are noted at the junction between granules where a higher amount of suspension has dried out. They may originate from improper drying conditions or from a differential shrinkage between granules and the surrounding material. If one looks at

the evolution of the microstructure, the first infiltration creates large necks around granules where the suspension is probably accumulating. Those necks are becoming even larger with the second infiltration and finally surround completely the granules after the third one.

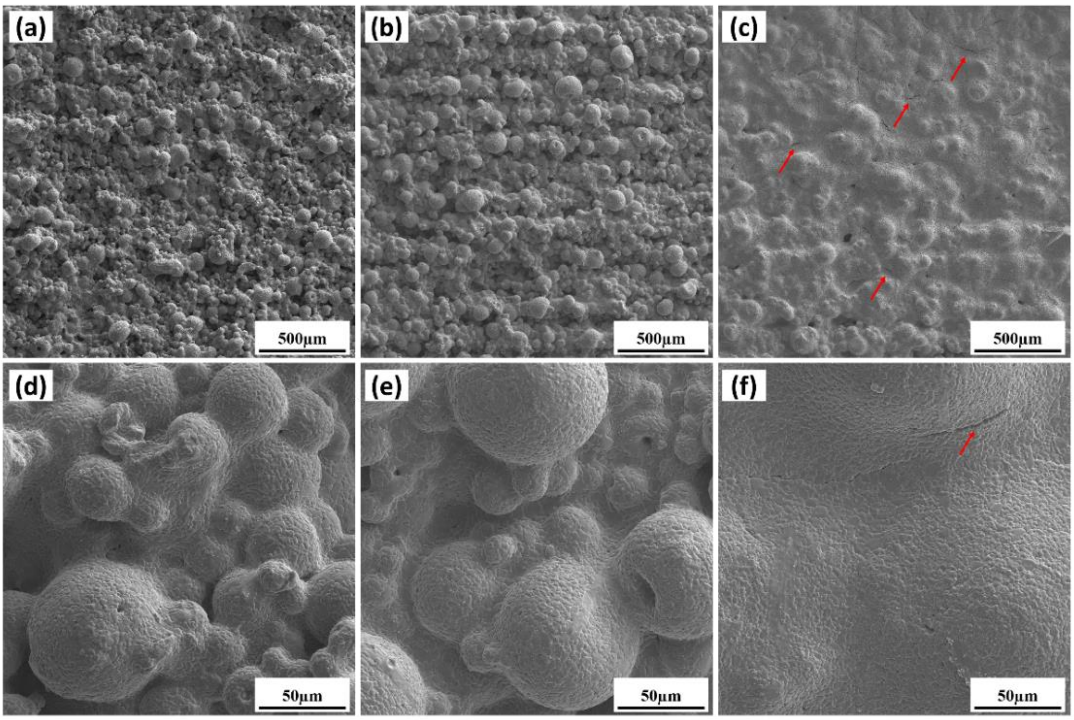


Figure 90. Surface morphology of samples printed with Al-SP powders, pre-sintered at 1200°C and after 1st infiltration (a and d), after 2nd infiltration (b and e) and 3rd infiltration process (c and f)

Figure 91 plots the evolution of the relative density with the number of successive infiltrations. The density improvement is continuous reaching almost 90% of the T.D in the best case. It should be noticed that the three plots are very similar suggesting that the variations between the powder properties (average size and PSD) used for printing exert almost no influence. The highest average relative densities of sample groups, ie. Al-SP-1200-3rd, Al-SP1-1200-3rd, Al-SP2-1200-3rd reach 87.9±0.5 %, 87.5±0.7 %, and 86.4±1.3% respectively, which are all much higher than the density of sintered parts without infiltration treatment, ie. 57.1±1.4 %, 55.3±1.1 %, and 55.9±0.5% respectively.

As shown on Figure 91, the density was enhanced significantly with the number of successive infiltrations but finally seems to saturate after the third one. Although a 4th infiltration was not tested in the present work, it is expected that a very limited gain would have been obtained, considering the general trend of the curves. It can be assumed that as porosity decreases, the suspension has less access to the inner part of the samples as the infiltration channels reduce in size such that the efficiency of infiltration decreases.

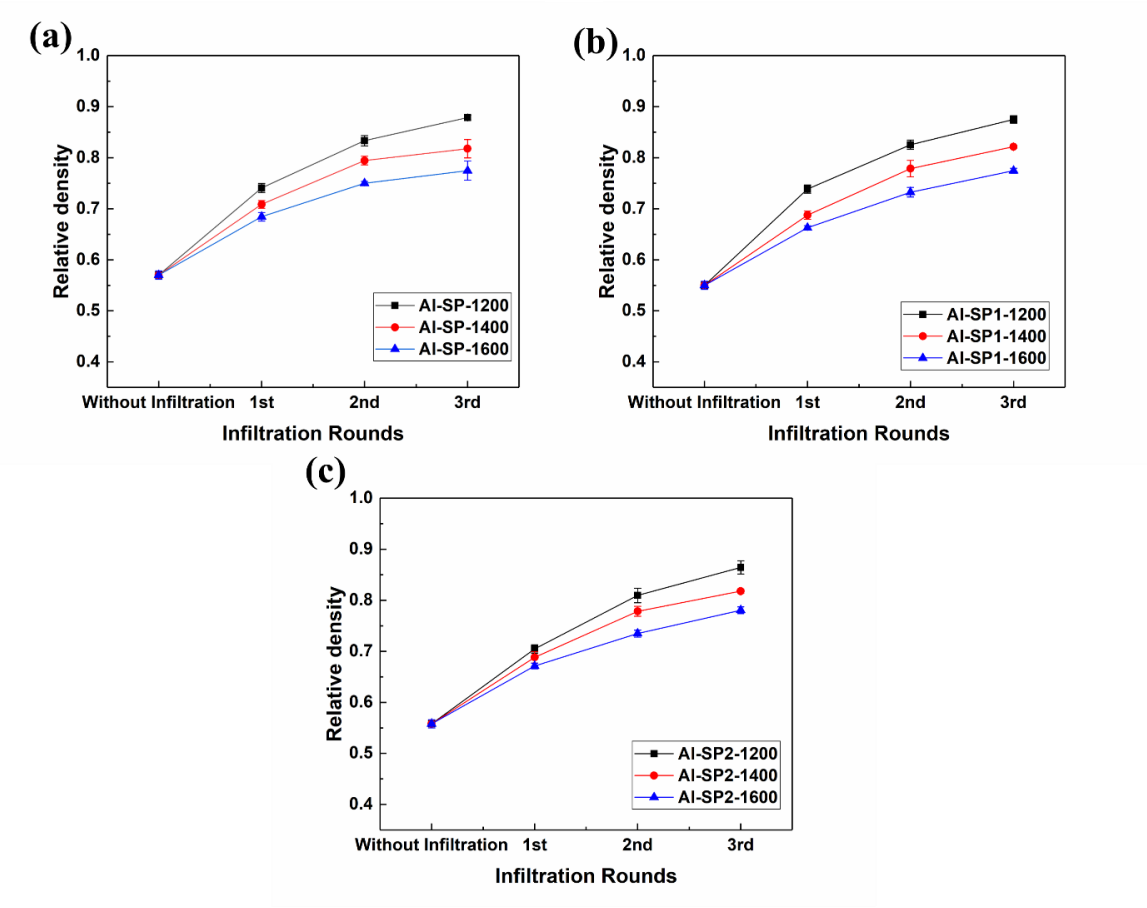


Figure 91. Evolution of the relative density of samples for successive infiltration and pre-sintering temperatures. a): Samples printed with un-sieved spray dried powder Al-SP; b): Samples printed with fine fraction of spray dried powder Al-SP1; c): Samples printed with coarse fraction of spray dried powder Al-SP2

Figure 92 reveals the evolution of pore size distribution with successive infiltrations. Porosity in general and large pores in particular are progressively disappearing whatever the pre-sintering temperature. The effect is more pronounced for the lower pre-sintering temperature thus explaining the density evolution reported previously. The disappearance of the smallest pores (below a few µm) is less obvious. Pore peaks between 1 µm and 10 µm appeared after 1$^{st}$ infiltration (pre-sintered at 1200 °C and 1400 °C) while the large pores were filled with introduced slip and smaller pores generated after thermal treatment. These pores were efficiently eliminated after the sequent infiltration operation.

It is expected that the shape and size of pores influence the infiltration result as a consequence to capillary forces and size of infiltration channels. In binder jetting, the characteristics of the pores are highly related to packing but also to the morphology and the particle size distribution (PSD) of the particles. In general, broader distributions are expected to be highly beneficial to improve packing density but may reduce the size of the inter-connect pores while fine particles

fill the voids between large granules[87, 88]. Coarse particles on the contrary will enlarge the channel size and will be responsible for larger voids.

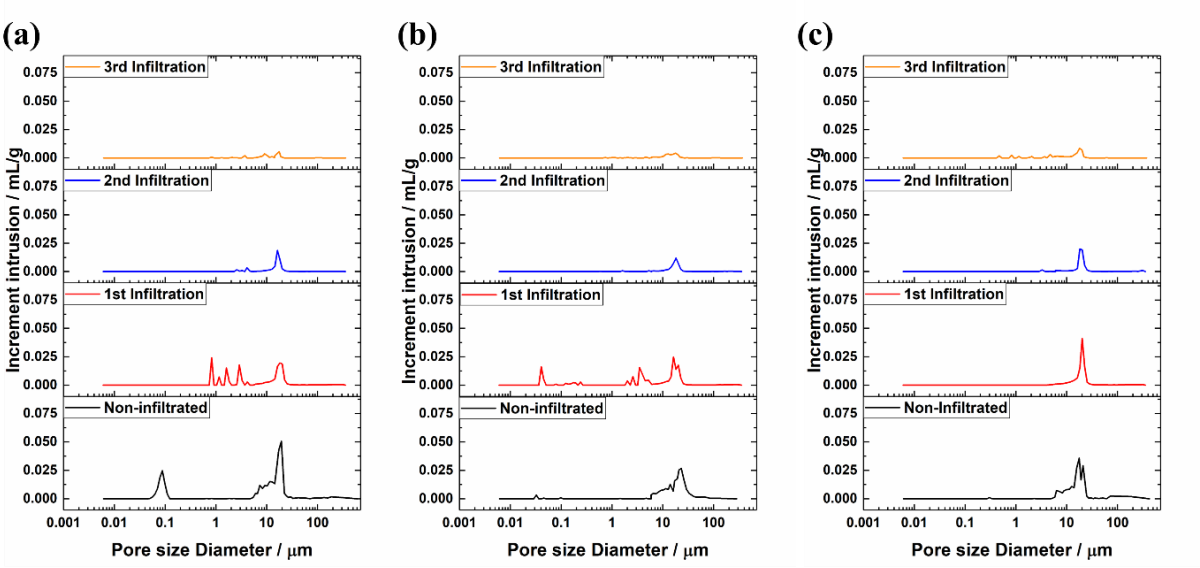


Figure 92. Pore size distribution evolution with multi-rounds infiltration with Al-SP printed parts pre-sintered at different temperatures. a): Al-SP pre-sintered at 1200°C; b): Al-SP pre-sintered at 1400°C; c): Al-SP pre-sintered at 1600°C

Back scattered electron (BSE) images of cross sections were taken at middle of each sample to check the effect of infiltration (Figure 93). Cut samples were fixed with cold resin and polished to observe the smooth surface. The white area indicates the cut sample and grey area are correspond to the resin that is inside the pores of the sample. Picture (a) shows that non-infiltrated sample was highly porous (around 40 % porosity). On the contrary, after the 3$^{rd}$ infiltration the sample looks much denser although big closed pores can still be noticed.

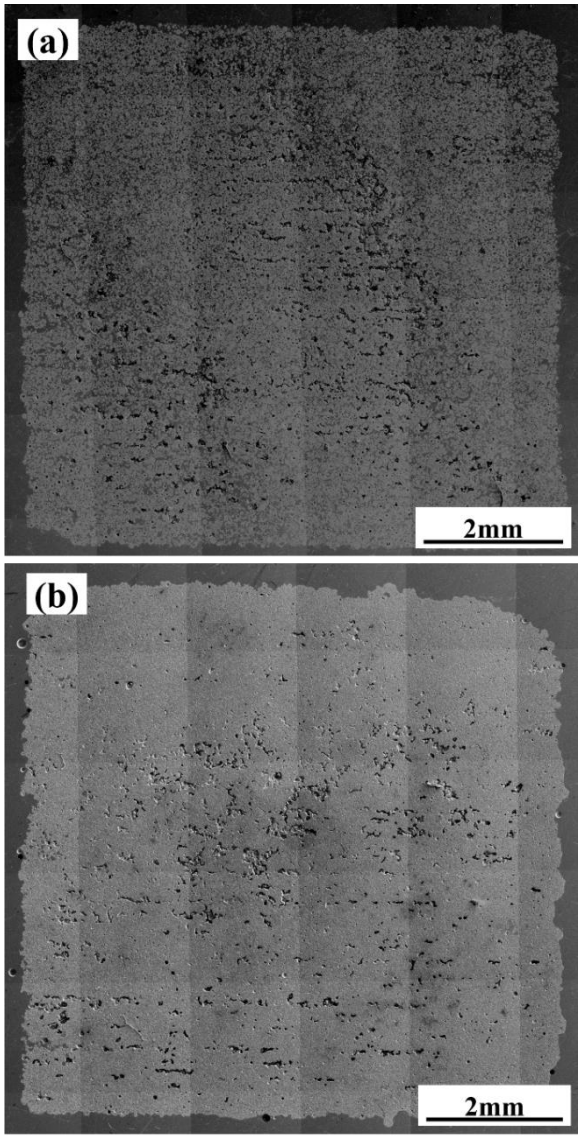


Figure 93. Surface morphology of cross-section of sintered parts printed with powder Al-SP. a): non-infiltrated; b): 3rd infiltrated

As a complement to these 2D images, µ-CT reconstruction of the whole parts after multi-infiltrations are shown in Figure 94 (together with the corresponding calculated porosity) for Al-SP samples. Colors reveal the local amount of porosity in the following order: red > green > blue. In each row, the top image represents the global porosity structure in the whole sample. The difference between non infiltrated sample and the two others is particularly obvious. The images located in the middle show the closed pores only whose volume is less than 0.2 $mm^3$. The differences between samples are much less obvious suggesting that infiltration mostly affects the open porosity. Finally, the bottom images show the pores structure in a smaller volume (1.4 x 1.4 x 1.4 $mm^3$) located at the center of each sample. Again, the difference between the first and second infiltration is perfectly noticeable but it is much more discrete between the second and third one.

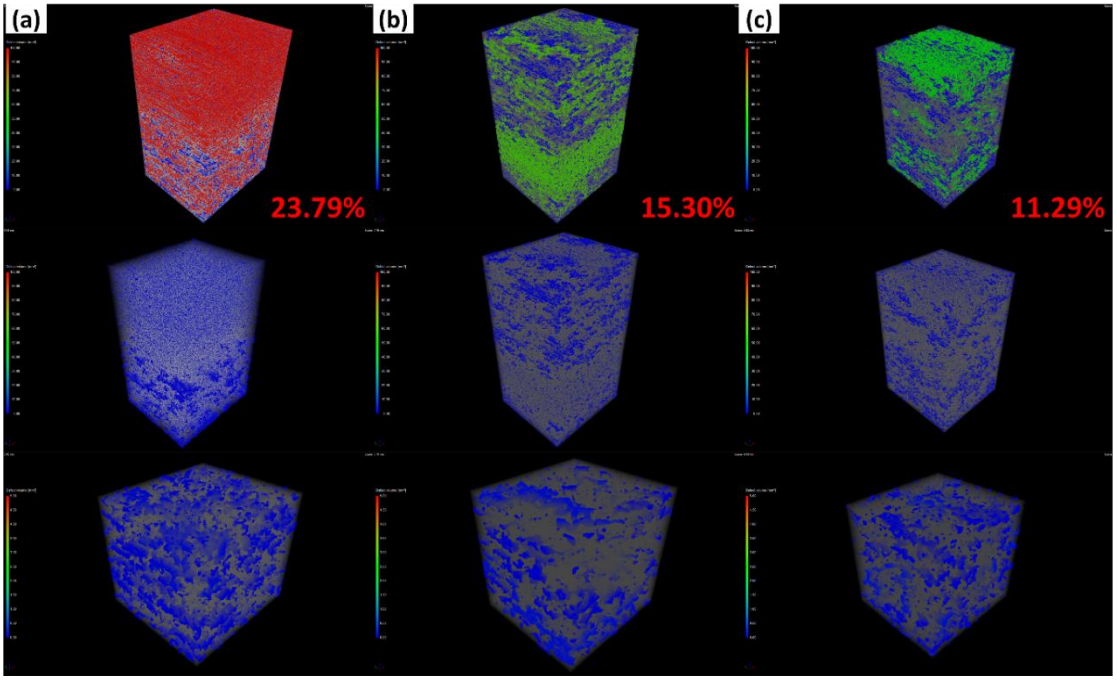


Figure 94. Micro-CT 3D structures of samples after multiple infiltrations. From top to bottom in the column: Pore structure of the whole sample, closed pores structure of whole sample, pores structure in the centre; a): Sample Al-SP-1200-1st; b): Sample Al-SP-1200-2nd; c) Sample Al-SP-1200-3rd

### 3.4.2. Influence of pre-sintering temperature on non-infiltrated samples

The influence of the pre-sintering temperature is particularly interesting: the lower it is, the higher is the final density. The same behaviour is noticed whatever the number of infiltration rounds. There are several possible explanations for this. One may assume that the samples pre-sintered at lower temperature have larger infiltration channels that help the suspension to go through. As the pre-sintered density increases, the internal channels reduce in size thus hindering infiltration. Internal channels within dense specimens are also more prone to absorb the suspension moisture due to the capillary action, making the suspension viscous and severely restricting the infiltration process. Another explanation can be found by considering the presence of the cracks noticed Figure 90. If the pre-sintering is operated at a too high temperature, the granules densify more and shrink a lot on themselves. The differential shrinkage between the denser granules and the surrounding powder deposited by the suspension is large and cracks are formed at the interfaces. The density reduction as noted Figure 91 may be explained by such cracks created in a significant amount. Finally, a slip shell might be formed on the surface of infiltrated samples which may reduce further the infiltration efficiency, although this last hypothesis is less supported by the results. As shown in Figure 91, samples (printed with same powder) pre-sintered at lower temperature showed higher density after infiltration and thermal treatment under same condition. For instance, densities of sample

groups Al-SP1-1200-3$^{rd}$, Al-SP1-1400-3$^{rd}$ and Al-SP1-1600-3$^{rd}$ achieved 87.5±0.7 %, 82.2±0.3 %, and 77.4±0.5 % separately.

Figure 95 shows the pore size distribution variation through changing the pre-sintering temperature (before infiltration). CI in the figure means cumulative mercury intrusion (in mL/g). As expected, porosity of samples pre-sintered at 1200℃ was higher compared to samples pre-sintered at 1400℃ and 1600℃ - Figure 95 (a). According to Figure 95. (b), (c) and (d), CI amount decreases drastically after infiltration treatment which also supports the results in Section 3.4.1 (Chapter 3). Meanwhile, narrower and lower pore size distribution peak resulted from infiltration process and smaller CI amount both implied that pores were infiltrated more effective with lower pre-sintering temperature applied no matter how many infiltrations repeated. Besides, the difference of CI amount of samples pre-sintered at lower temperature between adjacent infiltration rounds was showed always higher which implicated more sufficient infiltration effect since less shrinkage and large pores resulted from lower pre-sintering temperature positively affected the working efficiency as reported in [239, 240] as well.

At 1200°C, there is a large peak centered around 0.1 μm which almost completely disappear for higher pre-sintering temperatures. For coarser pores however, the difference is less obvious between samples. According to Figure 95. (b), (c) and (d), CI amount decreases drastically after infiltration treatment which also supports the results in section 3.4.1 (Chapter 3).

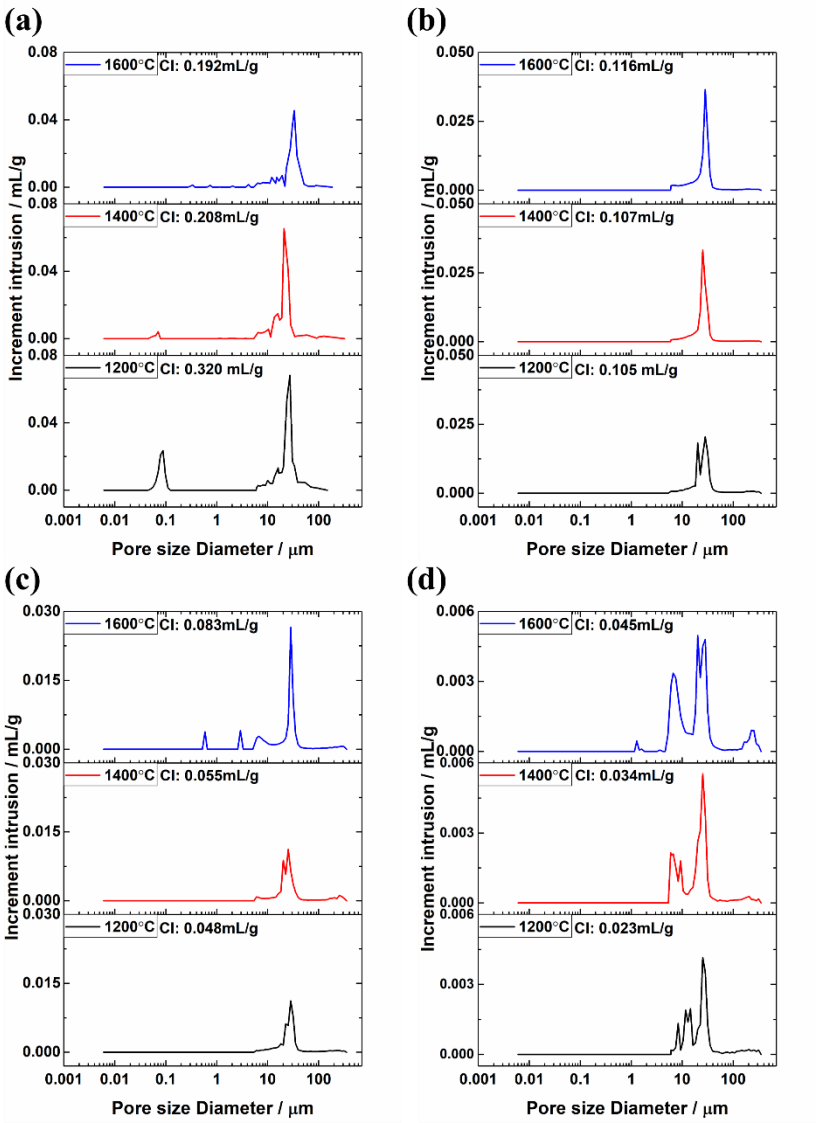


Figure 95. Pore size distribution evolution with different pre-sintering temperatures with Al-SP2 printed samples treated with various infiltration rounds. a): Non-infiltrated; b): After 1st infiltration; c): After 2nd infiltration; d): After 3rd infiltration

### 3.4.3. Influence of granulated powder properties

Figure 96 presents the relative density values of the infiltrated samples after different pre-sintering temperatures from the different powders used for printing. In general, broader PSD of powders as in the case of Al-SP should lead to higher powder bed packing density and sintered density of final printed parts as proved in Chapter 2. In fact, no significant difference is observed according to the density of parts printed by different powders after infiltration under the same condition.

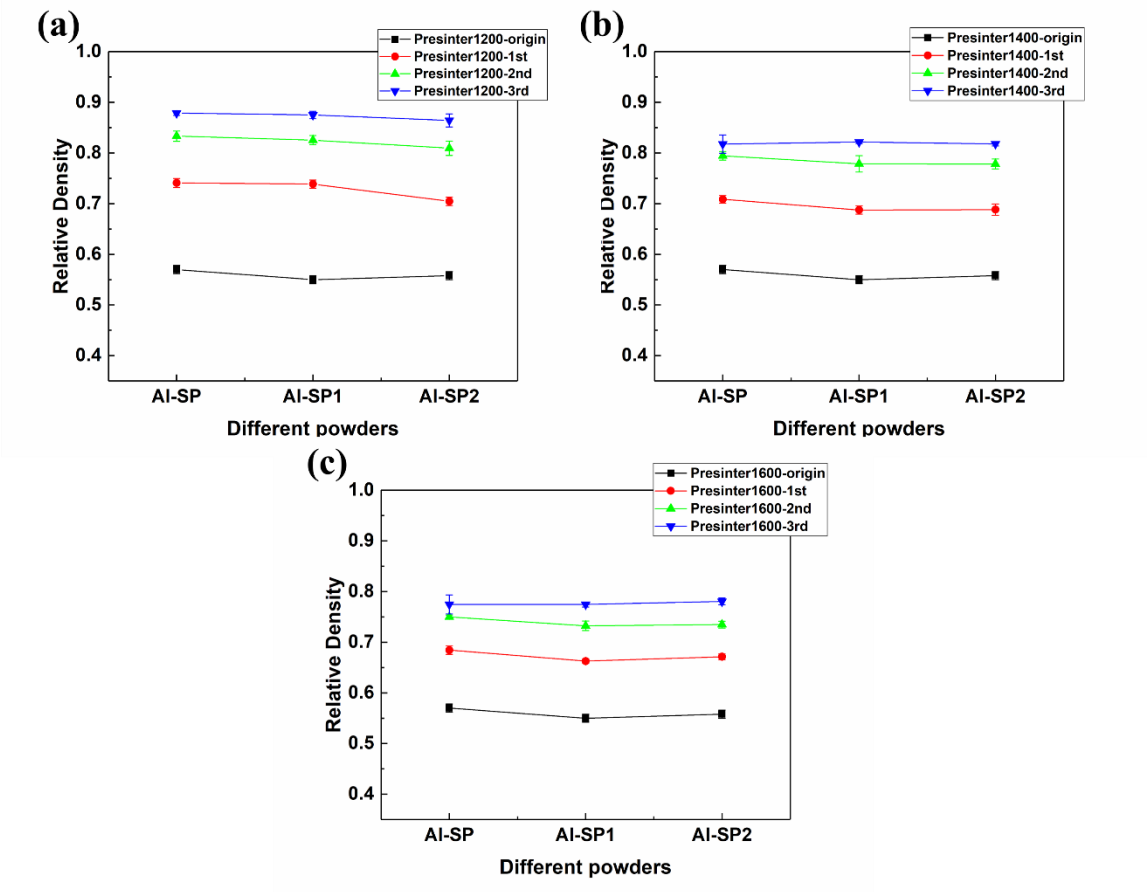


Figure 96. Relative density of samples printed from different powders and treated with multi-infiltration rounds. a): Samples pre-sintered at 1200 °C; b): Samples pre-sintered at 1400°C; c): Samples pre-sintered at 1600°C

### 3.4.4. Influence of suspension solid loading

Enhancing the solid loading of suspension could be an option to further increase the density of final parts. However, strongly increase the solid loading of suspension might inhibit the infiltration process and reduce the dimensional accuracy of infiltrated parts if the suspension accumulates around the objects instead of going inside. To have an insight of the influence of the solid loading, suspensions containing 70 wt% solid loading were prepared. Infiltration was carried out using the same route as depicted in section 2.2 (Chapter 3) and new results were compared with previous ones using 50 wt% solid loading.

As shown in Figure 97, the improvement is very significant and renders the process more effective and less time-consuming by using a higher solid loading suspension. As previously, the samples pre-sintered at 1200°C exhibit the highest sintered density reaching almost 90% of the theoretical density. A very remarkable point here is that the highest average density obtained with the 70 wt% suspension after one single infiltration step is very similar to the one obtained with 3 consecutive infiltrations with the 50 wt% suspension. The highest average

density of parts infiltrated with 70 wt% suspension reached 87.2 % compared with value of parts infiltrated 3 times with 50 wt% suspension achieved 87.9 %. The biggest different of relative density caused by modifying solid loading happened in samples group Al-SP2-1200, which reached 16.6 %. The density differences of groups Al-SP-1200 and Al-SP1-1200 were 13.1 % and 13.2 % respectively. Non-infiltrated samples were all sintered at 1600℃ to have relative density be parallel compared (origin group in Figure 97).

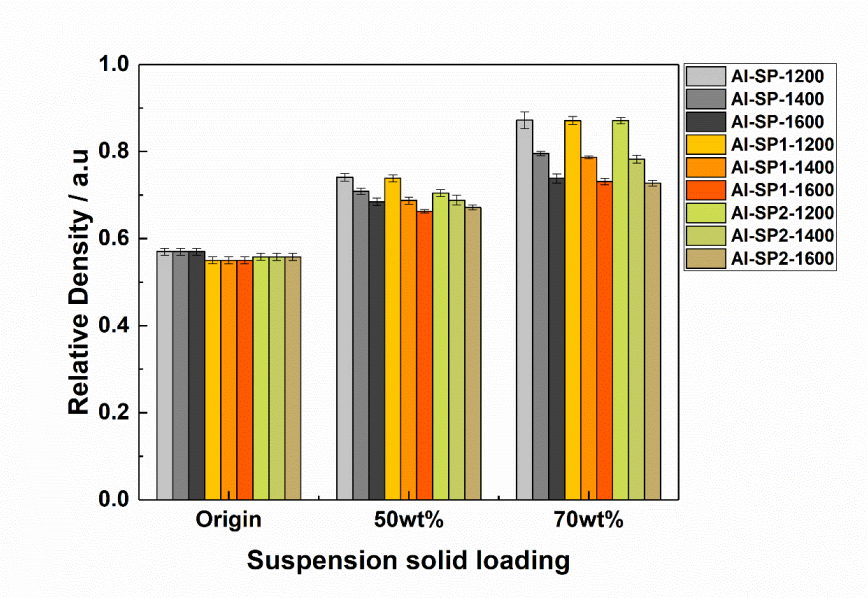


Figure 97. Relative density of different samples infiltrated with suspensions contain different amounts of solid loading

The reached relative density values of samples infiltrated with suspensions containing different solid loading are listed in Table 18. Since results obtained with a 70% solid loading look more promising, it might be a temptation to further increase this solid loading. However, it is expected some issue in doing so. As seen on Figure 98, the 70% suspension is already firmly sticking around the object after infiltration. It is considered that this excess suspension might easily formed a surrounding shell around the object if the solid loading was higher. This will of course prohibit any diffusion of the suspension inside the skeleton body, degrade the infiltration efficiency and might enhance the overall density of the sample.

Table 18. Reached relative density of samples infiltrated with suspensions containing different solid loadings and pre-sintered at different temperatures (infiltrated for 2 hours)

| Powder | Pre-sintering temp./°C | Suspension solid loading / wt% | Average Relative density / % |
|---|---|---|---|
| Al-SP | 1200 | 50 | 74.1±0.9 |
| Al-SP | 1200 | 70 | 87.2±1.8 |
| Al-SP | 1400 | 50 | 70.9±0.8 |
| Al-SP | 1400 | 70 | 79.5±0.5 |
| Al-SP | 1600 | 50 | 68.4±0.8 |
| Al-SP | 1600 | 70 | 73.8±1.0 |
| Al-SP1 | 1200 | 50 | 73.9±0.8 |
| Al-SP1 | 1200 | 70 | 87.1±0.9 |
| Al-SP1 | 1400 | 50 | 68.7±0.8 |
| Al-SP1 | 1400 | 70 | 78.7±0.3 |
| Al-SP1 | 1600 | 50 | 66.3±0.4 |
| Al-SP1 | 1600 | 70 | 73.1±0.8 |
| Al-SP2 | 1200 | 50 | 70.5±0.8 |
| Al-SP2 | 1200 | 70 | 87.1±0.7 |
| Al-SP2 | 1400 | 50 | 68.8±1.1 |
| Al-SP2 | 1400 | 70 | 78.2±0.9 |
| Al-SP2 | 1600 | 50 | 67.1±0.6 |
| Al-SP2 | 1600 | 70 | 72.7±0.6 |

Figure 98. Samples infiltrated with viscous suspension containing 70 wt% solid loading

### 3.4.5. Influence of infiltration duration

Since we noticed that the suspension tends to accumulate in the bottom part of the sample, one may ask if the infiltration duration might affect the infiltration efficiency. Therefore, different infiltration durations (2 hours, 3 hours and 4 hours) were tested for samples of the three groups: Al-SP-1200, Al-SP-1400 and Al-SP-1600. After sintering, the densities were measured as precedingly and the obtained values are plotted in Figure 99.

In each group, the densities are very similar whatever the infiltration duration. Of course, no smaller or longer durations were tested but the absence of trend in the plot suggests that we

may assume that the duration (in a sufficient range) during which the samples are immersed in the suspension has no effect on the final density.

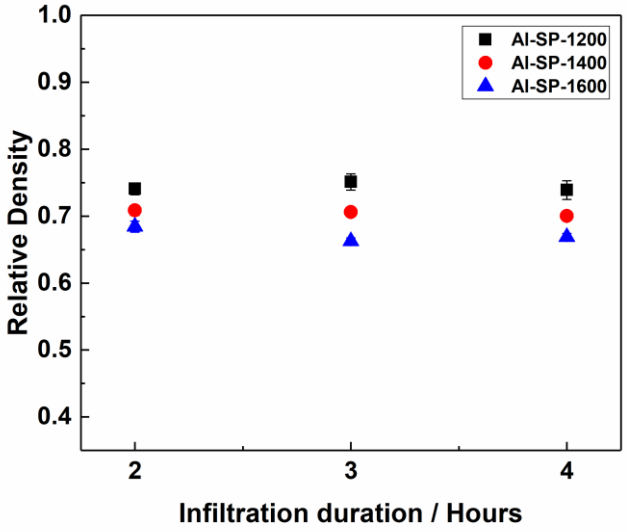


Figure 99. Relative density of different samples infiltrated with different infiltration durations

# 4. Conclusion

In this part, the post-infiltration of porous BJ samples with a ceramic suspension has shown its potential to increase the sintered density. The influence of successive infiltrations was highlighted: the relative density of samples could reach up to 74.1±0.9% (after one infiltration), 83.3±1.0% (after 2 infiltrations) and 87.9±0.5% (after 3 infiltrations) by using a 50 wt% well-dispersed ceramic suspension. These values have to be compared with the sintered density of non-infiltrated samples not exceeding 60% of TD. SEM and micro-CT observations showed that infiltration is mainly dominated by the gravity forcing the particles to settle down at the bottom of the porous bodies. As a consequence, the pore size and density were higher at the top than at the bottom of samples. Improvement of surface roughness was also noticed as a collateral but beneficial effect.

The influence of pre-sintering temperature has been highlighted. Lower pre-sintering temperature led to denser final products probably because it favors larger open pore sizes, helping suspension infiltration. On the contrary, the size of granules used for printing or the infiltration duration exert no influence on the properties of infiltrated parts.

Finally, it has been demonstrated that a higher solid loading reduces the number of successive infiltrations required to get the maximum density. A single infiltration with a 70% solid loading suspension has the exact same effects as three consecutive infiltrations with a 50% solid

loading. It is believed that the possibility to reach densities close to 90% after a single infiltration round may open new opportunities for binder jetting.

# Chapter 3. Post-infiltration to densify porous BJ ceramic parts

# Chapter 4. Hybridization between BJ and laser machining

## 1. Introduction

The aim of this part is to demonstrate the benefit of a laser refinement to improve the quality of printed parts, especially in terms of surface finish and sharpness. As described in previous chapters, conventional BJ is plagued by rough surface finishes. It will be shown that a pulsed laser may offer a nice solution to this old problem. For a better understanding of the present part, Appendix 3 was added to remind some basic information about the laser/ceramic interactions and the use of laser to mill ceramics in details. Reading of the Appendix 3 for the reader not fully familiar with the notions of fluence, absorption, ablation, heat affected zone, is recommended. The results presented hereafter are the subject of the third paper which was written as part of this thesis. The following text is an excerpt from this article.

### 1.1. Laser absorption

Various interactions happen when the laser incidents on the surface of ceramic workpieces: reflection, absorption, scattering and transmission (Figure 100) [253]. Absorption is the most critical one and is related to the interaction of the electromagnetic radiation with the electrons of the materials. The absorption level is depended on wavelength of the laser and absorptivity of the materials [254, 255]. Meanwhile, the absorption degree also can be affected by the orientation of the surface in respect to the beam direction with horizontal plane which should be reached above 80° to achieve the highest efficiency [255].

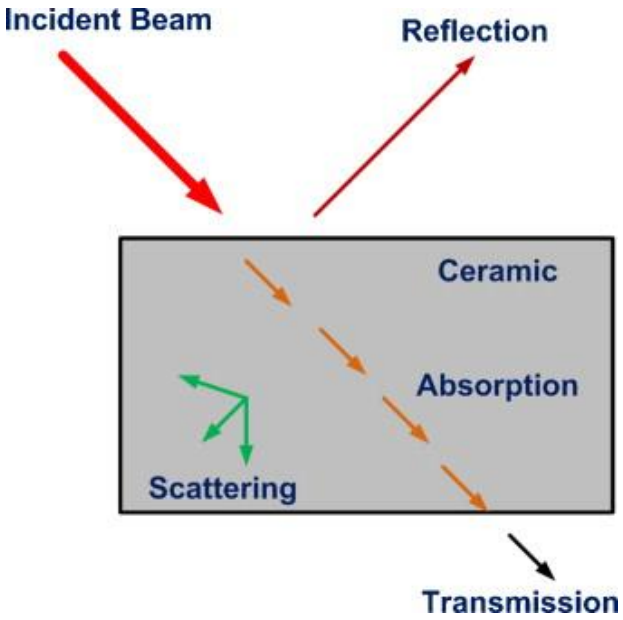


Figure 100. Interaction of a laser beam with a ceramic workpiece from[253]

The absorptivity depends on the used ceramic material itself and wavelength of the laser. Figure 101 shows the absorptivity versus the wavelength from 200 nm to 1200 nm [256]. The value was calculated from the measured transmission and reflection. Clearly the absorptivity of $Al_2O_3$ at visible and infrared region is extremely poor and increases drastically in ultra-violet (UV) range (infrared range: 780 nm – 1 mm; visible range: 400 nm – 780 nm; UV range: 10 nm – 400 nm). Therefore, addition of additives (e.g. graphite[257]) is necessary to significantly improve the laser energy absorptivity of ceramic materials in visible-infrared range due the constraints of the available machine [257, 258].

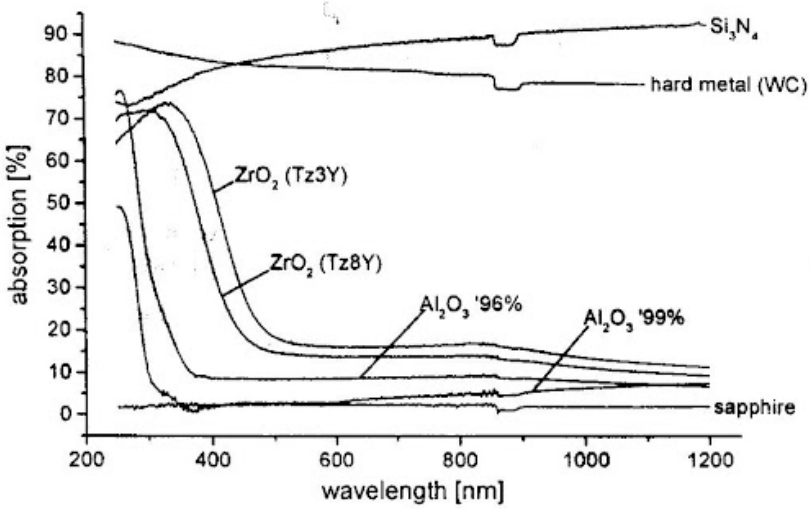


Figure 101. Absorption of different ceramic materials from [256]

Whenever the laser beam hits on ceramic workpieces, various interactions may occur. These interactions can be classified by the temperature reached after energy absorption such as melting, sublimation, vaporization, dissociation, plasma formation and ablation.

## 1.2. Laser treatment of porous ceramics

Limited researches have been performed on laser machining of porous ceramics. The interaction of laser beam incident in the porous structure is more complex than the surface reflection on dense non-machined workpieces with smooth surface. Figure 102 shows the multi-reflection of laser beam inside of a machined cavity or a porous structure where $I_0$ is the incident energy of the laser beam. $I_{a1}$, $I_{a2}$, and $I_{a3}$ are first, second and third absorbed energy respectively, meanwhile, $I_{r1}$, $I_{r2}$, and $I_{r3}$ are the first, second and third reflected energy. In this case, it is obvious that the apparent refractive index of the treated sample is not simply the value of the dense and monolithic material. In general, an accurate estimation of the absorbed energy in a porous body is difficult to assess as it depends on the porous structure which is usually not well known. Also, in porous ceramic parts, heat conduction is much more complex than in monolithic materials.

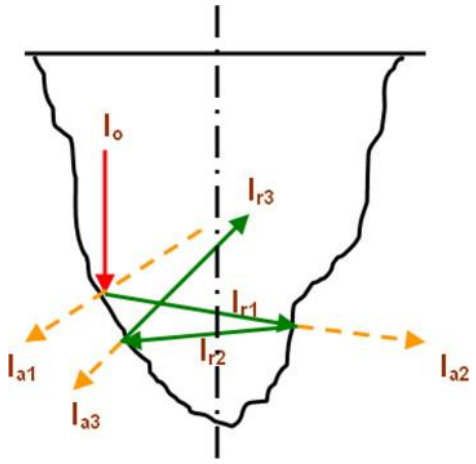


Figure 102. Multi-reflections in the machined cavity or porous substrate from [253]

## 1.3. Motivation

As said in the introduction part of this thesis, the low packing density in conventional binder jetting is responsible for the low density of sintered parts and their roughness. The rough surfaces originate from the granule size (which usually has to be coarse to help flowability) and the lateral diffusion of the binder outside the printed areas. Therefore, it is necessary to improve the finished surfaces of BJ parts by additional technical help. This can be done of course after printing the whole part (using CNC machining for instance) but in this case, the freedom of design is lost. It seems much more appealing to improve the finish surface in situ, e.g., layer after layer (or after a certain number of layers) to keep the free form possibility offered by binder jetting.

As shown in Figure 103, the binder diffusion along lateral direction on the contour of each printed layer aggregates some grains on the surface of the printed parts, thus decreasing the printing accuracy and degrading the roughness. In this work, the possibility of using laser machining to remove the excessive grains that are stuck around the object was considered. As it is non-contact treatment, there are limited risks to destroy the powder beds unlike in-situ CNC machining for instance.

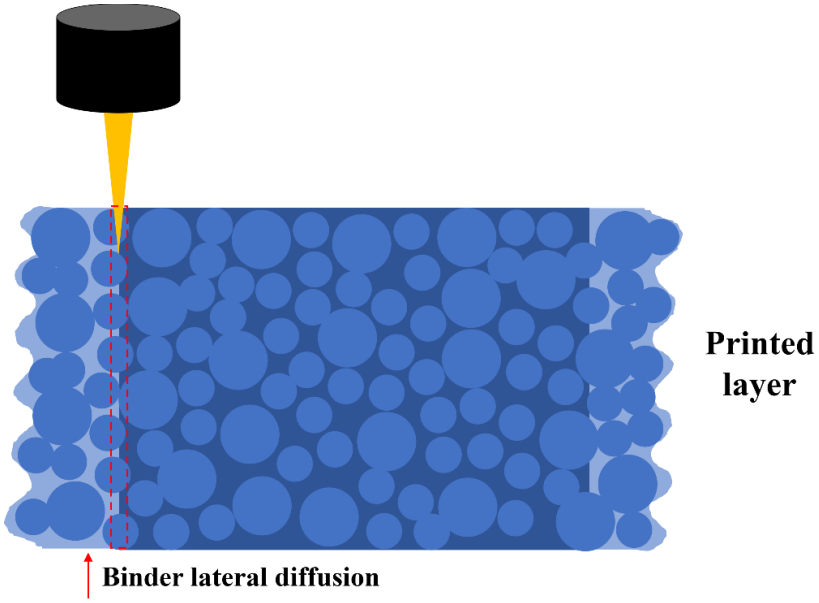


Figure 103. Mechanism of hybridized laser machining on binder jetted layer

The idea is to use laser machining to refine the periphery of each printed layer immediately after binder deposition, thus removing the sticking grains outside the printed areas. By doing so for each printed layers, a significant enhancement of the smoothness and sharpness of the whole fabricated part is expected (Figure 104).

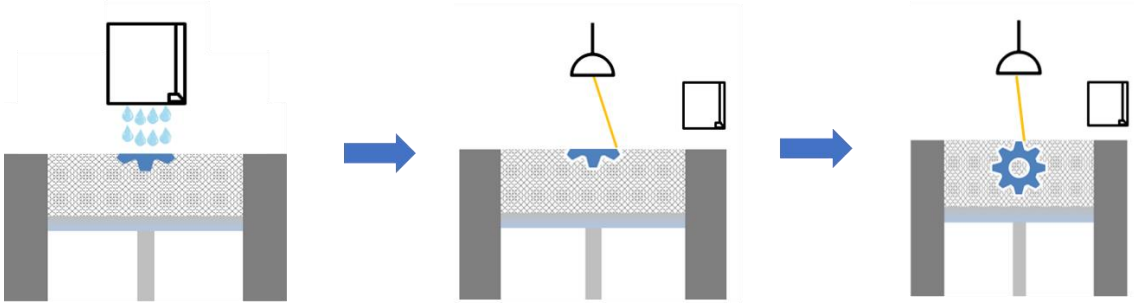

Figure 104. Scheme of the laser machining hybridized with printing process

As shown in the Appendix 3, most of the literature is focused on laser machining of dense ceramics and only a very few papers are dealing with porous ceramic bodies. No relevant paper was found using pulsed lasers to “mill powder beds” or for treating BJ parts. Interaction between laser and powders will be much more complicated due to the higher porosity inside

the powder bed and extremely low strength which are completely different to those of dense ceramics. The thermal behaviour of a porous body is also much more complex than that of a denser object.

This part presents the different experimental studies conducted with the machine in an attempt to increase the resolution and sharpness of alumina printed bodies [259]. Laser parameters were fine-tuned so as to identify the most suitable conditions for powder-bed laser ablation, such as laser power, pulse duration / repetition frequency, scanning speed. Dimension of ablated tracks, roughness and sharpness of lasered parts after sintering were characterized to evaluate the quality of final products and demonstrate the benefit of the approach. The hybrid machine is equipped with a conventional nanosecond fiber laser operating at 1.06 µm. At this wavelength, alumina is transparent. Therefore, in order to make it compatible with the laser, a very small amount of dopant was added to alumina to increase its absorptivity. As it will be shown later, a tiny amount of absorbing dopant is enough to dramatically enhance the optical coupling between the ceramic powder and the laser beam.

# 2. Experimental

## 2.1. Powder preparation

Fine alumina powder (P172LSB, Alteo, France) was selected as the raw materials ($d_{50}$ = 0.4 µm). An aqueous slurry containing 52 wt% of alumina dispersed with 1 wt% (in respect to the weight of powder) of carboxylic acid dispersant (Dolapix CE64, Zschimmer & Schwarz, Germany) was ball milled during 12 hours with alumina media to break agglomerates.

Dopant was added in the slurry after the milling step and homogeneously mixed to introduce dopant in the powders. The volume amount of dopant (vs the volume of ceramics) is calculated to be 0.1 vol%. Meanwhile, Nitric acid (65%, CHEM-LAB, Belgium) was added to adjust the pH of the ceramic suspension at 8.0 [260] to modify the sphericity of granules. Spray drying (Niro, GEA, Germany) was used to produce free-flowing powder as required for powder spreading in printing process. $d_{10}$, $d_{50}$, and $d_{90}$ of obtained granules were 6.1 µm, 28.2 µm, 80.0 µm respectively. Spherical morphology of granules was confirmed by scanning electron microscopy (SEM) (Tescan, Czech Republic) and is shown in Figure 105. Absorptivity of powders was assessed using a UV-Vis spectrum analysis (Lambda 750, PerkinElmer, USA). For comparison purposes, granulated powders not containing dopant were also prepared using the same recipe without performing pH modification.

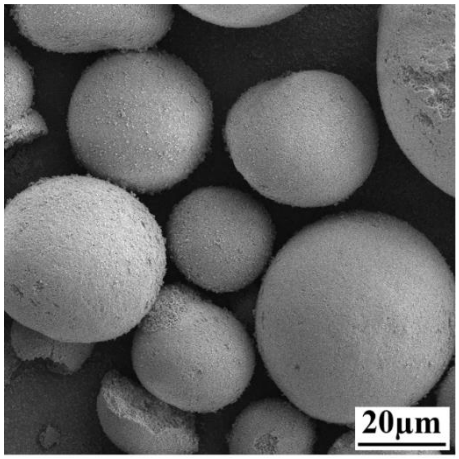


Figure 105. Morphology of spray dried Al0.1C granules

## 2.2. Printing process

Printing process is described in Chapter 2 & 3 conducted in the same customized machine. The same binder was used to print. Layer thickness (LT) and binder saturation (BS) during process were both fixed at 150 µm and 67 %.

## 2.3. Laser machining

Above the manufacturing tank, an "in-situ laser" is mounted together with a scanning head with a marking area covering the whole printed surface. This laser is a fiber source (SPI, redENERGY G4) that can operate in continuous mode or pulsed mode. The rated average output power is 20 W. Maximum pulse energy and peak powder exceed 1 mJ and 10 kW. Pulse duration range varies from 3 to 500 ns at an emission wavelength of 1070 nm. Focal length and marking area of laser scanner (Newson AT800) are 250 mm and 200 mm * 100 mm. The size of laser spot is 60 µm (Table 19).

The refining laser experiments were carried out directly on the fresh powder beds in air under atmospheric pressure.

Table 19. Laser parameters of the G4 pulsed fiber laser

| Parameters | Value |
|---|---|
| Emission wavelength | Approx. 1060 nm |
| Rated average output power | 20 W |
| Focal length | 250 mm |
| Marking area | 200 mm * 100 mm |
| Beam waist | Approx. 60 µm |
| Maximum pulse energy | > 1 mJ |
| Maximum peak power | > 10 kW |
| Pulse duration range | 3 – 500 ns |
| Pulse repetition frequency (PRF) range | 1 – 1000 kHz |

Different combinations of laser parameters (laser power (100%, 90%, 80%, 70%), waveform numbers (5, 10, 15, 20) and scanning speeds (30 mm/s, 50 mm/s, 70 mm/s, 90 mm/s)) were tested after printing of 5 consecutive layers containing dopant or not) (Figure 106). Waveform numbers correspond to variations in the nominal pulse repetition frequency: 32 kHz, 41 kHz, 54 kHz, 76 kHz but also variations in the max pulse energy and duration. The laser settings corresponding to the various waveforms used are summarized in Figure 107 and Table 20.

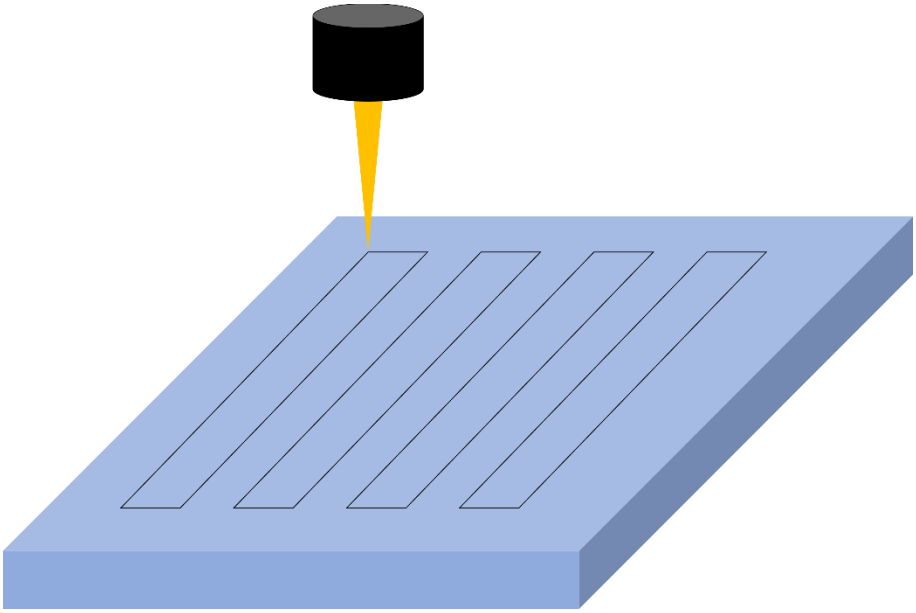

Figure 106. Scheme of conducted laser tracks on printed parts

Table 20. Pulse waveform settings in G4 pulsed fiber laser

| Waveform ID | $PRF_0$/kHz | $PRF_{max}$/kHz | Max. pulse energy $E_{max}$ / mJ | Typ. FWHM pulse duration at $E_{max}$ / ns | Pulse duration at 10 % / ns | Typ. peak power / kW |
|---|---|---|---|---|---|---|
| 0 | 20 | 1000 | 1.00 | 40 | 241 | 14 |
| 5 | 32 | 1000 | 0.63 | 28 | 144 | 14 |
| 10 | 41 | 1000 | 0.49 | 26 | 100 | 14 |
| 15 | 54 | 1000 | 0.37 | 27 | 60 | 13 |
| 20 | 76 | 1000 | 0.26 | 15 | 36 | 13 |

The different tested combinations of parameters are listed in Table 21 hereafter.

Table 21. Settings of applied laser parameters in preliminary ablation tests

| Settings | Power / % | Waveform ID | Frequency / kHz | Scanning speed / mm/s |
|---|---|---|---|---|
| 1 | 100 | 10 | 41 | 50 |
| 2 | 90 | 10 | 41 | 50 |
| 3 | 80 | 10 | 41 | 50 |
| 4 | 70 | 10 | 41 | 50 |
| 5 | 100 | 5 | 32 | 50 |
| 6 | 100 | 10 | 41 | 50 |
| 7 | 100 | 15 | 54 | 50 |
| 8 | 100 | 20 | 76 | 50 |
| 9 | 100 | 10 | 41 | 30 |
| 10 | 100 | 10 | 41 | 50 |
| 11 | 100 | 10 | 41 | 70 |
| 12 | 100 | 10 | 41 | 90 |

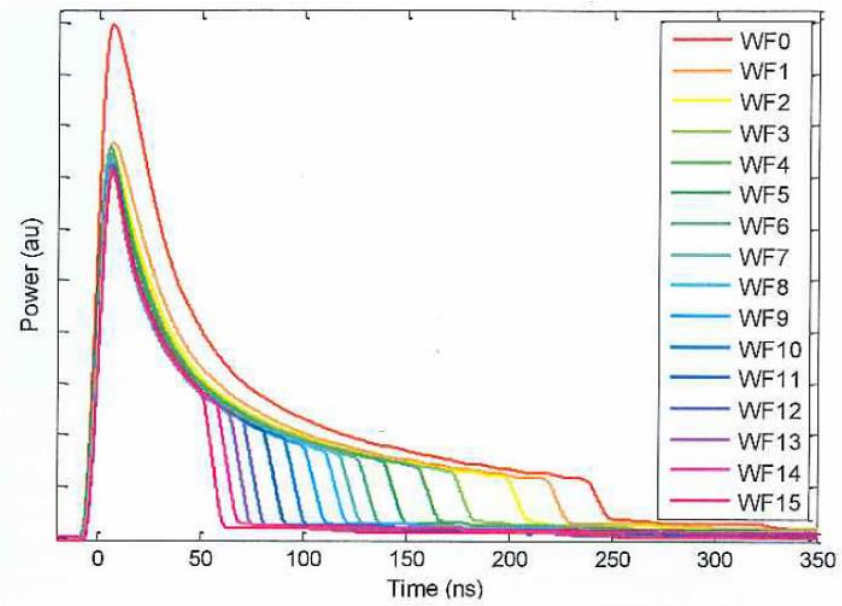


Figure 107. Pulse shapes for waveform 0 to 15 at respective $PRF_0$ from SPI lasers specifications

The ablation results (e.g., the tracks created by the laser in the powder) were analyzed with a 3D scanner (VR-3200, Keyence, Japan). 5 vertical lines perpendicular to the laser track were used to have an average profile of the track, the surface was calibrated to be perfectly horizontal.

After assessing the effect of different laser parameters, optimal settings were chosen to conduct printing/laser machining hybrid process in a simple case (Figure 108) but layer after layer. Small cuboids were printed and refined but the laser trajectory was not exactly following the contours (Figure 108). By doing so, it is possible to compare sides which have been laser

refined or not. 4 different waveforms (5, 10, 15 ,20; corresponding to pulse repetition frequency: 32 kHz, 41 kHz, 54 kHz, 76 kHz) values were chosen for testing with the same laser power (100%) and scanning speed (50 mm/s) as shown in Table 22.

Table 22. Settings of laser parameters applied in hybridized laser machining process

| Settings | Power / % | Frequency / kHz | Scanning speed / mm/s |
|---|---|---|---|
| 1 | 100 | 32 | 50 |
| 2 | 100 | 41 | 50 |
| 3 | 100 | 54 | 50 |
| 4 | 100 | 76 | 50 |

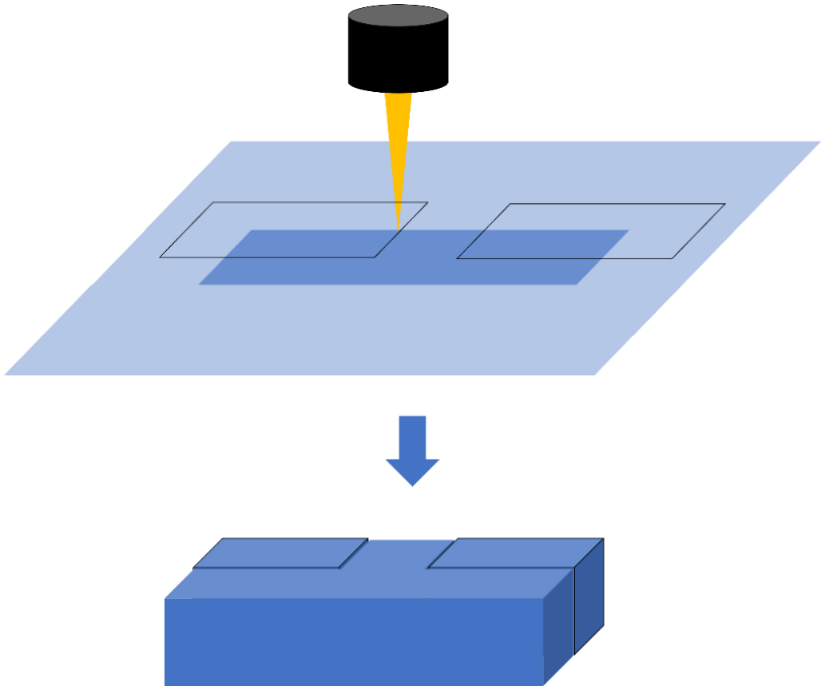

Figure 108. Scheme of laser machining hybridized with printing process

## 2.4. Sintering and characterization

Hybrid printed cuboids (e.g., with laser cutting) were first debinded at 500℃ (heating rate: 3℃/min, dwelling time: 4 hours) and then sintered at 1600 ℃ (heating rate: 5℃/min, dwelling time: 6 hours) in air which is the recommended temperature for the alumina powder (see Chapter 2). The sintered samples were further characterized in terms of surface roughness (VKX-250, Keyence, Japan) to check the effect of the laser refining. Roughness was calculated on 6mm track length with no cutoff applied along the printing direction. Furthermore, the sharpness and dimensional accuracy of lasered and non-lasered part were also compared by assessing the angles and curvatures of the cubes using the 3D scanner. Each point was the average value from 5 measured groups data at each condition.

# 3. Results and discussion

## 3.1. Preliminary laser tests with alumina powders

### 3.1.1. Effect of dopant content on laser/matter interaction and optical coupling with powder beds

The absorptivity of alumina powder is dramatically enhanced by adding a small amount of dopant. For 0.1vol% of added dopant, the absorptivity reaches 55.2% when it was only 5.2% for the pure alumina powder (Figure 109).

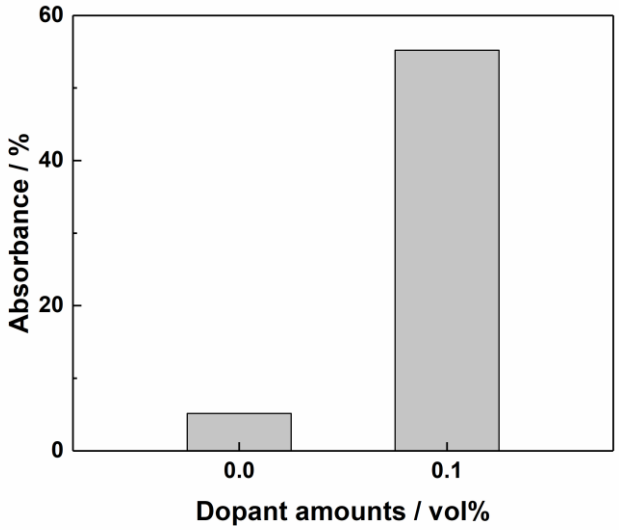


Figure 109. Absorptivity of powders with 0.1 vol% and without dopant content

The results of laser ablation on the 5 printed layers (depth = 750µm) on different powder beds (Al and Al0.1C powders) are shown in Figure 110. Before commenting these results, it must be said that a 10 minutes-drying after printing was considered prior laser ablation. Figure 110 (a) and (b) compare the laser tracks on beds without dopant and containing dopant respectively. Laser tracks on Al0.1C powder bed are much finer and precise with much less fluctuation or inaccuracy. On the contrary, the laser tracks on the Al powder bed appear discontinuous with a limited amount of powder removed. They also look much wider at the locations where the grains have been removed. This is even more obvious at a higher magnification. Laser tracks shown in Figure 110 (c) reveal the poor and very inefficient interaction between the powder and the laser. Penetration depth is very shallow and sometimes cannot be distinguished from the surrounding suggesting that maybe nothing happened. On the other hand, laser track on Al0.1C powder bed was well-performed, clean and accurate (Figure 110 (d)). Changing to the side view (Figure 110 (e), (f)), the influence of absorptivity becomes more obvious. Penetration was very deep with the Al0.1C and almost inexistent with the Al powder bed. Despite the best

results obtained in the presence of dopant, it should nevertheless be noticed that the ablation depth was not perfectly continuously neither (Figure 110 (f)). This may be due to the non-homogeneous pore distribution that caused scattering and heterogeneous energy absorption along the track.

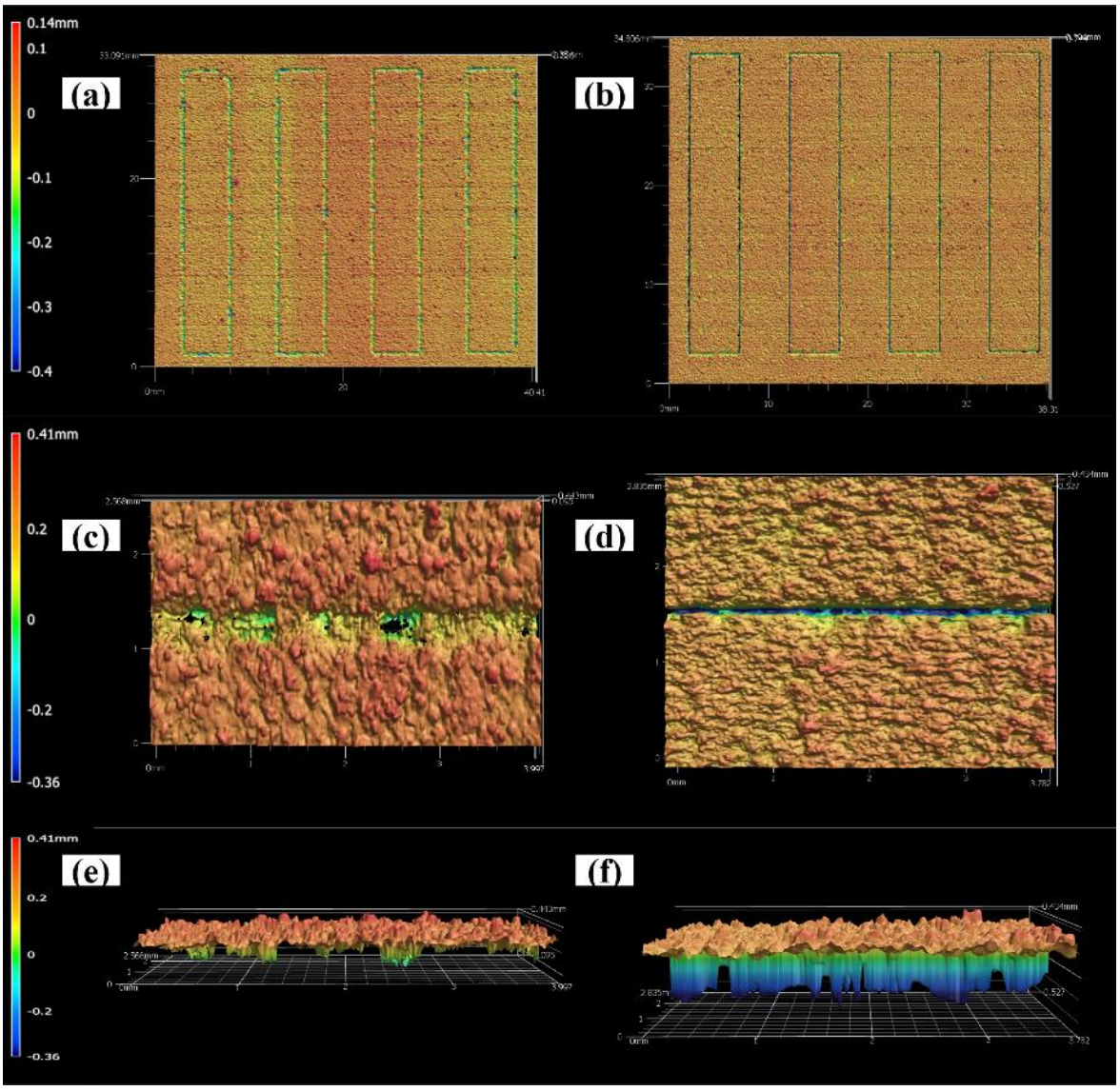


Figure 110. Topography images of laser tracks on Al powder bed. (a), (c) and (e); on Al0.1C powder bed: (b), (d) and (f); a): Overview of profiles of laser tracks at laser parameters with different scanning speed: power: 100%, WF: 0, Frequency: 10 kHz; b): Overview of profiles of laser tracks at laser parameters with different scanning speed: power: 100%, WF: 10, Frequency: 41 kHz; c): Top view of profile of laser track at laser parameters: power: 100%, WF: 0, Frequency: 10 kHz, Scanning speed: 50mm/s; d): Top view of profile of laser track at laser parameters: power: 100%, WF: 10, Frequency: 41 kHz, Scanning speed: 50mm/s; e): Side view of profile of laser at laser parameters: power: 100%, WF: 0, Frequency: 10 kHz, Scanning speed: 50mm/s; f): Side view of profile of laser track at laser parameters: power: 100%, WF: 10, Frequency: 41 kHz, Scanning speed: 50mm/s

### 3.1.2. Effect of dopant content on layer by layer in situ laser operation

The addition of dopant content strongly helps to improve the laser / powder bed interactions. But the tests were carried out after letting the binder dried for some time. In a real hybridized process, the laser should operate immediately after printing. Thus, the question of the influence of the liquid binder on the laser efficiency is legitimate. To answer this question, tests similar to the ones described previously were performed on different powders, right after printing, e.g., layer after layer with (almost) no drying in between. Optical images of laser operated on different powder beds to cut printed layers are shown in Figure 111.

It is noticed that the interaction between the laser and the powder beds that do not contain dopant becomes this time completely inexistent (or so limited that it cannot be detected anymore) – Figure 111 (a). The presence of wet binder in the porosity obviously exerts a very negative influence on the absorptivity maybe by changing the apparent refractive index that favours reflection of the beam instead of its absorption. The presence of water (which is the main constituent of the binder) may also act as a heat sink, reducing some necessary thermal effects to cut the powder bed with the laser. On the contrary, in the presence of dopant, no such deleterious effect of the binder is noticed. The absorptivity remains high enough for an efficient cutting of the powder bed (Figure 111 (b)).

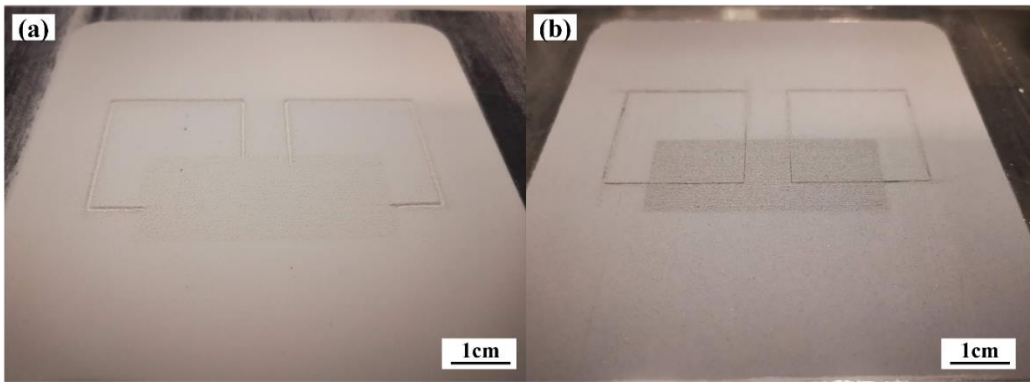


Figure 111. Optical images of laser effects on different powder beds. a): Al powder bed; b): Al0.1C powder bed with laser parameters: Powder: 100%, WF: 5, Frequency: 32 kHz, Scanning speed: 50mm/s

## 3.2. Hypothesis about the interaction mechanism

According to Eq.17, the laser fluence during our test can be easily calculated. By considering the range of tested values, the fluence is comprised between 4.7 J/cm$^2$ to 11.1 J/cm$^2$. According to Florian et al. [261], the ablation threshold for pure alumina is around 30 J/cm$^2$ which is much higher than the achieved fluence in our tests. Of course, a powder bed is not fully dense alumina and it is therefore not completely surprising that it can be laser machined at much lower fluences. However, the granules themselves are not even dense. Every granule is a complex

and heterogeneous medium composed with alumina, dopant, organic and water contents (pores are important as well). Since dopant is mandatory to couple the laser with the powder bed, it also has the highest absorption coefficient of any materials inside the granule. Therefore, it is expected that dopant will first "react" when a granule is hit by the laser beam. As dopant absorbs preferentially the laser energy, the surrounded material is progressively heated up through thermal conduction and finally, melt or even vaporizes in the case of organic phases. The gases generated during vaporization expand rapidly and create a local recoil pressure which produces the granule explosion. This disruption will finally affect the powder bed itself. It cannot be excluded that dopant is vaporized during the laser treatment (and even a limited amount of alumina) but the final result would be the same as rapidly expanding gases would be generated as well. Once a granule has been impacted and destroyed, the adjacent granules are likely to be ejected as well, which resulting in a local cavity. By moving the laser on the powder bed, a succession of such cavities will create ablated/disrupted tracks as those shown Figure 112.

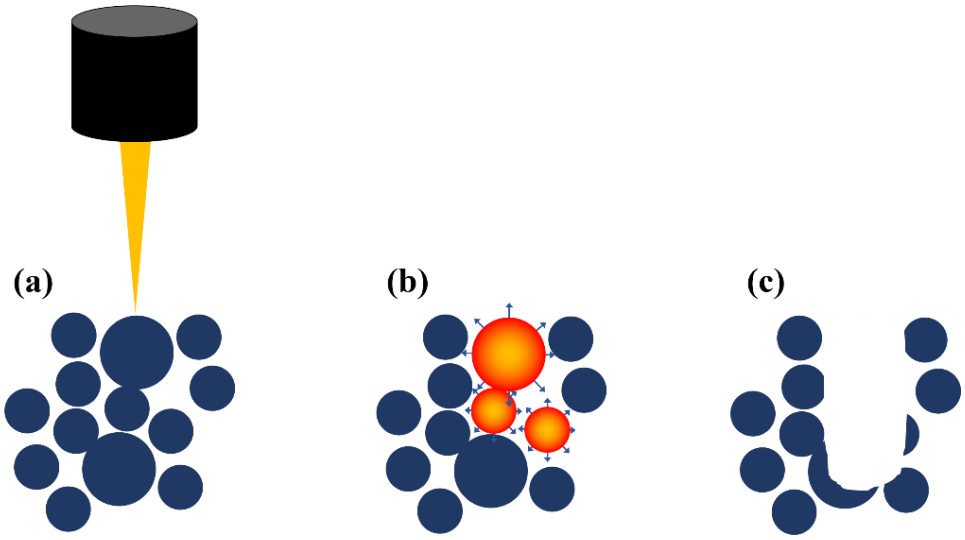


Figure 112. Hypothesized mechanism of reactions inside of powder bed (with dopant contents) during ablation

## 3.3. Influence of laser settings on laser ablation

### 3.3.1. Laser ablation tracks

The influence of laser parameters was studied by creating different laser tracks just on Al0.1C powder bed. For each experiment, tracks were studied by combining optical and 3D topography images. Figure 113 (a) and (c) are examples of such laser tracks under a given set of laser parameters (power: 100%, WF: 10, frequency: 41 kHz and scanning speed: 50 mm/s). Figure 113 (b) is a cross section of the laser track along the vertical direction. The profile of the cross section is triangular in shape which may indicate that more materials were removed from the centre since the laser energy follows Gaussian distribution. The possibility of a reconstruction

artifact by the scanner cannot be completely ruled out. Furthermore, there was no evidence of powders/dusts stacking along the sides of the laser tracks after the treatments (and more generally no visible heat affected zone was noticed).

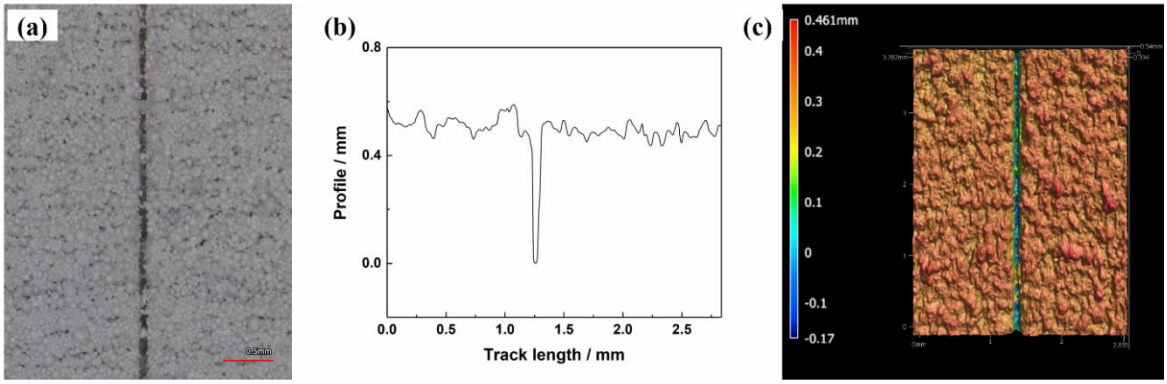


Figure 113. Laser track images and profile of vertical line scanning with laser parameter: Power: 100%, WF: 10, Frequency: 41 kHz, Scanning speed: 50 mm/s. a): Optical image of the laser track; b): a profile of the laser track; c): Topography image of the laser track

The laser track dimension was remarkably thin (yet larger than the laser spot size, e.g., 60 µm) and deep because of high value of laser energy. Changing the laser parameters also led to non-negligible width and depth variations. The trends are shown Figure 114 for different laser power, waveform/frequency and scanning speeds.

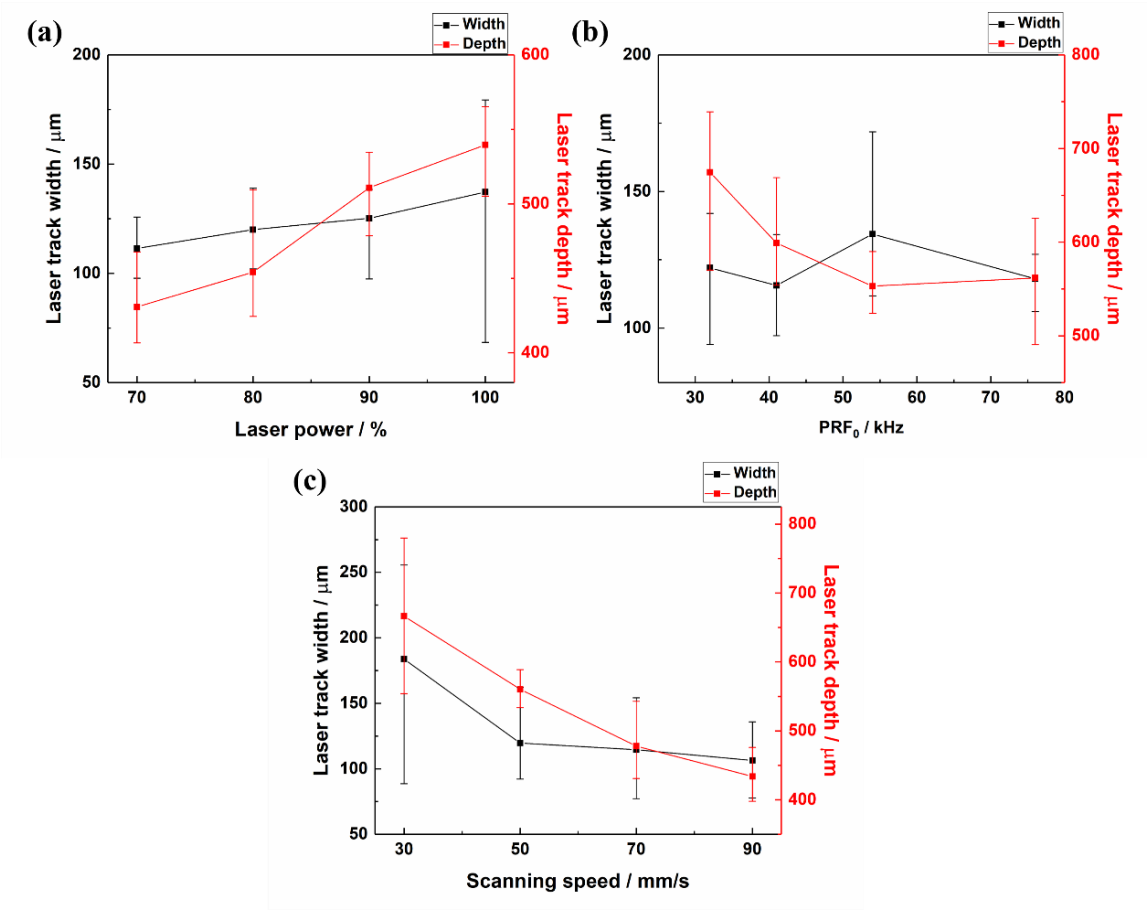


Figure 114. Width and depth evolution of different laser parameters on Al0.1C powder bed. a): Different laser power with WF:10, Frequency: 41 kHz, scanning speed: 50 mm/s; b): Different WF with Power: 100%, Scanning speed: 50 mm/s; c): Different scanning speed with power: 100%, WF:10, Frequency: 41 kHz

Laser fluence should be evaluated to investigate the influence of different laser parameters on ablation behaviour. $F_0$ is the peak fluence which could be calculated by Eq.17 [262]:

$$F_0 = \frac{2P}{\pi {\omega_0}^2 f} = \frac{2E}{\pi {\omega_0}^2} \tag{17}$$

where P is the mean power, E is the laser energy and f is the repetition rate.

Increasing laser power definitely results in higher energy densities at the contact point. Profile depth are deeper in this case while the width of the kerfs also become larger indicating a more pronounced disruption of granules and powder bed as shown in Figure 114 (a). On the contrary, extremely low laser energy is not sufficient to produce ablation and ejection of materials. One might think that there should be also a high-limit to the laser fluence. An excessive laser energy might cause intensive binder degradation producing large recoil pressure, thermal shock, tensile stress or even cracks formation. Meanwhile, excessive materials ablated may stack on the brims of the track which should also influence the process accuracy and resolution [259, 263, 264].

From Figure 114 (b), laser depth and width both decrease firstly until reaching 54 kHz and then slightly increase again at 76 kHz. This strange behaviour can be explained by a competition between frequency and pulse energy whose effects are opposite. Any decrease of the laser frequency will increase the single pulse energy as expressed by Eq.17 (as shown in Table 20 as well). Consequently, the ablated depth increases linearly because of higher energy [264]. On the contrary, higher frequency increases the number of pulses which causes an accumulation of deposited energy per unit area. Thus, there will be a competition between these two effects which is revealed by the inflexion point at 54 kHz.

Increasing the scanning speed decreases the width and depth of individual tracks as shown in Figure 114 (c). As explained in Eq 18, at a given frequency the number of pulses per unit area is determined by the scanning speed. Lowering the scanning speed will create more pulses in a unit area with a denser pulses overlapping [265]:

$$Overlapping = 1 - \frac{v_{ls}}{2f\omega_0} \tag{18}$$

Therefore, at lower scanning speed the energy accumulates more and consequently, ablation depth and ablation width are deeper and broader (Figure 114 c). It should be noted that an extremely slow scanning speed might cause severe ablation with potentially molten materials which of course, would negatively influence the process [263].

As shown in Figure 114, the error bars at each point show a significant scatter which is most likely due to heterogeneous structure of the powder bed. This requires however an explanation of the methodology used to determine the width and depth of each laser track. As shown in Figure 115, the red line is the horizontal zero plane of the powder beds assessed by the 3D scanner software. The two crossing points (orange stars) between the profile and the red line serve to define the width of the laser track. The distance between the red line and the lowest point of the profile (red star) is regarded as the depth of the laser track.

However, the depth and especially width of different laser tracks obtained with the same laser parameters vary significantly. It is assumed that during the laser treatment, some of the granules adjacent to the hit point may fall down into the laser track or even are ejected out as illustrated in Figure 115 (c). This random phenomenon may explain why the plots on Figure 114 are so scattered.

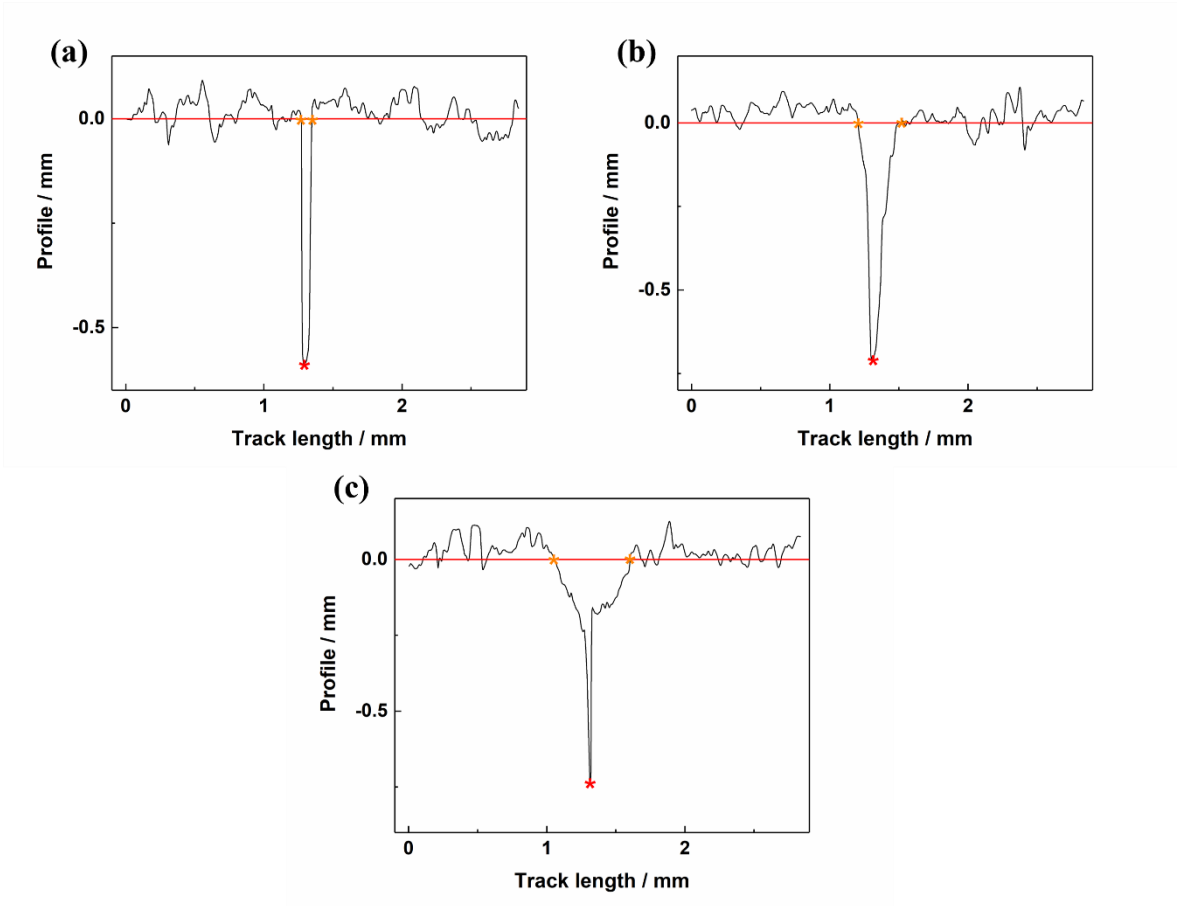


Figure 115. Profile of laser tracks comparison of different scanning line (A and B) under parameters. a): laser power: 100%, $PRF_0$: 41 kHz, scanning speed: 50 mm/s; b): laser power: 100%, $PRF_0$: 41 kHz, scanning speed: 30 mm/s; a): laser power: 100%, $PRF_0$: 32 kHz, scanning speed: 50 mm/s

### 3.4. Laser ablation hybridized with printing process

After optimizing the laser parameters (laser power, waveform number / $PRF_0$, scanning speed), a few suitable settings were selected to perform laser refining on each layer directly after printing (the criteria of selection were qualitative: homogeneous tracks, sharp and deep engraving, limited disruption of the surrounding bed). According to evaluation of kerf width and depth under different laser parameters in section 3.3.1 (Chapter 4), laser power at 100% was kept fixed to ensure reproducible laser tracks. A scanning speed of 50 mm/s was chosen as well as it promotes a high ablation depth combined with a limited width scattering. However, since the effects of laser frequency and pulse energy were not easily handled, these two were chosen as variables (pulse repetition frequency: 32 kHz, 41 kHz, 54 kHz, 76 kHz). Finally, 4 sets of laser parameters were defined with different waveform number / $PRF_0$ as shown in Table 23. For these tests, the idea was just to investigate the benefit of laser refining on the simple shape shown in Figure 116. For this first attempt, the effect of the laser is similar to a simple cut of the printed body except that cutting is done layer after layer and not after printing completion.

Table 23. Chosen laser parameter settings to conduct laser ablation hybridized with printing process

| Treated samples | Laser power / % | Scanning speed / mm/s | Frequency / kHz |
|---|---|---|---|
| A | 100 | 50 | 32 |
| B | | | 41 |
| C | | | 54 |
| D | | | 76 |

For settings A, B, C, parts could be easily separated after laser machining as illustrated in figure 18. However, for the D set (the one with $PRF_0$ = 76 kHz / waveform 20), there were some connections between different pieces of the parts showing an improper cutting. This is because of the binder lateral diffusion and the subsequent laser refining did not ablate the region completely due to the lower resulted energy.

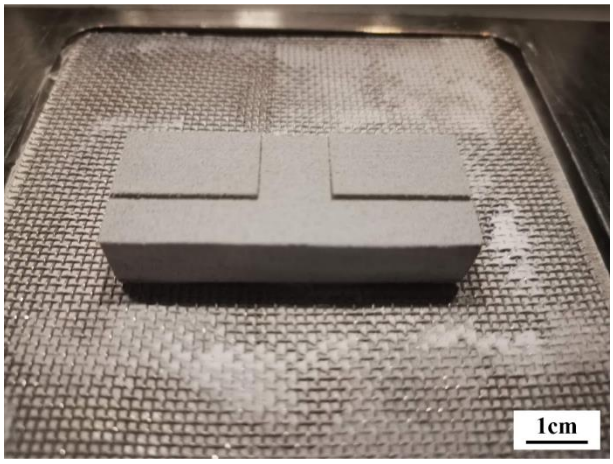


Figure 116. Laser cut cubes under laser parameter: power: 100%, WF: 10, Frequency: 41 kHz, Scanning speed: 50 mm/s

### 3.4.1. Morphology of treated surfaces

SEM images shown in Figure 117 illustrate the difference between non-lasered and lasered (ie. cut) surfaces. It can be noticed that the granules themselves are well cut by the laser and no obvious melting nor strange phases resulting from the laser before sintering was observed. Contrarily to the initial expectations, the granules do not explode completely during the treatment. This can be well noticed on Figure 117 (c) showing the connection between a laser refined surface and a pure-printed one. On the edge, perfectly cut granules can be seen. Lasered surface shown in Figure 117 (b) may suggest that some dust of powder is redepositing at some places in the layer tracks.

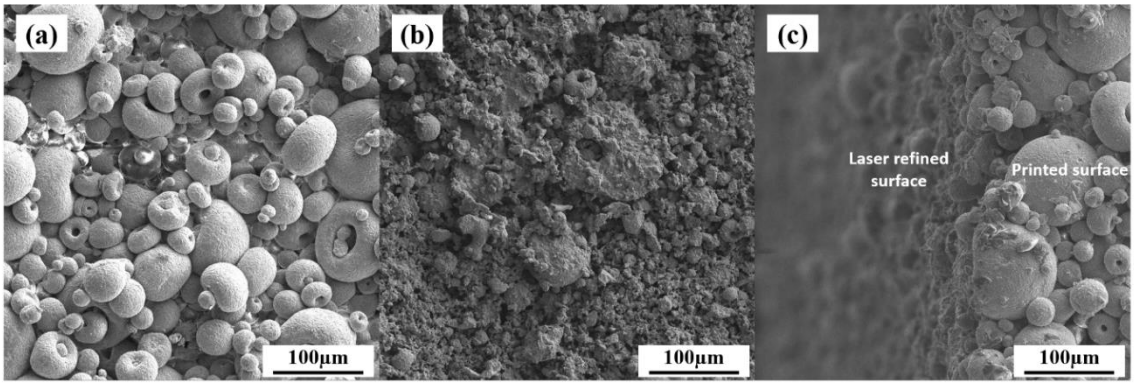


Figure 117. Morphology of printed-lasered-sintered samples. a): printed-sintered surface; b): printed-lasered-sintered surface (laser power 100%, $PRF_0$ = 41 kHz, scanning speed 50 mm/s); c): connecting zone of lasered surface and non-lasered surface

Figure 118 shows the morphological details of treated samples at different frequencies $PRF_0$ (32 kHz, 41 kHz, 54 kHz, 76 kHz) and various magnifications. As explained in section 3.3.1 (Chapter 4), lower pulse frequency increases the incident single pulse laser energy which has a direct influence on the laser machining efficiency. It turns out indeed that the powder bed was ablated more completely with higher incident laser fluence caused by the lower frequency i.e., at 32 kHz. From the figure sequences a-d-g-j and b-e-h-k in Figure 118, the original shape of granules tends to show up progressively with the increase of the repetition frequency. A closer look on the ablated surfaces reveals a dusty like aspect suggesting that some of the ablated materials redeposit on the machined surface.

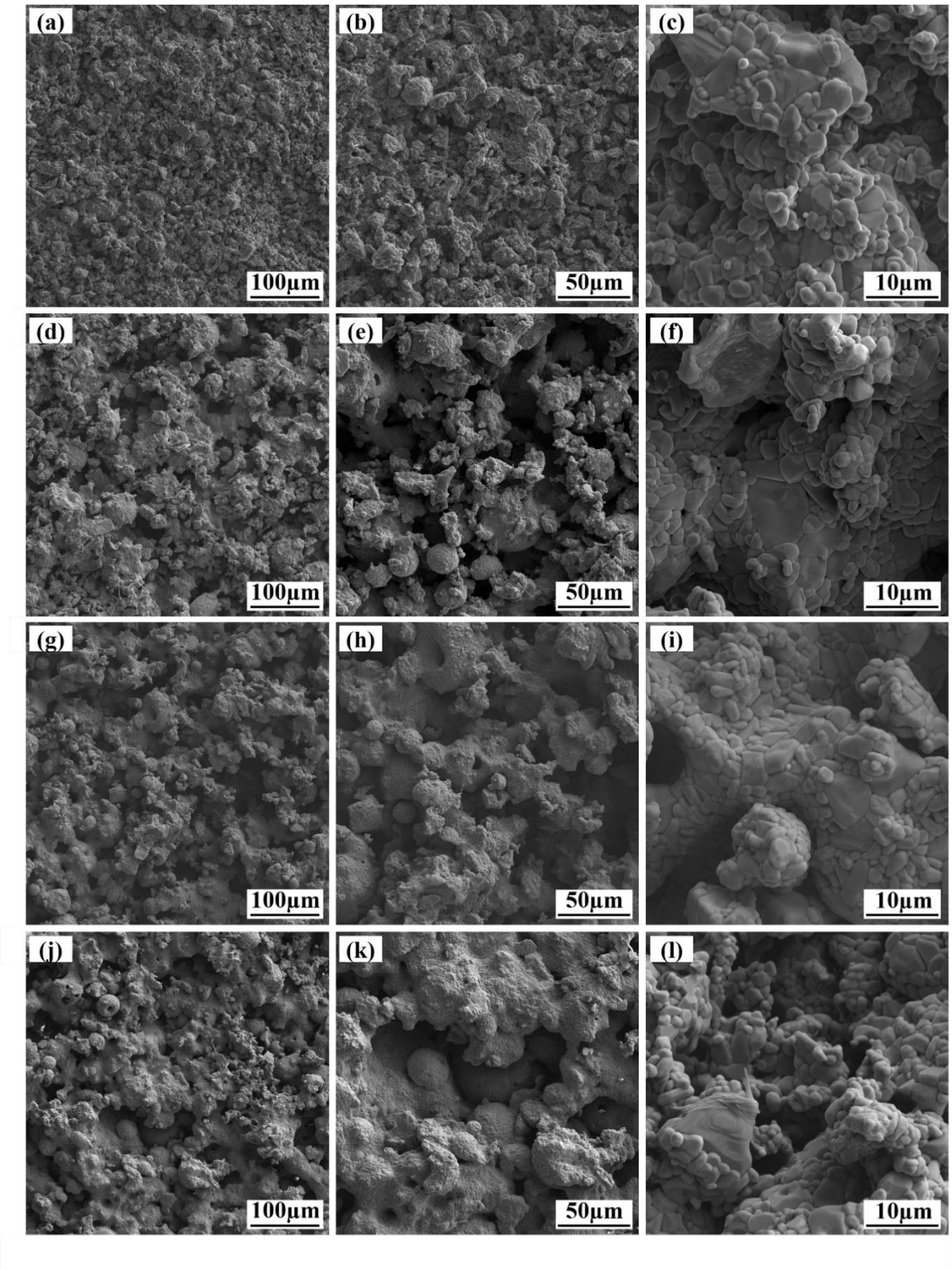


Figure 118. Morphology images of lasered surface with different parameters, laser power 100%, $PRF_0$ = 32 kHz, scanning speed 50 mm/s. (a) – (c); laser power 100%, $PRF_0$ = 41 kHz, scanning speed 50 mm/s: (d) – (f)); laser power 100%, $PRF_0$ = 54 kHz, scanning speed 50 mm/s: (g) – (i)); laser power 100%, $PRF_0$ = 76 kHz, scanning speed 50 mm/s: (j) – (l)

XRD analysis (Figure 119) suggests that there was no phase transformation on laser treated surface after hybridized process. The material phase of lasered surface is α-alumina as same as non-lasered surface.

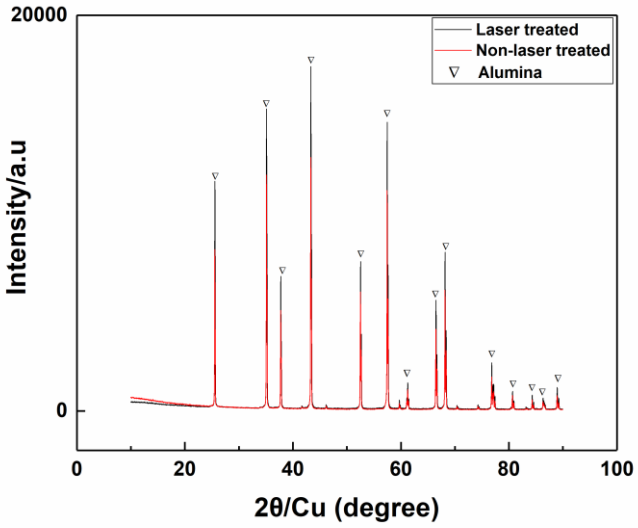


Figure 119. XRD on laser treated and non-laser treated surfaces of the sintered part (laser power 100%, $PRF_0$= 41 kHz, scanning speed 50 mm/s)

### 3.4.2. Roughness of laser refined surfaces

The roughness (arithmetical mean deviation – Ra and maximum height of profile - Rz) value was the average of 11 scanned lines (6 mm) along the printing direction (z-axis) for each sample. Figure 120 shows some typical profiles of scanning lines on parts treated with various $PRF_0$. Whatever the laser settings, the lasered refined surfaces are all much smoother than the raw printed surfaces by a factor of 3 on the average (Ra: decreased from 30 µm to approx. 10 µm ie. by a factor of 3; Rz: decreased from 204 µm to approx. 100 µm ie. by a factor of 2).

Table 24. Measured roughness (Ra, Rz) of surfaces on samples applied with different laser parameters

| Treated samples | $PRF_0$/kHz | Ra / µm | Deviation (Ra) / µm | Rz / µm | Deviation (Rz) / µm |
|---|---|---|---|---|---|
| Non-lasered | - | 30.25 | ±0.45 | 207.34 | ±1.66 |
| A | 32 | 7.69 | ±0.13 | 69.03 | ±1.71 |
| B | 41 | 12.83 | ±0.060 | 108.74 | ±0.47 |
| C | 54 | 17.16 | ±0.097 | 131.10 | ±4.16 |
| D | 76 | 13.71 | ±0.16 | 124.96 | ±2.48 |

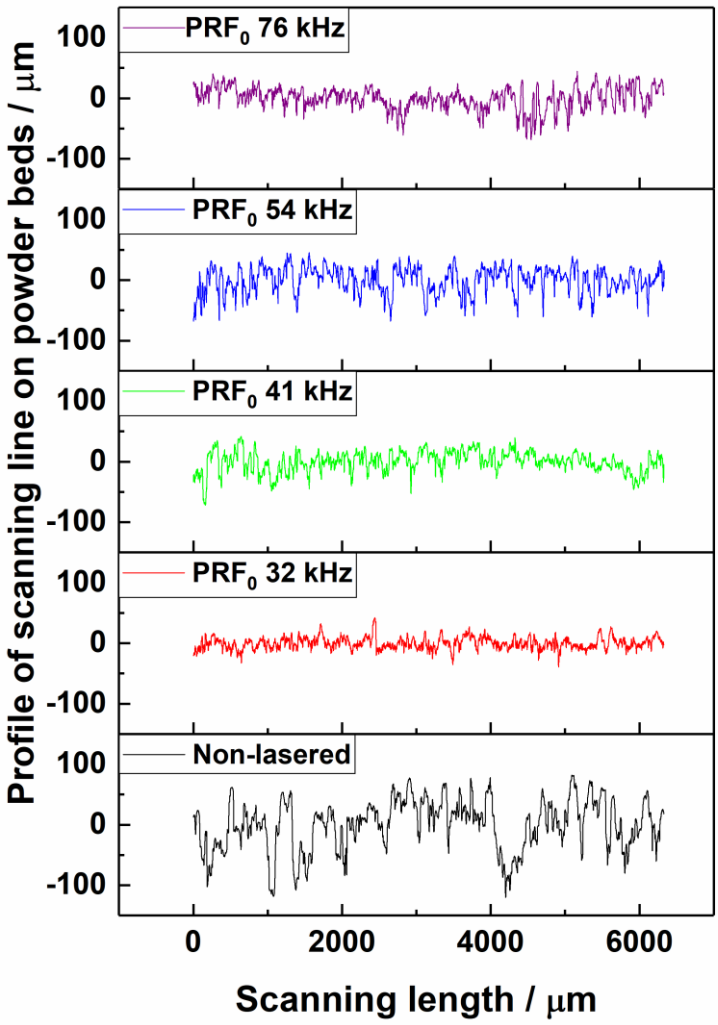


Figure 120. Scanning profile on surfaces of printed-sintered and printed-lasered-sintered parts performed under different laser waveform at constant laser power 100% and scanning speed (5, 10, 15, 20 mm/s)

Among all lasered surfaces treated with different applied laser frequency, lowest repetition frequency (highest single pulse energy ≈ 11.1 J/cm$^2$) lead to the smoothness surface while almost all cavities between granules were ablated by the pulsed laser beam. Surface roughness gets poorer when increasing the $PRF_0$ from 32 kHz to 54 kHz due to smaller laser fluence that results in an imperfect granule disruption (ie. cutting) as already noticed in Figure 118. Surprisingly, the roughest surface among the four laser treated samples was obtained at 54 kHz but roughness decreases again as $PRF_0$ reaches 76 kHz. Therefore, roughness does not follow a simple linear trend with frequency.

Again, this is most likely due to the competition between the single pulse energy at lower frequencies and the reduced numbers of pulse per unit area, the former being responsible to

more pronounced milled cavities while the latter reduces the number of such cavities (and overlapping between them). According to our result, a frequency of 54 kHz roughly corresponds to the inflexion point where the number of repeats and laser fluence have a similar effect. Additionally, the effective laser fluence could be influenced by surface cavities generated from deposited laser which causes complex laser beam reflections. Thus, the ablation efficiency might be impacted as well [266]. Surface morphology of different samples as shown in Figure 118 also helps the comprehension that samples treated at lowest frequency 32 kHz showed the smoothest surface.

Figure 121 shows the morphology of cut surfaces for samples treated at different laser frequencies on a larger scale. The red arrow indicates the building direction. Surfaces and pores distributions in Figure 121 (a) (at 32 kHz) and Figure 121 (c) (at 54 kHz) look homogeneous. Ablation seems homogeneous on lengths superior to a few millimetres which is consistent with the fine roughness of these samples. At 32 kHz, the surface looks less bumpy and finer. At 54 kHz and lower fluences, the granules are only partially ablated and some of them look weakly bonded on the cut surface (Figure 121 (c)). This was due to the enhanced laser energy from lower repetition frequency (Eq. 12) which resulted in a more pronounced ablation.

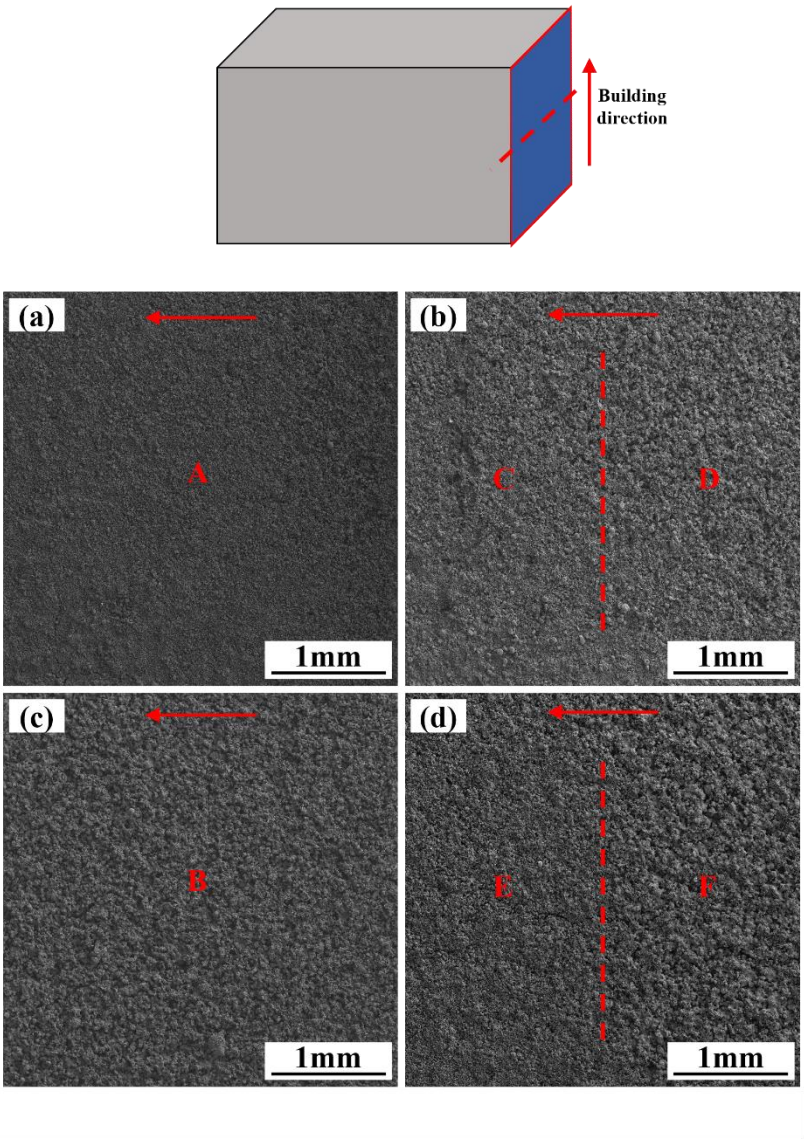


Figure 121. Surface morphology of samples conducted under four different laser frequencies. (a): 32 kHz; (b): 41 kHz; (c): 54 kHz; (d): 76 kHz; in condition (b) and (d) appear separation phenomenon along the printing direction as illustrated from the scheme

However, more interesting are the pictures b (at 41 kHz) and d (at 76 kHz) shown in Figure 121. A careful look shows a tenuous but nevertheless real border between two distinct zones (underlined with the discontinuous red lines). The laser-ablated surface comprised two regions, one in the lower part of sample and the other one located above. The transition also looks sharp.

A closer look is shown in Figure 122. In the bottom region along the printing direction (Figure 122 (D) and (F)), huge amounts of large pores distributed are visible. Ablation seemed to be less efficient there. On the contrary, in the upper region, the structure looks much finer suggesting that for some reasons the laser was more efficient (Figure 122 (C) and (E)).

The exact reason for this phenomenon is not clear and confusing. It should be further investigated and might be a simple hardware artefact (laser variations during testing, part

motion during printing …). Nonetheless, this observed transition surface as shown in Figure 122 also could explain the roughness result in Table 24. The finer region (small grains dispersed) on samples (treated with frequency 41 kHz and 76 kHz) enhanced the overall smoothness of the surfaces.

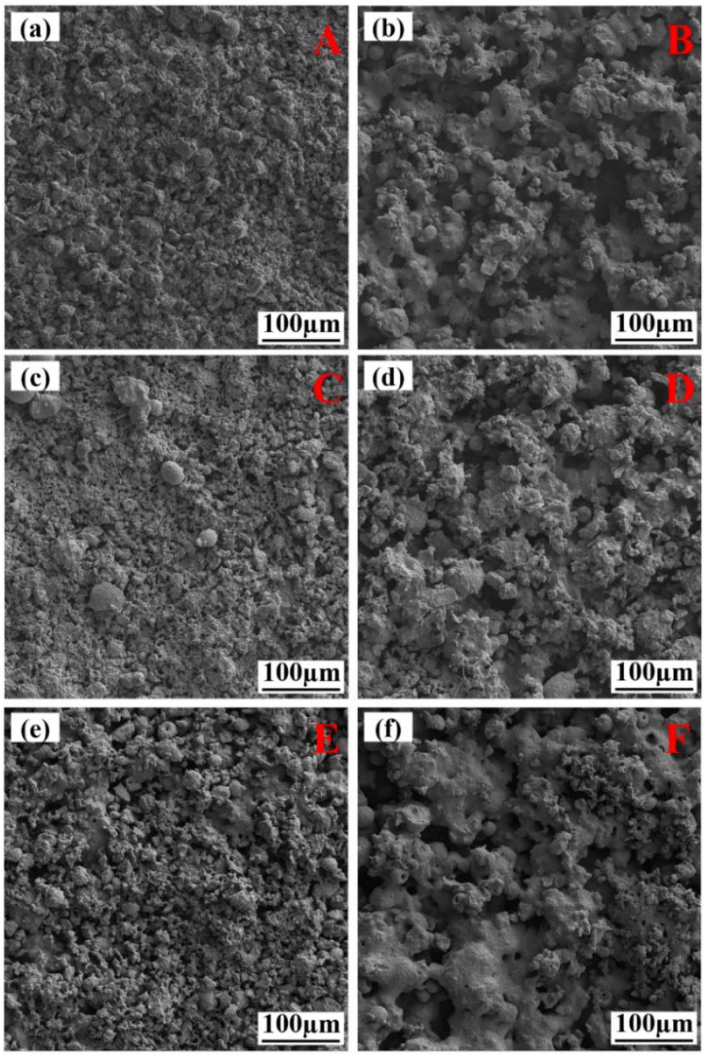


Figure 122. Surface morphology of samples conducted under four different laser frequencies. (a): 32 kHz (A); (b): 54 kHz; (c), (d): 41 kHz; (e), (f): 76 kHz; C and D are different areas from Figure 121 (b); E and F are different areas from Figure 121 (d)

### 3.4.3. Sharpness of treated surfaces

In addition to roughness measurements, the benefit of a laser refinement was estimated by doing preliminary shape assessment. Sharpness of laser refined parts was evaluated by measuring curvature radius $r_s$ (as shown in Figure 123 (a)) at the corner and angle $\theta$ (90° in STL file, as shown in Figure 123 (b)) between two adjacent printed or lasered-refined planes as shown in Figure 124 (these measurements have been carried out on the sintered samples).

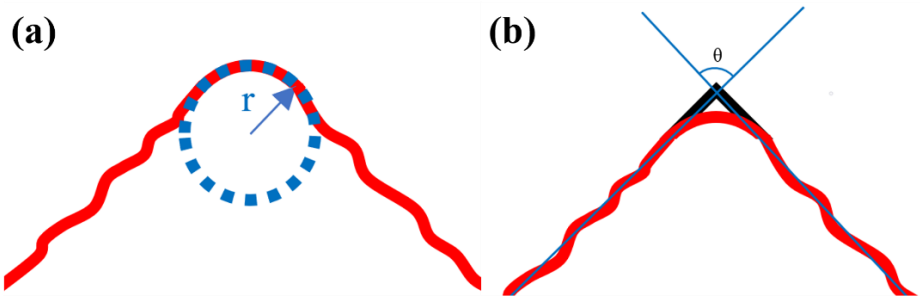


Figure 123. Scheme of measured curvature radius and angle of connected surfaces

Without laser refining, the average corner angle reached 93.35° with 3.7% deviation from the standard value (90°). The corner surface average angle of laser cut parts with different $PRF_0$ (32, 41, 54, 76 kHz) achieved 89.95°, 89.97°, 89.68° and 89.47° respectively (Figure 125 (a)). The deviations from the expected value (90°) decreased to 0.059%, 0.036%, 0.36% and 0.59% respectively. The average improvement achieved by the laser is more than ten times the order of magnitude that of purely printed parts which is remarkable. The difference is significant enough to be visible at a macroscopic scale (Figure 124).

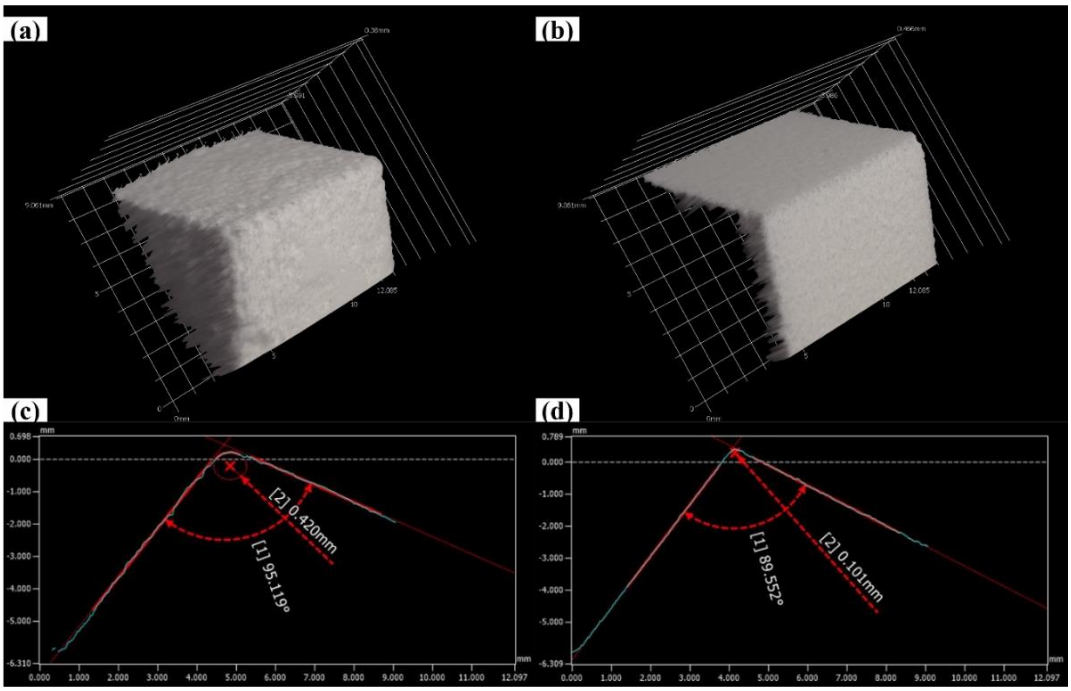


Figure 124. Topography of non-lasered part corner (a) and lasered part corner (b) (laser power 100%, $PRF_0$ = 54 kHz, scanning speed 50 mm/s) after sintering, and the measured angle between two surfaces and radius of the connecting corner surface (c,d); the defined angle of the corner should be 90°

Furthermore, the real curvature radius was compared to the theoretical sharp right-angle bevel. The value of non-lasered part was about 319 mm and the highest value of lasered surface was

194 for the part treated with $PRF_0$ 32 kHz (the theoretical value is 0). This is an improvement by a factor of 2 compared to the purely printed part.

Smaller values of the curvature radius mean sharper right-angle bevel. The benefit of increasing $PRF_0$ is obvious if one compares the measurements reported in Table 25. The fact that the trend in here is opposite to the one found for roughness where lower frequencies were more suitable, is not so surprising. A sharp angle is a delicate geometrical feature that can be easily damaged when high fluences are used.

Table 25. Assessed sharpness laser machined surfaces under different laser parameters

| Samples | Angle θ / ° | Deviation (angle) / ° | Radius $r_s$ / µm | Deviation (r) / µm |
|---|---|---|---|---|
| Non-lasered | 93.35 | ±1.77 | 319.0 | ±101.0 |
| A | 89.95 | ±0.60 | 194.0 | ±74.0 |
| B | 89.97 | ±0.48 | 163.4 | ±51.6 |
| C | 89.68 | ±0.12 | 148.4 | ±79.6 |
| D | 89.47 | ±0.18 | 148.4 | ±54.6 |

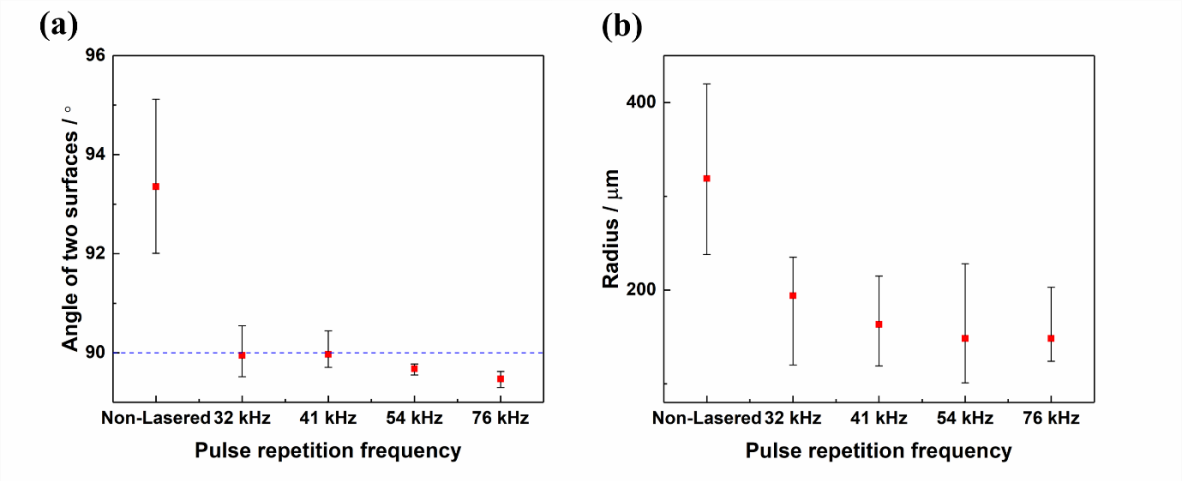


Figure 125. Measured angle (a) and curvature radius (b) of two connecting surfaces with different applied laser parameters

# 4. Conclusion and outlook

Even if is still in an infant stage of development, in situ laser refinement of binder jetting part is a concept that works. Smoothness and sharpness of parts (yet very simple ones to date) can be improved by a factor of 3 compared to conventional binder jetting. To be able to process the alumina powder beds, the addition of dopant was necessary to improve the absorptivity of the incident laser energy and helping the ablation process. Laser ablation was therefore done in the green state, cutting granules very efficiently and neatly without cracks / defects formation. The

arithmetical mean deviation of measured surface was improved from approx. 30 µm (original printed surface) to approx. 10 µm (laser-ablated surface) while the maximum height of profile was refined from approx. 204 µm (original printed surface) to approx. 100 µm (laser-ablated surface). The sharpness of the laser treated parts assessed by angles and curvature measurements and it was dramatically improved as well. Of course, much remains to be done. It could be argued that separate results could have been obtained by using a different powder and/or a different machine. That is true. However, the laser spot can be made so fine (down to a few micrometers) that the approach should work as well on completely different systems.

During the process, influences derived from laser power, repetition frequency and scanning speed on ablation efficiency were evaluated in terms of measured dimensions of ablated tracks. The values scattered a lot due to the interaction was conducted on highly porous printed layers.

# Conclusion and prospects

## 1. General conclusion

The present thesis was part of a more general research framework that aims to improve the binder jetting technology in terms of its drawbacks. In this manuscript, the main results obtained successfully reached the aim to enhance the sintered densities and surface finish of printed parts. Alumina was selected as a model material but other ceramics could have been selected as well. It is assumed that most of the results obtained are transposable to other ceramic systems. The following paragraphs summarize the main results obtained and the conditions under which they were obtained.

In Chapter 2, a fine alumina powder, unsuitable in terms of particle size and flowability for the available machine, was agglomerated by different processes such as freeze drying and spray drying to produce more suitable powders. Only spray dried powders could be successfully used in the machine thanks to their good flowing behaviour. More cohesive powders (finer and/or of arbitrary shapes) were not suitable to obtain homogeneous beds free of cracks and other defects. The packing density of these beds was also too low to guarantee the success of the whole process chain. The quality of the beds was also determined by the recoating speed. A faster speed was more beneficial while lower ones caused defects aligned perpendicularly to the recoater displacement.

It was shown that the most important printing parameters are the layer thickness and binder saturation. Both of them were optimized for the different powders. From an empirical point of view, these results confirmed that the layer thickness should be at least equal to the $d_{90}$ powder to ensure a successfully printing. Among all the parameters considered, binder saturation is probably the most important one. It dictates not only the strength and resolution of printed green body, but also the final density and mechanical strength. The overall trend shows an improvement in mechanical performance for increasing levels of binder saturation. The trend is however bounded from the top since an over-saturation is detrimental to guarantee the physical integrity of the printed part. According to the experiments, a value close to 70 % is an optimum no matter of which powder is used. After optimizing the powder properties and printing parameters, well-formed alumina parts were printed reaching a sintered density up 64.2±1.9 % of theoretical density and a compressive strength of about 113 MPa. Both values are in the top range of what was previously reported in the literature. SEM observations of the dense parts revealed that consolidation takes place through the necks formed in between the

granules. During sintering, the inter-porosity cannot be resorbed by diffusion. On the contrary, granules shrink on themselves and look fully dense.

In Chapter 3 an approach to increase the final sintered density by infiltrating ceramic suspensions into pre-sintered parts has been explored. A protocol was designed with practicality in mind. Alumina suspensions with various solid loadings and rheological behaviours were prepared and tested.

The influence of different factors was evaluated to optimize the efficiency of the process. The number of successive infiltrations, pre-sintering temperature, infiltration duration and particle size of powders used to print the ceramic scaffolds were all studied. In the best case, the relative density of samples reached 74.1±0.9% after only one infiltration. The density rose up to 83.3±1.0% after two infiltrations and finally it reached 87.9±0.5% after a third infiltration. These values have to be compared with the relative density of the non-infiltrated body which was close to 55%. A density improvement of about 35% was thus obtained. SEM images showed that the pores were gradually eliminated after infiltration and sintering. The influence of the pre-sintering temperature was highlighted. It was reported here for the first time that lowering the pre-sintering temperature is beneficial to get denser parts after infiltration. In fact, the pre-sintering temperature must remain as low as possible to avoid a reduction in the porous channels diameter while guaranteeing good mechanical strength (required to allow the part to resist the various treatments). From an industrial point of view, the necessity to use 3 successive infiltrations to reach 90 % of the density is a handicap. But it was shown that the use of a more loaded suspension (70 wt%) allows to reach this level of density after only one infiltration. The study of the influence of the immersion time did not yield any results. This one does not seem to impact the density after sintering.

The use of micro-CT has proven to be very valuable in understanding the mechanisms of suspension infiltration into the pore network of the parts. If the internal path of a ceramic grain in the suspension is governed by a complex set of forces, gravity is clearly dominant. All post-infiltrated and sintered samples revealed the existence of a density gradient in the z-direction, the lower zone being systematically denser than the top of the object. The explanation put forward lies in the rapid diffusion of the suspension in the porous network under the effect of gravity and its stagnation in the lower part of the objects. The use of more loaded suspensions and/or additional infiltration steps could possibly improve these results but we have no certainty on this point. A performance plateau (density, resistance) seems to have been reached after 3 infiltrations.

Chapter 4 describes the results obtained from the additive/subtractive hybridization. Using a ns pulsed laser mounted directly in the machine, it was possible to improve the finish surface (roughness) and sharpness of simple shaped objects. Since alumina did not absorb laser

radiation, a technical prerequisite was to mix the powder with an absorbent additive. It has been demonstrated that adding 0.1%vol of colloidal dopant enhances dramatically the optical coupling between the laser and the powder beds, even if the layers are not completely dried. In preliminary tests, different laser parameters like power, repetition frequency and scanning speed were investigated to determine their respective influence on the dimensions of ablated tracks. The dominant influence of the laser frequency was highlighted.

In a second stage of the study, a simple shape was printed and laser refined (in fact cut layer after layer). Using SEM on the sintered bodies, it was shown that lower frequencies gave the smoothest surfaces. Surprisingly, the laser does not only remove individual granules, it also cut them. This unexpected result has a significant impact on the roughness. The typical Ra was decreasing from approx. 30 µm (original printed surface) to approx. 10 µm (laser-ablated surface) while the maximum height of profile was refined from approx. 204 µm (original printed surface) to approx. 100 µm (laser-ablated surface). Similarly, the sharpness can be improved significantly. Deviation from right-angle and curvature radius measurements were performed on laser refined parts and compared with their printed counterparts. For the laser-ablated parts, the deviation from right angle was only 0.59 % (angle = 89.47°) while it was 3.7 % (angle = 93.35°) for the un-refined part. This is a ten times order of magnitude difference which alone demonstrates the validity of this hybrid approach.

# 2. Future prospects

The advances made in this work are significant to us. However, the work remains substantial and several aspects should be the subject of complementary and/or more detailed studies. Here are a few avenues of work that are proposed to further improve the quality of the pieces.

*i. Recoating & Multi-modal powders systems*

Though the influence of several powder properties were identified and optimized, the packing density of the powder beds remained low. To improve it, an obvious solution would be to replace the current recoater of the machine (a simple blade) by a roller. The literature is full of examples showing that a counter-rotative roller is the most efficient way to create more compact powder beds (as long as they are dry). Developments in this direction are currently underway at CRIBC. Nevertheless, it is unlikely that this solution alone will solve the problem of low compactness (otherwise, this would have already been demonstrated in the literature, which is not the case). The other limitation of this approach is that increasing the compactness to a higher level would not necessarily achieve 100% sintered density but would possibly impair post-infiltration.

The use of multi-modal powders systems may be a more suitable option. The idea is to use a bimodal distribution so that the finer particles fill the gaps between the coarser particles. Some

preliminary tests in this direction have been carried out in this work (Appendix 2). Nevertheless, this approach was not pursued because the impact of introducing fine particles into a mixture with granules was deleterious for the flowability. The powders in question were no longer compatible with the current equipment and its scraping system. However, this option remains totally relevant with a roller-type system and should be the subject of an exhaustive study.

*ii. Optimization of post-infiltration*

The post-infiltration process was quite effective, although the reported improvements did not reach fully density. It is believed that ceramic suspension with higher solid loading should be investigated. The critical point to be paid attention is the viscosity that might negatively affect the dimensional accuracy of treated parts especially for complex shapes. Using a surfactant to improve the wetting behaviour of the suspension with the ceramic scaffold could possibly help the penetration of more viscous slurries (and/or with an applied pressure but this would be at the expense of the simplicity of the procedure).

Using post-infiltration also opens the door to interesting material combinations. It should be possible to print scaffolds with one material and use a suspension containing another one so as to create a composite part. For instance, CaP bio-ceramic (such as hydroxyapatite or beta tri-calcium phosphate) could be introduced inside of an alumina skeleton body to combine the advantages of both materials: alumina stiffness and CaP bioactivity. Suspensions containing graphene oxide could infiltrate a printed scaffold and then freeze casted. The finished part might have potential interest in sensor industry.

*iii. Further investigation on hybridized hardware*

The parts refinement considered in this work remains excessively simple. Refining was in fact limited to a layer-by-layer cutting. It is not yet a laser refinement of a complex shaped object having curved surfaces. With the current software, this was unfortunately impossible in the present thesis. To improve the resolution, the refinement should work as depicted Figure 126. For one single laser pass, the height of removed material should be much lower that the thickness of one printed layer so that the laser could be used to “re-sculpt” the printed layer. There will be obviously some limitations (the bottom of the printed layer cannot be laser treated) but a general improvement of the resolution and smoothness of the printed body is expected similar in magnitude to the ones shown in the previous section on simple shapes.

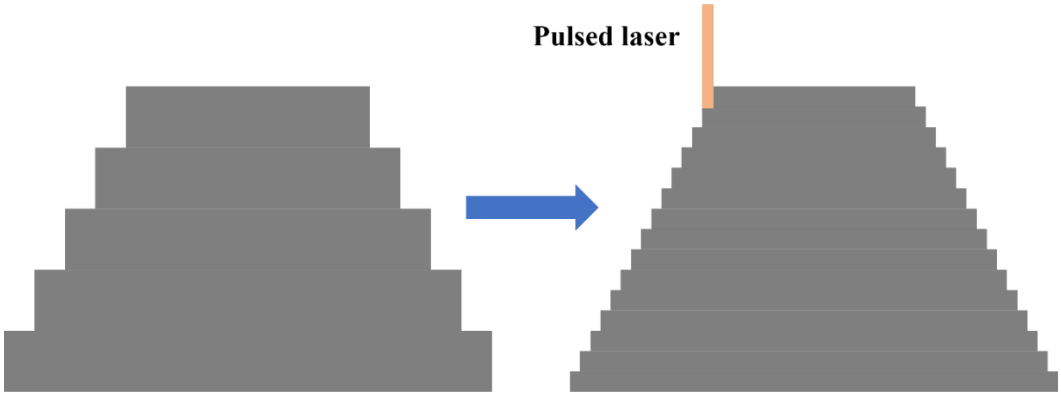


Figure 126. Scheme of multiple laser ablations on each printed layer to produce curved surface with higher smoothness

Since the ablation depth and width are difficult to control with a good accuracy, dopant or other additive helping the laser energy absorption could be transferred from powder to binder. As discussed in the text, printed layer with pure alumina powders hardly absorbs the laser energy with very limited laser-ceramic interaction compared to powders containing dopant. By modulating the local amount of ink deposited, more or less dopant could be added and consequently the optical coupling could be adjusted for a better control of the ablation level. It could even be imagined that dopant could be deposited only where laser has to hit the surface, for instance along the contours (Figure 127). It is probably a smarter approach than the one reported in this document (as the process would become compatible with every kind of powder) but it requires substantial developments that are left for future works.

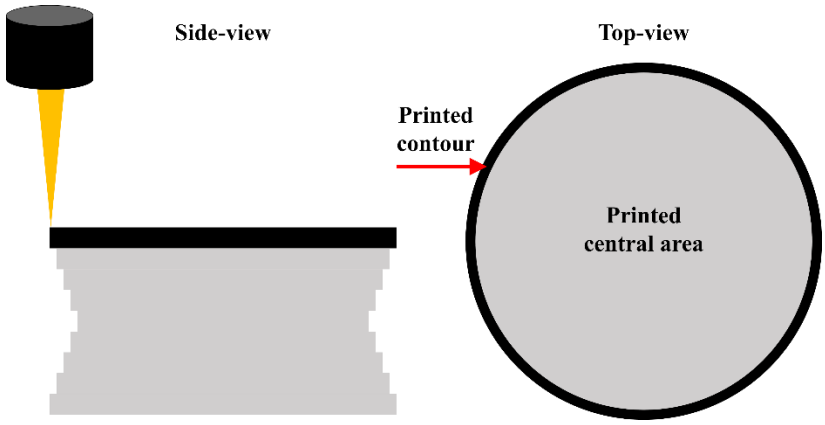


Figure 127. Scheme of using binder containing additive to perform hybridized laser machining

# Conclusion and prospects

# Appendix 1. Other AM technologies and their use to shape ceramics

## 1. Landscape of additive manufacturing (AM) techniques

### 1.1. Stereolithography

Stereolithography (SLA) is the earliest developed AM technology in 1983 [267]. Ultraviolet (UV) light or visible light at around 400 nm is normally used as catalyst to process the polymerized reaction to solidify a liquid monomer (acrylic-based or epoxy-based polymers) containing photo-initiators to initiate the polymerization (radicalization generally). Digital light processing (DLP) is a variation of the original SLA process. In DLP however, a projector replaces the laser and flashes in one single shot the whole layer which of course speeds up the processing time at the expense of a slight degradation of the resolution. In both technologies, the pattern irradiated by light becomes solidified and attached on the platform, waiting for connecting the next printed layer. As uncured resin is still liquid, it is perfectly separated from printed areas are ready for another layer. After the part has been built up by stacking layers, unreacted polymers are removed by rinsing the object with solutions. Additional post-treatment such as photo-curing and heating may be considered to help photopolymerization to end.

Basic principle of SLA is shown in Figure 128 hereafter. The resolution of SLA is the finest among all AM processes achieving 10 µm[268]. Besides, the resolution is strongly dependent to the light source energy, curing time and the presence of fillers (like ceramic particles) in the resin. It is also affected by the layer thickness which is also dependent by the machine itself. Successful printing with layer thickness down to 100 µm can be easily achieved and even finer [269]. During the SLA process, the curing/photon polymerization influences and controls the quality of final products. Overcuring happens when the polymerization degree is excessive or the energy source is scattered to the place outside the treated area. On the other hand, less curing or even no curing may also occur if the photo initiator is not efficient enough or too weak to activate the polymerization reaction. Therefore, the composition of resin is a matter of careful investigation with critical choices that have to be done during the resin development.

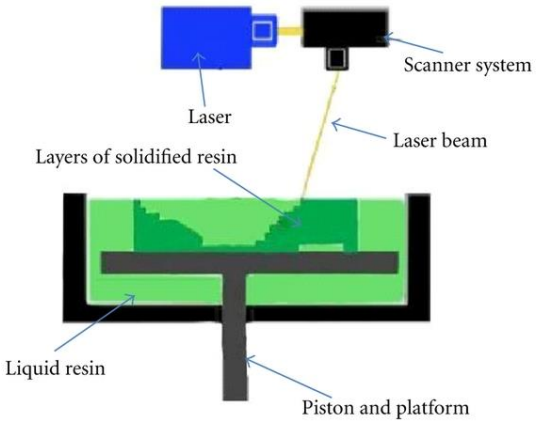


Figure 128. Principle of Stereolithography [12]

When it comes to metal or ceramic printing, fine particles are added to the resin. Particles with size ranging from 0.2 to 2 µm are usually considered at a filling rate of about 40/50 % per vol of resin. Specific issues come into play whenever the refractive indices of pure resin and particles differ too much (as it is the case for SiC for instance). Low polymerization or even no polymerization at all occurs if the light is absorbed and not refracted. After printing, parts still need to be debinded and sintered to reach (hopefully) full density. The removal of all organic phases through thermal debinding remains a challenging and time-consuming task (up to 6 days sometimes) that may cause the formation of cracks or defects in the final sintered parts.

### 1.2. Fused deposition modelling

Fused deposition modelling (FDM) or materials extrusion make use of thermoplastic filaments to extrude materials in a semi-liquid state on a platform or previous layers through heated nozzles. The schematical principle of FDM is shown in Figure 129. The thermo elasticity and rheology is critical in FDM, since the filament (initially in a solid state) needs to be extruded in a smooth way (in a semi-liquid state) and then solidifies at room temperature after printing. Compared with other AM techniques, the resolution of FDM parts is lower, however as it is low cost and the printing speed is high, the technique became one of the most successful AM from a commercial point of view. Mechanical strength, resolution and limited choices of materials are sometimes considered as the weak points of this technology. Some researchers have investigated using fibers to reinforce the filaments (in an attempt to increase the mechanical performance of printed parts). However, fiber orientation, bonding between fiber and the matrix filament, the gap or defects that exist inside form new challenges in final products[268, 270].

## Appendix 1. Other AM technologies and their use to shape ceramics

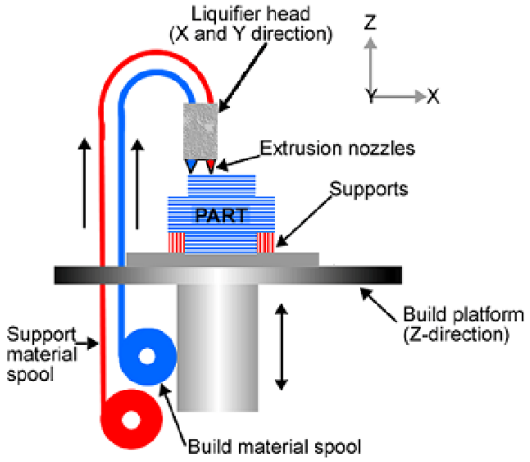


Figure 129. The schematic of the FDM process from[271]

### 1.3. Robocasting / Direct ink writing

Robocasting also known as Direct ink writing (DIW), shares similar principles with FDM. However, it makes use of pastes or suspensions with particles dispersed instead of plastic filaments. It was originally patented and developed by J. Cesarano at the Sandia National Laboratories in the USA with the name 'Robocasting'[272]. The technology is mainly used for printing complex structures or scaffolds for tissue engineering or 3D structures for the energy industry. Robocasting has high requirements on rheology of the paste as it governs the extrusion behaviour and the properties of parts in the green state. Extruded paste needs to solidify quickly to support the subsequent printing structures (i.e., to avoid collapse or sagging). During the process, the ceramic paste with high solid loading undergoes a transformation from a pseudoplastic to a dilatant behaviour [4]. This mechanism is graphically illustrated in Figure 130. The control of this behaviour is absolutely critical and it can be dramatically affected by paste aging. The ceramic paste has usually to be extremely viscous and dense to ensure good mechanical properties and low porosity of final products. Sometimes, shearing stresses break the gel structure and the viscosity may decrease drastically after extrusion due to shear thinning behaviour which might be a major issue of the process. The paste behaviour can be controlled by flocculation of a ceramic suspension to form a gel (by modifying PH value, ionic strength of the solvent, addition of poly-electrolytes, gelling additives etc)[273]. Compared to other technologies, Robocasting is cost efficient. Typical nozzle sizes are in the range between 100 – 1000 μm and dictate the overall resolution of the printed objects. Decreasing the size of the nozzle not only increases the complexity of the process but also increases dramatically printing time. Nevertheless, this technology is one of the most used AM technology (especially from a scientific point of view) as it is compatible virtually with any material.

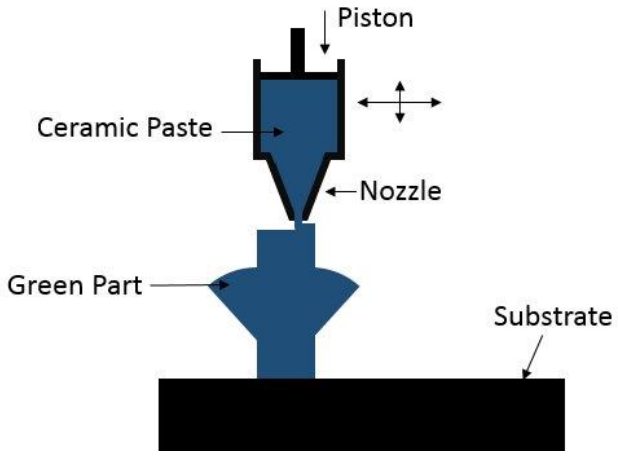


Figure 130. Schematic illustrating the robocasting process from [274]

### 1.4. Powder bed fusion

Powder bed fusion (PBF) is powder bed-based AM technology using thin layers of powders, which are spread on a building platform and fused together with a laser or electron beam to reproduce an object through slicing [3, 257, 258]. A new layer is deposited on top of the previous printed one and fused through deposited energy. This creates a dense layer which is strongly bonder with the layer beneath. The whole object is reproduced by stacking layers. After finishing, the remaining powder is removed by blowing or brushing the fabricated parts. Principle of PBF is graphically explained in Figure 131. Additional steps may be considered to enhance the properties of final products such as coating, infiltration and thermal treatment. The principle of PBF is very similar to Binder Jetting, except that laser or electron beam replace the function of binder to bond powders together. In both technologies, powder properties like PSD and packing rate of powder bed strongly influence the obtained properties of parts. Selective laser sintering (SLS) and selective laser melting (SLM) are two derived methods from PBF system. SLS is mostly used when it comes to polymers while SLM is mostly a terminology for metals [3]. EBM is a declination of SLM which just replaces the laser source by an electron beam. Compared to SLM, EBM uses a hot power bed (>870K) to decrease the amount of energy required to fully melt the powder. EBM is characterized by objects exhibiting coarser microstructures and poorer finish surfaces. Additionally, EBM operates under vacuum instead of inert atmosphere (air, $N_2$, Ar) which also affects the properties of fabricated parts[11]. Since laser scanning in SLS does not completely melt the powders, consolidation of parts is obtained through local sintering at the beam spot[275]. Laser powder, scanning speed and scanning strategies are main factors affecting sintering or melting [6]. Thanks to the relatively fine particle size, nice resolution and part quality can be reached in beam melting. PBF is also the most widely used AM process in the metal industry especially for manufacturing precision parts in aerospace, electronics and automotive. For ceramics unfortunately, the process is much more limited due to thermal properties of these materials and their high sensitivity to thermal

shocks. Besides, the main drawbacks of powder bed fusion are that the process is time consuming, high cost of economy and energy as well.

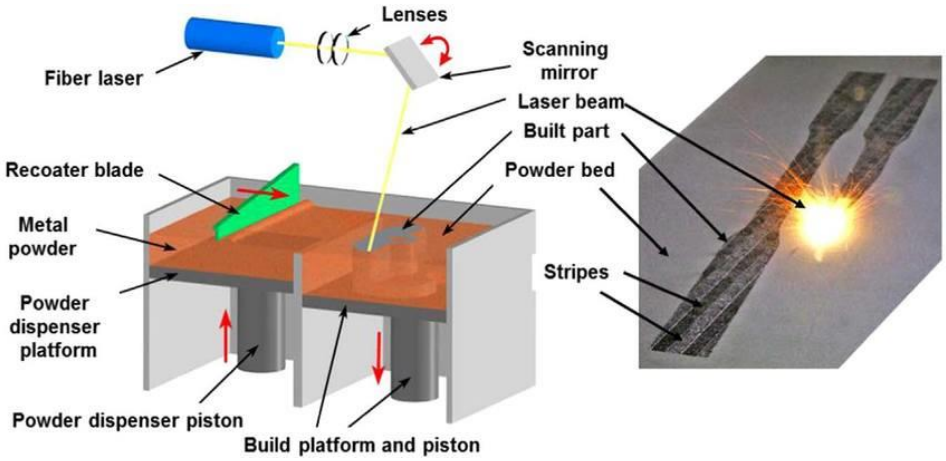


Figure 131. Laser powder bed fusion system (direct metal laser sintering by EOS GmbH) from[276]

### 1.5. Direct energy deposition

Direct energy deposition (DED) exploits a laser source which is directly focused on a small region to melt a feedstock material (be it a powder or a wire) directly on a substrate. The melted materials is deposited and fused with the material of the substrate (a metal) and then solidified after movement of the beam source[5]. The principle of process (also known as cladding) is shown in Figure 132[14]. Difference between DED and PBF is that there is no powder bed in DED and the feedstock is molten at extremely high laser energy (typically more than 1 kW). According to the literature[3], different terminologies are used to describe the same process : laser engineered net shaping (LENS$^{TM}$), laser solid forming (LSF), directed light fabrication (DLF), direct metal deposition (DMD), electron beam AM (EBAM) and wire + Arc AM (WAAM). This approach is mostly used to retrofit manufactured parts containing defects and/or worn objects. Sometimes DED is combined with traditional subtractive manufacturing (to improve surface finish) to become a complete hybrid process[277]. DED can possibly be conducted in multi-axis setups and different kind of materials as well which make it very flexible and suitable to process complicated parts. It is generally applied for parts made in titanium, Inconel, stainless steel, aluminum and related alloys for aerospace applications. DED has a high manufacturing speed from 0.5kg/h for LENS up to 10kg/h for WAAM, and also huge work envelopes (up to 6 m * 1.4 m * 1.4 m for commercial printers) [3]. Nevertheless, the achieved resolution of DED process cannot be compared with PBF process (in DED, a single line track has a width of 1 mm approx.).

## Appendix 1. Other AM technologies and their use to shape ceramics

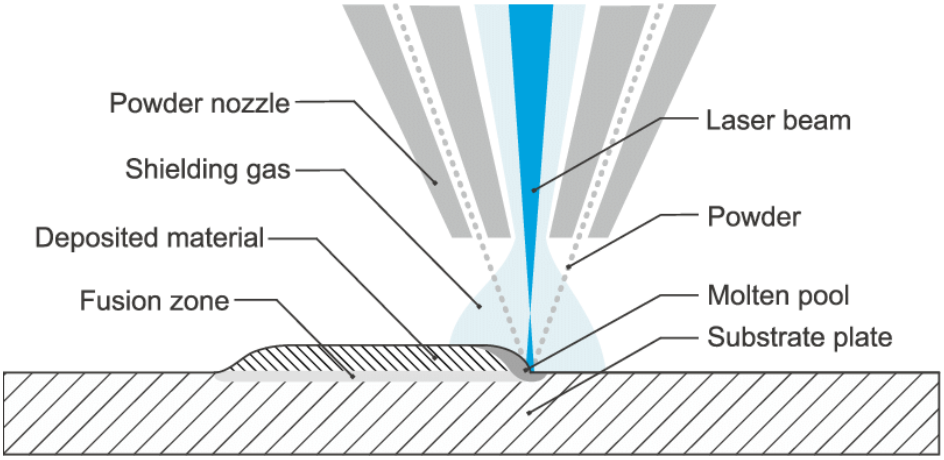


Figure 132. Laser based direct energy deposition process from [278]

### 1.6. Sheet lamination / Laminated object manufacturing

Sheet lamination also known as laminated object manufacturing (LOM) is a rather old AM technology. In 1986, the Helisys Corporation developed the LOM process for fabricating 3D parts from sheets of paper, plastic or metal [16]. LOM is based on cutting and lamination of sheets or rolls of materials in a layer-by-layer manner. Each layer is cut by laser or different mechanical tools and then different layers are bonded together (form them bond) or vice versa (bond then form)[3]. The mechanism of LOM is illustrated in Figure 133. Over the years, LOM has been used for a variety of materials such as polymers, ceramics, paper and also metals. Compared to other AM processes, it has a few advantages described in [4]: (1) the method doesn't introduce organic phase which have to be eliminated after printing process, (2): it has lower applied pressure and temperature compared with low-temperature lamination process, thus avoiding delamination of layers due to inhomogeneous distribution of materials; (3): it doesn't require a substantial capillary force to promote the union between adjacent layers; (4): it allows the lamination of water-based green tapes which cannot be achieved by thermo-compression. The process is also affected by the roller speed, size, and the temperature on interfacial stresses and lamination[16]. According to the work from F. Sonmez et al.[279], bigger rollers lead to better lamination of the sheets, while small rollers generate shorter process time due to concentrated stress distribution on the interface. Influence of temperature was investigated [280, 281] as well as that from cutting seed, laser power and cut[282]. Nonetheless, the most critical point of LOM process is the quality of interfaces between tapes which may result in formation of defects.

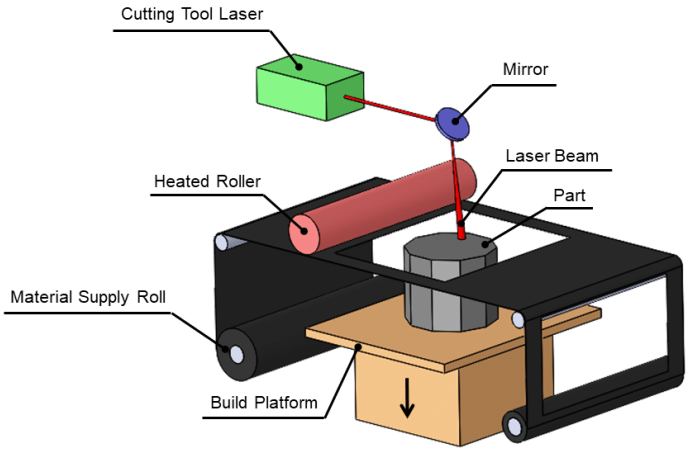


Figure 133. Laminated object manufacturing process from [283]

### 1.7. Binder jetting

Together with SLS, BJ composes the family of powder-based 3D printing (P-3DP) [284]. The major difference resides in the bonding mechanism of powders. While the latter method uses a printhead to eject liquid binder selectively, the former method employs the energy of a focused laser beam to sinter/melt powders [4].

### 1.8. Hybrid technologies

Except the 7th different AM families described above, the hybrid family has recently emerged. It combines the principles of any one of the 7 AM families with a subtractive approach. For instance, DED can be combined with CNC milling which results in a hybrid process of 'additive' and 'subtractive' manufacturing in one system thus combining the advantages of both technologies in a synergistic way. The most interesting compelling point of the hybrid approach is to alleviate some manufacturing difficulty of pure AM that cannot be resolved without recourse to subtraction of matter. Using a subtractive technology is especially valuable to improve the finish surface of AM parts that are not satisfying industrial requirements.

## 2. Applications of AM with ceramic materials

Before describing AM of ceramics, it is good to remind that those materials may exhibit outstanding properties like a high mechanical strength, biomimetic properties, excellent thermal stability, remarkable hardness and wear resistance [22]. Over the years, various technologies have been developed to shape ceramics. Conventional manufacturing processes are composed of several steps, including powder preparation, mold making, granulation, forming, dewaxing, sintering, machine finishing, …[36]. For conventionally fabricated ceramic parts with complicated shape, the cost of machining could be up to 80 % of overall cost [285]. As they are non-ductile materials, ceramics cannot usually be shaped using the same technologies than metals. In most cases, obtaining complex shapes is a time-consuming and

tricky process involving various post-treatment (to sinter the material for instance) which may be also rather expensive. For all those reasons, AM appears as a very attractive approach to manufacture ceramic parts with complex shape and this justifies the scientific interest that surrounds AM of ceramics[244].However, due to the limitations of existing AM technologies there are still many challenges when it comes to produce ceramic objects. AM processing of ceramic materials is thriving in different researches and applications in recent years. Japanese government for instance has launched a national R&D project 'High-value added ceramic products manufacturing technologies (HCMT)' in 2014 for this purpose [36].

**SLA**

Almost every existing AM technology has been applied to ceramics. To date, SLA is the most advanced approach, at least the one for which turns out as the most successful one. The interest of SLA for ceramics was driven by applications in tissue engineering and bone restoration. SLA applied to ceramics does not differ much from conventional SLA. The main difference is the resin which contains a very high solid loading of fine ceramic particles homogeneously distributed inside. After printing the part is a composite made by a plastic network surrounding the ceramic grains. Thermal debinding is used to remove the organic fraction and then high temperature sintering permits to densify the part. These two thermal treatments are the most critical steps in ceramics-SLA. Cracks and other defects (like delamination) may occur quite easily during the organic phase removal. Thus, the heating process has to be performed extremely slowly just for keeping the pressure inside the part below a critical threshold to avoid the formation of defects [4]. Another limitation of SLA comes from the interaction between the ceramic particles and the incident light beam. Certain ceramics may scatter or reflect light (depending on their optical properties) which decreases the efficiency of photo-polymerization [16]. Composition of the resin itself needs to be adjusted for a better matching with the ceramic optical properties. Thus, the amounts of photo-initiator, photo-inhibitor and monomer, all have to be carefully selected to optimize the curing behaviour. Different ceramic fillers have been studied such as silica, alumina or zirconia to cite the most current ones. Kirihara et al.[286] have produced types of samples with ordered porosity, in total 75 vol%. Porous hydroxyapatite implants with designed 40 % porosity and orthogonal pores were successfully printed out[287]. Chartier et al.[40] printed alumina parts with a very high solid loading slurry (60 vol%) at a low layer thickness (25 µm). Usually after a careful optimization of debinding, sintered densities close to the theoretical values are obtained but this may be strongly affected by the design and size of the printed parts. There is a wealth of literature reporting crack and pore-free oxide ceramics processed using SLA and having similar mechanical properties to those of conventional produced materials [14].

On the other hands, instead of using a ceramic filled, some authors have considered polymer-derived ceramic (PDC) materials in SLA. Usually, these precursors are blended with a conventional SLA resin and the parts are printed as usual. After pyrolysis and sintering, objects made in silicon oxycarbide are obtained as shown in Figure 134 [288]. The advantage of using PDC in SLA is that liquid phase without solid contents can be directly photo-polymerized into 3D complex shapes (absorptivity of the powder is no more an issue). Other negative influence of ceramic fillers can also be completely eliminated (dispersion issue, sedimentation etc…). This approach is still plagued by the level of density reached after sintering which remains far below the ones which can be obtained in the more classical approach.

The resolution and accuracy of SLA is the highest among all AM processes which leads to a perfect surface finish. However, the choice of ceramic materials that can be processed this way is still limited and raw materials (slurries) are quite expensive compared to conventional ceramic feedstocks (simple powders or CIM grades for instance). Thus, this technology is recommended when the need and requirements of products are specifics and when cost is not an issue. As an example, some PDC like materials have been recently processed using SLA. By the way, SLA technology is the most commercially exploited AM process for ceramics with several well-known actors like Lithoz, Admatec, 3D-CERAM (all located in Europe). There are slight differences in between the technologies proposed by these companies. For instance, Admatec combines SLA process with tape-casting for spreading thin layers of resin. 3D-CERAM uses pastes instead of slurries while Lithoz keeps the conventional way of vat photopolymerization.

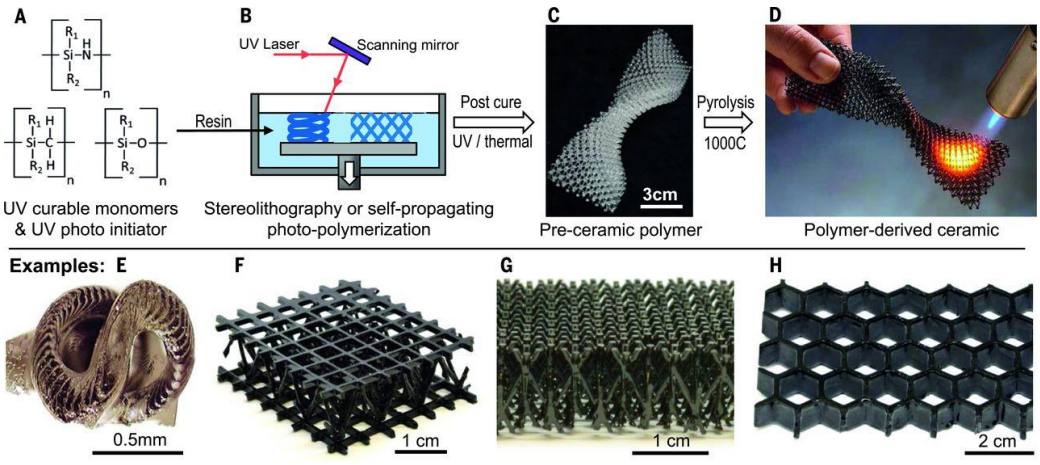


Figure 134. Additive manufacturing of polymer-derived ceramics. (A) UV-curable preceramic monomers are mixed with photo initiator. (B) The resin is exposed with UV light in a SLA 3D printer or through a patterned mask. (C) A preceramic polymer part is obtained. (D) Pyrolysis converts the polymer into a ceramic. Examples: (E) SLA 3D printed cork screw. (F and G) SPPW formed micro lattices. (H) Honeycomb. [288]

## Appendix 1. Other AM technologies and their use to shape ceramics

### DIW

DIW or robocasting is the process which has been the most investigated. The main reasons lie in its convenience and the fact that it is a rather cheap technology (both in terms of materials and equipment). In addition, this method is the only one suitable when desired dense parts may not need any post-treatment. It is also highly versatile as it is compatible with a very broad range of ceramics (oxides, carbides…). The key point of the process is the ceramic ink that has to fulfil some basic requirements: it should contain a high enough ceramic loading and has to be very stable with an appropriate rheological behaviour (shear-thinning during printing). An obvious requirement is that it should not clog the nozzle which implies using ceramic particles at least 10 times smaller than the nozzle size. More precisely, in the case of ceramic inks containing particles, properties such as PSD, average particle size, specific surface area and surface charge influence the quality of parts and the reliability of the process dramatically. Other parameters such as the liquid to solid ratio, the presence of air bubbles inside ink as well the temperature have also effects on the process. The drying stage is the most critical part as cracks and delamination tend to occur as a result of a too fast solvent evaporation [289, 290]. As robocasting is limited in terms of resolution, it is mostly restricted to specific uses such as filters or scaffolds. As an example, Maurath et al. produced highly open porous and hierarchically structured ceramics via robocasting thanks to a fine tuning of ink rheology and its homogeneity. They obtained undeformed cellular ceramics parts with a honeycomb structure without cracks [291]. In another paper, a mixture of ceramic foam ink was prepared to produce a hierarchal porous ceramic with a high strength to weight ratio[292]. Large pores were generated directly by the design of the scaffold while micro-pores were created by the air bubbles of the foam. Usually, micro porosity is controlled by adding a pore former into ceramic paste. In several papers, Poly methyl methacrylate (PMMA) microspheres are added into the ceramic ink to print scaffolds with different levels of porosity: macropores (100 – 600 µm) are produced by controlling the arrangement and spacing between printed rods; micropores (1 - 30 µm) are produced in the rods by including PMMA microspheres; sub-micrometer pores (< 1 µm) result from sintering [293].

Tissue engineering is the main application for robocasting and different bio ceramics have been printed in numerous papers. Although the resolution of the scaffold is much lower than similar counterparts obtained by SLA, parts exhibit better mechanical properties with less variability. Miranda et al. [294] have produced hydroxyapatite scaffolds which contained 39 % porosity and 15 % strut microporosity. They studied the fracture modes under uniaxial compression and showed that very good values of strength can be reached.

## Appendix 1. Other AM technologies and their use to shape ceramics

### FDM

The preparation of thermoplastic filament containing ceramic powders is difficult and challenging. This approach is more recent than robocasting but exhibit obvious advantages in comparison with other extrusion-based technologies and SLA (most notably, the fact that the feedstock is not aging and there is no material restriction). In order to keep the filament flexible (to prevent breakage to occur during printing) a not so low percentage of polymer has to be added to ceramic (typically above 40%). As in SLA where green parts contain huge amount of volatile phase, debinding of green-FDM parts is challenging. Furthermore, even if the resolution of FDM parts is better than that obtained in robocasting, it is still poorer than in SLA. In terms of results presented in the literature, various ceramics have been shaped using FDM. For this reason, hybrid method to combine FDM / Robocasting with other machining (like computer numerical control machining) is necessary and beneficial to enhance the final quality. Mixture of 55 vol % zirconia powders in wax was extruded from nozzles with diameter between 76 and 510 µm[295]. Park et al.[296] extruded 40 wt% hydroxyapatite powder with polycaprolactone at 100 °C with nozzles of diameters comprised between 400 - 600 µm. Both of them have measured the influence of deposition pattern on the compressive modulus as well as the attachment and proliferation of osteoblast-like cells. Another advantage of FDM is the possibility to combine multiple extruders in one single machine thus opening the door to FGM or even multi-material printing [297]. Fraunhofer IKTS is developing a machine which is close to FDM and compatible with multimaterial printing.

### PBF

Powder bed fusion is also gaining more attention for processing ceramic materials. However, thermal shocks during heating up and cooling down to room temperature create cracks and other defects in ceramics which strongly restricts the usage of this technology [16]. PBF is sometimes used in an “indirect approach”. Instead of trying to melt the ceramic, the laser beam is used to fuse an additive or a binder with has a lower melting temperature [3]. The additive or binder absorbs the energy and holds the shape of printed part. As the additive is usually an organic phase, the body has to be debinded and sintered at a high temperature to form the ceramics. This approach has been applied to ceramic-glass and ceramic -polymer composites for instance[3]. Vorndorn et al. [223] have used phosphoric acid as the binder to produce beta-tricalcium phosphate ceramics. Friedel et al.[298] have used a laser light to selectively melt and crosslink a solid silicon resin mixed with silicon carbide powders so as to generate complex structure. All in all, the quality of products obtained from PBF strongly depends on the properties of powder beds. The density of parts is usually poor due to the low packing density and very close in fact to BJ. The PSD, flowability of powders, density and shrinkage all affects the final properties. The problem is faced with all powder bed-based AM processes and post-

treatments are mandatory to get parts performing similarly to those obtained using other AM techniques. Most of the time, SLS/SLM is followed by an infiltration step with metals or semi-metals in order to get denser parts. One typical approach combines SLS followed by infiltration by metal silicon to get Si/SiC parts. During the SLS process, SiC particles are glued together as a result of the formation of $SiO_2$ bridges in oxidizing atmospheres [299]). Some authors have tried to improve the density of PBF parts using materials containing a liquid phase at high temperature to favor a better densification[300]. As an obvious statement (also underlined by Zocca) SLS/SLM are the only processes which could possibly deliver ceramic parts from the obligation of sintering[4]. JUSTE et al. [257] have obtained the promising result of pure alumina parts produced by SLM process as shown in Figure 135.

Figure 135. Pure alumina parts manufactured by SLM process from [257]

**LOM**

LOM is now a quite old AM technology which is less appealing now. Nevertheless, many authors reported processing of ceramics using LOM with certain successes (especially in terms of mechanical strength). For instance, Alumina tape was processed with LOM in [16] and the resulted part showed distinctive mechanical properties compared to other AM methods. Not surprisingly bending strength was found to be non-isotropic with significant variations along directions parallel and perpendicular to lamination. Generally, alumina sheets are prepared with organic solvents but some rare papers mention using water-based tape-casting process to reduce the ecological and environmental imprints. Most of the time, the tape consists in a mix between alumina powders, a styrene-acrylic latex binder and some other additives [301]. Except alumina, other ceramics have been tested such like glass fiber reinforced polymers, SiC, SiC-fiber-SiC, AlN, HA and TiC/Ni etc[16]. Printed silicon nitride parts have reached a mechanical strength of 475 ± 34 MPa which is rather good for AM [302] and higher than parts fabricated from gel casting (as mentioned by the authors).

# Appendix 2: Powder mixing and packing

## 1. Introduction to powder mixing models

Different models for multi-components powders packing have been introduced by Senthil Kumar V et al [231]. Developing these models not only help us to understand the combination of particles pack in one system, but also turns out as a powerful tool to optimize packing in powder-bed AM. The concept of particle packing is graphically illustrated in Figure 136 which follows the idea from Johansen to pack concrete particles [303]. It shows that small particles fill voids between large particles in multi-powder packing system. Small particles contain even smaller voids that can also be filled by the smaller particles. The process can be repeated at smaller and smaller scales.

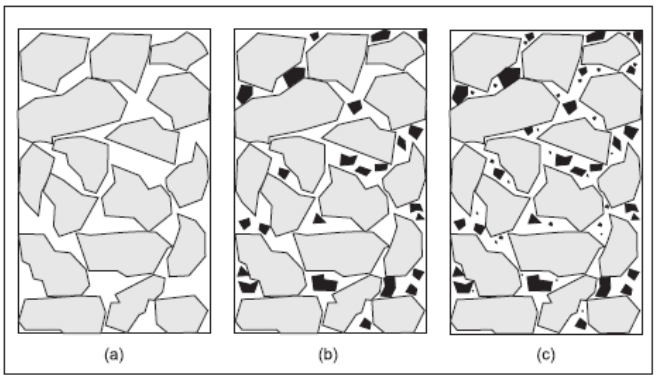


Figure 136. Concept of particle packing from[231]

Particle packing models could be categorized as discrete models and continuous models. Systems of discrete models contain multi-particles with discrete PSD and rely on the assumption that the coarsest particle size is much larger than the smallest one. Compared to discrete models, continuous models assume particles with different size evenly distributed in the system and no big gaps between size classes.

Discrete models also can be classified into different groups by the number of components, binary mixture model, ternary mode and multimodal mixture models. In binary-components situation, Furnas model [44] is considered as the ideally binary packing system, including one fine fraction and one coarse fraction (sometimes, the Westman and Hugill model [73]). As already explained, the principle underlying the Furnas model is that smaller particles are introduced and distributed in the interstices of coarser particles in order to reduce the porosity[233]. Furthermore, Furnas model only works in the case of infinite size ratio of coarse particles to fine particles. Again, measurements in real powders system showed lower packing

than predicted values especially when the particle size ratio decreased. Strong interaction effects not well handled by the model, happen as the particle size of two different classes becomes similar (named as wall and loosening effect as shown in Figure 137). When a single coarse particle locates in the matrix of fine particles, it disturbs the well packing of fine particles matrix, which is called as wall effect. Loosening effect happens when a fine particle is in the matrix of coarse particles and when this fine particle is too large to fill the interstices of coarse particles, which also breaks the packing of coarse powders. Aim and Goff powder models are also summarized in Kumar [231]. Toufar model and modified Toufar model proposed by Goltermann, are all based on ternary mixture models. Both of them regard the system as a set of binary mixtures to perform the calculation of packing density. Indeed, binary mixtures can be formed in any multi-components system and the packing density of the whole system is then the summation of all different binary mixtures. Additionally, linear packing density model (LPDM), solid suspension model (SSM) and compressible packing model (CPM) were also developed in order to obtain complex multi-component mixture packing models (De Larrard models)[231].

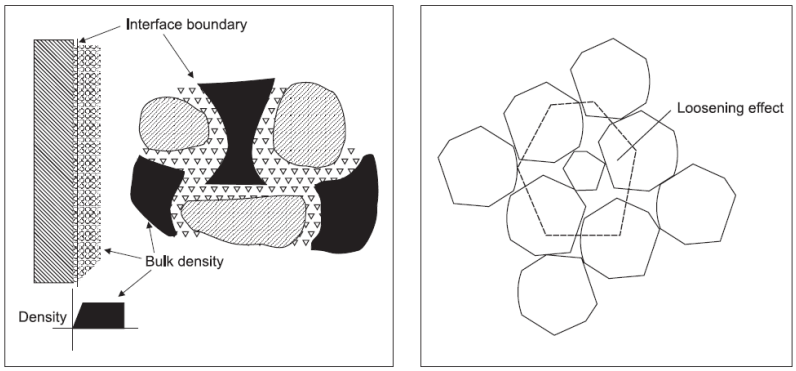


Figure 137. Wall effect and loosening effect. a): The wall effect at the interface of the aggregates fraction; b): The loosening effect caused by the fine grain particles

In opposite, continuous models have not categories related to any number of components, since all possible sizes of particle distribution are taken into consideration. Fuller and Thomson proposed a model [231] which considered an "ideal gradation curve" to reach maximum density. The model could be described by the equation:

$$CPFT = (\frac{d_m}{D_m})^n 100 \quad (19)$$

where CPFT is the cumulative (volume) percent finer than, n was 0.5 first and then was adapted to 0.45 while $d_m$ and $D_m$ are particle size and maximum particle size respectively. This model is generally applied in highway pavement mixture design. The model was revised by Shakmenko and Birsh [304] to forecast the mixture result for concrete material and can be expressed by equation:

$$CPFT = T_n(d_{mi} - d_{m0})^n \quad (20)$$

Where n is the degree of an "ideal" curve equation and $T_n$ is an index which relies on maximum size of aggregate and the n value. Afterwards, Andreassen came up with the model[305] thought over the continuous size distribution for packing and named as "Andreassen model" for the ideal packing. The model expresses the empirical theory for multi-particles packing and is written as:

$$CPFT = (\frac{d_m}{D_m})^q \quad (21)$$

where q is the distribution index or exponent. However, Andreassen considered in the model that the finer particle is infinitely small which is the most theoretically ideal situation. Therefore, Dinger and Funk took the realistic fact that even the smallest particles have finite size into consideration and modified the expression of the model [306]. The newly developed model is named as AFDZ (Andreassen, Funk, Dinger and Zheng) which is shown in equation:

$$CPFT = (\frac{(d_m - d_{m0})}{(D_m - d_{m0})})^q 100 \quad (22)$$

where $d_{m0}$ is the minimum particle size of the distribution. The coefficient q in the model varies from 0.21 to 0.37 which depends on the working requirements. The coefficient will be reduced if the proportion of finer particles increases. Nonetheless, the model is mainly used for concrete materials or refractory ceramics.

McGEARY[98] was inspired by Furnas model[44] and Wetman with Hugill[73]. According to experiments with different materials inside of cylindrical container, he concluded that neither materials density nor a difference in size from one material to another significantly affects final packing density. However, the size and shape of the container used for packing powders influence the final packing density. Also, it is well-known that fine particles couldn't pack as well as coarse particles due to inter-particle forces that destroy the systematic packing. For monomodal spheres packing, there were four theoretically packing arrangements: simple cubic, orthorhombic, double-nested and close packed as revealed in Figure 138, which ideally packed at 53.36%, 60.46%, 69.81% and 74.05% of true density. Nevertheless, measured average packing density only reached 62.5% because of inter-force between each particle. Besides, such close packed arrangements won't happen in reality due to mechanical forces inside of the powder bed.

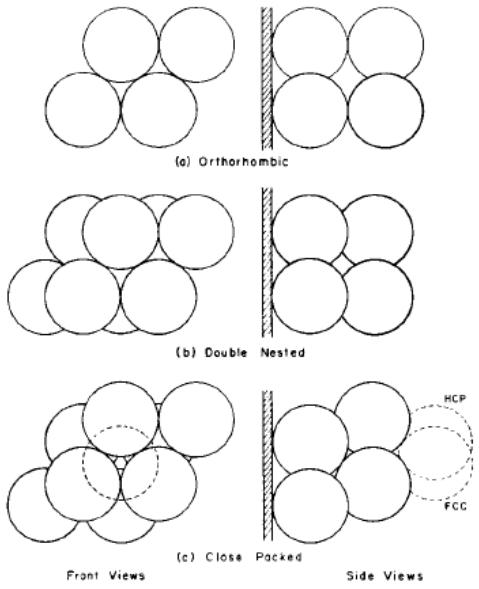


Figure 138. Possible situations of one-size spheres packing from[98]

Binary packing was also investigated with particles of different sizes. The authors chosen coarse spheres (7 mesh) and 7 different fine spheres to mimic the packing situation and it was found that smaller diameter for the finer particles resulted in a higher packing density. The trend for different binary packing situations is illustrated in Figure 139. A packing density of 84.7% is predicted by mixing 70% of coarse particles (7 mesh) with 30% of fine particles (100 mesh). To get this value, the authors detailed their process: they first vibrate the coarse component until it attained its minimum volume, and then they add the fine component into the container with vibration continued. They have also mentioned that well blending of powders mixture (coarse fraction and fine fraction) cannot be achieved because of an unavoidable segregation formed after blending even with sufficient time and intensity.

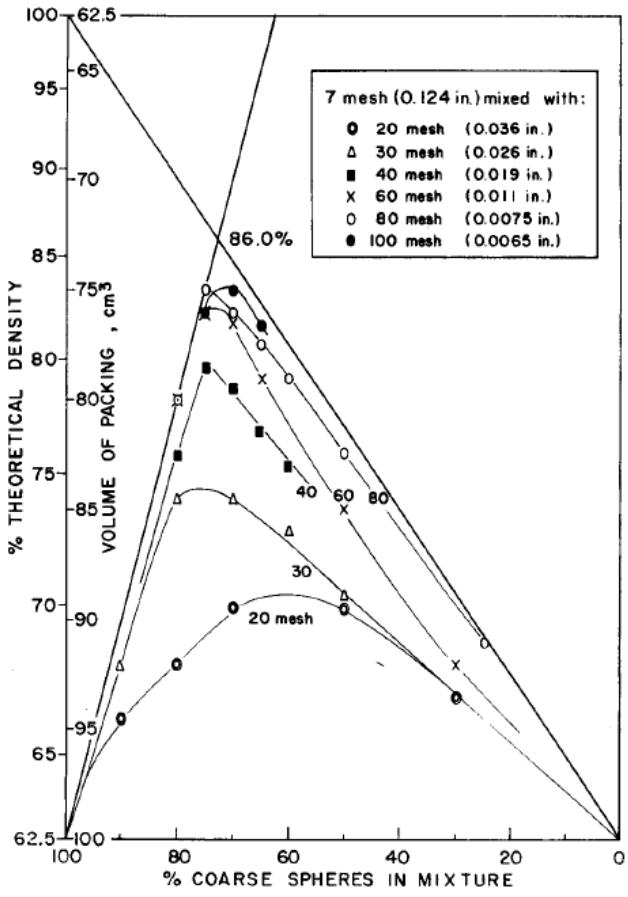


Figure 139. Binary packing system with situations of different sizes comparison from[98]

Meanwhile, German et al.[234] have also investigated a binary system by considering variations of coarse particles proportion. Five possible packing structures were given in Figure 140. In this figure, fraction of small particles is $f_S$ and fraction of coarse particles is $f_L$. The proportion of large particles in the mixtures is expressed by X. $f_L$ is slightly larger than $f_S$. The maximum packing density is noted $f^*$ and can be calculated with the following equation:

$$f^* = f_L + (1 - f_L)f_s \tag{23}$$

where 1-$f_L$ is the remaining interstitial volume between large particles when the large particles compose a packing at density $f_L$. Besides, wall effect and loosening effect are revealed in packing situations ii and iv. And the composition of large particles at maximum packing density ($f^*$) of whole system $X^*$ given as:

$$X^* = f_L/f^* \tag{24}$$

Furthermore, the density of the whole system $f_1$ could be expressed in Eq. 25 when there are more large particles in the mixture. In this case, small particles are hypothetically filling the voids between large granules without enlarging the total volume which leads to a higher density compared with the realistic one ($X > X^*$). The density of whole system $f_2$ is shown in Eq. 26 when the small particles dominate, and the large particles increase the packing density by

displacing numbers of small particles ($X < X^*$). In here the large particle is considered as a complete solid without inner pores[234].

$$f_1 = f_L/X \tag{25}$$

$$f_2 = f_S/(f_S X + 1 - X) \tag{26}$$

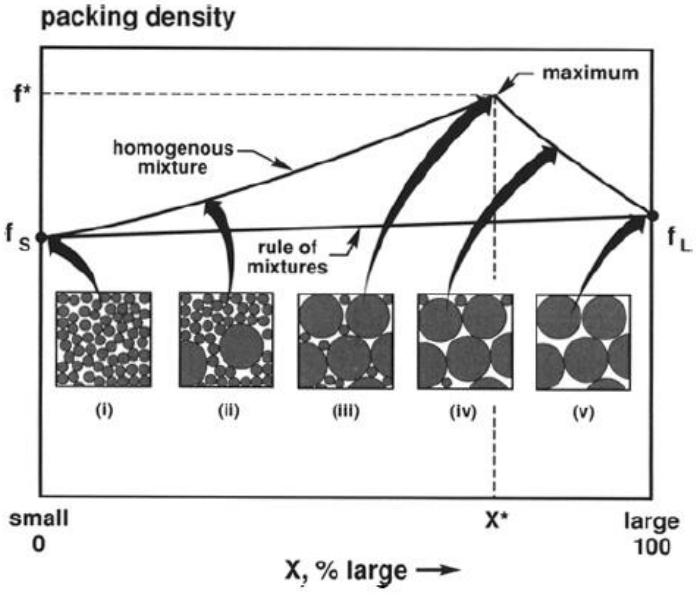


Figure 140. Packing density situations with different composition in binary system from[234]

Ternary packings and quaternary packings are also discussed in[98] as well. In ternary packing case, theoretical maximum density is reached at volume percentages 66 : 25 : 9 for coarse, medium and fine particles with size ratio 77 : 7 :1. Again there were some discrepancy between the calculated and experimental values. The experimental achieved a best 90 % relative density at the composition ratio at 67 : 23 : 10. In general, the density in system with at least three components can be calculated with equation[98]:

$$\rho = 100\left[1 - \frac{v_n X_n}{v_n X_n + V}\right] \tag{27}$$

in which n is the number of components in packing and normally larger than 3, $v_n$ is the volume fraction of voids in finest component, $X_n$ is the volume fraction of finest component and V is the volume of the solid which is a constant. As reported by the authors, theoretically calculated values and experimental ones were roughly the same.

Quaternary components packing or more components packing share similar theoretical background to the ternary situation. The highest experimental packing density of quaternary components system reached 95.1% of true density which can be prepared from particles with

diameter ratio 1:7:38:316 and volume compositions 6.1% : 10.2% : 23.0% : 60.7%. The experimental value is close to the theoretical relative density of 97.5 % [98]. It should be noticed that this value is approaching the value of pressed and well-sintered ceramic parts, which is highly appreciated. It is however something that is quite difficult to obtain practically speaking especially in powder-bed AM.

Nowadays, numerical methods to simulate multi-powders system have been developed. Different softwares are existing such as SPACE [307] (Software Package for the Assessment of Compositional Evaluation) which is a dynamic simulation system to aid the understanding of multi-powders packing system.

# 2. Powder mixing

Multi-modal powder mixing is considered as an effective method to enhance the packing rate of dry powder bed as described in section 1 (Appendix 2) and section 3.2.2 (Chapter 1) [73, 88, 97, 100, 233, 234, 308].. Voids existing in base powder bed formed by the large granules could be filled by adding the fine powders. The PSD becomes broader and non-Gaussian distribution (monomodal distribution) after mixing. Since the powder bed-based AM processes generally require the flowability of powders to have a smooth surface of finished powder bed, therefore, coarse granules could ensure the flowability at least and the fine powders enhance the packing rate which benefits both sides in the such system.

However, homogeneous mixing of powders was always not easy to handle according to authors experience. The segregation would appear with two fraction powders and the fine particles could form agglomerates which negatively affects the powder spreading and printing[90]. Additionally, mixing with extra-large particles with fine particles is also not the good option due to the limited sign of necking and coarsening during sintering[100].

In some preliminary tests carried out during this thesis, powder Al-CSP was chosen as fine fraction, Al-SP1 and Al-SP2 in Chapter 2 were chosen as two coarse fractions to conduct the mixing. The mixing operation failed since the Al-CSP powders always formed big agglomerates after mixing even the mixing strength (rotating speed of the container on roller bank).

Afterwards, two spray dried powders (SP1 and SP2 as described in Table 26) were chosen to carry out mixing despite the particle size distinction was not as huge as in preliminary test. Powders were both from main fraction of spray drying process demonstrated in Chapter 2. The morphology of the two powders is displayed in Figure 141 which are spherical with a partial “donut-shape” particles due to the imperfect spray drying process parameters setting.

## Appendix 2: Powder mixing and packing

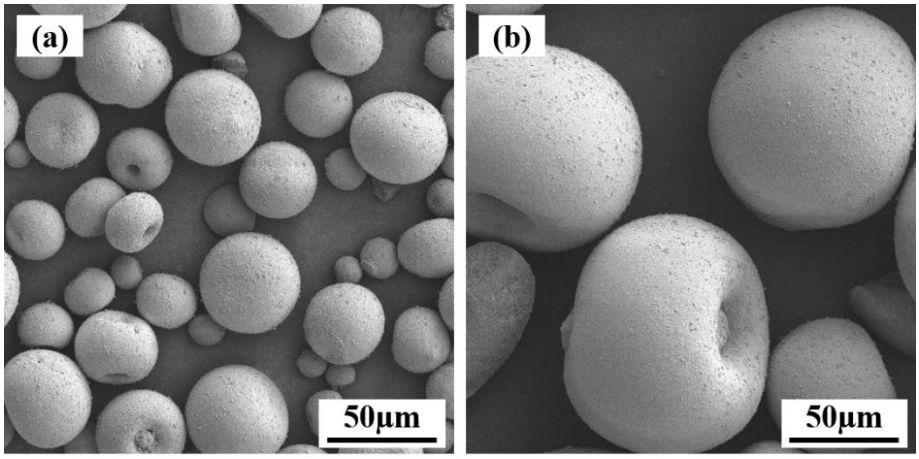


Figure 141. Morphology of powders a): SP1 and b): SP2

As said, the difference between PSD of two powders is not as huge as ones mentioned in [98, 100, 308]. The particle size of two powders were still discrete (SP1: $d_{90}$ = 80.6 µm; SP2: $d_{90}$ = 160.0 µm) to obtain efficient mixing behaviour. SP1 was regarded as the finer fraction and therefore SP2 was the coarser one.

Table 26. Composition and PSD of mixed powders

| Powders | Fraction of SP1 / % | Fraction of SP2 / % | d10 / µm | d50 / µm | d90 / µm |
|---|---|---|---|---|---|
| SP1 | 100 | 0 | 13.3 | 40.8 | 80.6 |
| SP2 | 0 | 100 | 40.1 | 92.9 | 160.0 |
| SP3 | 70 | 30 | 14.3 | 47.5 | 116 |
| SP4 | 50 | 50 | 21.4 | 69.3 | 156 |
| SP5 | 30 | 70 | 29.2 | 96.0 | 171 |

3 different mixed composition were prepared with powders ratios (SP1 : SP2): 7:3 (SP3), 5:5 (SP4) and 3:7 (SP5) respectively. In consequence, five powders were finally obtained to carry out further tests on flowability and packing density. PSD of the five powders are shown in Figure 142 and Table 28. Of course, PSD became broader for mixed powders while average particle size was larger with higher content of SP2.

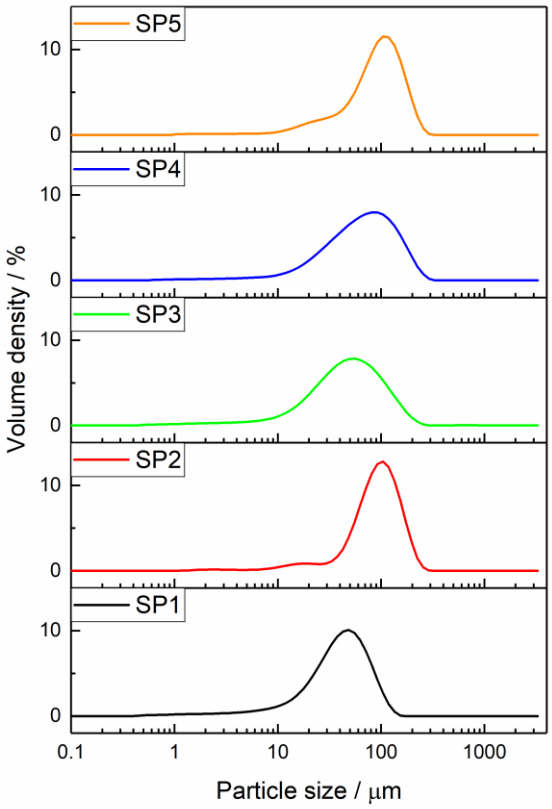


Figure 142. PSD of different powders

## 3. Flowability and packing density

The flowability measurement in this part is different to that presented in Chapter 2 which used Carr index and Hausner ratio as flowability indexes [46, 309]. Angle of repose was here determined to express the flowability with a "more direct" vision expression [55]. Angle of repose is defined as the steepest slope of the material which is measured from the horizontal plane on which powder could be stable without collapsing [50]. It is strongly related with static friction coefficient, angle of internal friction, powder properties, roughness of the base, pouring height and etc [55]. The concept and influencing factors are also summarized in section 3.2.2 (Chapter 1). Meanwhile, angle of repose is also linked with Hausner ratio and Carr index [55, 310]. The relation between values of angle of repose, Carr index and Hausner ratio is shown in Table 27. Measurement of angle of repose mimics the equipment developed by HosokawaMicron (Japan) as shown in Figure 143. Enough amounts of powders flowed from the conical funnel above the smooth circular plane. The flowing stopped until no more powders could steady keep on the powder cone and the slope did not change. The radius of the circular plane is 45.68 mm.

Table 27. Relationship of Angle of repose, Carr index and Hausner ratio with flowability of powders

| Angle of repose / ° | Carr index | Hauser ratio | Flowability |
|---|---|---|---|
| 25 - 30 | < 10 | 1.00 – 1.11 | Excellent |
| 31 - 35 | 11 - 15 | 1.12 – 1.18 | Good |
| 36 - 40 | 16 - 20 | 1.19 – 1.25 | Fair |
| 41 - 45 | 21 - 25 | 1.26 – 1.34 | Passable |
| 46 - 55 | 26 - 31 | 1.35 – 1.45 | Poor |
| 56 - 65 | 32 - 37 | 1.46 – 1.59 | Very poor |
| > 66 | > 38 | > 1.60 | Extremely poor |


Figure 143. Scheme of artificial angle of repose measurement

In this work, two different ways were considered and compared for measuring the angle of repose (θ). The first one is optical and consisted in taking images from front view with the same magnification[311]. The other one consisted in measuring the length and height of the cone shape with a ruler to calculate tan(θ). The results are reported in Table 28. The difference measured between the two methods is marginal.

Table 28. Angle of repose measured optically and calculated by the cone dimension

| Powders | Height / mm | Radius / mm | Tan(θ) | θ / ° | Optical degree / ° |
|---|---|---|---|---|---|
| SP1 (100:0) | 28.55 | 45.68 | 0.625 | 32.01 | 31.9 |
| SP2 (0:100) | 30.35 | 45.68 | 0.669 | 33.78 | 33.2 |
| SP3 (70:30) | 24.85 | 45.68 | 0.544 | 38.55 | 29.1 |
| SP4 (50:50) | 28.35 | 45.68 | 0.621 | 31.84 | 32.5 |
| SP5 (30:70) | 27.35 | 45.68 | 0.599 | 30.92 | 30.1 |

The data of angle of repose are plotted in Figure 144 as a function of the fine fraction. As explained before, coarser powders exhibit better flowability. Addition of fine powders impacts the flowability detrimentally. Even though, for the chosen fine powder, the angle of repose is

approx. 33° which is not a bad value [48, 310]. The trend shown Figure 144 is in line with expectations.

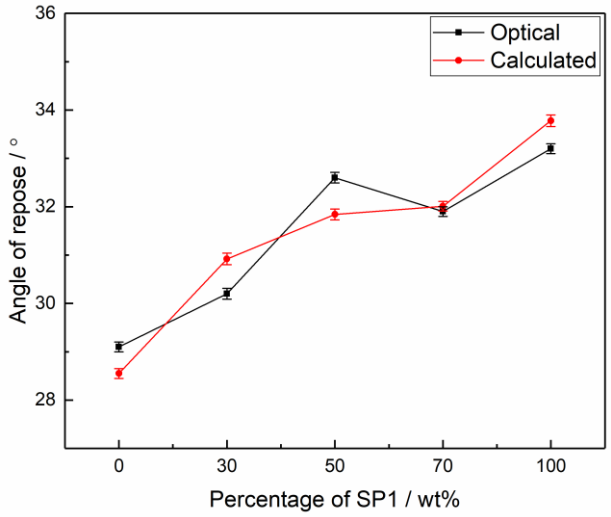


Figure 144. Angle of repose measured optically and cone dimensional calculated

As described in section 2.2 (Chapter 2), a rubber container was used to perform packing density measurements. Different powders were spread with the wiper inside of the container put above the manufacturing tank. The packing density was calculated by dividing the cavity volume with powder mass introduced in the mold after powder spreading. The ratio of packing density with true density of alumina powder (3.93 g/cm$^3$) is the packing rate. As expected, powder mixing improved the powder bed packing ratio. According to Figure 145, when the fraction of fine powders is increased to 70 wt%, the packing ratio is the highest and achieved 34.9 %. According to McGeary for binary-powders mixing system[98], a packing density of 84.7% could be reached by mixing 70% of coarse particles (7 mesh) and 30% of fine particles (100 mesh). This is obviously very different from our experimental results. There are two main reasons for this difference: The first one concerns the ratio between the sizes of fine and coarse particles. In our case, this ratio is close to 2. This value is much lower than the one used by McGeary. The measurement protocol is also different. McGeary used a vibratory system to maximize the compactness which our equipment does not contain.

Even though, the triangle shape (Figure 145) of the packing ratio distribution according to fine particles percentage was very similar to the one shown by McGeary and German [234].

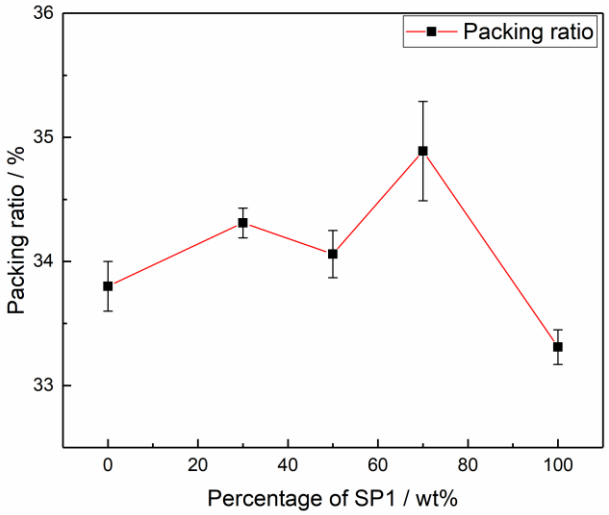


Figure 145. Resulted packing rate of mixed powders

Additionally, the results perfectly fit the model proposed by Du et al. [308]. It also explained that packing density of mixed powder bed could be higher when the ratio of coarse powders and fine powders become larger. With more fine powders added in the system, the voids will be filled between coarse granules which is called filling effect [312]. However, much more fine particles would cause loosen effect [231] as described in section 3.3.2 (Chapter 1). Furthermore, occupying effect [312] will happen when increasing the amount of coarse particles since they could occupy the voids between fine particles. Nonetheless, excessive coarse particles lead to the wall effect as explained before [231]. Compared with the packing density predicted by the models [98, 234, 308], real packing density of powder beds is always lower because of the complex inter-particle forces and environmental conditions (temperature, moisture, etc).

# Appendix 3. Overview of laser/matter interactions and laser milling of ceramics

## 1. Laser machining

Machining or cutting of ceramics remains highly challenging because of their high hardness and inherent brittleness [313]. According to Anoop et al. [253], ceramic fabrication techniques comprise different machining operations such as: mechanical, chemical, electrical using radiation and more recently hybrid machining as shown in Figure 146.

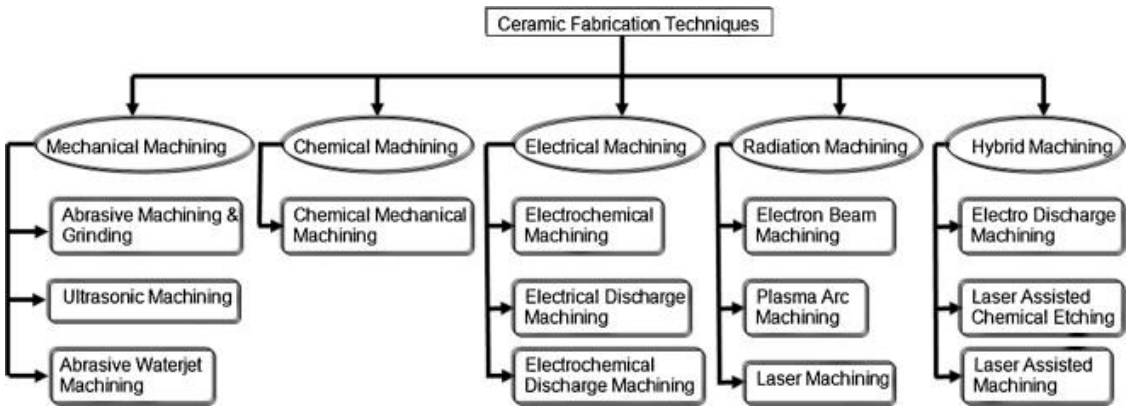


Figure 146. Different ceramic fabrication techniques from[253]

Conventional machining methods more or less generate surface cracks and/or residual stresses that may decrease the final mechanical strength [314]. Some of these issues are related to the contact between the tool and the workpiece. Therefore, laser machining (Figure 147) also called laser ablation [313] is sometimes preferred as it is a non-contact machining with almost no mechanical stresses exerted on the part and with a limited thermal impact [313].

During laser machining, a lens concentrates the laser beam on the focus spot to produce an energy density sufficient to remove the material by melting, dissociation/decomposition (by breaking chemical bonds), evaporation and melt expulsion [253, 315]. Moreover, laser machining often limits residual stress inside of parts and surface defects that may weaken the treated piece. High resolution machining can be achieved with a laser especially at small wavelengths [316, 317].

## Appendix 3. Overview of laser/matter interactions and laser milling of ceramics

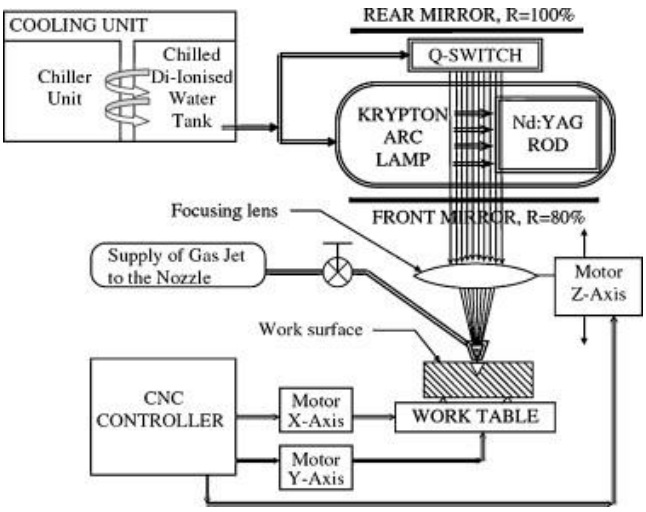


Figure 147. Scheme of laser machining from [253]

There are 3 main features of laser machining summarized in [255]:

- Non-contact process: the energy or force is transferred from the laser on workpiece through irradiation. The material removal can be controlled by modifying laser parameters instead of using mechanical forces or tools;
- Thermal process: Thermal and optical properties dictate the efficiency of laser processing. Generally, hard and brittle ceramics with poor thermal diffusivity and conductivity would benefit from laser machining;
- Flexible process: Laser could be manipulated easily and precisely to perform machining. Drilling, cutting, grooving, welding and heat treating all could be conducted by altering laser parameters.

Nowadays there are different lasers for industrial uses that differ by their wavelength, operating mode (continuous or pulsed) and pulse duration. Most used lasers in the industry are $CO_2$, Nd:YAG, Excimer [253, 255] and Fibers. They are shortly described hereafter.

- $CO_2$ laser is molecular type system which uses gas molecules (combination of dopant dioxide, nitrogen and helium) as medium. Excitation of dopant dioxide is induced by enhancing the vibrational energy of the molecule. It operates at quite long wavelength (far infra-red: 10.6µm) and usually in a continuous mode.
- Nd:YAG is a solid state laser which uses dopants ($Nd^{3+}$) dispersed in the crystalline medium to generate the active material. Excitation is achieved by krypton or xenon flash lamps and the output wavelength is 1.06µm. The Nd:YAG laser generates higher peak power but low energy efficiency and beam quality. By using conventional $CO_2$ and Nd:YAG lasers, thermal stresses and microcracking as well as amorphous glassy phase formation are usually generated because of rapid melting and re-solidification

during laser-ceramic interaction [318]. Using ultra-short pulse duration (pico and femtosecond) allows reducing those defects (the so-called "heat affected zone" or HAT) at the expense of the system price and average power.

- Excimer laser is a form of ultraviolet laser that is composed of two identical species which exist in excited states. Argon fluoride, krypton fluoride, xenon fluoride and xenon chloride could be used as complexes with an output wavelength ranging from 0.193 to 0.351 μm. UV light pulsed laser interacting with ceramics is dominated by a direct band-band excitation and only a few heat is transferred to the surrounding, thus reducing the heat affected zone [318].
- Fiber laser is a kind of laser which takes optical fiber doped with rare-earth elements (such as erbium, ytterbium, neodymium, dysprosium, praseodymium, thulium and holmium) as active gain medium. This kind of laser is nowadays the most popular one as they offer the best power density and are very affordable [319].

# 2. Laser/matter interactions

Lasers can be operated in different modes: continuous mode or pulsed mode (in which the pulse duration is a critical parameter). Consecutive pumping of the laser emits continuous light while pulsed laser has off-time between two pulses emission [320]. It is also chosen to work with pulsed mode to reach the highest energy during an extremely short duration to conduct machining [253].

## 2.1. Laser absorption

In real cases, interaction is even more complex if the substrate contains porosity. Laser beam also reflects along the wall of cavities which may influence the energy absorption efficiency as explained in [253].

The laser energy absorption ($Q_a$) of ceramic after reflection could be expressed by Eq. 28[321]:

$$Q_a = Q(r)^n \tag{28}$$

where Q is the input laser energy, r is the angle-dependent reflection coefficient of the ceramic material, and n is the number of multiple reflections which is calculated in Eq. 29 [321]:

$$n = \frac{\pi}{4\theta} \tag{29}$$

where θ is the angle that the cavity wall makes with normal direction. Since the thermal conductivity of structural ceramic materials is less than metals, therefore, the incident energy is more rapidly absorbed [322, 323]. Additionally, in the case when heat transfer via convective and radiative routes are negligible, the temperature distribution derived from laser radiation absorption is expressed by the heat conduction in Eq 30 [266]:

$$\frac{\rho(T)C_P(T)\,\partial(x,z,t)}{\partial t} = \nabla[\kappa(T)\nabla T(x.z.t)] + Q(x,z,t) \quad (30)$$

where x and z are space coordinate in the transverse direction and normal direction to the target surface respectively. ρ, $C_P$ and κ are density, specific heat at constant pressure and thermal conductivity of material separately. The right side are heat conduction and energy input which is the laser incident energy.

## 2.2. Thermal effects

Whenever the laser beam hits on ceramic workpieces, various interactions may occur as shown in Figure 148. These interactions can be classified by the temperature reached after energy absorption such as melting, sublimation, vaporization, dissociation, plasma formation and ablation.

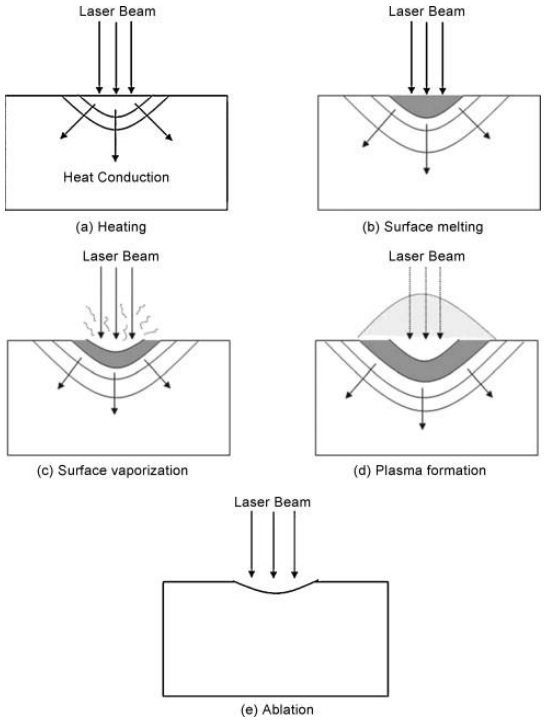


Figure 148. Various phenomena resulting from laser-material interaction [321]

Heat transfer is highly dependent on properties of treated material and laser parameters. The absorbed energy is rapidly converted into heat in the workpiece (conduction, radiation and convection). Conduction of heat is dominated by Fourier's second law of heat transfer as shown in Eq. 31 [253]:

$$\frac{\partial T(x,y,z,t)}{\partial t} = \alpha(T)\left[\frac{\partial^2 T(x,y,z,t)}{\partial x^2} + \frac{\partial^2 T(x,y,z,t)}{\partial y^2} + \frac{\partial^2 T(x,y,z,t)}{\partial z^2}\right] \quad (31)$$

where T is the temperature field, t is time and x, y, z are spatial directions. α(T) is thermal diffusivity which depends on temperature as in Eq. 32 [253]:

$$\alpha(T) = \frac{k(T)}{\rho C_p(T)} \tag{32}$$

where k(T) and $C_P$(T) are temperature dependent specific heat and thermal conductivity respectively, and ρ is the density of the material. Melting and sublimation

Melting happens when the temperature becomes higher than the melting point of the ceramic material [324]. Melting should be avoided as much as possible as it influences negatively the quality of finished part (solidification of the melt pool may create an amorphous phase, full of cracks). The phenomenon can be handled more easily by considering a critical thermal relaxation time which is about the dissipation of heat during pulse irradiation (Eq. 33).

$$\tau = \frac{d^2}{\alpha} \tag{33}$$

where d is the adsorption depth and α is the thermal diffusivity. In the interaction between laser and the ceramic workpiece, electrons absorb the energy emitted from the laser and they thermalize in approx. 100 fs. Thus, an equilibrium between electrons and the lattice is reached after multi-electron-phonon relaxation time. Generally, time of relaxation ranges from 0.5 – 50 ps. It should be noted that no heat will be transferred to the lattice if the laser pulse duration is less than the relaxation time, in another word, no melting nor other thermal damages could happen (something which is possible if one uses femtosecond lasers). However, evaporation starts for continuous ns and the materials melt for pulse durations longer than 10 ns. Consequently, thermal processes happen in the ns regime but could reach a minimum [325] by modifying the laser parameters and/or ceramic properties.

### 2.2.1. Vaporization and dissociation

Materials removal is obtained by evaporation when the surface temperature reaches the boiling point [253]. During the process, the liquid-vapor surface moves into the workpiece and materials are progressively vaporized from the surface above liquid-vapor interface [321]. The expressions of liquid-vapor velocity and vaporization depth are shown in Eq. 34 and Eq. 35 [326]:

$$V_{evaporation} = \frac{Q_a}{\rho(cT_b + L_V)} \tag{34}$$

$$d_{evaporation} = \frac{Q_a t_p}{\rho(cT_b + L_V)} \tag{35}$$

where $Q_a$ is the absorbed laser energy, ρ is the density, c is the light speed, $T_b$ is the boiling point, $L_V$ is the latent heat of vaporization and $t_p$ is laser ON-time. The enthalpy of vaporization should be larger than the value of melting and the required energy of vaporization is also higher

spontaneously [327]. Different physical changes mentioned above exist in the laser machining simultaneously instead of the single process[253, 328].

### 2.2.2. Plasma formation

Ceramics are vaporized rapidly and get ionized to form plasma which shows extremely high temperature up to 50,000°C (and sometimes even more) with a pressure that raises to 500 MPa when the laser energy density exceed the threshold value [329].

As explained in[253], the plasma plume forms a layer over the machining area which reduces the energy for the workpiece and the machining efficiency decreases as well. Special gas nozzle was invented to prevent the deposition of aerosols from ionized vapor [330].

### 2.2.3. Ablation

Thermal ablation is conceptualized as the behaviour that combines evaporation and melt expulsion [325]. It is achieved for high power laser only (usually pulsed ones) [259]. Ablation happens when the incident laser energy is larger than the threshold laser energy which is the minimum value of energy to remove the materials through ablation. The ablation threshold is related to various factors such as materials properties and laser parameters [262]. Theoretically, materials ablation conducted with nanosecond laser is highly thermal. The laser energy absorbed is transferred to the lattice through electron-photon which results heating and phase transition. The cumulated energy leads to the evaporation of the target materials under different physical forms, such as fine vapor, liquid droplets, solid flakes or fragments [266]. Laser-ceramic interaction includes different complex reactions as described by Samant et al.[331]. According to these authors, laser machining of ceramics combines melt expulsion, dissociation and evaporation. Besides, it is also mentioned that laser-ceramic materials interaction is dominated by photo-thermal (under threshold energy) and photo-chemical (above threshold energy) processes [253]. The ablation depth inside of workpieces could be presented in Eq. 36:

$$d_{ablation} = \frac{1}{\mu_a} \ln\left(\frac{Q_a}{Q_{th}}\right) \tag{36}$$

where $\mu_a$ is the adsorption coefficient of the ceramic material, $Q_a$ and $Q_{th}$ are incident laser energy and threshold laser energy respectively. Meanwhile, ablation crater diameter could also be expressed by Eq. 37 [262]:

$$D^2 = 2{\omega_0}^2 In\left(\frac{F_0}{F_{th}(N)}\right) \tag{37}$$

where $\omega_0$ is the beam waist (Figure 149), $F_0$ and $F_{th}(N)$ are laser fluence and the ablation threshold with N effective pulses respectively.

Besides, $F_{th}(N)$ also could be calculated according to Eq. 38 [262]:

$$F_{th}(N) = F_{th}(1)N^{S-1} \quad (38)$$

where S is the incubation coefficient and $F_{th}(1)$ is the ablation threshold with 1 pulse. And N could be obtained from Eq. 39 [262]:

$$N = \frac{2\omega_0 f}{\upsilon_{ls}} \quad (39)$$

where $\upsilon_{ls}$ is the scanning speed which governs the number of pulses.

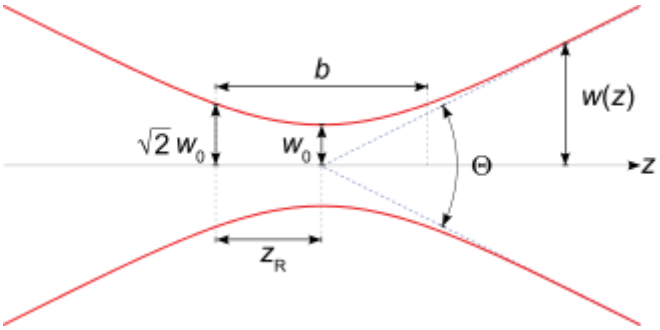


Figure 149. Beam waist. Gaussian beam width as a function of the distance z along the beam, in where beam waist: ω0, focal depth: b, Rayleigh range: $z_R$ , total angular spread: Θ [332]

As discussed in [259], the laser beam is supposed to have a Gaussian profile and the phase transformation is assumed to be from solid to vapor without melting, however, it is not possible in reality. Therefore, minimizing the degree of melting during ablation by using short-pulse lasers to achieve the highest quality of finished part is necessary [316, 333-335]. Furthermore, ablation or materials may modify the reflectivity of the target surface with results in scattering loss of the laser beam [266]. Hence, normally a general value reflectivity is preferred in the model. There are some requirements on the pulse duration as longer laser pulses may promote the crack formation [266, 325, 336]. There is always compromise between rapid ablation rate and quality of surface finishing during the process, however, the optimization of laser parameters could establish a balance between them [325]. The ablation process for dense $Al_2O_3$ parts includes melting at 2323 K and vaporization at 3773 K [337]. Besides, the recast layer of melt materials formed by re-solidification surrounds the hole which might be problematic on precision machining [338].

As explained before, the physical process within nanosecond laser ablation is extremely complex and an accurate theoretical model to perform prediction is also very difficult to build.

### 2.3. Ceramic machining with pulsed lasers

The critical factors affecting laser machining are reflectivity, thermal conductivity, specific heat and latent heats of melting and evaporation [253]. It should be noticed that inert atmosphere is required when processing reactive materials [315]. Firstly, ultrashort-pulse (picosecond and femtosecond) lasers show huge amounts of benefits in parts machining

(especially micro-machining) as they strongly reduce the heat affected zone. Picosecond lasers are commonly used for processing metals while femtosecond lasers are very efficient to process dielectrics (but not only) [325]. Ultrafast laser machining uses high energy pulse with ultrashort duration (< 10 ps) and thus, megawatt of power could be generated to vaporize materials with minimal thermal diffusion[313]. The thermal affected zone is dramatically reduced within the cutting/milling area which is crucial. For long pulse durations, laser ablation depends on absorption of laser photons and consequently laser wavelength has to match the material properties. On the contrary, ultrafast lasers ablate materials through multiphoton absorption at high peak intensities even the material is transparent [321].

In comparison, nanosecond lasers ($\lambda$=1064 nm) could machine ceramic parts with high quality and high ablation rate [338]. However they tend to generate a significant heat-affected zone because of high energy density and longer material-laser interaction duration[263]. Since the typical time for heat conduction is around 100 fs [339], the incident laser energy during nanosecond laser interaction involves necessary thermal effects [259]. Partial energy is reflected at the surface and the rest is absorbed with a penetration depth characterized by the material absorption coefficient [266]. Nevertheless, nanosecond laser owes high productivity and low costs compared with femtosecond and picosecond lasers [263]. One nanosecond laser is utilized in this work due to its advantages.

### 2.4. Laser parameters

As said before, different factors will exert a critical influence on treated ceramic parts, such as ablation rate, raster pitch, traverse speed, focal position, average power, scanning speed, polarization and processing sequence[313]. In general, an exact model of the laser-material interaction cannot not be built especially when it comes to porous ceramic bodies. However, the influences of these different factors on ablation result can be investigated numerically and compared with experiments. Chen et al. [259] have proposed a model to assess the influence of various parameters on laser ablation including: laser fluence, energy-distribution radius, pulse duration at full width at half maximum (FWHM), optical penetration depth as well as certain materials parameters (reflectivity, evaporation latent heat, thermal diffusivity, mass density, heat capacity and evaporation temperature).

They found that the ablated depth and crater diameter per pulse increase with increasing laser fluence, however, the effects raised from increasing reflectivity, evaporation temperature and mass density showed opposite. The small energy-distribution radius could reduce the squared crater diameter as well. When the optical penetration depth increased, squared crater decreased. Meanwhile, the ablation rate started at higher fluence and the value per pulse was less at lower laser fluences at bigger optical penetration depth [259].

# 3. Laser treatment of dense ceramics

Compared to laser machining of metals, the treatment of ceramics is even more challenging since the large scattering of material at various laser wavelength which also restricts the laser absorption. As a rule of thumb, laser with both shorter pulses and wavelength always gives better results for ceramics with more limited thermal (and deleterious) effects [325].

For instance, Beausoletil et al.[313] have developed a laser cutting strategy with picosecond laser to obtain alumina ceramic parts with high precision, deep and defects-free laser cutting tracks. Different parameters have been considered to optimize the laser finishing by evaluating cut quality (cut depth, kerf width, kerf taper, surface roughness and cleanness), such as focal position, linear speed and wobble amplitude (partially shown in Figure 150). Furthermore, material removal rate and efficiency were assessed as well. It was concluded that an optimized processing by using a circular wobble pattern at linear speeds between 20 – 30 mm/s, with coordinated motion between the laser scanner and the stage benefited the final property of laser-cut parts. Besides, laser energy density varied by altering the laser parameters which also led to the difference of heat affected zone / heating effect (melting regime, transition regime and ablation regime).

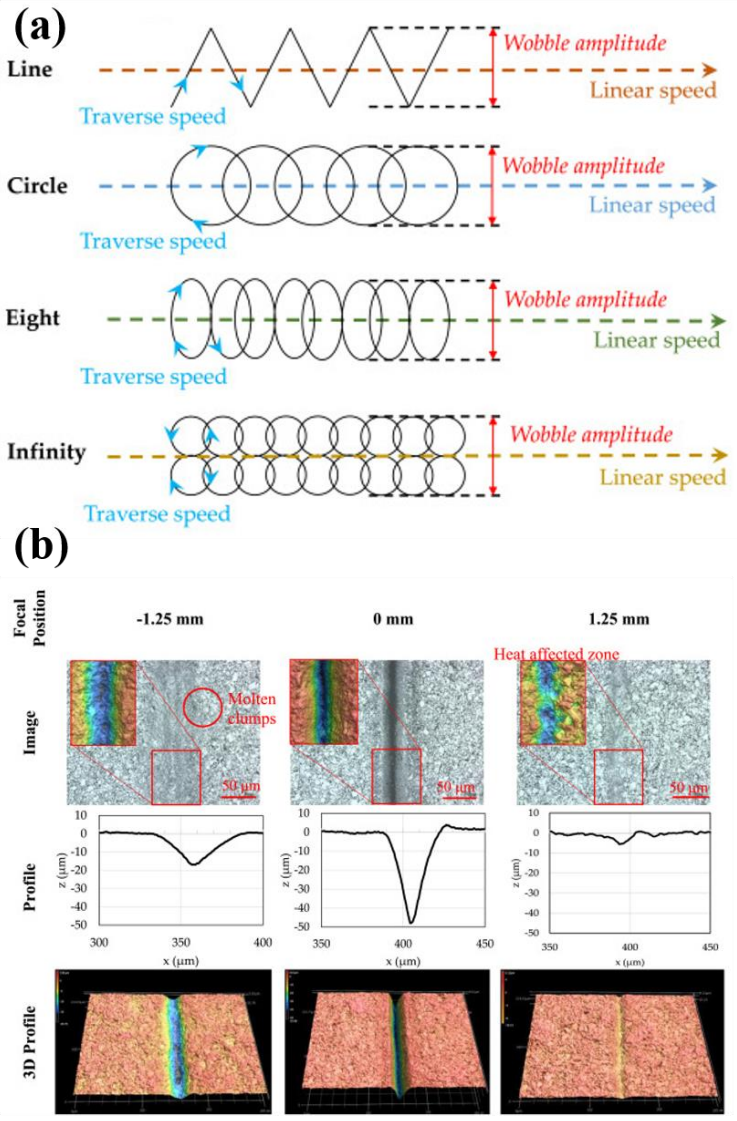


Figure 150. Laser machining on dense ceramic. a): Different wobble pattern shapes and parameters; b): 3D laser scanning microscope images and topography of ceramics for various focal position from [313]

Xing et al.[263] have used nanosecond laser to create micro-channels on $Al_2O_3$/TiC ceramic parts. Micro-channels on ceramic substrates were well-conducted and the different laser parameters had apparently influence on finished surface quality. The width and depth of the kerfs were affected by different laser process parameters (voltage, scanning speed, frequency and numbers of over-scanning) with resulted in energy accumulation and surface chemistry modifications (Figure 151). Optimized laser parameter recipe was defined afterwards and evolution of chemical composition after laser treatment was also investigated.

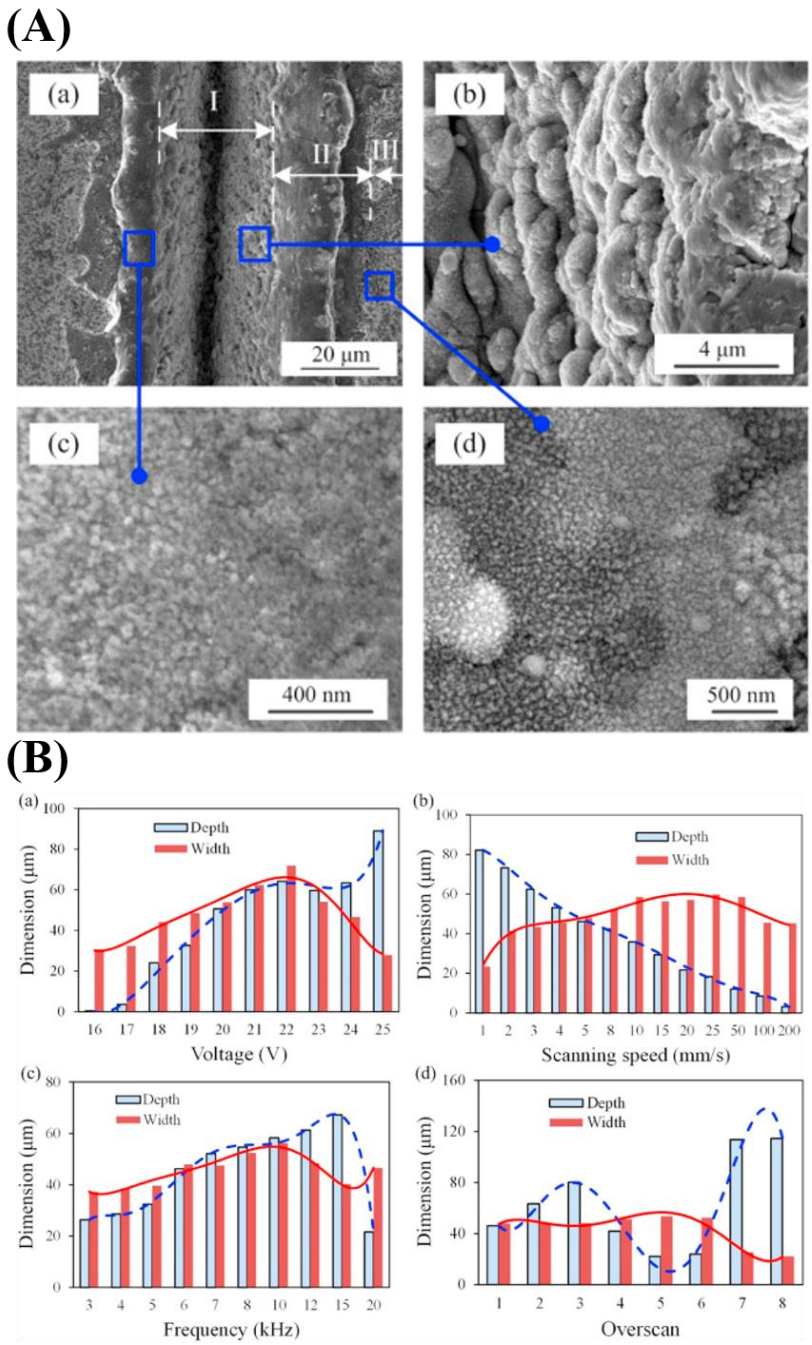


Figure 151: Influence of laser machining on dense ceramic. A): SEM images of heat-affected zone. I: micro-channel, II: deposition zone, III: modification zone; B): Variations of channel width and depth with different parameters (voltage, scanning speed, frequency and numbers of overscanning) from[263]

Pulsed laser (ArF laser) treatment was also used to smooth out the asperities of sintered and partially polished ceramic products. The laser was used to fill in the voids and pores of ceramic surfaces by sputtered and redeposited materials, and chemical decomposition of aluminum oxide was avoided [318].

# Appendix 3. Overview of laser/matter interactions and laser milling of ceramics

# Appendix 4. Materials and characterization methods

## 1. Introduction

This appendix describes the different materials that have been used to carry out the thesis. The processing routes for the granules (freeze drying and spray drying) are presented. The most relevant characterization techniques used are also introduced.

## 2. Materials

Two different raw alumina powders were used: a fine alpha-alumina powder (P172LSB, Alteo, France). Carboxylic acid dispersant Dolapix CE64 (Zschimmer&Schwarz, Germany) was the dispersant used for all ceramic suspensions. A commercial water-based binder (Tethon, United States) was chosen because of the smooth printing without clogging the printhead (Xaar, United Kingdom) and relatively good interaction with alumina granules (the binder penetrates easily the powder bed porosity). Dopant was chosen to supply dopant content to the powder for the laser treatment and nitric acid (65%, CHEM-LAB, Belgium) was added in the ceramic suspension to adjust the pH in presence of dopant. All used raw materials are listed in Table 29 as follow.

Table 29. Materials information in this work

| Name | Components | Supplier | Used for/as |
|---|---|---|---|
| Raw alumina P172LSB | Alumina | Alteo, France | Granule preparation, ceramic suspension, printing test |
| Tethonite binder | Water, glycerol, etc | Tethon, United States | Printing |
| Dolapix CE64 | Carboxylic acid | Zschimmer&Schwarz, Germany | Dispersant |
| Dopant | - | - | Laser additive |
| Nitric acid 65% | $HNO_3$ | Chem-Lab, Belgium | pH modification |

# 3. Materials processing

## 3.1. Freeze drying

Freeze drying was aimed at obtaining slightly agglomerated particles non spherical in shape. A ceramic suspension containing 70 wt% ceramic powders, 30 wt% deionized water and 1.5 wt% (in respect to the weight of powder) of dispersant (Dolapix CE64) was frozen at 77K with liquid nitrogen. It was then dried using a Freeze dryer (Martin Christ, Germany) at the following settings: pressure: 0.5 mbar; trap temperature: 183K; duration: 24 hours. After the process completion, the grains are grinded and sieved at 200µm.

## 3.2. Spray drying

Spray drying process is the most efficient approach to produce dry granules from a slurry by rapidly drying droplets with hot gas and pressure. There are four stages in the whole process: atomization of the feeding slurry, contact of droplet-air, droplet drying and separation of dried particles from the hot gas[340]. The atomization takes place either via a rotary atomizer or high-pressure swirl nozzles. The process of the spray dryer is graphically shown in Figure 152. It is based on moisture elimination using a heat medium / atmosphere to which the feed product is subjected [341]. The prepared suspension with well-dispersed particles is pumped into atomizer / nozzle, ejecting the liquid feedstock into a spray of droplets. The droplets are dried in a chamber where the liquid phase evaporated, resulting in the formation of dried granules. Consequently, the dried granules are separated from the drying medium and collected.

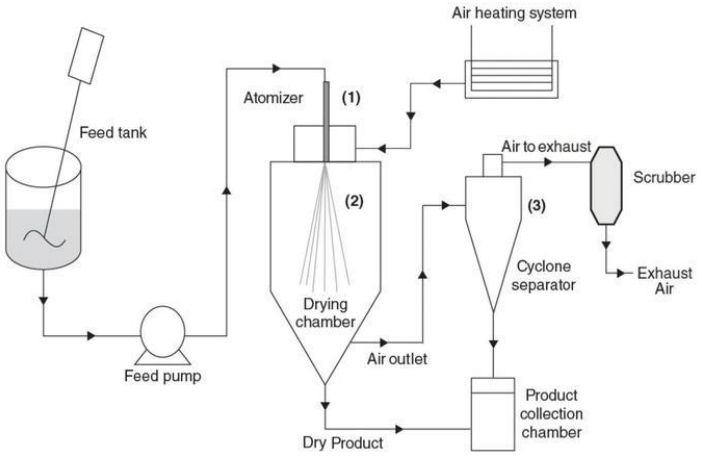


Figure 152. Scheme of the spray dryer from [341]

Difference factors influencing the properties of final dried products such as inlet temperature, solid loading of the suspension, feeding rate, organic content and so on. The influences are highlighted with the arrows in Figure 153 and the strengthen of the influences is indicated by the width of the arrow.

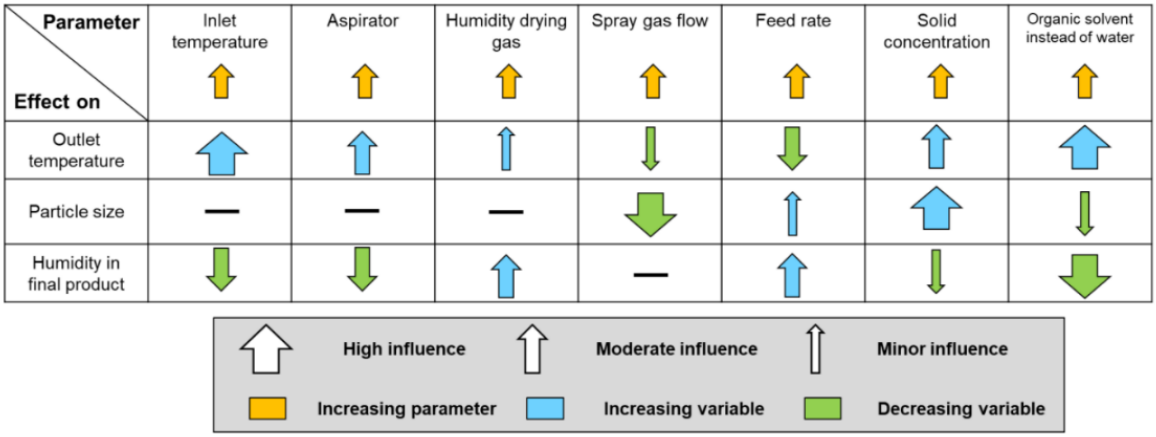


Figure 153. Influencing factors in spray drying process on products from[341]

Normally the produced granules are spherical. However, different shapes of granules could be obtained as well such as donut, convex and mushroom because of hydrodynamics effects [342]. Excessive high temperature or the existence of surfactant might cause shape variations as well. Okuyama et al. [342] also found that donut shape particles express higher surface area and higher porosity.

For this conducted work, spray drying was performed with a Niro machine (GEA, Germany) with 9 kg raw alumina powders produced for each batch. The ceramic suspensions where prepared using the same protocol than freeze drying. The inlet temperature ranged from 210°C - 225°C and the outlet temperature was controlled at around 95°C. The inlet air flow rate was 70 L/min and the feeding rate of suspension was 25 rpm. After the spray drying, powders from main fraction and cyclone fraction were both dried at 110°C to evaporate the residual moisture.

# 4. Characterization methods

## 4.1. Powder granulometry by laser diffraction

For the work done in Chapter 2, the particle size distribution (PSD) was measured on a Malvern Mastersizer 2000 in dry mode (Malvern Instruments GmbH, Germany). The machine is suitable to measure PSD ranges from 70 nm to 2 mm by applying a single optical measurement path. It uses a sequential combination of measurements with red (632.8 nm) and blue light (470.0 nm) sources to measure across the entire particle size range. Each sample was measured at least 3 times to obtain an average value.

PSD measurements in Chapter 3 and 4 were measured with a Mastersizer 3000 (Malvern Instruments GmbH, Germany) because of lab upgrading. This time, the PSD of dispersed particles in ceramic suspension was carried under hydro mode. Suitable particle size could be measured was extended to 3.5 mm. The measurements were conducted with external ultrasonic probe and the water was under agitation at 2000 rpm.

### 4.2. BET surface measurement

All specific surface area (SSA) measurements were carried out with a FlowSorb III surface area analyzer (Micromeritics, UNITED STATES). The machine provides both single-point and multi-points BET surface measurements for surface areas ranging from 0.01 $m^2/g$ to more than 1000 $m^2/g$. Prior SSA measurements each powder was further dried in an oven for 24 hours at 110 ℃ and previously degassed at 120 ℃ under nitrogen flow. Each sample was measured at least 3 times to obtain a mean value.

### 4.3. Surface tension

Surface tension is a critical parameter to assess the suitability of a binder for inkjet printing. For the thesis it was determined for the commercial binder with a Tensiometer (KRÜSS, Germany) with SFT plate method according to Du Noüy. In this case, the force applying on a wettable ring as a result of the tension of the withdrawn liquid lamella when removing the ring is measured. KRÜSS standard curved platinum plate (perimeter: 19.9 mm, depth: 2 mm) was used and should be cleaned by deionized water and acetone. The detection speed, sensitivity and immersion depth were 2 mm/min, 0.005g, and 2 mm respectively. 20 points were conducted in each measurement and the deviation was controlled within 0.1 mN/m.

### 4.4. X-ray Diffraction (XRD)

X-ray diffraction was used to clarify whether there was phase transformation after hybridized process with laser as described in Chapter 4. The data was collected by using a Rigaku diffractometer (Miniflex 600, Rigaku, Japan). The measurement is conducted with Cu tube (Kα radiation, $\lambda = 1.5406$ Å) and $2\theta$ values from 20° to 70°. The step size was 0.02°. Scanning speed was 0.3°/min.

### 4.5. Scanning Electron Microscope and Energy Dispersive X-ray Spectroscopy (EDX)

SEM was used to characterize the morphology and microstructures of samples, the shape of granules and the cut profiles. Main observations were conducted with scanning electron microscopy (Tescan Gaia 3, Czech Republic). The measurements have been conducted applying a 10 kV voltage. Previously to SEM analysis, the samples have been coated with platinum under vacuum in case of electrons charging by using an evaporating system JEOL JFC-1300.

### 4.6. Pycnometer

True density of raw powders was measured with a helium pycnometer Accypyc III (Micromeritics, UNITED STATES). Each sample was measured at least 3 times to obtain a mean value.

### 4.7. Absorption spectroscopy

Adsorption spectroscopy measures the absorption of radiation as a function of frequency or wavelength resulting from optical interactions with the sample. The technique was used to qualify the absorptivity of the powders at the laser wavelength (1060 nm) in Chapter 4. Pellets samples were prepared with following dimensions: 3mm thick, 15mm diameter. The measurement was conducted on Lambda 750 (PerkinElmer, USA) and analyzed on UV WinLab version 6.4.1 (PerkinElmer, USA. Scanning wavelength ranged from 2500 nm – 300 nm. the scanning speed and interval data were 854.87 nm/min and 10 nm respectively. Reflection signal was measured and the background calibration was done for each measurement.

### 4.8. Acoustosizer

Acoustosizer IIX (Acoustosizer II-M system, USA) as shown in Figure 154 allows a complete characterization of concentrated colloidal dispersions: particle size, zeta potential, pH, conductivity, viscosity and temperature can all be measured. The machine uses electrical fields and acoustic waves to generate particle vibrations or resonance. The acoustic wave emitted as a backreaction of the particles is detected by a piezo-electrical sensor.

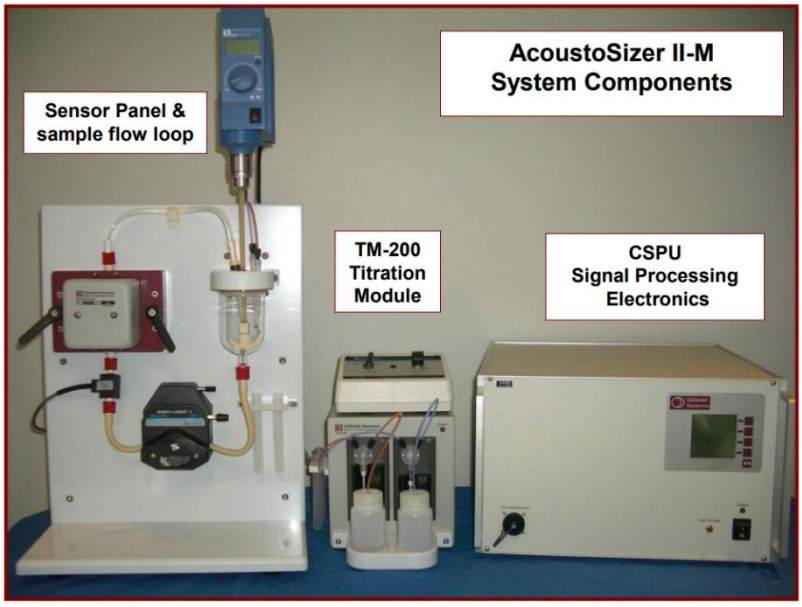


Figure 154. Scheme of the Acoustosizer IIX from [343]

Unlike conventional methods that are not suitable to characterize the stability of suspensions with solid loading as much as 40 vol%, Acoustosizer is functional on highly concentrated suspensions. The system also comprises a ZetaProbe Analyzer to measure Zeta-potential. Optimal amounts of dispersant to prepare stable suspensions and stability aging test for infiltration were carried out with this equipment (Chapter 2 and 3).

### 4.9. Rheology

Rheological tests were performed in 2 cases: to evaluate the viscosity of the binder (Chapter 2) and to prepare the ceramic suspensions for infiltration (Chapter 3). The measurements were done with a Haake Mars III rheometer (ThermoFisher Scientific) in a cone plate configuration with a shearing rate increasing linearly from 1 $s^{-1}$ to 200 $s^{-1}$ at a ramp rate of 1 $s^{-1}$. at regulate temperature of 22°C. Each sample was measured at least 3 times to obtain a mean value.

### 4.10. Flowability (Carr index and Hausner ratio / angle of repose)

As explained in Chapter 1, flowability could be expressed by different terms, such as Carr index and Hausner ratio, Angle of repose, Flow rate, Revolution analyser, Flow factor coefficient etc. Carr index and Hausner ratio are the most common values to assess the flowability of powder materials through simple measurements of the bulk density and tapped density. The operation is repeated by performing 10, 500 and 1250 taps on the same sample and read the corresponded volume $V_{10}$, $V_{500}$ and $V_{1250}$. If the difference between $V_{500}$ and $V_{1250}$ is less than or equal to 2 ml, $V_{1250}$ is tapped volume. It is this value that will be used to calculate tapped density. Another 1250 taps will be repeated if the difference is larger than 2 ml until the difference between succeeding measurements is less than or equal to 2 ml. Calculation of Carr index and Hausner ratio are described in Chapter 1. Each sample was measured at least 3 times to obtain a mean value.

Angle of repose is defined as the steepest angle of the materials which is measured from the horizontal plane on which powder could be kept stable instead of collapsing [50]. The measurements reported in the Appendix 2 were done according to the ASTM (B213) standard.

### 4.11. Thermogravimetry (TG)

Thermogravimetric analysis -TGA (Linseis, Germany) was conducted on printed green bodies fabricated with spray dried alumina granules with deposited binder with heating rate of 3°C/min up to 1500°C.

### 4.12. Dilatometry

The measurement was conducted with pressed sample (P172LSB, Alteo, France) on DIL 402 Supreme (Netzsch, Germany) with program (target temperature: 1550°C, heating rate: 3°C/min,

cooling rate: 5°C/min, atmosphere: air). Sample dimension was required: diameter: approx.8 mm, length: approx. 10 mm.

### 4.13. Rugosimeter and 3D-scanner

The rugosimeter used in the present work (VK-X200, Keyence, Japan) is a laser scanning confocal microscope capable of ultra-fine, non-contact profile measurements. The machine offers observation at up to 28,800x magnification with a measuring resolution of 0.5 nm [344]. It was used for roughness measurements (Ra & Rz) in various cases: to characterize the powder beds in Chapter 2, the sintered and infiltrated samples in Chapter 3 and finally the laser treated samples in Chapter 4.

Some measurements were also carried out using a 3D-scanner (VR-2000, Keyence, Japan). This machine is an optical profilometer which conducts non-contact measurements of surfaces with a resolution of 0.4 µm. This scanner was used in addition to the rugosimeter for certain roughness measurements in Chapter 3, profile analysis of laser tracks or laser treated samples in Chapter 5. Each sample was measured at least 3 times to obtain a mean value.

### 4.14. Mercury porosimetry

All the analysis reported in this document have been performed using an AutoPore IV 9500 (Micromeritics, USA). The whole measurement includes low-pressure analysis (up to 30 psia) and high-pressure analysis (from 30 – 33000 psia maximum pressure). It enables to measure pore diameters from 0.003 to 360 µm.

### 4.15. X-ray microtomography

X-ray microtomography (µ-CT) uses X-rays to create a 3D image composed by numerous 2D images which are re-constructed and processed in 3D without destroying the original samples. It also offers high resolution images of cross-section images of skeleton structure of samples which is popularly applied in biomedical researches [340]. The dimensional resolution of µ-CT can reach pixel size of a few micro-meters. The measurement was conducted on Phoenix Nanotom (Baker Hughes, USA) in CIRIMAT (Université de Toulouse, France). For this work, high-resolution X-ray micro-computed tomography analyses were performed with a phoenix nanotom equipped with a 180 kV / 15 W high powder nanofocus X-ray tube (9 µm voxel size, resolution). VG Studio MAX 4.4 software was used to reconstruct the data sets and visualize the objects in 3 dimensions.

### 4.16. Compressive strength

In the work of Chapter 3, the compression tests were conducted with a Z100 Universal testing machine (Zwick, Germany) equipped with a 100 kN cell force. The ratio between length and width of the cuboid samples for all the tests was approx. 1.5. The two side surfaces put in

compression were hand polished to be parallel. Compressive strength was calculated according to Eq 40.

$$CS = \frac{F}{l_1 \cdot l_2} \tag{40}$$

where CS, F, $l_1$, $l_2$ are compressive strength (Pa), rupture load (N) and side lengths of the cuboids (m).

# Appendix 5 Scientific communications

## Conferences

**10.2021: Materials Science & Technology (MS&T21), Virtual, Columbus, USA**

Hybrid binder jetting of ceramic: investigation of powder, process and innovative post-treatments

Authors: Qirong CHEN, Fabrice PETIT, Enrique JUSTE, Marie LASGORCEIX, Anne LERICHE

**05.2021: Belgian ceramic annual society conference 2021 (Oral), Virtual**

Hybrid binder jetting of ceramic: investigation of powder, process and innovative post-treatments

Authors: Qirong CHEN, Fabrice PETIT, Enrique JUSTE, Marie LASGORCEIX, Anne LERICHE

**04.2021: Deutsche Keramishce Gesellshaft 2021 (Oral), Virtual, Julich, Germany**

Hybrid binder jetting of ceramic: investigation of powder, process and innovative post-treatments

Authors: Qirong CHEN, Fabrice PETIT, Enrique JUSTE, Marie LASGORCEIX, Anne LERICHE

**04.2021: 8$^{th}$ International Congress on Ceramics (Oral), Virtual, Busan, Korea**

Hybrid additive/subtractive manufacturing system to prepare dense and complex shape ceramic parts (**Best presentation award**)

Authors: Qirong CHEN, Fabrice PETIT, Enrique JUSTE, Marie LASGORCEIX, Anne LERICHE

**01.2021: 45$^{th}$ International Conference and Expo on Advanced Ceramics and Composites (Oral), Virtual, Daytona, USA**

Hybrid additive/subtractive manufacturing system to prepare dense and complex shape ceramic parts

Authors: Qirong CHEN, Fabrice PETIT, Enrique JUSTE, Marie LASGORCEIX, Anne LERICHE

## Appendix 5 Scientific communications

**10.2020: yCAM 2020 (Oral), Virtual, Toulouse, France**

Hybrid additive/subtractive manufacturing system to prepare dense and complex shape ceramic parts

Authors: Qirong CHEN, Fabrice PETIT, Enrique JUSTE, Marie LASGORCEIX, Anne LERICHE

**12.2019: Belgian ceramic annual society conference 2019 (Oral), Ghent, Belgium**

Hybrid additive/subtractive manufacturing system to prepare dense and complex shape ceramic parts

Authors: Qirong CHEN, Fabrice PETIT, Enrique JUSTE, Marie LASGORCEIX, Anne LERICHE

**09.2019: Shaping 7 (Poster), Aveiro, Portugal**

Hybrid additive/subtractive manufacturing system to prepare dense and complex shape ceramic parts

Authors: Qirong CHEN, Fabrice PETIT, Enrique JUSTE, Marie LASGORCEIX, Anne LERICHE

**06.2019: European ceramic society annual conference 2019 (Poster), Turin, Italy**

Hybrid additive/subtractive manufacturing system to prepare dense and complex shape ceramic parts

Authors: Qirong CHEN, Fabrice PETIT, Enrique JUSTE, Marie LASGORCEIX, Anne LERICHE

**04.2019: yCAM 2019 (Poster), Mons, Belgium**

Hybrid additive/subtractive manufacturing system to prepare dense and complex shape ceramic parts

Authors: Qirong CHEN, Fabrice PETIT, Enrique JUSTE, Marie LASGORCEIX, Anne LERICHE

**12.2018: Belgian ceramic annual society conference 2018 (Poster), Liege, Belgium**

Hybrid additive/subtractive manufacturing system to prepare dense and complex shape ceramic parts

Authors: Qirong CHEN, Fabrice PETIT, Enrique JUSTE, Marie LASGORCEIX, Anne LERICHE

# Papers

Binder jetting process with ceramic powders: influence of powder properties and printing parameters; Journal: Open Ceramics; DOI: 10.1016/j.oceram.2022.100218.

Authors: Qirong CHEN, Fabrice PETIT, Enrique JUSTE, Marie LASGORCEIX, Anne LERICHE

Three papers pending:

Post-infiltration to improve the density of binder jet ceramic parts (under process);

Hybridization between binder jetting and laser machining to enhance the surface smoothness and sharpness of ceramic parts (under process);

Experimental and simulation methods to assess multi-powder packing systems in binder jetting process (under process)

# Appendix 5 Scientific communications

# References

[1] Hart LD, Lense E. Alumina chemicals: science and technology handbook. 1990.
[2] Kingery WD, Vandiver PB. Ceramic masterpieces: art, structure, technology. 1986.
[3] Ngo TD, Kashani A, Imbalzano G, Nguyen KTQ, Hui D. Additive manufacturing (3D printing): A review of materials, methods, applications and challenges. Composites Part B: Engineering. 2018;143:172-96. https://doi.org/10.1016/j.compositesb.2018.02.012
[4] Zocca A, Colombo P, Gomes CM, Günster J. Additive Manufacturing of Ceramics: Issues, Potentialities, and Opportunities. J Am Ceram Soc. 2015;98:1983-2001. 10.1111/jace.13700
[5] Ian Gibson IG. Additive Manufacturing Technologies 3D Printing, Rapid Prototyping, and Direct Digital Manufacturing. 2015.
[6] Utela B, Storti D, Anderson R, Ganter M. A review of process development steps for new material systems in three dimensional printing (3DP). Journal of Manufacturing Processes. 2008;10:96-104. https://doi.org/10.1016/j.jmapro.2009.03.002
[7] Standard A. Standard terminology for additive manufacturing technologies. ASTM International F2792-12a. 2012.
[8] Noorani R. Rapid prototyping: principles and applications. 2006.
[9] Singh S, Ramakrishna S, Singh R. Material issues in additive manufacturing: A review. Journal of Manufacturing Processes. 2017;25:185-200.
[10] Guo N, Leu MC. Additive manufacturing: technology, applications and research needs. Frontiers of Mechanical Engineering. 2013;8:215-43. 10.1007/s11465-013-0248-8
[11] Gokuldoss PK, Kolla S, Eckert J. Additive manufacturing processes: Selective laser melting, electron beam melting and binder jetting-selection guidelines. Materials. 2017;10. 10.3390/ma10060672
[12] Wong KV, Hernandez A. A review of additive manufacturing. ISRN Mechanical Engineering. 2012;2012.
[13] Wu P, Wang J, Wang X. A critical review of the use of 3-D printing in the construction industry. Automation in Construction. 2016;68:21-31.
[14] Deckers J, Vleugels J, Kruthl JP. Additive manufacturing of ceramics: a review. Journal of Ceramic Science and Technology. 2014;5:245-60.
[15] 7 Families of Additive Manufacturing. hybrid-am.com
[16] Travitzky N, Bonet A, Dermeik B, Fey T, Filbert‐Demut I, Schlier L, et al. Additive manufacturing of ceramic‐based materials. Advanced Engineering Materials. 2014;16:729-54.
[17] Sachs EM, Haggerty JS, Cima MJ, Williams PA. Three-dimensional printing techniques. 1993.
[18] Cima M, Sachs E, Fan T, Bredt JF, Michaels SP, Khanuja S, et al. Three-dimensional printing techniques. 1995.
[19] Lauder A, Cima M, Sachs E, Fan T. Three dimensional printing: surface finish and microstructure of rapid prototyped components. MRS Online Proceedings Library Archive. 1991;249.
[20] Ziaee M, Crane NB. Binder jetting: A review of process, materials, and methods. Additive Manufacturing. 2019;28:781-801. 10.1016/j.addma.2019.05.031
[21] Costa ECE, Duarte JP, Bartolo P. A review of additive manufacturing for ceramic production. Rapid Prototyping Journal. 2017;23:954-63. 10.1108/rpj-09-2015-0128
[22] Du W, Ren X, Ma C, Pei Z. Binder Jetting Additive Manufacturing of Ceramics: A Literature Review. 2017:V014T07A06. 10.1115/IMECE2017-70344

## References


[23] Ligon SC, Liska R, Stampfl J, Gurr M, Mulhaupt R. Polymers for 3D Printing and Customized Additive Manufacturing. Chemical Reviews. 2017;117:10212-90. 10.1021/acs.chemrev.7b00074

[24] Dini F, Ghaffari SA, Jafar J, Hamidreza R, Marjan S. A review of binder jet process parameters; powder, binder, printing and sintering condition. Metal Powder Report. 2019.

[25] Katz-Demyanetz A, Popov VV, Kovalevsky A, Safranchik D, Koptyug A. Powder-bed additive manufacturing for aerospace application: Techniques, metallic and metal/ceramic composite materials and trends. Manufacturing Review. 2019;6. 10.1051/mfreview/2019003

[26] Lores A, Azurmendi N, Agote I, Zuza E. A review on recent developments in binder jetting metal additive manufacturing: materials and process characteristics. Powder Metallurgy. 2019;62:267-96. 10.1080/00325899.2019.1669299

[27] Lv XY, Ye F, Cheng LF, Fan SW, Liu YS. Binder jetting of ceramics: Powders, binders, printing parameters, equipment, and post-treatment. Ceramics International. 2019;45:12609-24. 10.1016/j.ceramint.2019.04.012

[28] Kessler A, Hickel R, Reymus M. 3D Printing in Dentistry-State of the Art. Operative Dentistry. 2020;45:30-40. 10.2341/18-229-l

[29] Methani MM, Revilla-Leon M, Zandinejad A. The potential of additive manufacturing technologies and their processing parameters for the fabrication of all-ceramic crowns: A review. Journal of Esthetic and Restorative Dentistry. 2020;32:182-92. 10.1111/jerd.12535

[30] Mostafaei A, Elliott A, Barnes J, Cramer C, Nandwana P, Chmielus M. Binder jet 3D printing – process parameters, materials, properties, and challenges. Progress in Materials Science. 2020:100684. 10.1016/j.pmatsci.2020.100684

[31] Kruth J-P. Material incress manufacturing by rapid prototyping techniques. CIRP annals. 1991;40:603-14.

[32] Pham DT, Gault RS. A comparison of rapid prototyping technologies. International Journal of Machine Tools and Manufacture. 1998;38:1257-87. https://doi.org/10.1016/S0890-6955(97)00137-5

[33] Song JH, Edirisinghe MJ, Evans JRG. Formulation and multilayer jet printing of ceramic inks. J Am Ceram Soc. 1999;82:3374-80.

[34] Li J, Chen M, Fan X, Zhou H. Recent advances in bioprinting techniques: approaches, applications and future prospects. J Transl Med. 2016;14:271. 10.1186/s12967-016-1028-0

[35] Krujatz F, Lode A, Seidel J, Bley T, Gelinsky M, Steingroewer J. Additive Biotech—Chances, challenges, and recent applications of additive manufacturing technologies in biotechnology. New Biotechnology. 2017;39:222-31. 10.1016/j.nbt.2017.09.001

[36] OHJI T. Additive manufacturing of ceramic components: —Towards innovation of ceramic industry—. Synthesiology English edition. 2019;11:81-92. 10.5571/syntheng.11.2_81

[37] Gibson I, Rosen DW, Stucker B. Additive manufacturing technologies. 2014;17.

[38] Sachs E, Cima M, Cornie J, Brancazio D, Bredt J, Curodeau A, et al. Three-Dimensional Printing: The Physics and Implications of Additive Manufacturing. CIRP Annals. 1993;42:257-60. https://doi.org/10.1016/S0007-8506(07)62438-X

[39] Yap CY, Chua CK, Dong ZL, Liu ZH, Zhang DQ, Loh LE, et al. Review of selective laser melting: Materials and applications. Applied physics reviews. 2015;2:041101.

[40] Chartier T, Chaput C, Doreau F, Loiseau M. Stereolithography of structural complex ceramic parts. Journal of materials science. 2002;37:3141-7.

[41] Klammert U, Reuther T, Jahn C, Kraski B, Kübler A, Gbureck U. Cytocompatibility of brushite and monetite cell culture scaffolds made by three-dimensional powder printing. Acta Biomaterialia. 2009;5:727-34.

[42] Seitz H, Rieder W, Irsen S, Leukers B, Tille C. Three-dimensional printing of porous ceramic scaffolds for bone tissue engineering. Journal of Biomedical Materials Research - Part B Applied Biomaterials. 2005;74:782-8. 10.1002/jbm.b.30291

## References


[43] Binder jetting speed. makepartsfast.com/binder-jetting-boasts-high-production-speed-and-quantity/

[44] Bai Y, Wagner G, Williams CB. Effect of Particle Size Distribution on Powder Packing and Sintering in Binder Jetting Additive Manufacturing of Metals. J Manuf Sci Eng-Trans ASME. 2017;139:6. 10.1115/1.4036640

[45] Butscher A, Bohner M, Hofmann S, Gauckler L, Müller R. Structural and material approaches to bone tissue engineering in powder-based three-dimensional printing. Acta Biomaterialia. 2011;7:907-20. 10.1016/j.actbio.2010.09.039

[46] Hausner HH. Vibratory Compacting: Principles and Methods. 1967;2.

[47] Carr RL. Evaluating flow properties of solids. 1965.

[48] Attia UM, Fones A, Trepleton R, Hamilton H, Davies S, Wimpenny D. HIPing of Pd-doped titanium components: A study of mechanical and corrosion properties.

[49] Liu Z. Measuring the angle of repose of granular systems using hollow cylinders. 2011.

[50] Mehta A, Barker G. The dynamics of sand. Reports on Progress in Physics. 1994;57:383.

[51] Riley R, Hausner H. Effect of particle size distribution on the friction in a powder mass. Int J Powder Met. 1970;6.

[52] Cain J. Flowability Testing-An Alternative Technique fore Determining ANSI/CEMA Standard 550 Flowability Ratings for Granular Materials. Powder Handling and Processing. 2002;14:218-21.

[53] Beddow JK. Professor Dr. Henry H. Hausner, 1900–1995. Particle & Particle Systems Characterization. 1995;12:213-.

[54] Riley G, Mann S, Jesse R. Angles of Repose of Cohesive Powders, J. Powder Bulk Solids Technol. 1978;2:15-8.

[55] Al-Hashemi H, Al-Amoudi O. A review on the angle of repose of granular materials. Powder Technology. 2018;330:397-417. 10.1016/j.powtec.2018.02.003

[56] Suwanprateeb J, Sanngam R, Panyathanmaporn T. Influence of raw powder preparation routes on properties of hydroxyapatite fabricated by 3D printing technique. Materials Science and Engineering: C. 2010;30:610-7.

[57] Chumnanklang R, Panyathanmaporn T, Sitthiseripratip K, Suwanprateeb J. 3D printing of hydroxyapatite: Effect of binder concentration in pre-coated particle on part strength. Materials Science and Engineering: C. 2007;27:914-21.

[58] Leukers B, Gülkan H, Irsen SH, Milz S, Tille C, Schieker M, et al. Hydroxyapatite scaffolds for bone tissue engineering made by 3D printing. Journal of Materials Science: Materials in Medicine. 2005;16:1121-4.

[59] Leukers B, Gülkan H, Irsen S, Milz S, Tille C, Seitz H, et al. Biocompatibility of ceramic scaffolds for bone replacement made by 3D printing. Materialwissenschaft und Werkstofftechnik: Entwicklung, Fertigung, Prüfung, Eigenschaften und Anwendungen technischer Werkstoffe. 2005;36:781-7.

[60] Freeman R. Measuring the flow properties of consolidated, conditioned and aerated powders—a comparative study using a powder rheometer and a rotational shear cell. Powder Technology. 2007;174:25-33. 10.1016/j.powtec.2006.10.016

[61] Nase ST, Vargas WL, Abatan AA, McCarthy JJ. Discrete characterization tools for cohesive granular material. Powder Technology. 2001;116:214-23.

[62] Chen H, Wei Q, Wen S, Li Z, Shi Y. Flow behavior of powder particles in layering process of selective laser melting: Numerical modeling and experimental verification based on discrete element method. International Journal of Machine Tools and Manufacture. 2017;123:146-59. 10.1016/j.ijmachtools.2017.08.004

[63] Schade CT, Murphy TF, Walton C. Development of atomized powders for additive manufacturing. Powder Metallurgy Word Congress, Accessed on 2nd July. 2014.

[64] Chan LC, Page NW. Particle fractal and load effects on internal friction in powders. Powder Technology. 1997;90:259-66. 10.1016/S0032-5910(96)03228-7
[65] Bai Y, Williams CB. An exploration of binder jetting of copper. Rapid Prototyping Journal. 2015.
[66] Slotwinski JA, Garboczi EJ, Stutzman PE, Ferraris CF, Watson SS, Peltz MA. Characterization of metal powders used for additive manufacturing. Journal of research of the National Institute of Standards and Technology. 2014;119:460.
[67] Faqih AMN, Mehrotra A, Hammond SV, Muzzio FJ. Effect of moisture and magnesium stearate concentration on flow properties of cohesive granular materials. International journal of pharmaceutics. 2007;336:338-45. 10.1016/j.ijpharm.2006.12.024
[68] Hirschberg C, Sun CC, Risbo J, Rantanen J. Effects of Water on Powder Flowability of Diverse Powders Assessed by Complimentary Techniques. Journal of pharmaceutical sciences. 2019;108:2613-20. 10.1016/j.xphs.2019.03.012
[69] Sachs EM. Powder dispensing apparatus using vibration. 2000.
[70] Sachs EM, Cima MJ, Caradonna MA, Grau J, Serdy JG, Saxton PC, et al. Jetting layers of powder and the formation of fine powder beds thereby. 2003.
[71] Butscher A, Bohner M, Roth C, Ernstberger A, Heuberger R, Doebelin N, et al. Printability of calcium phosphate powders for three-dimensional printing of tissue engineering scaffolds. Acta biomaterialia. 2012;8:373-85.
[72] Zocca A, Gomes CM, Bernardo E, Müller R, Günster J, Colombo P. LAS glass–ceramic scaffolds by three-dimensional printing. J European Ceram Soc. 2013;33:1525-33. 10.1016/j.jeurceramsoc.2012.12.012
[73] Lu K, Hiser M, Wu W. Effect of particle size on three dimensional printed mesh structures. Powder Technology. 2009;192:178-83. 10.1016/j.powtec.2008.12.011
[74] Gonzalez JA, Mireles J, Lin Y, Wicker RB. Characterization of ceramic components fabricated using binder jetting additive manufacturing technology. Ceramics International. 2016;42:10559-64. 10.1016/j.ceramint.2016.03.079
[75] Pruitt BL. The design of an automated powder deposition system for a three-dimensional printing machine. 1991.
[76] Butscher A, Bohner M, Doebelin N, Galea L, Loeffel O, Müller R. Moisture based three-dimensional printing of calcium phosphate structures for scaffold engineering. Acta biomaterialia. 2013;9:5369-78. 10.1016/j.actbio.2012.10.009
[77] Miao G, Du W, Moghadasi M, Pei Z, Ma C. Ceramic binder jetting additive manufacturing: Effects of granulation on properties of feedstock powder and printed and sintered parts. Additive Manufacturing. 2020;36:101542. https://doi.org/10.1016/j.addma.2020.101542
[78] Du W, Ren X, Ma C, Pei Z. Ceramic binder jetting additive manufacturing: Particle coating for increasing powder sinterability and part strength. Materials Letters. 2019;234:327-30. 10.1016/j.matlet.2018.09.118
[79] Craik DJ, Miller BF. THE FLOW PROPERTIES OF POWDERS UNDER HUMID CONDITIONS. Journal of Pharmacy and Pharmacology. 1958;10:136T-44T. 10.1111/j.2042-7158.1958.tb10392.x
[80] Romagnoli M, Bondioli F. POWDER FLOWABILITY CHARACTERISING TECHNIQUES. American Ceramic Society Bulletin. 2004.
[81] Althaus TO, Windhab EJ. Characterization of wet powder flowability by shear cell measurements and compaction curves. Powder Technology. 2012;215-216:59-65. https://doi.org/10.1016/j.powtec.2011.09.007
[82] Zainuddin MI, Yasuda M, Liu Y-H, Maruyama H, Matsusaka S. Development of vibration shear tube method for powder flowability evaluation. Powder Technology. 2012;217:548-53. https://doi.org/10.1016/j.powtec.2011.11.013
[83] Feenstra FK. Method for making a dental element. 2005.

[84] Lanzetta M, Sachs E. The line formation with alumina powders in drop on demand three dimensional printing. PRIME 2001, 1st Int CIRP Seminar on: PRogress in Innovative Manufacturing Engineering. 2001:189-96.
[85] Santos LCd, Condotta R, Ferreira MdC. Flow properties of coarse and fine sugar powders. Journal of Food Process Engineering. 2018;41:e12648. 10.1111/jfpe.12648
[86] Li LG, Zhuo HX, Zhu J, Kwan AKH. Packing density of mortar containing polypropylene, carbon or basalt fibres under dry and wet conditions. Powder Technology. 2019;342:433-40. 10.1016/j.powtec.2018.10.005
[87] German RM. Particle packing characteristics. 1989.
[88] Mostafaei A, De Vecchis PR, Nettleship I, Chmielus M. Effect of powder size distribution on densification and microstructural evolution of binder-jet 3D-printed alloy 625. Materials & Design. 2019;162:375-83. 10.1016/j.matdes.2018.11.051
[89] Sohn HY, Moreland C. The effect of particle size distribution on packing density. The Canadian Journal of Chemical Engineering. 1968;46:162-7.
[90] Zhou Z, Buchanan F, Mitchell C, Dunne N. Printability of calcium phosphate: calcium sulfate powders for the application of tissue engineered bone scaffolds using the 3D printing technique. Materials Science and Engineering: C. 2014;38:1-10.
[91] Ziegelmeier S, Christou P, Wöllecke F, Tuck C, Goodridge R, Hague R, et al. An experimental study into the effects of bulk and flow behaviour of laser sintering polymer powders on resulting part properties. Journal of Materials Processing Technology. 2015;215:239-50.
[92] Cao S, Qiu Y, Wei X-F, Zhang H-H. Experimental and theoretical investigation on ultra-thin powder layering in three dimensional printing (3DP) by a novel double-smoothing mechanism. Journal of Materials Processing Technology. 2015;220:231-42.
[93] Tan JH, Wong WLE, Dalgarno KW. An overview of powder granulometry on feedstock and part performance in the selective laser melting process. Additive Manufacturing. 2017;18:228-55.
[94] Mao T, Kuhn DC, Tran H. Spread and rebound of liquid droplets upon impact on flat surfaces. AIChE Journal. 1997;43:2169-79.
[95] Benson JM, Snyders E. The need for powder characterisation in the additive manufacturing industry and the establishment of a national facility. South African Journal of Industrial Engineering. 2015;26:104-14.
[96] Liu J, Ryneson ML. Blended powder solid-supersolidus liquid phase sintering. 2006.
[97] Miyanaji H, Zhang SS, Yang L. A new physics-based model for equilibrium saturation determination in binder jetting additive manufacturing process. International Journal of Machine Tools & Manufacture. 2018;124:1-11. 10.1016/j.ijmachtools.2017.09.001
[98] McGEARY RK. Mechanical Packing of Spherical Particles. J Am Ceram Soc. 1961;44:513-22. 10.1111/j.1151-2916.1961.tb13716.x
[99] Karapatis N, Egger G, Gygax P, Glardon R. Optimization of powder layer density in selective laser sintering. 1999 International Solid Freeform Fabrication Symposium. 1999.
[100] Bai Y, Wagner G, Williams CB. Effect of bimodal powder mixture on powder packing density and sintered density in binder jetting of metals. 2015 Annual International Solid Freeform Fabrication Symposium. 2015;62:758-71.
[101] Lanzetta M, Sachs E. Improved surface finish in 3D printing using bimodal powder distribution. Rapid Prototyping Journal. 2003.
[102] Sun C, Tian X, Wang L, Liu Y, Wirth CM, Günster J, et al. Effect of particle size gradation on the performance of glass-ceramic 3D printing process. Ceramics International. 2017;43:578-84.
[103] Spath S, Drescher P, Seitz H. Impact of particle size of ceramic granule blends on mechanical strength and porosity of 3D printed scaffolds. Materials. 2015;8:4720-32.

[104] Zhu H, Fuh J, Lu L. The influence of powder apparent density on the density in direct laser-sintered metallic parts. International Journal of Machine Tools and Manufacture. 2007;47:294-8.
[105] Bai Y, Wagner G, Williams CB. Effect of particle size distribution on powder packing and sintering in binder jetting additive manufacturing of metals. Journal of Manufacturing Science and Engineering. 2017;139.
[106] Sachs EM, Hadjiloucas C, Allen S, Yoo HJ. Metal and ceramic containing parts produced from powder using binders derived from salt. 2003.
[107] Bredt JF, Clark S, Gilchrist G. Three dimensional printing material system and method. 2006.
[108] Greil P. Polymer derived engineering ceramics. Advanced engineering materials. 2000;2:339-48.
[109] Peuckert M, Vaahs T, Brück M. Ceramics from organometallic polymers. Advanced Materials. 1990;2:398-404.
[110] Bredt JF. Binder composition for use in three dimensional printing. 1997.
[111] Wang H-R, Cima MJ, Kernan BD, Sachs EM. Alumina-doped silica gradient-index (GRIN) lenses by slurry-based three-dimensional printing (S-3DP™). Journal of non-crystalline solids. 2004;349:360-7.
[112] Suwanprateeb J, Chumnanklang R. Three-dimensional printing of porous polyethylene structure using water-based binders. Journal of Biomedical Materials Research Part B. 2006;78:138-45.
[113] Bynum DK. Automated manufacturing system using thin sections. 1992.
[114] Bredt JF, Anderson TC, Russell DB. Three dimensional printing material system and method. 2003.
[115] Oriakhi C, Lambright TM. Calcium aluminate cement compositions for solid freeform fabrication. 2007.
[116] Shen J. Material system for use in three dimensional printing. 2006.
[117] Khoshnevis B. Selective inhibition of bonding of power particles for layered fabrication of 3-D objects. 2003.
[118] Kunchala P, Kappagantula K. 3D printing high density ceramics using binder jetting with nanoparticle densifiers. Materials & Design. 2018;155:443-50. 10.1016/j.matdes.2018.06.009
[119] Bai Y, Williams CB. Binder jetting additive manufacturing with a particle-free metal ink as a binder precursor. Materials & Design. 2018;147:146-56. 10.1016/j.matdes.2018.03.027
[120] Bai Y, Williams CB. The effect of inkjetted nanoparticles on metal part properties in binder jetting additive manufacturing. Nanotechnology. 2018;29. 10.1088/1361-6528/aad0bb
[121] Bai JG, Creehan KD, Kuhn HA. Inkjet printable nanosilver suspensions for enhanced sintering quality in rapid manufacturing. Nanotechnology. 2007;18:185701.
[122] Bai JA, Creehan KD, Kuhn HA. Powder particle layerwise three-dimensional printing process. 2018.
[123] Derby B, Reis N. Inkjet printing of highly loaded particulate suspensions. MRS bulletin. 2003;28:815-8.
[124] Reis N, Ainsley C, Derby B. Viscosity and Acoustic Behavior of Ceramic Suspensions Optimized for Phase-Change Ink-Jet Printing. J Am Ceram Soc. 2005;88:802-8.
[125] Moon J, Grau JE, Knezevic V, Cima MJ, Sachs EM. Ink-jet printing of binders for ceramic components. J Am Ceram Soc. 2002;85:755-62.
[126] Grau JE, Uhland SA, Moon J, Cima MJ, Sachs EM. Controlled cracking of multilayer ceramic bodies. J Am Ceram Soc. 1999;82:2080-6.
[127] Bredt JF. Binder composition for use in three dimensional printing. 1998.

[128] Derby B. Inkjet printing of functional and structural materials: fluid property requirements, feature stability, and resolution. Annual Review of Materials Research. 2010;40:395-414.
[129] McKinley GH, Renardy M. Wolfgang von ohnesorge. Physics of Fluids. 2011;23:127101. 10.1063/1.3663616
[130] Fromm J. Numerical calculation of the fluid dynamics of drop-on-demand jets. IBM Journal of Research and Development. 1984;28:322-33.
[131] Reis N, Derby B. Ink jet deposition of ceramic suspensions: Modeling and experiments of droplet formation. MRS Online Proceedings Library (OPL). 2000;625.
[132] Duineveld PC, De Kok MM, Buechel M, Sempel A, Mutsaers KA, Van de Weijer P, et al. Ink-jet printing of polymer light-emitting devices. Organic Light-Emitting Materials and Devices V. 2002;4464:59-67.
[133] Stow CD, Hadfield MG. An experimental investigation of fluid flow resulting from the impact of a water drop with an unyielding dry surface. Proceedings of the Royal Society of London A Mathematical and Physical Sciences. 1981;373:419-41.
[134] Miyanaji H, Momenzadeh N, Yang L. Effect of powder characteristics on parts fabricated via binder jetting process. Rapid Prototyping Journal. 2019;25:332-42. 10.1108/rpj-03-2018-0069
[135] Bai Y, Wall C, Pham H, Esker A, Williams CB. Characterizing Binder–Powder Interaction in Binder Jetting Additive Manufacturing Via Sessile Drop Goniometry. Journal of Manufacturing Science and Engineering. 2019;141.
[136] Bechtel S, Bogy D, Talke F. Impact of a liquid drop against a flat surface. IBM Journal of Research and Development. 1981;25:963-71.
[137] Pasandideh‐Fard M, Qiao Y, Chandra S, Mostaghimi J. Capillary effects during droplet impact on a solid surface. Physics of fluids. 1996;8:650-9.
[138] Fan T. Droplet-powder impact interaction in three dimensional printing. 1996.
[139] Miyanaji H, Orth M, Akbar JM, Yang L. Process development for green part printing using binder jetting additive manufacturing. Frontiers of Mechanical Engineering. 2018;13:504-12.
[140] Salehi M, Maleksaeedi S, Nai SML, Meenashisundaram GK, Goh MH, Gupta M. A paradigm shift towards compositionally zero-sum binderless 3D printing of magnesium alloys via capillary-mediated bridging. Acta Materialia. 2019;165:294-306.
[141] Emady HN, Kayrak-Talay D, Litster JD. Modeling the granule formation mechanism from single drop impact on a powder bed. Journal of colloid and interface science. 2013;393:369-76.
[142] Emady HN, Kayrak-Talay D, Schwerin WC, Litster JD. Granule formation mechanisms and morphology from single drop impact on powder beds. Powder technology. 2011;212:69-79.
[143] Parab ND, Barnes JE, Zhao C, Cunningham RW, Fezzaa K, Rollett AD, et al. Real time observation of binder jetting printing process using high-speed X-ray imaging. Scientific reports. 2019;9:1-10.
[144] Forderhase PF, Deckard CR, Klein JM. Apparatus and method for producing parts with multi-directional powder delivery. 1993.
[145] Ehlert R. The design of a volumetric dispensing system for free-flow powders used in three dimensional printing. 1995.
[146] Heywood B. The design and manufacture of a powder deposition system for a large powder bed on a three dimensional printer. 1993.
[147] Shrestha S, Manogharan G. Optimization of Binder Jetting Using Taguchi Method. Jom. 2017;69:491-7. 10.1007/s11837-016-2231-4

[148] Parteli EJRRR, Pöschel T. Particle-based simulation of powder application in additive manufacturing. Powder Technology. 2016;288:96-102. 10.1016/j.powtec.2015.10.035
[149] Pond SF. Inkjet technology and product development strategies. 2000.
[150] Miyanaji H, Momenzadeh N, Yang L. Effect of printing speed on quality of printed parts in Binder Jetting Process. Additive Manufacturing. 2018;20:1-10.
[151] Oh JW, Nahm S, Kim B, Choi H. Anisotropy in Green Body Bending Strength due to Additive Direction in the Binder-Jetting Additive Manufacturing Process. Korean Journal of Metals and Materials. 2019;57:227-35. 10.3365/kjmm.2019.57.4.227
[152] Zhang W, Melcher R, Travitzky N, Bordia RK, Greil P. Three‐dimensional printing of complex‐shaped alumina/glass composites. Advanced Engineering Materials. 2009;11:1039-43. 10.1002/adem.200900213
[153] Salehi M, Gupta M, Maleksaeedi S, Sharon NML. Inkjet based 3D additive manufacturing of metals. 2018.
[154] Li SJ, Cao S. Print Parameters Influence on Parts' Quality and Calibration with 3DP-Part I: Print Parameters Influence on Parts' Surface Topography. Advanced Materials Research. 2012;399:1639-45.
[155] Bergmann C, Lindner M, Zhang W, Koczur K, Kirsten A, Telle R, et al. 3D printing of bone substitute implants using calcium phosphate and bioactive glasses. J European Ceram Soc. 2010;30:2563-7.
[156] Utela BR, Storti D, Anderson RL, Ganter M. Development process for custom three-dimensional printing (3DP) material systems. Journal of manufacturing science and engineering. 2010;132. 10.1115/1.4000713
[157] Lu K, Reynolds WT. 3DP process for fine mesh structure printing. Powder Technology. 2008;187:11-8. 10.1016/J.POWTEC.2007.12.017
[158] Nandwana P, Elliott AM, Siddel D, Merriman A, Peter WH, Babu SS. Powder bed binder jet 3D printing of Inconel 718: Densification, microstructural evolution and challenges☆. Current Opinion in Solid State and Materials Science. 2017;21:207-18. 10.1016/j.cossms.2016.12.002
[159] Cooke A, Slotwinski J. Properties of metal powders for additive manufacturing: a review of the state of the art of metal powder property testing. 2012. 10.6028/NIST.IR.7873.
[160] Spierings AB, Levy G. Comparison of density of stainless steel 316L parts produced with selective laser melting using different powder grades. Proceedings of the Annual International Solid Freeform Fabrication Symposium. 2009:342-53.
[161] Hoffmann A, Finkers H. A relation for the void fraction of randomly packed particle beds. Powder Technology. 1995;82:197-203. 10.1016/0032-5910(94)02910-G
[162] Miyanaji H, Zhang S, Lassell A, Zandinejad A, Yang L. Process Development of Porcelain Ceramic Material with Binder Jetting Process for Dental Applications. Jom. 2016;68:831-41. 10.1007/s11837-015-1771-3
[163] Chen H, Zhao YF. Process parameters optimization for improving surface quality and manufacturing accuracy of binder jetting additive manufacturing process. Rapid Prototyping Journal. 2016. 10.1108/RPJ-11-2014-0149
[164] Schmutzler C, Stiehl TH, Zaeh MF. Empirical process model for shrinkage-induced warpage in 3D printing. Rapid Prototyping Journal. 2019. 10.1108/RPJ-04-2018-0098
[165] Hodder KJ, Nychka JA, Chalaturnyk RJ. Process limitations of 3D printing model rock. Progress in Additive Manufacturing. 2018;3:173-82. 10.1007/s40964-018-0042-6
[166] Caputo M, Solomon CV, Nguyen P-K, Berkowitz AE. Electron microscopy investigation of binder saturation and microstructural defects in functional parts made by additive manufacturing. Microscopy and Microanalysis. 2016;22:1770-1. 10.1017/S1431927616009697

[167] Miyanaji H, Yang L. Equilibrium saturation in binder jetting additive manufacturing processes: theoretical model vs. experimental observations. International Solid Freeform Fabrication Symposium. 2016.
[168] Enneti RK, Prough KC. Effect of binder saturation and powder layer thickness on the green strength of the binder jet 3D printing (BJ3DP) WC-12% Co powders. International Journal of Refractory Metals and Hard Materials. 2019;84:104991. 10.1016/j.ijrmhm.2019.104991
[169] Vaezi M, Chua CK. Effects of layer thickness and binder saturation level parameters on 3D printing process. The International Journal of Advanced Manufacturing Technology. 2011;53:275-84. 10.1007/s00170-010-2821-1
[170] Castilho M, Gouveia B, Pires I, Rodrigues J, Pereira M. The role of shell/core saturation level on the accuracy and mechanical characteristics of porous calcium phosphate models produced by 3Dprinting. Rapid Prototyping Journal. 2015. 10.1108/RPJ-02-2013-0015
[171] Fayazfar H, Salarian M, Rogalsky A, Sarker D, Russo P, Paserin V, et al. A critical review of powder-based additive manufacturing of ferrous alloys: Process parameters, microstructure and mechanical properties. Materials & Design. 2018;144:98-128. 10.1016/j.matdes.2018.02.018
[172] Wang Y, Jia P, Yang W, Peng K, Zhang S. Simulation and experimental study of binder droplet infiltration in 3DP technology. Modern Physics Letters B. 2018;32:1850272.
[173] Szucs TD, Brabazon D. Effect of saturation and post processing on 3D printed calcium phosphate scaffolds. Key Engineering Materials. 2009;396:663-6.
[174] Gaytan SM, Cadena MA, Karim H, Delfin D, Lin Y, Espalin D, et al. Fabrication of barium titanate by binder jetting additive manufacturing technology. Ceramics International. 2015;41:6610-9. 10.1016/j.ceramint.2015.01.108
[175] Melcher R, Martins S, Travitzky N, Greil P. Fabrication of Al2O3-based composites by indirect 3D-printing. Materials Letters. 2006;60:572-5.
[176] Patirupanusara P, Suwanpreuk W, Rubkumintara T, Suwanprateeb J. Effect of binder content on the material properties of polymethyl methacrylate fabricated by three dimensional printing technique. journal of materials processing technology. 2008;207:40-5. 10.1016/j.jmatprotec.2007.12.058
[177] Hapgood KP, Litster JD, Biggs SR, Howes T. Drop penetration into porous powder beds. Journal of Colloid and Interface Science. 2002;253:353-66.
[178] ASTM B312 - Standard Test Method for Green Strength of Specimens Compacted from Metal Powders 2014.
[179] MPIF STANDARD TEST METHOD 41: METHOD FOR DETERMINATION OF

TRANSVERSE RUPTURE STRENGTH OF POWDER METALLURGY (PM MATERIALS 2016.
[180] Bai Y, Williams CB. Binderless jetting: additive manufacturing of metal parts via jetting nanoparticles. International Solid Freeform Fabrication. 2017.
[181] Sachs EM, Cima MJ, Bredt JF, Khanuja S. Process for removing loose powder particles from interior passages of a body. 1996.
[182] Becker FH. Debinding processes: Physical and chemical conclusions and their practical realisations. Ceramic Forum International. 2006;83.
[183] German RM. Theory of thermal debinding. Int J Powder Metall. 1987;23:237-45.
[184] Enneti RK, Park SJ, German RM, Atre SV. thermal debinding process in particulate materials processing. Materials and Manufacturing Processes. 2012;27:103-18.
[185] Levenfeld B, Varez A, Torralba J. Effect of residual carbon on the sintering process of M2 high speed steel parts obtained by a modified metal injection molding process. Metallurgical and Materials Transactions A. 2002;33:1843-51.

[186] Wu Y, German R, Blaine D, Marx B, Schlaefer C. Effects of residual carbon content on sintering shrinkage, microstructure and mechanical properties of injection molded 17-4 PH stainless steel. Journal of materials science. 2002;37:3573-83.
[187] Ishizaki K, Komarneni S, Nanko M. Sintering mechanisms and advanced sintering methods for porous materials. Porous Materials. 1998:38-66.
[188] Rockland JG. The determination of the mechanism of sintering. Acta Metallurgica. 1967;15:277-86.
[189] German RM. Coarsening in sintering: grain shape distribution, grain size distribution, and grain growth kinetics in solid-pore systems. Critical reviews in solid state and materials sciences. 2010;35:263-305.
[190] Kuczynski G. The mechanism of densification during sintering of metallic particles. Acta Metallurgica. 1956;4:58-61.
[191] Kingery W. Densification during sintering in the presence of a liquid phase. I. Theory. Journal of Applied Physics. 1959;30:301-6.
[192] Wheat E, Vlasea M, Hinebaugh J, Metcalfe C. Sinter structure analysis of titanium structures fabricated via binder jetting additive manufacturing. Materials & Design. 2018;156:167-83.
[193] Suwanprateeb J, Sanngam R, Suvannapruk W, Panyathanmaporn T. Mechanical and in vitro performance of apatite–wollastonite glass ceramic reinforced hydroxyapatite composite fabricated by 3D-printing. Journal of Materials Science: Materials in Medicine. 2009;20:1281.
[194] Zocca A, Gomes CM, Mühler T, Günster J. Powder-bed stabilization for powder-based additive manufacturing. Advances in Mechanical Engineering. 2014;6:491581.
[195] Chinellato F, Wilbig J, Al-Sabbagh D, Colombo P, Günster J. Gas flow assisted powder deposition for enhanced flowability of fine powders: 3D printing of α-tricalcium phosphate. Open Ceramics. 2020;1:100003. 10.1016/j.oceram.2020.100003
[196] Zocca A, Lüchtenborg J, Mühler T, Wilbig J, Mohr G, Villatte T, et al. Enabling the 3D Printing of Metal Components in μ - Gravity. Advanced Materials Technologies. 2019;4:1900506. 10.1002/admt.201900506
[197] Zocca A, Lima P, Günster J. LSD-based 3D printing of alumina ceramics. Journal of Ceramic Science and Technology. 2017;8:141-7.
[198] Cima MJ, Oliveira M, Wang H, Sachs E, Holman R. Slurry-based 3DP and fine ceramic components. Proceedings of Solid Freeform Fabrication. 2001:216-23.
[199] Williams CB. Design and development of a layer-based additive manufacturing process for the realization of metal parts of designed mesostructure. 2008.
[200] Grau J, Moon J, Uhland S, Cima M, Sachs E. High green density ceramic components fabricated by the slurry-based 3DP process. 1997 International Solid Freeform Fabrication Symposium. 1997.
[201] Krause T, Engler S, Gunster J, Heinrich JG. Process and a device for producing ceramic molds. 2004.
[202] Gahler A, Heinrich JG, Günster J. Direct laser sintering of Al2O3-SiO2 dental ceramic components by layer-wise slurry deposition. J Am Ceram Soc. 2006;89:3076-80. 10.1111/j.1551-2916.2006.01217.x
[203] Mühler T, Gomes CM, Heinrich J, Günster J. Slurry-based additive manufacturing of ceramics. International Journal of Applied Ceramic Technology. 2015;12:18-25. 10.1111/ijac.12113
[204] Zocca A, Lima P, Günster J. LSD-based 3D printing of alumina ceramics. Journal of Ceramic Science and Technology. 2017;8:141-8.
[205] Lima P, Zocca A, Acchar W, Günster J. 3D printing of porcelain by layerwise slurry deposition. J European Ceram Soc. 2018:0-1. 10.1016/j.jeurceramsoc.2018.03.014

[206] Zocca A, Lima P, Diener S, Katsikis N, Günster J. Additive Manufacturing of SiSiC by Layerwise Slurry Deposition and binder jetting (LSD-print). J European Ceram Soc. 2019;39:3527-33. 10.1016/j.jeurceramsoc.2019.05.009
[207] Le Néel TA, Mognol P, Hascoët J-Y. A review on additive manufacturing of sand molds by binder jetting and selective laser sintering. Rapid Prototyping Journal. 2018;24:1325-36. 10.1108/RPJ-10-2016-0161
[208] Upadhyay M, Sivarupan T, El Mansori M. 3D printing for rapid sand casting—A review. Journal of Manufacturing Processes. 2017;29:211-20. https://doi.org/10.1016/j.jmapro.2017.07.017
[209] Walker JM, Prokop A, Lynagh C, Vuksanovich B, Conner B, Rogers K, et al. Real-time process monitoring of core shifts during metal casting with wireless sensing and 3D sand printing. Additive Manufacturing. 2019;27:54-60. https://doi.org/10.1016/j.addma.2019.02.018
[210] Walker J, Harris E, Lynagh C, Beck A, Lonardo R, Vuksanovich B, et al. 3D Printed Smart Molds for Sand Casting. International Journal of Metalcasting. 2018;12:785-96. 10.1007/s40962-018-0211-x
[211] Shangguan H, Kang J, Yi J, Zhang X, Wang X, Wang H, et al. The design of 3D-printed lattice-reinforced thickness-varying shell molds for castings. Materials. 2018;11:535.
[212] Shangguan H, Kang J, Deng C, Yi J, Hu Y, Huang T. 3D-printed rib-enforced shell sand mold for aluminum castings. The International Journal of Advanced Manufacturing Technology. 2018;96:2175-82. 10.1007/s00170-018-1783-6
[213] Snelling D, Kay R, Druschitz A, Williams C. Mitigating gas defects in castings produced from 3D printed molds. 117th Metalcasting Congress. 2012.
[214] Chhabra M, Singh R. Mathematical Modeling of Surface Roughness of Castings Produced Using ZCast Direct Metal Casting. Journal of The Institution of Engineers (India): Series C. 2015;96:145-55. 10.1007/s40032-014-0139-8
[215] Gill SS, Kaplas M. Comparative Study of 3D Printing Technologies for Rapid Casting of Aluminium Alloy. Materials and Manufacturing Processes. 2009;24:1405-11. 10.1080/10426910902997571
[216] Mostafaei A, Stevens EL, Ference JJ, Schmidt DE, Chmielus M. Binder jetting of a complex-shaped metal partial denture framework. Additive Manufacturing. 2018;21:63-8. https://doi.org/10.1016/j.addma.2018.02.014
[217] Inzana JA, Olvera D, Fuller SM, Kelly JP, Graeve OA, Schwarz EM, et al. 3D printing of composite calcium phosphate and collagen scaffolds for bone regeneration. Biomaterials. 2014;35:4026-34. https://doi.org/10.1016/j.biomaterials.2014.01.064
[218] Trombetta R, Inzana JA, Schwarz EM, Kates SL, Awad HA. 3D Printing of Calcium Phosphate Ceramics for Bone Tissue Engineering and Drug Delivery. Annals of Biomedical Engineering. 2017;45:23-44. 10.1007/s10439-016-1678-3
[219] Trenfield SJ, Madla CM, Basit AW, Gaisford S. Binder jet printing in pharmaceutical manufacturing. 3D Printing of Pharmaceuticals. 2018:41-54.
[220] Goyanes A, Buanz ABM, Hatton GB, Gaisford S, Basit AW. 3D printing of modified-release aminosalicylate (4-ASA and 5-ASA) tablets. European Journal of Pharmaceutics and Biopharmaceutics. 2015;89:157-62. https://doi.org/10.1016/j.ejpb.2014.12.003
[221] Fu Y, Yang S, Jeong SH, Kimura S, Park K. Orally fast disintegrating tablets: developments, technologies, taste-masking and clinical studies. Critical Reviews™ in Therapeutic Drug Carrier Systems. 2004;21.
[222] Wu BM, Borland SW, Giordano RA, Cima LG, Sachs EM, Cima MJ. Solid free-form fabrication of drug delivery devices. Journal of Controlled Release. 1996;40:77-87. https://doi.org/10.1016/0168-3659(95)00173-5

[223] Vorndran E, Klarner M, Klammert U, Grover LM, Patel S, Barralet JE, et al. 3D powder printing of β-tricalcium phosphate ceramics using different strategies. Advanced Engineering Materials. 2008;10:B67-B71.
[224] Fielding GA, Bandyopadhyay A, Bose S. Effects of silica and zinc oxide doping on mechanical and biological properties of 3D printed tricalcium phosphate tissue engineering scaffolds. Dental Materials. 2012;28:113-22.
[225] Zocca A, Elsayed H, Bernardo E, Gomes C, Lopez-Heredia M, Knabe C, et al. 3D-printed silicate porous bioceramics using a non-sacrificial preceramic polymer binder. Biofabrication. 2015;7:025008.
[226] Brown A, Zaky S, Ray H, Sfeir C. Porous magnesium/PLGA composite scaffolds for enhanced bone regeneration following tooth extraction. Acta Biomaterialia. 2015;11:543-53. https://doi.org/10.1016/j.actbio.2014.09.008
[227] Huang G-L, Zhou S-G, Yuan T. Development of a wideband and high-efficiency waveguide-based compact antenna radiator with binder-jetting technique. IEEE Transactions on Components, Packaging and Manufacturing Technology. 2017;7:254-60.
[228] Rojas-Nastrucci EA, Nussbaum JT, Crane NB, Weller TM. Ka-band characterization of binder jetting for 3-D printing of metallic rectangular waveguide circuits and antennas. IEEE Transactions on Microwave Theory and Techniques. 2017;65:3099-108.
[229] Zocca A, Gomes CM, Staude A, Bernardo E, Günster J, Colombo P. SiOC ceramics with ordered porosity by 3D-printing of a preceramic polymer. Journal of Materials Research. 2013;28:2243.
[230] Chen Q, Juste E, Lasgorceix M, Petit F, Leriche A. Binder jetting process with ceramic powders: Influence of powder properties and printing parameters. Open Ceramics. 2022;9:100218. https://doi.org/10.1016/j.oceram.2022.100218
[231] Kumar SV, Santhanam M. Particle packing theories and their application in concrete mixture proportioning: A review. Indian concrete journal. 2003;77:1324-31.
[232] Venables HJ, Wells JI. Powder mixing. Drug development and industrial pharmacy. 2001;27:599-612. 10.1081/DDC-100107316
[233] Zheng J, Carlson WB, Reed JS. The packing density of binary powder mixtures. J European Ceram Soc. 1995;15:479-83. 10.1016/0955-2219(95)00001-B
[234] German RM. Prediction of sintered density for bimodal powder mixtures. Metallurgical Transactions A. 1992;23:1455-65. 10.1007/BF02647329
[235] Cramer CL, Elliott AM, Kiggans JO, Haberl B, Anderson DC. Processing of complex-shaped collimators made via binder jet additive manufacturing of B4C and pressureless melt infiltration of Al. Materials & Design. 2019;180:9. 10.1016/j.matdes.2019.107956
[236] Freeze dryer scheme. biobase.en.made-in-china.com/product/MvAnyjSrfIYs/China-Biobase-Laboratory-Vacuum-Freeze-Dryer-with-Factory-Price
[237] Scopigno R, Cignoni P, Pietroni N, Callieri M, Dellepiane M. Digital fabrication techniques for cultural heritage: A survey. Computer Graphics Forum. 2017;36:6-21.
[238] Spray dryer scheme. labrotovap.com/how-does-spray-dryer-work/
[239] Maleksaeedi S, Eng H, Wiria F, Ha T, He Z. Property enhancement of 3D-printed alumina ceramics using vacuum infiltration. Journal of Materials Processing Technology. 2014;214:1301-6.
[240] Cao S, Xie FX, He XM, Zhang CF, Wu MP. Postprocessing Study for the Controllable Structures of Ceramic Green Parts Realized by a Flexible Binder Jetting Printing (BJP) Solution. Adv Mater Sci Eng. 2020;2020:17. 10.1155/2020/3865752
[241] Vogt U, Gorbar M, Dimopoulos-Eggenschwiler P, Broenstrup A, Wagner G, Colombo P. Improving the properties of ceramic foams by a vacuum infiltration process. J European Ceram Soc. 2010;30:3005-11.

[242] Lee I. Infiltration of alumina sol into SLS processed porous Al2O3-Al4B2O9 ceramic composites. Journal of materials science letters. 2001;20:223-6.
[243] Stumpf M, Travitzky N, Greil P, Fey T. Sol-gel infiltration of complex cellular indirect 3D printed alumina. J European Ceram Soc. 2018;38:3603-9.
[244] Kim EH, Choi HH, Jung YG. Fabrication of a ceramic core for an impeller blade using a 3D printing technique and inorganic binder. Journal of Manufacturing Processes. 2020;53:43-7. 10.1016/j.jmapro.2020.01.055
[245] Ayres TJ, Sama SR, Joshi SB, Manogharan GP. Influence of resin infiltrants on mechanical and thermal performance in plaster binder jetting additive manufacturing. Additive Manufacturing. 2019;30:10. 10.1016/j.addma.2019.100885
[246] Fleisher A, Zolotaryov D, Kovalevsky A, Muller-Kamskii G, Eshed E, Kazakin M, et al. Reaction bonding of silicon carbides by Binder Jet 3D-Printing, phenolic resin binder impregnation and capillary liquid silicon infiltration. Ceramics International. 2019;45:18023-9. https://doi.org/10.1016/j.ceramint.2019.06.021
[247] Robert JG. Contact angle, wetting, and adhesion: a critical review. Journal of adhesion science and technology. 1992;6:1269-302.
[248] Sayuti M, Sulaiman S, Vijayaram T, Baharudin B, Arifin M. Manufacturing and properties of quartz (SiO2) particulate reinforced Al-11.8% Si matrix composites. Composites and Their Properties, InTech. 2012:411-36.
[249] Washburn EW. The dynamics of capillary flow. Physical review. 1921;17:273.
[250] Rao SP, Tripathy SS, Raichur AM. Dispersion studies of sub-micron zirconia using Dolapix CE 64. Colloids and Surfaces A: Physicochemical and Engineering Aspects. 2007;302:553-8. https://doi.org/10.1016/j.colsurfa.2007.03.034
[251] Xie Z, Ma J, Xu Q, Huang Y, Cheng Y-B. Effects of dispersants and soluble counter-ions on aqueous dispersibility of nano-sized zirconia powder. Ceramics international. 2004;30:219-24.
[252] Rahaman M. Kinetics and mechanisms of densification. Sintering of advanced materials. 2010:33-64.
[253] Samant AN, Dahotre NB. Laser machining of structural ceramics—A review. J European Ceram Soc. 2009;29:969-93.
[254] Islam M, Campbell G. Laser machining of ceramics: a review. Material and Manufacturing Process. 1993;8:611-30.
[255] Chryssolouris G. Laser machining: theory and practice. 2013.
[256] Hellrung D, Yeh L-Y, Depiereux F, Gillner A, Poprawe R. High-accuracy micromachining of ceramics by frequency-tripled Nd: YAG lasers. Laser Applications in Microelectronic and Optoelectronic Manufacturing IV. 1999;3618:348-56.
[257] Juste E, Petit F, Lardot V, Cambier F. Shaping of Ceramic Parts by Selective Laser Melting of Powder Bed. Journal of Materials Research. 2014;29:2086-94. 10.1557/jmr.2014.127
[258] Pfeiffer S, Florio K, Makowska M, Sanchez DF, Swygenhoven H, Aneziris C, et al. Iron Oxide Doped Spray Dried Aluminum Oxide Granules for Selective Laser Sintering and Melting of Ceramic Parts. Advanced Engineering Materials. 2019;21. 10.1002/adem.201801351
[259] Chen B-C, Tsai Y-H, Ho C-Y, Chen C-S, Ma C. Parametric effects on femtosecond laser ablation of Al2O3 ceramics. Ceramics International. 2013;39:S341-S4. https://doi.org/10.1016/j.ceramint.2012.10.090
[260] Naglieri V, Gutknecht D, Garnier V, Palmero P, Chevalier J, Montanaro L. Optimized Slurries for Spray Drying: Different Approaches to Obtain Homogeneous and Deformable Alumina-Zirconia Granules. Materials. 2013;6:5382-97. 10.3390/ma6115382

[261] Preusch F, Adelmann B, Hellmann R. Micromachining of AlN and Al2O3 using fiber laser. Micromachines. 2014;5:1051-60.
[262] Liang J, Liu W, Li Y, Luo Z, Pang D. A model to predict the ablation width and calculate the ablation threshold of femtosecond laser. Applied Surface Science. 2018;456:482-6. https://doi.org/10.1016/j.apsusc.2018.06.093
[263] Xing Y, Liu L, Wu Z, Wang X, Huang P, Tang L. Fabrication and characterization of micro-channels on Al2O3/TiC ceramic produced by nanosecond laser. Ceramics International. 2018;44:23035-44. https://doi.org/10.1016/j.ceramint.2018.09.106
[264] Li D, Chen X, Guo C, Tao J, Tian C, Deng Y, et al. Micro Surface Texturing of Alumina Ceramic with Nanosecond Laser. Procedia Engineering. 2017;174:370-6. https://doi.org/10.1016/j.proeng.2017.01.155
[265] Xia M. Laser Theory and Technology. 2016.
[266] Sinha S. Thermal model for nanosecond laser ablation of alumina. Ceramics International. 2015;41:6596-603. https://doi.org/10.1016/j.ceramint.2015.01.106
[267] Melchels FPW, Feijen J, Grijpma DW. A review on stereolithography and its applications in biomedical engineering. Biomaterials. 2010;31:6121-30. https://doi.org/10.1016/j.biomaterials.2010.04.050
[268] Wang X, Jiang M, Zhou Z, Gou J, Hui D. 3D printing of polymer matrix composites: A review and prospective. Composites Part B: Engineering. 2017;110:442-58.
[269] Halloran JW, Tomeckova V, Gentry S, Das S, Cilino P, Yuan D, et al. Photopolymerization of powder suspensions for shaping ceramics. J European Ceram Soc. 2011;31:2613-9.
[270] Parandoush P, Lin D. A review on additive manufacturing of polymer-fiber composites. Composite Structures. 2017;182:36-53.
[271] Sa'ude N. Layered Manufacturing of Polymer Matrix Composites (PMC) Materials Via Fused Deposition Modeling (FDM). 2016.
[272] Cesarano P. Calvert, and Inventor: Sandia Corporation, Assignee,"Freeforming Objects with Low-Binder Slurry". US Patent.6027326.
[273] Lewis JA, Smay JE, Stuecker J, Cesarano J. Direct ink writing of three‐dimensional ceramic structures. J Am Ceram Soc. 2006;89:3599-609.
[274] Feilden E. Additive manufacturing of ceramics and ceramic composites via robocasting. 2017.
[275] Lee H, Lim CHJ, Low MJ, Tham N, Murukeshan VM, Kim Y-J. Lasers in additive manufacturing: A review. International Journal of Precision Engineering and Manufacturing-Green Technology. 2017;4:307-22.
[276] Criales L, Arisoy Y, Lane B, Moylan S, Donmez M, Özel T. Laser Powder Bed Fusion of Nickel Alloy 625: Experimental Investigations of Effects of Process Parameters on Melt Pool Size and Shape with Spatter Analysis. International Journal of Machine Tools and Manufacture. 2017;121. 10.1016/j.ijmachtools.2017.03.004
[277] Grzesik W. Hybrid manufacturing of metallic parts integrated additive and subtractive processes. Mechanik. 2018;91:468-75.
[278] Petrat T, Brunner-Schwer C, Graf B, Rethmeier M. Microstructure of Inconel 718 parts with constant mass energy input manufactured with direct energy deposition. Procedia Manufacturing. 2019;36:256-66. 10.1016/j.promfg.2019.08.033
[279] Sonmez FO, Hahn HT. Thermomechanical analysis of the laminated object manufacturing (LOM) process. Rapid Prototyping Journal. 1998.
[280] Liao Y, Li H, Chiu Y. Study of laminated object manufacturing with separately applied heating and pressing. The International Journal of Advanced Manufacturing Technology. 2006;27:703-7.

[281] Bryant ED. Development and verification of a thermal model for curved-layer laminated object manufacturing of polymer matrix composites. 1999.
[282] da Silva Bartolo PJ, Bártolo P. Innovative Developments in Design and Manufacturing: Advanced Research in Virtual and Rapid Prototyping: Proceedings of the 4th International Conference on Advanced Research in Virtual and Rapid Prototyping, Leiria, Portugal, 6-10 October 2009. 2010.
[283] Razavykia A, Brusa E, Delprete C, Yavari R. An Overview of Additive Manufacturing Technologies—A Review to Technical Synthesis in Numerical Study of Selective Laser Melting. Materials. 2020;13. 10.3390/ma13173895
[284] Bourell DL, Marcus HL, Barlow JW, Beaman JJ. Selective laser sintering of metals and ceramics. International journal of powder metallurgy (1986). 1992;28:369-81.
[285] Klocke F. Modern approaches for the production of ceramic components. J European Ceram Soc. 1997;17:457-65.
[286] Kirihara S. Creation of functional ceramics structures by using stereolithographic 3D printing. Transactions of JWRI. 2014;43:5-10.
[287] Chu T-MG, Orton DG, Hollister SJ, Feinberg SE, Halloran JW. Mechanical and in vivo performance of hydroxyapatite implants with controlled architectures. Biomaterials. 2002;23:1283-93.
[288] Eckel ZC, Zhou C, Martin JH, Jacobsen AJ, Carter WB, Schaedler TA. Additive manufacturing of polymer-derived ceramics. Science. 2016;351:58-62.
[289] Derby B. Additive manufacture of ceramics components by inkjet printing. Engineering. 2015;1:113-23.
[290] Bienia M, Lejeune M, Chambon M, Baco-Carles V, Dossou-Yovo C, Noguera R, et al. Inkjet printing of ceramic colloidal suspensions: Filament growth and breakup. Chemical Engineering Science. 2016;149:1-13.
[291] Maurath J, Willenbacher N. 3D printing of open-porous cellular ceramics with high specific strength. J European Ceram Soc. 2017;37:4833-42.
[292] Minas C, Carnelli D, Tervoort E, Studart AR. 3D printing of emulsions and foams into hierarchical porous ceramics. Advanced Materials. 2016;28:9993-9.
[293] Dellinger JG, Cesarano III J, Jamison RD. Robotic deposition of model hydroxyapatite scaffolds with multiple architectures and multiscale porosity for bone tissue engineering. Journal of Biomedical Materials Research Part A: An Official Journal of The Society for Biomaterials, The Japanese Society for Biomaterials, and The Australian Society for Biomaterials and the Korean Society for Biomaterials. 2007;82:383-94.
[294] Miranda P, Pajares A, Saiz E, Tomsia AP, Guiberteau F. Fracture modes under uniaxial compression in hydroxyapatite scaffolds fabricated by robocasting. Journal of Biomedical Materials Research Part A: An Official Journal of The Society for Biomaterials, The Japanese Society for Biomaterials, and The Australian Society for Biomaterials and the Korean Society for Biomaterials. 2007;83:646-55.
[295] Grida I, Evans JR. Extrusion freeforming of ceramics through fine nozzles. J European Ceram Soc. 2003;23:629-35.
[296] Park SA, Lee SH, Kim WD. Fabrication of porous polycaprolactone/hydroxyapatite (PCL/HA) blend scaffolds using a 3D plotting system for bone tissue engineering. Bioprocess and biosystems engineering. 2011;34:505-13.
[297] Jafari M, Han W, Mohammadi F, Safari A, Danforth S, Langrana N. A novel system for fused deposition of advanced multiple ceramics. Rapid Prototyping Journal. 2000.
[298] Friedel T, Travitzky N, Niebling F, Scheffler M, Greil P. Fabrication of polymer derived ceramic parts by selective laser curing. J European Ceram Soc. 2005;25:193-7.

[299] Löschau W, Lenk R, Scharek S, Teichgraber M, Nowotny S. Prototyping of complex-shaped parts and tools of Si/SiC-ceramics by selective laser sintering. Advances in science and technology. 1999:B567-B73.
[300] Wilkes J, Hagedorn YC, Meiners W, Wissenbach K. Additive manufacturing of ZrO2-Al2O3 ceramic components by selective laser melting. Rapid Prototyping Journal. 2013.
[301] Cui X, Ouyang S, Yu Z, Wang C, Huang Y. A study on green tapes for LOM with water-based tape casting processing. Materials Letters. 2003;57:1300-4.
[302] Liu S, Ye F, Liu L, Liu Q. Feasibility of preparing of silicon nitride ceramics components by aqueous tape casting in combination with laminated object manufacturing. Materials & Design (1980-2015). 2015;66:331-5.
[303] Andersen P. Particle packing and concrete properties. Materials Science of Concrete II. 1995:111-46.
[304] Shakhmenko G, Birsh J. Concrete mix design and optimization. Proceedings of the 2nd International Symposium in Civil Engineering. 1998:1-8.
[305] Banerjee S. Monolithic refractories: a comprehensive handbook. 1998.
[306] Reed JS. Principles of ceramics processing. 1995.
[307] Stroeven P, Stroeven M. Assessment of particle packing characteristics at interfaces by SPACE system. Image Analysis & Stereology. 2000;19:85-90.
[308] Du W, Ren X, Chen Y, Ma C, Radovic M, Pei Z. Model guided mixing of ceramic powders with graded particle sizes in binder jetting additive manufacturing. International Manufacturing Science and Engineering Conference. 2018;51357:V001T01A14.
[309] Carr LW, Chandrasekhara MS. Compressibility effects on dynamic stall. Progress in Aerospace Sciences. 1996;32:523-73. https://doi.org/10.1016/0376-0421(95)00009-7
[310] Agarwal P, Goyal A, Vaishnav R. Comparative Quality Assessment of Three Different Marketed Brands of Indian Polyherbal Formulation -Triphala Churna. 2021.
[311] Tool to measure anlge of repose optically. ginifab.com/feeds/angle_measurement/
[312] Wong HH, Kwan AK. Packing density of cementitious materials: part 1—measurement using a wet packing method. Materials and structures. 2008;41:689-701.
[313] Beausoleil C, Sarvestani HY, Katz Z, Gholipour J, Ashrafi B. Deep and high precision cutting of alumina ceramics by picosecond laser. Ceramics International. 2020;46:15285-96.
[314] Li K, Liao TW. Surface/subsurface damage and the fracture strength of ground ceramics. Journal of Materials Processing Technology. 1996;57:207-20.
[315] Wee LM, Crouse PL, Li L. A statistical analysis of striation formation during laser cutting of ceramics. The International Journal of Advanced Manufacturing Technology. 2008;36:699-706. 10.1007/s00170-006-0888-5
[316] Wang XC, Zheng HY, Chu PL, Tan JL, Teh KM, Liu T, et al. High quality femtosecond laser cutting of alumina substrates. Optics and Lasers in Engineering. 2010;48:657-63. https://doi.org/10.1016/j.optlaseng.2010.02.001
[317] Ma C, Ma Z, Gao L, Wu T, Wang F, Ishida H. Zirconium carbide-modified polymer-matrix composites with improved reflectivity under high-energy laser ablation. Ceramics International. 2019;45:17681-7. https://doi.org/10.1016/j.ceramint.2019.05.335
[318] Cappelli E, Orlando S, Sciti D, Montozzi M, Pandolfi L. Ceramic surface modifications induced by pulsed laser treatment. Applied Surface Science. 2000;154-155:682-8. https://doi.org/10.1016/S0169-4332(99)00422-5
[319] Radmanesh M, Ghanatir F, Radmanesh R. Comparing the efficacy of pulsed dye laser, Q-Switched Nd-YAG, CO2, and combined CO2 and Q-Switched Nd-YAG lasers for the treatment of cutaneous macular amyloidosis. Journal of Dermatological Treatment. 2021;32:258-60.
[320] Sun S, Durandet Y, Brandt M. Parametric investigation of pulsed Nd: YAG laser cladding of stellite 6 on stainless steel. Surface and Coatings Technology. 2005;194:225-31.

[321] Dahotre NB, Harimkar S. Laser fabrication and machining of materials. 2008.
[322] Andrews J, Atthey D. Hydrodynamic limit to penetration of a material by a high-power beam. Journal of Physics D: Applied Physics. 1976;9:2181.
[323] Mazumder J, Steen W. Heat transfer model for CW laser material processing. Journal of Applied Physics. 1980;51:941-7.
[324] Salonitis K, Stournaras A, Tsoukantas G, Stavropoulos P, Chryssolouris G. A theoretical and experimental investigation on limitations of pulsed laser drilling. Journal of Materials Processing Technology. 2007;183:96-103.
[325] Knowles MRH, Rutterford G, Karnakis D, Ferguson A. Micro-machining of metals, ceramics and polymers using nanosecond lasers. The International Journal of Advanced Manufacturing Technology. 2007;33:95-102. 10.1007/s00170-007-0967-2
[326] Steen W. Laser materials processing", London: Springer. 1991.
[327] Baeuerle D. Laser Processing and Chemistry Springer Verlag. Heidelberg Berlin. 2000;13.
[328] Samant AN, Dahotre NB. Differences in physical phenomena governing laser machining of structural ceramics. Ceramics International. 2009;35:2093-7.
[329] Tönshoff H, Kappel H. Surface modification of ceramics by laser machining. CIRP Annals. 1998;47:471-4.
[330] Tönshoff H, Hesse D, Gonschior M. Microstructuring with excimer lasers and reduction of deposited ablation products using a special gas nozzle with a vacuum system. International Congress on Applications of Lasers & Electro-Optics. 1994;1994:333-42.
[331] Samant AN, Dahotre NB. Computational predictions in single-dimensional laser machining of alumina. International Journal of Machine Tools and Manufacture. 2008;48:1345-53.
[332] Paschotta R. Encyclopedia of laser physics and technology. 2016.
[333] Wen Q, Luan X, Wang L, Xu X, Ionescu E, Riedel R. Laser ablation behavior of SiHfC-based ceramics prepared from a single-source precursor: Effects of Hf-incorporation into SiC. J European Ceram Soc. 2019;39:2018-27. https://doi.org/10.1016/j.jeurceramsoc.2019.01.040
[334] Luan X, Yuan J, Wang J, Tian M, Cheng L, Ionescu E, et al. Laser ablation behavior of Cf/SiHfBCN ceramic matrix composites. J European Ceram Soc. 2016;36:3761-8. https://doi.org/10.1016/j.jeurceramsoc.2016.04.010
[335] Yan Z, Ma Z, Liu L, Zhu S, Gao L. The ablation behavior of ZrB2/Cu composite irradiated by high-intensity continuous laser. J European Ceram Soc. 2014;34:2203-9. https://doi.org/10.1016/j.jeurceramsoc.2014.02.006
[336] Rihakova L, Chmelickova H. Laser micromachining of glass, silicon, and ceramics. Adv Mater Sci Eng. 2015;2015.
[337] McColm I. Refractory oxide ceramics. Ceramic Science for Materials Technologists, Chapman and Hall, New York. 1983:257.
[338] Nedialkov NN, Atanasov P, Sawczak M, Sliwinski G. Ablation of ceramics with ultraviolet, visible, and infrared nanosecond laser pulses. XIV International Symposium on Gas Flow, Chemical Lasers, and High-Power Lasers. 2003;5120:703-8.
[339] von Allmen M. Heating by Laser Light. Laser-Beam Interactions with Materials. 1987:49-82.
[340] SEGADO PN. Optimisation de poudres de phosphate de calcium à propriétés

contrôlées pour la fabrication additive. 2021.
[341] Santos D, Maurício AC, Sencadas V, Santos JD, Fernandes MH, Gomes PS. Spray drying: an overview. Pignatello, R(Comp) Biomaterials-Physics and Chemistry-New Edition InTech UK. 2018:9-35.

## References

[342] Dani NAB, OKUYAMA K. Progress in developing spray-drying methods for the production of controlled morphology particles: From the nanometer to submicrometer size ranges. Advanced powder technology: the international journal of the Society of Powder Technology, Japan. 2011;22:1-19.
[343] Dynamics C. Acoustosizer. pragolab.cz/documents/AcoustoSizer%20II-M.pdf
[344] Keyence. Rugosimeter. keyence.com/landing/microscope/pr_vk-x_feauture.jsp

# Acknowledgements

After 39 months of study & work, I have conducted this work with the help of everyone. I would like to express my sincere gratitude to all the people who have ever aided me during the work. Though the results could still be improved further, the scientific research never ends up reaching the best solution. It could be said that I'm satisfied with what we have done together after such a short period.

My sincere and hearty thanks and appreciations go firstly to my thesis director Prof. Anne LERICHE, whose suggestions and encouragement on the sides of study and life have given me much insight. It has been a great privilege to study under her guidance and supervision. Though sometimes I'm stubborn like a little donkey, she always patiently explained to me her experiences and shows generosity.

Of course, my big appreciation and gratitude go to my kind thesis supervisor Dr. Fabrice PETIT. It's my honor to benefit from his personality and intelligence, which will treasure my whole life. No matter the experiment design, scientific discussion, hypothesis on various results, and manuscript writing, we have deeply discussed together and his serious attitude and brilliant ideas definitely influence me a lot. Meanwhile, straight at point is what mainly he taught me, although I'm still not excellent at this. I do hope we could have time to have talks no matter what subjects in future.

Meanwhile, I want to great thanks Dr. Enrique JUSTE and Dr. Marie LASGORCEIX to be my excellent supervisors. I have troubled Enrique many times during 3 years with the machine and other experiments. His attitude toward work is extremely serious which I admire a lot. And his encouragements and rich discussion with him also make me confident. Marie helps me a lot when I worked in Maubeuge, especially for the work about post-infiltration. Her positive feedbacks always render me happy.

Special thanks to my dear friend Dr. Nicolas Somers, who has helped me a lot with research, administration work, and rich my entertainment life in Belgium together. I also would like to thanks all my colleagues in Belgium Ceramic Research Centre (BCRC), Laboratoire de Matériaux Céramiques et de Mathématiques (LMCPA) and Marion Technologies. Without your support, my work has no possibility to be finished.

The project "DOC-3D-PRINTING" funded my study and gave me the opportunity to do such interesting work and know lots of nice colleagues. Thanks to Dr. David Grossin and Guillaume

**Acknowledgements**

Gentils who created the project. Appreciations to all my friends in “DOC-3D-PRINTING”, who make my life fantastic.

Last, but not least, my warm and heartfelt gratitude to my mother Liping and father Guang, and all my family members and friends for their tremendous support, encouragement, and concerns, from more than 6000 miles away in China. Even though you cannot physically show up in my “happy end” defense, your support always exists in my mind. Without your hope, belief, and strength you gave me, I could not make this or even come to Europe. My gratitude to you is overwhelming.

We have passed extremely tough and unfortunately 3 years with the existence of COVID-19. All of us have suffered a lot from this disease. However, on the other side, we are reminded by this virus that a strong will and belief on scientific truth will lead us to the dawn.

# Abstract / Résumé


## Abstract:

Binder jetting (BJ) is an additive manufacturing process in which powders are selectively joined by a binder to reproduce an object layer by layer. Despite numerous advantages, BJ is still plagued by two main limitations. Ceramics printed with BJ remain very porous after sintering and exhibit poor finish surfaces. The present thesis is an attempt to circumvent these limitations.

A first part or our work was devoted to the study and development of an alumina powder compatible with a custom BJ equipment as well as to the optimization of the printing and densification conditions. The aim of this preliminary work was two-fold: firstly, to reproduce the state of the art of alumina manufacturing by binder jetting and secondly to develop a comprehensive methodology for the preparation of suitable ceramic powders for our machine (but in fact for all the machines technologically similar). This was also the technological baseline from which all further developments have been evaluated.

The influence of the powder characteristics (particle size distribution, morphology, flowability, packing density and roughness of powder beds) and printing parameters (recoating speed, layer thickness and binder saturation) were carefully assessed. The mechanical performances of sintered bodies were also evaluated and compared with the literature. Densities up to 64% of the theoretical density and average compressive strengths up to 102 MPa were obtained, similar to previously reported results.

To improve further the sintered density, we then developed a processing route involving a post-infiltration of pre-sintered bodies with a ceramic suspension. Different factors suspected to influence the process have been carefully studied such as the number of successive infiltrations, the influence of the pre-sintering temperature (rarely reported), solid loading, the infiltration duration, etc. The density and porosity distributions inside of the samples were also analysed using different tools combining SEM, X-ray Microtomography and porosity measurements. Using this approach, the densities of our sintered parts reached almost 90% of the theoretical density representing an increase of 33%.

Finally, the last part of our work was focused on the development of a hybrid process to improve the surface roughness and dimensional accuracy of fabricated parts. The idea was to use a laser directly mounted in the machine with the objective to refine the outline of each printed layers and produce sharper edges. A parametric study was carried out to assess the effects of different laser parameters like laser power, repetition frequency and scanning speed. The influence of the laser refining on the sharpness and roughness of simple bodies has been studied by comparing them with their “only printed” counterparts. It is shown that the laser refined samples exhibit better roughness (divided by 3) and sharpness thus demonstrating the benefit of the hybridization.


**Keywords**: Binder jetting, alumina, powder properties, printing parameters, post-infiltration, laser ablation

## Résumé:

Le Binder Jetting (BJ) ou projection de liant est un procédé de fabrication additive dans lequel des poudres sont sélectivement liées par un liant pour reproduire un objet couche par couche. Malgré ses nombreux avantages, le BJ souffre encore de deux limitations principales. Les céramiques imprimées avec cette technologie restent très poreuses après frittage et présentent des états de surface rugueux. La présente thèse est une tentative de contourner ces limitations.

Une première partie de notre travail a été consacrée à l'étude et au développement d'une poudre d'alumine compatible avec un équipement BJ conçu spécifiquement ainsi qu'à l'optimisation des conditions d'impression et de densification. L'objectif de ce travail préliminaire était double : d'une part, reproduire l'état de l'art de la fabrication d'alumine par jet de liant et d'autre part, développer une méthodologie complète pour la préparation de poudres céramiques adaptées à notre machine (mais en fait à toutes les machines technologiquement similaires). Il s'agissait également de constituer un point de reference en comparaison duquel tous nos développements ultérieurs ont été évalués.

L'influence des caractéristiques de la poudre (distribution granulométrique, morphologie, fluidité, densité de tassement et rugosité des lits de poudre) et des paramètres d'impression (vitesse de recouvrement, épaisseur de la couche et saturation du liant) a été soigneusement évaluée. Les performances mécaniques des corps frittés ont également été évaluées et comparées à celles de la littérature. Des densités allant jusqu'à 64% de la densité théorique et des résistances à la compression allant jusqu'à 102 MPa ont été obtenues, similaires aux résultats précédemment rapportés.

Afin d'améliorer encore la densité, nous avons ensuite développé un procédé de traitement impliquant une post-imprégnation des pièces préfrittées avec une suspension céramique. Différents facteurs susceptibles d'influencer le processus ont été soigneusement étudiés, tels que le nombre d'imprégnations successives, l'influence de la température de préfrittage (rarement rapportée), le taux de charge solide, la durée d'imprégnation, etc. Les distributions de densité et de porosité à l'intérieur des échantillons ont également été analysées à l'aide de différents outils combinant MEB, microtomographie à rayons X et mesures de porosité. Grâce à cette approche, les densités de nos pièces frittées ont atteint près de 90% de la densité théorique, soit une augmentation de 33%.

Enfin, la dernière partie de notre travail a porté sur le développement d'un procédé hybride pour améliorer la rugosité de surface et la précision dimensionnelle des pièces fabriquées. Notre idée était d'utiliser un laser directement monté dans la machine avec l'objectif d'affiner le contour de chaque couche imprimée et de produire des bords plus nets. Une étude paramétrique a été menée pour évaluer les effets de différents paramètres du laser comme la puissance du laser, la fréquence de répétition et la vitesse de balayage. L'influence du raffinage laser sur la netteté et la rugosité de pieces simples a été étudiée en les comparant avec leurs homologues "seulement imprimés". Il est montré que les échantillons repris au laser présentent une meilleure rugosité (divisée par 3) et une meilleure netteté, démontrant ainsi les avantages de l'hybridation.


**Mots-clés**: Jet de liant, alumine, propriétés de la poudre, paramètres d'impression, post-infiltration, ablation laser.